

UNIVERSITY OF TRENTO

DOCTORAL THESIS

**Eco-hydraulic quantification of
hydropeaking and thermopeaking:
development of modeling and
assessment tools**

Author:

Davide VANZO

Supervisor:

Prof. Guido ZOLEZZI

Dr. Annunziato SIVIGLIA

*A thesis submitted in fulfilment of the requirements
for the degree of Doctor of Philosophy*

in the

Department of Civil, Environmental and Mechanical Engineering

April 2015

Doctoral Thesis in Environmental Engineering, 27th cycle

Department of Civil, Environmental and Mechanical Engineering, University of Trento

Academic year 2013-2014

Supervisor: Prof. Guido Zolezzi, University of Trento

Dr. Annunziato Siviglia, ETH Zurich

Abstract

Eco-hydraulic quantification of hydropeaking and thermopeaking: development of modeling and assessment tools

River reaches worldwide historically experience morphological regulations, as channelization, as well as flow regime alterations, which often lead to degradation of freshwater ecosystems. In last seven decades a large number of dams have been designed and built worldwide contributing to such river hydromorphological alterations. In alpine and piedmont regions river reaches often experience anthropogenic flow regime alteration due to hydropower production. The fluctuating flow regime typical of river reaches downstream hydropower plant releases (*hydropeaking*) is known to produce several adverse ecological effects, strongly linked to morphological characteristics of the downstream channel. Hydropeaking can also alter the thermal regime of the receiving water body (*thermopeaking*) if released hypolimnetic water has different temperature from surface water; also thermopeaking can have adverse consequences on river environment. In a changing world with respect to renewable energy production but also to global warming, the understanding of hydropeaking and thermopeaking ecological impacts represent a lively research challenge.

The first part of the present thesis is dedicated to the characterization and quantification of hydropeaking and thermopeaking alterations. Adopting a statistical approach on an extended dataset of Alpine and Norwegian rivers, a suite of indicators have been designed and exploited to identify the degree of alteration of both hydrological and thermal regime. The study provides two screening tools that can be exploited by environmental managers in the identification of critically altered river reaches. The second part is dedicated to the development of a two-dimensional numerical shallow-water model able to simulate surface water passive tracer transport over complex morphologies, exploitable in the numerical investigation of river thermal transport dynamics. In the third part the interaction between hydropeaking waves and receiving reach morphology has been investigated via numerical modeling. The work consists on a first quantitative attempt to investigate the eco-hydraulic response of river reaches with different channel morphologies to hydropeaking waves of different intensities. Such general approach can be applied to a specific case to support the choice of the most effective river restoration strategy leading to the optimal specific eco-hydraulic conditions. Finally, the last part reports an application of the designed approaches and tools to Lundesokna River, a Norwegian river affected by hydropeaking.

Acknowledgements

First, and foremost, I would like to thank my supervisors Annunziato Siviglia and Guido Zolezzi for their support and encouragement during these 3 years of PhD programme. I am confident that their patience, dedication, intelligence and positiveness will continue to inspire me for a long time to come. I would also like to thank all the colleagues of my research group for their important feedback and advice on my work. A sincere thank also to all the co-authors of my scientific publications and to the master student who works with me for some months.

I had the opportunity to spend an abroad research period at the ETH in Zurich. I would like to thank the VAW group members for their hospitality and I am grateful to Prof. Robert M. Boes and Dr. David Vetsch for the great opportunity and experience. I also spent a period at the NTNU in Trondheim, thanks to the precious contribution of the Centre for Environmental Design of Renewable Energy-CEDREN. I am grateful to Prof. Knut Alfredsen for the welcome, the help and the constant support during my staying in Norway. I would also like to thank Dr. Roser Casas-Mulet for the fruitful collaboration and the sharing of data and opinions. The abroad research experiences had been important for my professional and human growth, hence I would like to thank also all the new friends and colleagues I met in Zurich and Trondheim.

I would like to thank Dr. Alejandra G. Garcia Lugo for sharing data of her laboratory experiments. For the same reason, I would like to thank the local and national authorities which provided the data series that I analysed in my thesis. In particular, Ufficio Dighe - Servizio Prevenzione Rischi of the Autonomous Province of Trento, Swiss Federal Office for the Environment (BAFU) and Norwegian Water Resources and Energy Directorate (NVE).

I am grateful to all the colleagues and friends I met in these years, whom share with me courses, efforts, fails and achievements. In particular I would like to thank Dr. Mauro Carolli for the fruitful professional collaboration as well as the sincere friendship. I am grateful to all my closest friends which always supported me in last 3 years, particularly to my beloved flatmates. Last, but not least, I would like to thank my parents and all my family for their unconditional and endless support.

Contents

Abstract	i
Acknowledgements	iii
Contents	v
List of Figures	ix
List of Tables	xv
1 General introduction	1
1.1 Context	1
1.2 Scientific background	2
1.2.1 Hydropeaking and thermopeaking alterations	3
1.2.2 Overview of the possible mitigation strategies	4
1.3 Specific research questions and thesis outline	5
2 Characterization of sub-daily hydrological and thermal alterations in Alpine rivers affected by hydropeaking	9
2.1 Introduction	9
2.2 Methods	11
2.2.1 River temperature dataset	11
2.2.2 Indicators	12
2.2.2.1 Sub-daily temperature rate of change: TP_{Δ}	16
2.2.2.2 Frequency of sub-daily temperature fluctuations: TP_{En}	16
2.2.3 Thermopeaking thresholds	18
2.2.4 Correlation analysis	19
2.3 Results	20
2.3.1 Thermo-peaked vs thermo-unpeaked stations: comparison of thermopeaking indicators	20
2.3.2 Correlation between physiographic station characteristics and indicators	21
2.3.3 Time-interval selection and threshold calculation	22
2.3.4 Quantification of thermopeaking alteration for the peaked stations	25
2.4 Discussion	25

2.5	Conclusions	30
3	Two-dimensional numerical model of hydro- and thermo-dynamics in rivers with complex morphology	31
3.1	Introduction	31
3.2	Governing equations	33
3.2.1	Hyperbolic reformulation of the equations	34
3.2.2	Hyperbolicity of the relaxation system	36
3.2.3	Relaxation system versus the original system	38
3.2.4	Wave patterns and maximum eigenvalue	39
3.3	Numerical solution	41
3.3.1	Splitting procedure	41
3.3.1.1	Solution of IVP1 and IVP3	42
3.3.1.2	Solution of IVP2	42
3.3.1.3	Second order extension	43
3.3.1.4	Second order locally implicit ADER scheme for relaxation source terms	45
3.3.1.5	Numerical treatment of the bed topography	45
3.4	Numerical tests	46
3.4.1	Extended C-property	46
3.4.2	Second-order experimental convergence: 2D advection-diffusion test	48
3.4.3	Long term evolution of a squared wave: 1D advection-diffusion test	49
3.4.4	2D dam break over a complex domain	50
3.4.5	Advection-diffusion of a passive tracer in a complex morphology . .	54
3.5	Conclusions	56
4	An eco-hydraulic modeling of the interactions between hydropeaking and river morphology	59
4.1	Introduction	59
4.2	Methods	61
4.2.1	Hydropeaking events	62
4.2.2	Channel morphologies	63
4.2.3	Hydro-morphological configurations	64
4.2.4	Hydraulic modeling	66
4.2.5	Ecologically Relevant Hydraulic Parameters	66
4.2.5.1	Hydro-Morphological Index of Diversity	67
4.2.5.2	Macroinvertebrate drift	68
4.2.5.3	Fish stranding	69
4.2.5.4	Overall comparison of different ERHPs	70
4.3	Results	70
4.3.1	Spatial distribution of flow depth and velocity	71
4.3.2	Hydro-Morphological Index of Diversity	72
4.3.3	Macroinvertebrate drift	74
4.3.4	Fish stranding	77

4.3.5	Comparative analysis of ERHPs response to hydropeaking for different morphologies	78
4.4	Discussion	81
4.4.1	Morphological controls on hydropeaking effects	81
4.4.2	Implications for restoration of hydropeaking rivers	83
4.4.3	Applicability and limitations of the proposed approach	85
4.5	Conclusions	87
5	Unsteady modeling of fish stranding risk under hydropeaking conditions	89
5.1	Fish stranding risk and river morphology: unsteady numerical modeling . .	90
5.1.1	Methods	90
5.1.1.1	Hydropeaking events	91
5.1.1.2	Ecologically Relevant Hydraulic Parameters for fish stranding	92
5.1.2	Results	94
5.1.2.1	Spatial distribution of flow depth, velocity and rate of change	94
5.1.2.2	Longitudinal distribution of wetted area variation and maximum dewatering rate	96
5.1.2.3	Tradeoffs between wetted area variation and dewatering rate	103
5.1.2.4	Subarea length sensitivity analysis	105
5.1.3	Discussion	105
5.2	Dewatering scenario modeling in Lundesokna River	111
5.2.1	Study-site description	111
5.2.2	Model setup	114
5.2.2.1	Roughness calibration	114
5.2.3	Dewatering scenarios	115
5.2.4	Results	117
5.2.4.1	Reach-scale statistics	118
5.2.4.2	Local variation of wetted area	120
5.2.4.3	Local maximum dewatering rate	120
5.2.4.4	Local duration of dry conditions	126
5.2.5	Discussion	128
5.3	Conclusions	132
6	Conclusions	135
6.1	Summary of chapter conclusions	135
6.2	Synthesis of the research questions	137
6.3	Main conclusions	138
6.4	Recommendations for further research	139
	Bibliography	141
	Appendix A	152

List of Figures

1.1	Map of hydropower stations with power capacities of more than 10 <i>MW</i> in the Alps (Alpine Convention, 2009).	2
2.1	Location of the river temperature sampling stations in Switzerland and in the Autonomous Province of Trento (Italy).	12
2.2	Example of a 48-hours thermograph for an unpeaked station (A) and a peaked one (B).	15
2.3	Example of Power Spectral Density of thermal signal for one unaltered (A) and one altered (B) station, respectively.	17
2.4	Cumulative distributions of $TP_{\Delta,i}$ (with time interval of 30 minutes) for selected representative peaked and unpeaked stations.	21
2.5	Indicators for the reference group and the obtained thresholds.	25
2.6	Indicators TP_{En} and TP_{Δ} for the peaked group stations; labels refer to Table 2.2. The graph is horizontally splitted for the sake of clarity in visualizing the most impacted station in the dataset along with the other ones.	26
2.7	Thermopeaking indicators for Noce River's stations. Boxed stations (1,3 and 6) lay within the reference group (Table 2.1). The box illustrates schematically the location of the 8 stations along the Noce River system, where the key hydropower plants and their release locations, causing hydropeaking, are reported.	28
2.8	Recasted formulation of the indicators TP_{Δ} (exceeding probability of threshold) and TP_{En} scaled with threshold.	29
3.1	Sketch of water surface and channel bottom.	33
3.2	Possible wave patters in space ($n-t$) for the relaxation system.	39
3.3	Sketch of the triangular mesh with the adopted notation.	41
3.4	Extended C-property test: 3D snapshot of water and bottom elevation at $t = 60 s$	48
3.5	3D snapshot of advection-diffusion test: initial condition ($t = 0 s$) and final configuration at $t = 1 s$. The exact solution is given by the surface while blue rings represent the exact solution.	49
3.6	Concentration longitudinal profiles at different output times ($t = 300 s; 600 s; 1000 s$): black line represents the exact solution while blue diamonds and red circles represent first and order scheme, respectively. (A) $k = 10^{-4} m^2/s$, (B) $k = 1 m^2/s$	51

3.7	Dam break test over three humps: 3D snapshots of water elevation at different times.	52
3.8	Dam break test over three humps: 2D contour plots of water depth at different times.	53
3.9	Dam break test over three humps: 2D contour plots of pollutant concentration at different times.	53
3.10	Time evolution of the relative errors of water and passive tracer mass.	54
3.11	Pollutant concentration (C) wave input in time.	55
3.12	Distribution of simulated water depth and flow velocity for the real-scale test.	55
3.13	Pollutant concentration C distribution for pure advection ($k = 10^{-9} m^2/s$) and advection-diffusion ($k = 0.1 m^2/s$) tests; y direction is magnified for the sake of legibility.	57
4.1	Hydro-morphological alteration space: qualitative ecological response to interaction between hydropeaking pressure (vertical axis) and morphological complexity (horizontal axis) of receiving river reach, inspired by Baumann <i>et al.</i> , 2012. Downward vertical shifts in the plot correspond to reducing hydropeaking intensities, while horizontal shifts correspond to increasing morphological complexity (right to left). Red and blue regions represent the expected worst and best state from ecological point of view, respectively.	60
4.2	The hydropeaking event is schematized as a rectangular wave, varying from a base (Q_{base}) and a peak (Q_{peak}) discharge.	63
4.3	Example of (y-z) cross section (on the top) and (x-y) planar view for three different morphologies: flat bed (1), alternate bars (3) and braiding network (5), with a widening ratio W/W_0 of 1, 2 and 6.66 respectively.	65
4.4	Example of the transversal slices used for the local evaluation of the wetted area variation; morphology No. 3 ($W = 30 m$).	69
4.5	Box and whiskers plot for the distributions of water depth (A and B) and of longitudinal flow velocity (C and D) of the considered six morphologies (from 1 to 6) for the production pattern A, both for base (A and C) and peak flow conditions (B and D).	71
4.6	HMID index versus six widening ratios. Series represent the different release patterns (A,B and C) both for peak and base flow; dotted lines represent category thresholds proposed by Gostner <i>et al.</i> (2013a).	73
4.7	Hydro-morphological alteration space of HMID for base (A) and peak flow (B). Blue regions represent configuration with $HMID > 9$ (morphologically natural), red regions with $HMID < 5$ (morphologically heavily altered) while intermediate green regions represent transitional configurations. Black dots correspond to configurations of the numerical runs while blue labels are the obtained HMID values.	75

4.8	Panel A: mean of the bottom shear stress versus six widening ratios corresponding to the different morphologies; the dotted line denotes the drift threshold $\tau_{drift} = 10 \text{ N/m}^2$ (Hauer <i>et al.</i> , 2012). Panel B: percentage of area with bottom shear stress lower than the drift threshold τ_{drift} versus six widening ratios. In both panels the series represent the different release patterns (A,B and C) both for peak and base flow.	76
4.9	Hydro-morphological alteration space of macroinvertebrate drift for base (A) and peak flow (B). Blue regions represent configurations with dominant (more then 75%) settling of macroinvertebrate communities (sink areas) while red ones represent scenarios dominated by macroinvertebrate drifting (source areas). Black dots correspond to configurations of the numerical runs while blue labels are the percentages of area with sink behaviour.	76
4.10	Mean wetted area variation versus six widening ratios; dotted line is the threshold proposed in Swiss protocol (Baumann <i>et al.</i> , 2012) to discriminate the low stranding risk (good status).	77
4.11	Hydro-morphological alteration space of ERHPs variation passing from Q_{base} to Q_{peak} : (A) variation of HMID index; (B) variation of area with sink behaviour; (C) percentage of area with low risk of stranding.	79
4.12	Classes of hydro-morphological quality for the three ERHPs under repeated hydropeaking.	80
5.1	Simplified hydropeaking waves for the unsteady stranding risk modeling. In lowercase letters the output points for the dewatering rate evaluation are reported.	91
5.2	Stranding risk classification space based on both criteria of the Swiss water protection guidelines (Baumann <i>et al.</i> , 2012). Coloured region represent status classification: blue, green and red represent <i>very good</i> , <i>good</i> and <i>moderate-bad</i> status, respectively.	93
5.3	Flow velocity (A) and water depth (B) distributions at base ($Q_{base} = 5 \text{ m}^3/\text{s}$) and peak ($Q_{peak} = 50 \text{ m}^3/\text{s}$) flow stage of the dewatering pattern A. Morphologies 1, 3, and 5 correspond to flat bed ($W/W_0 = 1$), alternate bars ($W/W_0 = 2$) and braiding network ($W/W_0 = 6.66$), respectively.	95
5.4	Box and whiskers plot of water depth distributions during dewatering pattern A (from 50 to 5 m^3/s) for three different morphologies.	97
5.5	Box and whiskers plot of longitudinal flow velocity distributions during dewatering pattern A (from 50 to 5 m^3/s) for three different morphologies.	98
5.6	Box and whiskers plot of dewatering rate distributions during dewatering pattern A (from 50 to 5 m^3/s) for three different morphologies.	99
5.7	Wetted area variation along longitudinal direction x for three different morphological configurations: flat bed (No. 1), alternate bars (No. 3) and braiding network (No. 5). Panels A and B show the dewatering pattern A ($Q_{peak}/Q_{base} = 10$) and C ($Q_{peak}/Q_{base} = 3.25$), respectively.	100
5.8	Maximum dewatering rate along longitudinal direction x for three different morphological configurations: flat bed (No. 1), alternate bars (No. 3) and braiding network (No. 5). Panel A and B shows the dewatering pattern A ($Q_{peak}/Q_{base} = 10$) and C ($Q_{peak}/Q_{base} = 3.25$), respectively.	102

5.9	Maximum dewatering rate vs. wetted area variation for the six investigated morphologies (from No. 1 to No. 6). Each panel corresponds to a different dewatering pattern (A, B and C).	104
5.10	Stacked column chart of the stranding risk for the six considered morphologies (column 1 to 6) and the three dewatering pattern (panel A to C). . . .	106
5.11	Stacked column chart of the stranding risk for the six considered morphologies (column 1 to 6) and dewatering pattern A ($Q_{peak}/Q_{base} = 10$). Different panels (A to D) refer to different choice of subarea (i.e. transverse slice) length.	107
5.12	Stacked column chart of the stranding risk for the six considered morphologies (column 1 to 6) and dewatering pattern B ($Q_{peak}/Q_{base} = 5.5$). Different panels (A to D) refer to different choice of subarea (i.e. transverse slice) length.	108
5.13	Stacked column chart of the stranding risk for the six considered morphologies (column 1 to 6) and dewatering pattern C ($Q_{peak}/Q_{base} = 3.25$). Different panels (A to D) refer to different choice of subarea (i.e. transverse slice) length.	109
5.14	Maximum dewatering rate vs. wetted area variation for the 18 simulated hydro-morphological configurations. Triangles, circles and squares represent dewatering pattern A, B and C, respectively; colours identify the six investigated morphologies.	110
5.15	(a) Illustration of the Lundesokna hydropower system and (b) its location in Norway, from Casas-Mulet <i>et al.</i> (2014a).	112
5.16	Example of flow discharge fluctuations in Lundesokna River due to hydropeaking. Hydrograph shows the days from 16th (00:00 am) to 18th (11:00 pm) of December 2011.	113
5.17	Map of the lowermost 2km of Lundesokna River with location of some study-site from Casas-Mulet <i>et al.</i> (2014a).	113
5.18	Sketch of the computational domain in correspondence of the Site 2 of Casas-Mulet <i>et al.</i> (2014a).	114
5.19	Roughness calibration: simulated against measured water levels; red continuous line represents the linear regression.	116
5.20	Dewatering scenarios for stranding risk modeling in Lundesokna River. . .	117
5.21	Reach-scale statistics: water depth (A) and flow velocity (B) median values during dewatering phase for each simulated scenario.	118
5.22	Reach-scale statistics: wetted area variation (A) and dewatering rate median value (B) during dewatering phase for each simulated scenario. . . .	119
5.23	Variation of wetted area: in blue the wetted area at base flow, in red the area dried passing from production stage ($20\text{ m}^3/\text{s}$) to base flow ($0.5\text{ m}^3/\text{s}$). 120	
5.24	Variation of wetted area: in blue the wetted area at base flow, in red the area dried passing from production stage ($20\text{ m}^3/\text{s}$) to base flow ($0.5\text{ m}^3/\text{s}$). Particular of Site 1 and 2 (A) and Site 3 (B).	121
5.25	Maximum dewatering rate in last 20 cm of water column for scenarios S0 and S6.	123
5.26	Maximum dewatering rate in last 20 cm of water column for scenarios S0, S1, S2, S5 and S6; particular of Site 1 and 2.	124

5.27	Maximum dewatering rate in last 20 <i>cm</i> of water column for scenarios S0, S1, S2, S5 and S6; particular of Site 3.	125
5.28	Percentages of maximum dewatering rate in last 20 <i>cm</i> of water column for the entire domain and for all the simulated scenarios.	126
5.29	Duration of dry conditions (in minutes) for scenarios S0, S1, S2, S5 and S6; particular of Site 1 and 2.	127
5.30	Duration of dry conditions (in minutes) for scenarios S0, S1, S2, S5 and S6; particular of Site 3.	129
5.31	Percentages of dry condition duration for the entire domain and for all the simulated scenarios.	130
A.1	Geographic distribution of the a) Italian gauging stations, b) Swiss gauging stations, and c) Norwegian gauging stations. Circles represent the unpeaked stations, and crosses the peaked stations.	5
A.2	Cumulative distribution of $HP1_i$ for some representative (a) unpeaked and (b) peaked gauged stations.	12
A.3	Cumulative distribution of $HP2_i$ for some representative (a) unpeaked and (b) peaked gauged stations.	13
A.4	Dataset distribution in classes of different pressures for Italian (panel a), Swiss (panel b) and Norwegian (panel c) data. Thresholds are calculated for each country. Different groups are denoted with cross (unpeaked) and circles (peaked). The space in the $HP1$ and $HP2$ plane is divided in 4 different regions identified by the two thresholds TR_{HP1} and TR_{HP2} which were computed for the three geographical regions considered. The four regions identify the three different classes of hydropeaking pressure: class 1 (absent or low pressure, green colour, left bottom); classes 2a and 2b (moderate pressure, yellow colour, right bottom and left top respectively) and class 3 (high pressure, red colour, right top).	14
A.5	Global distribution of all datasets in classes of different pressures. Thresholds calculated over the entire unpeaked dataset. Different groups are denoted with cross (unpeaked) and circles (peaked). The four regions identify the three different classes of hydropeaking pressure: class 1 (absent or low pressure, green colour, left bottom); classes 2a and 2b (moderate pressure, yellow colour, right bottom and left top respectively) and class 3 (high pressure, red colour, right top).	15
A.6	Distribution of six stations used as control group. The displayed thresholds are the global thresholds. Different groups are denoted with cross (unpeaked) and circles (peaked). The four regions identify the three different classes of hydropeaking pressure: class 1 (absent or low pressure, green colour, left bottom); classes 2a and 2b (moderate pressure, yellow colour, right bottom and left top respectively) and class 3 (high pressure, red colour, right top).	18

List of Tables

2.1	Unpeaked station labels (reference group) and main physiographic characteristics of the subtended catchments.	13
2.2	Peaked station labels and main physiographic characteristics of the subtended catchments.	14
2.3	Example of TP_{En} (6 hour time span, $n = 6$ in Equation 2.5) for some representative peaked and unpeaked stations.	21
2.4	Spearman’s correlations between proposed indicators and physiographic characteristics of the reference group stations.	22
2.5	Threshold values of TP_{Δ} and number of peaked stations above them (outliers) for different time interval Δt	24
2.6	Threshold values of TP_{En} and number of peaked stations above them (outliers) for different oscillating period band T.	24
2.7	Thermal alteration classification for the Noce catchment stations. First 3 stations have no hydropeaking (HP column) and are within the reference group (Table 2.1).	27
3.1	Numerical verification of the extended C-property. Error norms at time $t = 60$ s for H , $q = \sqrt{q_x^2 + q_y^2}$ and q_c	47
3.2	2D advection-diffusion test: error norms and experimental convergence rates at final time $t = 1$ s.	49
4.1	Hydro-morphological configurations: three different hydropeaking patterns (column A, B and C of upper panel) characterized by same electricity production Q_{prod} but different ratio of Q_{peak}/Q_{base} . Six self-formed morphologies (row 1 to 6 of lower panel) upscaled from experimental runs; widening ratio refers to the first morphology of 15 m width.	63
4.2	Some examples of European river widening projects.	85
5.1	Swiss threshold on wetted area variation for stranding risk quantification (Baumann <i>et al.</i> , 2012).	92
5.2	Swiss threshold on dewatering rate for stranding risk quantification (Baumann <i>et al.</i> , 2012).	93
5.3	Roughness calibration: descriptive statistics (all in m) for the water level absolute error.	115
A.1	Summary of features of the three datasets.	4

A.2	Italian gauged stations grouped by the values of the hydropeaking indicators <i>HP1</i> and <i>HP2</i> , and relative hydropeaking pressure class (calculated from a one year data record).	7
A.3	Swiss gauged stations grouped by corresponding maximum and minimum value of hydropeaking indicators <i>HP1</i> and <i>HP2</i> and hydropeaking pressure class changes (calculated based on six year data record).	8
A.4	Norwegian gauged stations grouped by corresponding maximum and minimum value of hydropeaking indicators <i>HP1</i> and <i>HP2</i> and hydropeaking pressure class changes (calculated based on six year data record).	9
A.5	Hydropeaking threshold variability as function of: country, different years and number of gauged stations used for the computation.	16
A.6	Frequency of class changes for different hydropeaking threshold, calculated for all the possible sub-datasets. In round brackets the frequency of changes between class 1 and class 3.	17
A.7	Values of the two indicators calculated on the simulated data and comparison between classes of simulated data and measured data series.	19

Chapter 1

General introduction

1.1 Context

Being a crucial resource for human communities development, river reaches historically experienced anthropogenic hydromorphological alterations. Such modifications often lead to severe changes in morphodynamic processes and to degradation of freshwater ecosystems (e.g. Surian and Rinaldi, 2003; Elosegi *et al.*, 2010). In last century a large number of dams have been designed and built worldwide, strongly modifying the river environment at different scales (e.g. Grant *et al.*, 2003). The multiple impacts due to dams have been widely investigated from a biological, ecological, morphological and hydrological point of view (e.g. Petts and Gurnell, 2005; Schmidt and Wilcock, 2008; Tealdi *et al.*, 2011).

In last decades hydropower plants gained progressively a relevant role in the world of electricity production due to the high flexibility in responding to the request of the deregulated energy market and due to its storage potential. Sharp releases of water are nowadays operated on a daily and sub-daily time scales in order to follow the trend of the energy market (Holland and Mansur, 2008). Such dam operations cause downstream alterations which have to be identified, investigated and reduced, as prescribed by the Water Framework Directive (European Commission, 2000). This is a relevant task to be addressed by the European countries, as about 550 hydropower stations with power output greater than 10 *MW* (*large* stations) are distributed in Alpine area (Figure 1.1, Alpine Convention, 2009). In Italy there are currently about 300 large hydropower plants, mainly located in the Alpine region, which cover more than one third of the national electricity consumption (G.S.E., 2012).

In the near future an increase and improvement of the current hydropower production is expected in Europe, in order to reach the target of at least a 20% share of energy from renewable sources by 2020, as indicated in the European Directive 2009/28/EC (European

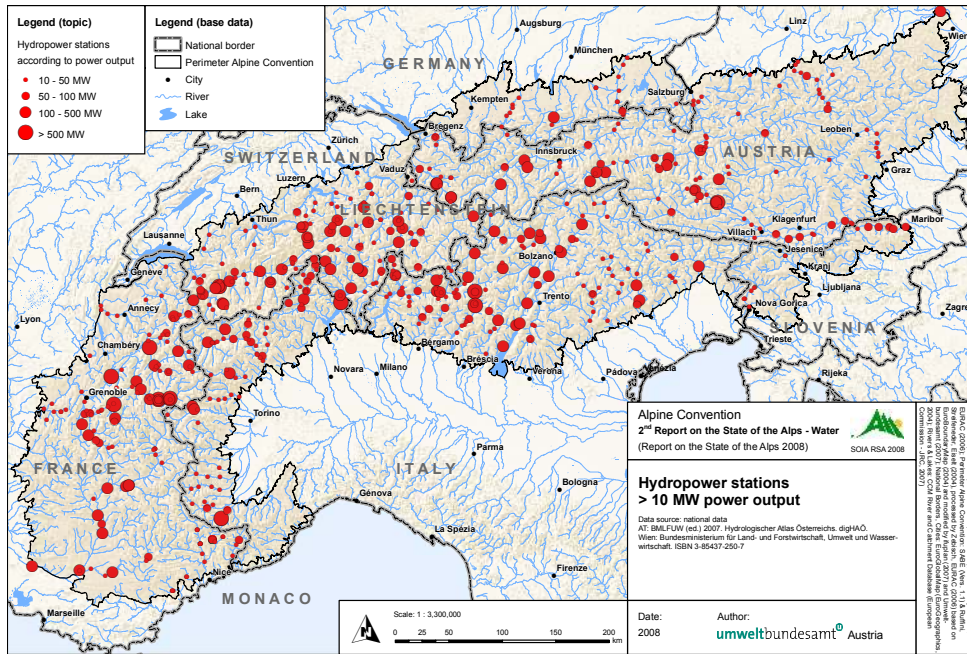


FIGURE 1.1: Map of hydropower stations with power capacities of more than 10 MW in the Alps (Alpine Convention, 2009).

Commission, 2009). Possible further increases of the hydropower production is currently under investigation also in Norway (Catrinu-Renstrom and Knudsen, 2011) as well as in Switzerland (Swiss Federal Office of Energy, 2013). In such context a more variable production is expected, with more frequent and unpredictable fluctuations of water levels in the receiving water bodies. Aiming at preserve or enhance river ecological quality, environmental strategies have to account also for river thermal regime which is intimately linked to flow regime and has a key-role in riverine ecosystem dynamics (e.g. Caissie, 2006; Webb *et al.*, 2008).

Furthermore, the mutable scenarios of hydropower production are blended into the more general context of climate and global environmental changes (e.g. Arismendi *et al.*, 2012; Hauer *et al.*, 2013b; Gebre *et al.*, 2014; Rheinheimer and Viers, 2014) and continuously pose challenging questions on the river environmental impacts of the hydrological and thermal alterations due to hydropower production.

1.2 Scientific background

The natural flow variability is a recognized key driver in sustaining the biodiversity and the functionality of river ecosystems. Natural floods, snowmelt, precipitations occur at several temporal scales, i.e. from sub-daily to yearly scale, and have a crucial role in maintaining hydraulic complexity, sediment transport, hyporheic exchanges, floodplain

connections and habitat structure and complexity (Poff *et al.*, 1997; Poff and Zimmerman, 2010). Such natural flow variability is often altered over all the different temporal scales due to anthropogenic interventions, i.e. by reducing natural high floods, flattening seasonal fluctuations, imposing artificial low flow stages (e.g. Gore and Petts, 1989; Graf, 2006; Jiang *et al.*, 2014). These hydrological alterations are recognized to affect environmental dynamics and ecosystem integrity (e.g. Poff and Zimmerman, 2010; Lytle and Poff, 2004), and several efforts have been put for their characterization and quantification so far (e.g. Gao *et al.*, 2009). In alpine and piedmont streams the hydropower plant production patterns often determine the most relevant alterations in term of flow magnitude, frequency, duration and fluctuations (e.g. Zolezzi *et al.*, 2009; Harby and Noack, 2013).

River water temperature is intimately connected to flow regime, is an important physical property of flowing waters and is widely recognized as a key driver in aquatic ecosystems (Caissie, 2006; Webb *et al.*, 2008). Its variability defines the thermal regime of a river and occurs at multiple temporal scales with distinct ecological signature. Alterations of the thermal regime at any of these temporal scales can adversely affect the river biota. On a decadal scale, different studies reported an increasing trend in water temperature (Webb and Nobilis, 2007; Kaushal *et al.*, 2010; Hari *et al.*, 2006; Bonacci *et al.*, 2008; Pekárová *et al.*, 2011). This altered trend can have adverse ecological consequences on ecosystem processes such as biological productivity and stream metabolism, contaminant toxicity and loss of aquatic biodiversity (Kaushal *et al.*, 2010; Hari *et al.*, 2006).

Anthropogenic influences, such as the use of water for cooling by power plants (e.g. Prats *et al.* 2010), the flow regulations (Zolezzi *et al.*, 2011; Dickson *et al.*, 2012) as well as wastewater from urbanized areas (Kinouchi, 2007) causes significant thermal regime alterations on a large spectrum of temporal scales from intra decadal, seasonal and daily time scales. On the longer scale, such alterations can cause selective disappearance of susceptible species from downstream reaches. Modified thermal patterns and day-length cues disrupt insect emergence patterns and reduce population success (Ward and Stanford, 1979). Cold water releases were found to delay spawning by up to 30 days in some fish species (Zhong and Power, 1996) and to have several impacts on brown trout growth (Hari *et al.*, 2006).

1.2.1 Hydropeaking and thermopeaking alterations

Among the different hydrological alterations, the repeated daily and sub-daily sudden water releases due to electricity production are known as hydropeaking (e.g. Zolezzi *et al.*, 2009). From an hydrodynamic point of view it consists on a repetition of small flood waves propagating downstream, with related artificially rapid fluctuations of water level,

near-bed shear stress and flow velocity patterns. From an abiotic point of view these sharp discharge variations interact with the river morphology and might strongly impact the biological habitats (Shen and Diplas, 2010; Thompson *et al.*, 2010). Although the biological effects on the river environment of such fluctuations are particularly relevant (e.g. Fette *et al.*, 2007; Formann *et al.*, 2007), not all the biophysical implications have been fully clarified yet (e.g. Young *et al.*, 2011; Harby and Noack, 2013). In particular, hydropeaking has known multiple effects on fish communities (e.g. Vehanen *et al.*, 2005; Nagrodski *et al.*, 2012), but the investigation of some contrasting evidences is a lively task (e.g. Flodmark *et al.*, 2004; Finch *et al.*, 2014; Puffer *et al.*, 2014). Hydropeaking is also recognized to impact macrobenthos communities, increasing the catastrophic drift during the rapid increasing phase of discharge (C er ghino *et al.*, 2004; Bruno *et al.*, 2010). Evidences of longitudinal zonation of macrobenthos had also been highlighted by C er ghino *et al.* (2002).

If the water storage basin is sufficiently large or there is a relevant elevation gap between the basin and the downstream receiving water body, it is possible that the released water has a significant different temperature from that of the receiving body (*thermo-peaking*) (Zolezzi *et al.*, 2011; Frutiger, 2004). This can induce the presence of a thermal wave which travels downstream (Toffolon *et al.*, 2010) affecting the biota. As example, evidences on behavioural macroinvertebrate drift alteration in presence of thermopeaking have been recorded (e.g. Carolli *et al.*, 2012; Bruno *et al.*, 2013). Moreover, relationship between thermal alterations induced by dam operations and spawning delay (Wang *et al.*, 2013a), growing rate (Flodmark *et al.*, 2004) and also fish survival (Horne *et al.*, 2004) have been investigated.

Hydropeaking and thermopeaking might not have only a direct impact on fish and macroinvertebrate communities, but also affect the river ecosystem in a broader outlook. Alternations might involve the hyporheic exchange dynamics (e.g. Fette, 2005; Boano *et al.*, 2007; Sawyer *et al.*, 2009; Fleckenstein *et al.*, 2010) as well as riparian vegetation (Gorla *et al.*, 2015). Finally, the importance of such alterations also in ice formation and breakup processes in cold regions is recognized and investigated (Gebre *et al.*, 2013).

1.2.2 Overview of the possible mitigation strategies

Hydromorphological alterations took place in many river reaches worldwide through channelization and alteration of the flow regime, and currently EU Directives require an improvement of river ecological quality (European Commission, 2000). A lively debate has been growing in this last decade (e.g. Formann *et al.*, 2007; Jager and Smith, 2008; Charmasson and Zinke, 2011; Nagrodski *et al.*, 2012) on the development of feasible mitigation

measures for hydropeaking in order to promote an environmentally friendly hydropower development. Such mitigation measures are of essentially two types. *Operational* measures focus on the reduction of streamflow alterations at the source, like e.g. pump & storage systems or restrictions in turbine operation mode, while *constructional* measures (Person *et al.*, 2013) focus on the management of the downstream river channel, like e.g. by promoting local river widening (Rohde *et al.*, 2006) or more engineered morphological diversification (e.g. Meile *et al.*, 2008).

Especially in Alpine areas, detection of the appropriate measures is often challenging: considering operational measures, one of the main advantages of hydropower production is the capability to follow almost instantly the fluctuations of electricity requests switching on/off turbines (Holland and Mansur, 2008). Therefore a reduction of electricity production can hardly be adopted as mitigation strategy. Nevertheless the variation of the released base flow (*sensu* environmental flow, or Minimum Vital Flow), though implying economical losses for the producer, has been proposed as a feasible mitigation strategy for the ecological effects of hydropeaking (see e.g. Person *et al.*, 2013). On the other hand large spaces are hardly available at reasonable costs in productive alpine valley floodplains. Giving “more room to the river” (Rohde *et al.*, 2006) is expected to locally improve the health of river systems by increasing physical habitat diversity in the restored reach; however evidence has been reported (e.g. Muhar *et al.*, 2007) of little ecological improvements in streams characterized by hydropeaking.

The mitigation of thermal regime alterations is still a challenging but unavoidable task in order to restore freshwater ecosystem integrity (Olden and Naiman, 2010). Efforts and attempts have been dedicated to investigate different operational strategies of reservoir releases in order to mitigate or even manage downstream water temperature (e.g. Carron and Rajaram, 2001). Operational strategies based on selective withdrawal from reservoirs, have been investigated and suggested to mitigate climate warming effects (Rheinheimer *et al.*, 2011) and ice dynamics alterations (Gebre *et al.*, 2013). However, the development of sub-daily scale strategies for thermopeaking mitigation is still an open and debated topic.

1.3 Specific research questions and thesis outline

The general goal of this thesis is to increase the scientific knowledge related to the abiotic effects of hydropeaking and thermopeaking phenomena and consequently in supporting the design of more effective mitigation strategies. The complexity of the matter, which

involves multidisciplinary processes at different scales, is faced pointing out three main objectives and attempting to answer some specific research questions.

The main objectives and the related research questions can be grouped according to the following three main research elements:

1. Characterization of hydropeaking and thermopeaking alterations:

development and assessment of simple procedures to identify river reaches which experience hydro- or thermopeaking alterations with respect to natural flow and thermal regimes. The goal is to develop a screening tool that can be adopted by river management agencies to preliminary identify critical reaches. Thus the specific research questions we address are:

- i) how to identify hydropeaked or thermopeaked reaches from at-a-station water discharge and temperature series?*
- ii) Which are the most adequate temporal scales to identify these rapid phenomena?*
- iii) Can we find a statistical, common behaviour for alpine rivers having near-natural flow or thermal regime?*

2. Modeling the surface water thermal transport:

development of a two-dimensional numerical model able to simulate main physical features of the surface water temperature transport and diffusion. Due to the continuous technological improvements in numerical computing, numerical models represent fundamental tools in reproducing and evaluating specific environmental scenarios (e.g. Wang *et al.*, 2013b). In hydro-thermopeaking context, a valuable numerical tool has to correctly simulate non-stationary hydraulic and thermal phenomena over complex river topographies. The main challenge to be faced is:

- i) build a numerical model able to describe the transport of river water temperature in real rivers characterized by complex topographies with affordable computational costs.*

3. Investigation of the role of river morphology under hydropeaking conditions:

systematically investigate the role of self-formed morphological diversity in translating a given hydropeaking event into the spatial variability of some ecologically-relevant hydraulic variables. Final attempt is to quantify to which extent river morphology influences the river eco-hydraulic response to hydropeaking alteration. In particular:

- i) how to model and quantify the tradeoffs between hydropeaking waves and river morphology?*
- ii) Can general trends of such interactions be underlined?*
- iii) Is this approach a valuable support in design target oriented mitigation strategies?*

In this thesis Chapters 2 to 5 and Appendix A are related to each of the proposed research elements and attempt to answer the related specific research questions. In particular Chapter 2 and Appendix A address the first research element, proposing two novel methodologies based on a suite of indicators to identify hydropeaking and thermopeaking alterations. The second research issue is faced in Chapter 3, where the development of a numerical model for the shallow water advection-diffusion problem on unstructured grids is presented. In Chapter 4 the challenges posed by the third research element are investigated by means of two-dimensional numerical modeling. Chapter 5 contains a development of the analysis presented in Chapter 4 in relation to the fish stranding phenomenon, addressed through 2D numerical modeling approach, together with a preliminary application for the case-study of Lundesokna River (Norway). The last chapter of this thesis (Chapter 6), combines and summarizes the main outcomes of the single chapters. In the same chapter, new scientific questions arising from this thesis are proposed for further research activities.

Chapter 2, 3, 4 and Appendix A are based on scientific papers elaborated during my 3-years PhD programme. Status and details of each paper, together with author credits, are reported at the beginning of each chapter.

Chapter 2

Characterization of sub-daily hydrological and thermal alterations in Alpine rivers affected by hydropeaking

Based on: Vanzo D., A. Siviglia, M. Carolli and G. Zolezzi (under review). Quantitative characterization of sub-daily thermal alterations in alpine rivers affected by hydropeaking. Submitted to Hydrological Processes (Wiley & Sons).

This chapter and Appendix A focus on the development of suitable indicators for the assessment of sub-daily thermal and hydrological alterations induced by hydropower plant water releases. Hence, this chapter is fully dedicated to the development of suitable indicators for thermopeaking alteration, while the hydrological indicators are presented in Appendix A.

2.1 Introduction

The thermal regime of rivers is threatened by anthropogenic stresses at a large variety of time scales. We focus on sub-daily thermal alterations induced by the release of hypolimnetic water for hydropower production. In particular the releases from hydropower plants (hydropeaking) fed by high elevation and stratified reservoirs are often characterized by a distinctly different temperature from that of the receiving water body (thermopeaking) (e.g. Frutiger 2004; Zolezzi *et al.* 2011). On such short temporal scales flume experiments demonstrated increased macroinvertebrate drift as a response to thermopeaking (Bruno

et al., 2013). Less is known about the reaction of fish to thermopeaking and further analyses have to be performed to answer this question in detail (Schmutz *et al.*, 2014).

Because of its fundamental ecological relevance, quantifying the alteration of river thermal regimes should be incorporated within existing procedures for the quantification of the alterations of the physical, hydromorphological and ecological quality in water courses, which is becoming increasingly important in legislation at a regional, national and international level. Examples cover international directives down to specific national regulations: the Water Framework Directive (European Commission, 2000), the Swiss national legislation (Baumann *et al.*, 2012), the Italian national methodology for hydromorphological quality assessment of rivers (Rinaldi *et al.*, 2013) and in the paperwork on the renewal of licensing (e.g. Norwegian Ministry of Petroleum and Energy 2012). However, while different approaches and methodologies are available for the quantification of sub-daily flow regime alteration (Bevelhimer *et al.*, 2014; Meile *et al.*, 2011; Sauterleute and Charmasson, 2014; Zimmerman *et al.*, 2010) little attention has been devoted to the sub-daily thermal alterations in rivers so far.

The quantification of such sub-daily thermal alterations (thermopeaking) is the main goal of this study. Specifically, We aim at characterizing thermal alterations caused by the release of hypolimnetic water from artificial reservoirs having a different temperature compared to the receiving water body during hydropeaking events. This is achieved by developing two quantitative indicators which are capable of disentangling between thermo-peaked and thermo-unpeaked river reaches fulfilling two main requirements. First, the indicators have to be easily computed only from the at-a-station temperature time series and they do not have to require temperature records both upstream and downstream each hydropower plant water restitution. Second, such indicators have to be independent from the physical characteristics of the measurement station (elevation and mean discharge) and of the catchment (mean elevation area, percentage of glacier cover) where the station is located. Once derived the indicators, we sought to develop a methodology to distinguish between different levels of “thermo-peaking alteration” which: i) can be easily computed from temperature time series which are those commonly available at sub-daily sampling resolution; ii) allows comparison among different stations in the same area; iii) distinguishes between types of thermopeaking alteration; iv) is statistically robust.

The chapter is organized as follows. In Section 2 we present the datasets and study area, the indicators development and the choice of their thresholds; moreover we describe the statistical methods used throughout the analysis. In Section 3 we present the results focusing on the correlations between the indicators and the physical characteristics of the gauging measurement station and on the classification of sub-daily thermal alterations for

all the analysed stations. In Section 4 we discuss the obtained results in the light of their potential practical implications.

2.2 Methods

Thermal alterations are computed from river temperature time series recorded in a group of gauging stations that display a broad range of characteristics of the subtended catchment. The first step of the workflow is the selection of an appropriate set of stations that are not subjected to hydropeaking, which represents our reference group (Section 2.2.1). The remaining stations in the dataset are subsequently identified in the “impacted” or “peaked” group. The second step is the design of two indicators able to synthetically represent the complexity of the thermopeaking signature onto a river temperature time series (Section 2.2.2). The reference group is exploited to define a “near-natural” (i.e. thermally unpeaked) behaviour in the space of indicators (Section 2.2.3), which is finally used to compare and evaluate the magnitude of thermopeaking alterations with in the subset of the impacted stations (Section 2.3).

It is worth pointing out that in the present chapter the term “non-impacted” (as well as “unpeaked”) refers to the reference group stations, which are neither affected by hydropeaking nor by thermopeaking. On the other hand, with “impacted” (as well as “peaked”) we refer to the analysed set of stations which are affected by hydropeaking, for which we aim at quantify the sub-daily thermal alterations (thermopeaking).

2.2.1 River temperature dataset

The entire available dataset is composed by 48 river temperature sampling stations: 40 Swiss stations and 8 Italian stations in the Autonomous Province of Trento (Trentino-Alto Adige region). Swiss records are 6-year long (2007-2012) while the Italian records refer to year 2007.

Among the entire dataset we identify 23 stations without upstream hydropower plant intermittent water releases (no hydropeaking, “reference group”). Selection has been performed combining GIS available information (presence of hydropower plants upstream the given station) and double-checked by hydrograph analysis (presence of sharp and repeated discharge variations) and through the hydropeaking screening methodology proposed in Appendix A. This first group is adopted as a reference group of non-impacted stations. Thermopeaking can occur in river sections subjected to hydropeaking, but not every section with hydropeaking may experience a significant thermopeaking, because e.g. i) the

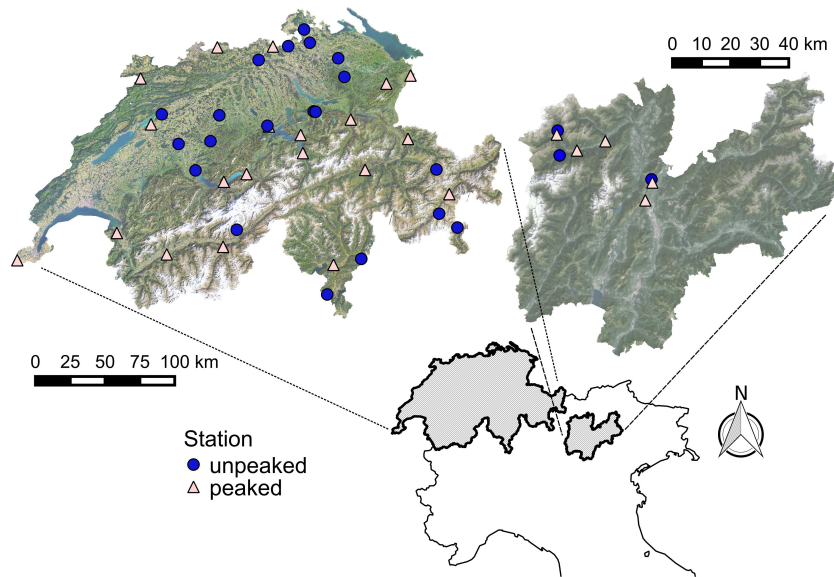


FIGURE 2.1: Location of the river temperature sampling stations in Switzerland and in the Autonomous Province of Trento (Italy).

temperature of the released water does not differ from the water temperature of the receiving water body, or ii) between the water release and the sampling station tributaries that reduce the upstream thermal alteration are present. According to the above criterion the whole dataset is therefore separated into a reference group (non-hydropeaked) and potentially-impacted group (hydropeaked). Table 2.1 lists the stations in the reference group along with the main physiographic characteristics of the subtended catchments. In particular we take into account the station elevation, the catchment area, the mean catchment elevation, the percentage of glacier cover of the catchment and the mean annual discharge. Station from 1 to 20 in Table 2.1 are located in Switzerland, the others in Italy.

The remaining 25 stations are affected by hydropeaking, and potentially have different magnitudes of thermopeaking alteration (including no thermal alteration). These stations are listed in Table 2.2 where stations from 1 to 20 are located in Switzerland.

Figure 2.1 shows the location of the stations in Switzerland and in the Autonomous Province of Trento (Italy). Blue circles refer to unpeaked stations (forming the reference group) while white triangles represent peaked stations.

2.2.2 Indicators

We aim at design indicators capable at catching the thermopeaking signature onto the river water temperature time series. Figure 2.2 shows a 48-hours thermograph for an unpeaked station (Station 3, Vermigliana River at Vermiglio IT, in Table 2.1) and a

#	Station code	River	Reach	Elev [<i>m a.m.s.l.</i>]	Area [<i>km</i> ²]	Catchment Elev [<i>m a.m.s.l.</i>]	Glaciation [% of catchment]	Discharge [<i>m</i> ³ / <i>s</i>]
1	2016	Aare	Brugg	332	11726	1010	2.0	298.9
2	2030	Aare	Thun	548	2466	1760	9.5	105.7
3	2044	Thur	Andelfingen	356	1696	770	0.0	45.6
4	2126	Murg	Wangi	466	79	650	0.0	1.8
5	2167	Tresa	Ponte tresa	268	615	800	0.0	118.0
6	2070	Emme	Emmenmatt	638	443	1070	0.0	12.0
7	2161	Massa	Blatten	1446	195	2945	65.9	15.4
8	2256	Rosegbach	Pontresina	1766	67	2716	30.1	2.9
9	2288	Rhein	Neuhausen	383	11887	1176	0.7	358.9
10	2327	Dischmabach	Davos	1668	43	2372	2.1	1.6
11	2343	Langeten	Huttwill, Haberenbad	597	60	766	0.0	1.2
12	2347	Riale di Roggiasca	Roveredo	980	8	1711	0.0	0.5
13	2029	Aare	Brugg - aegaerten	428	8293	1150	2.9	510.4
14	2366	Poschiavino	La Rosa	1860	14	2283	0.4	6.4
15	2414	Rietholzbach	Mosnang	682	3	795	0.0	100.1
16	2415	Glatt	Rheinsfelden	336	416	498	0.0	7.6
17	2425	Kleine Emee	Emmen	431	477	1050	0.0	15.1
18	2135	Aare	Bern-Schonau	502	2945	1610	8.0	118.1
19	2604	Biber	Biberburg	825	32	1009	0.0	1.1
20	2609	Alp	Einsiedeln	840	46	1155	0.0	2.3
21	1	Noce Bianco	Cogolo Pont upstream	1220	na	na	na	na
22	3	Vermigliana	Vermiglio	1122	na	na	na	na
23	6	Noce	Mezzocorona upstream	232	na	na	na	na

TABLE 2.1: Unpeaked station labels (reference group) and main physiographic characteristics of the subtended catchments.

#	Station code	River	Reach	Elev [m a.m.s.l.]	Area [km ²]	Catchment [m a.m.s.l.]	Elev	Glaciation [% of catchment]	Discharge [m ³ /s]
1	2009	Rhone	Porte du Scex	377	5244	2130	14.3	179.3	
2	2011	Rhone	Sion	484	3373	2310	18.4	100.0	
3	2019	Aare	Brienzwiler	570	554	2150	21.0	36.5	
4	2056	Reuss	Seedorf	438	832	2010	9.5	40.3	
5	2351	Vispa	Visp	659	778	2660	29.5	16.1	
6	2068	Ticino	Riazzino	200	1611	1640	0.7	73.2	
7	2084	Muota	Ingenbohl	438	316	1360	0.1	18.8	
8	2085	Aare	Hagneck	437	5104	1380	4.5	165.2	
9	2091	Rhein	Rheinfelden	262	34256	1039	1.3	1026.8	
10	2143	Rhein	Rekingen	323	14718	1080	0.6	449.2	
11	2174	Rhone	Chaney	336	10323	1580	8.4	311.3	
12	2033	Vorderrhein	Hanz	693	776	2020	3.8	32.3	
13	2210	Doubs	Ocourt	417	1230	950	0.0	30.0	
14	2112	Sitter	Appenzell	769	74	1252	0.1	3.1	
15	2152	Reuss	Luzern	432	2251	1500	4.2	110.4	
16	2372	Linth	Mollis	436	600	1730	4.4	30.9	
17	2150	Landquart	Felsenbach	571	616	1800	1.4	24.9	
18	2457	Aare	Ringgenberg, Goldswil	564	1129	1970	16.2	175.8	
19	2462	Inn	S-chanf	1645	618	2466	10.1	20.2	
20	2473	Rhein	Diepoldsau, Rietbrücke	410	6119	1800	1.4	227.3	
21	2	Noce Bianco	Cogolo Pont downstream	1200	na	na	na	na	
22	4	Noce	Pellizzano	930	na	na	na	na	
23	5	Noce	Male	702	na	na	na	na	
24	7	Noce	Mezzocorona downstream	232	na	na	na	na	
25	8	Noce	Zambana Vecchia	200	na	na	na	na	

TABLE 2.2.: Peaked station labels and main physiographic characteristics of the subtended catchments.

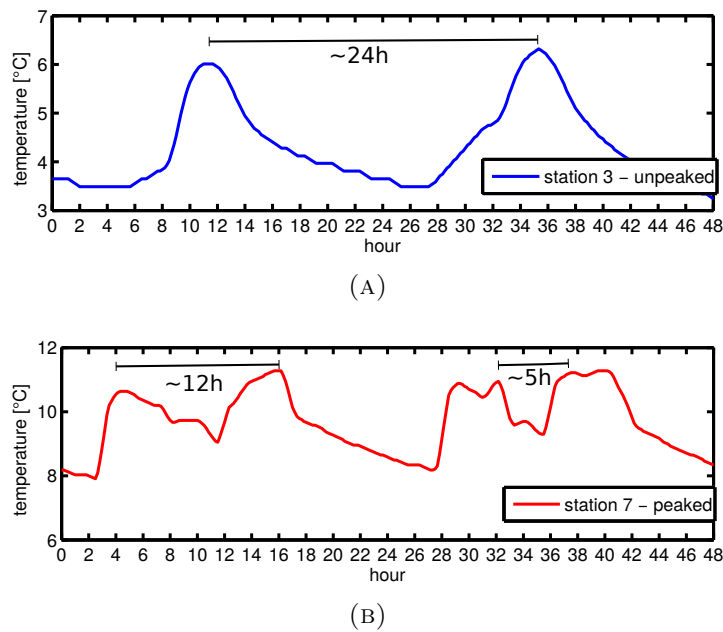


FIGURE 2.2: Example of a 48-hours thermograph for an unpeaked station (A) and a peaked one (B).

peaked one (Station 7, Noce River at Mezzocorona IT, in Table 2.2). It is illustrative of some general patterns of river thermal regimes and helps to clarify the rationale beyond the indicator definition. In particular: i) *river thermal signals* are constantly characterized by regular, *almost-sinusoidal* fluctuations at daily scale (24h), in direct relation with the thermal forcing associated with the sun cycle (Figure 2.2A) and also at year scale (seasonal forcing); ii) *thermal alterations due to hydropower production* normally occur at daily and sub-daily time scales and cause alterations of the temperature *rate of change* and of the *number of rise and fall stages* within the same day (Figure 2.2B). Additionally, iii) *occasional temperature fluctuations* may occur due to weather variability at local scale (e.g. cloud cover, rainfall) and iv) *temperature ranges of variability*, are controlled by site-specific characteristics, like catchment elevation, solar exposition, glacial cover, catchment size, flow regime (e.g. Caissie 2006).

Thermopeaking alterations are linked to repeated daily or sub-daily water releases (hydropeaking): they appear in the form of additional sharp and temporary increases/decreases of water temperature superimposed to the non-altered local thermal trend (Figure 2.2). Therefore, the thermopeaking signature on river thermograph is expected to increase the magnitude of short-scale, sub-daily temperature variations and the frequency of thermal oscillations at sub-daily scale. For example Zolezzi *et al.* (2011) point out that thermopeaking events in the heavily peaked Noce River (North-East of Italy) have typical

durations of 6 or 18 hours (Figure 6 in Zolezzi *et al.* 2011). In order to quantify sub-daily thermal alterations we propose two different indicators to capture the alteration of sub-daily temperature rate of change and of the frequency of sub-daily thermal oscillations, respectively.

2.2.2.1 Sub-daily temperature rate of change: TP_{Δ}

This first indicator TP_{Δ} aims at quantifying the temperature rate of change over short, sub-daily time scales. For a given sub-daily time interval Δt , TP_{Δ} is computed starting from the ratio between the maximum variation between two consecutive temperature readings over the whole day, and the difference between the maximum and minimum temperature values registered during the same day ($Tmax - Tmin$). Hence, for the i -th day, the daily indicator $TP_{\Delta,i}$ reads

$$TP_{\Delta,i} = \frac{\max |T_{k+\Delta t} - T_k|}{Tmax_i - Tmin_i} \sim \frac{\max \text{ sub-daily variation}}{\max \text{ daily variation}}, \quad (2.1)$$

where k refers to every temperature reading and Δt is the interval between two consecutive readings. The daily indicator ranges from 0 to 1 and basically normalizes the maximum short-scale temperature variation with the temperature daily range of variability.

For a gauging station, the representative TP_{Δ} indicator is defined as the median value of the $TP_{\Delta,i}$ distribution:

$$TP_{\Delta} = \text{median}(TP_{\Delta,i}). \quad (2.2)$$

The TP_{Δ} indicator can be computed with reference to different time intervals Δt : in the present study we have investigated the effect of choosing different time intervals ranging from 10 minutes (corresponding to the available breakdown interval) up to 12 hours. The sensitivity of TP_{Δ} to the chosen time interval and the criterion to detect its most appropriate value are discussed in Section 2.3.

2.2.2.2 Frequency of sub-daily temperature fluctuations: TP_{En}

Natural thermal regimes of rivers are intrinsically oscillating signals (Figure 2.2A) at almost fixed daily and seasonally oscillation frequencies. Thermopeaking events are expected to alter such characteristic frequencies by adding extra, sub-daily, thermal fluctuations (e.g. Figure 2.2B). These discrepancies can be investigated and quantified via a Fourier spectral analysis of the thermal signal. Hereinafter, for the sake of simplicity, we refer to oscillation period (expressed in *hours*) instead of frequency (typically expressed in *Hertz*), recalling they are just reciprocal metrics.

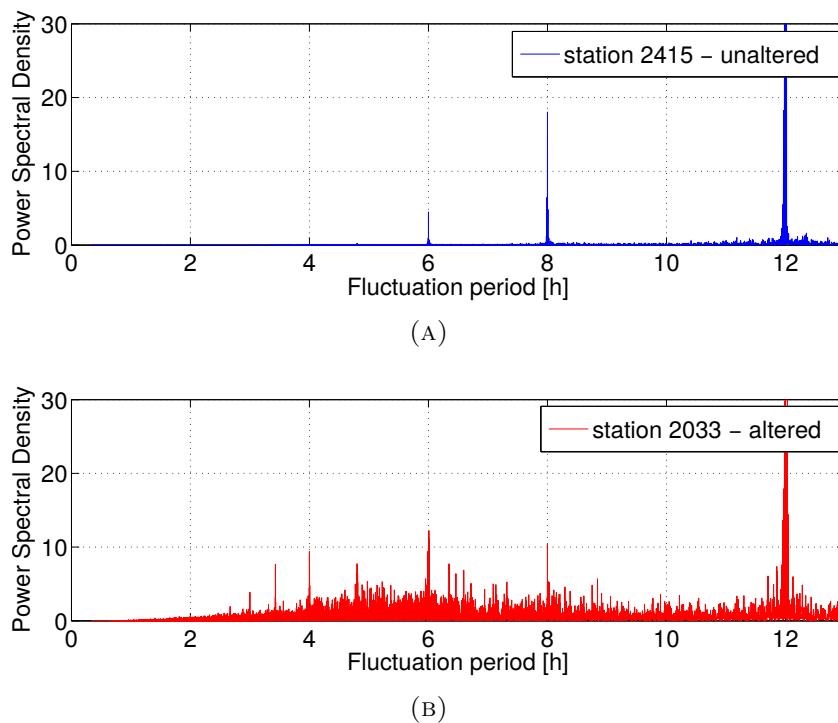


FIGURE 2.3: Example of Power Spectral Density of thermal signal for one unaltered (A) and one altered (B) station, respectively.

Figure 2.3 shows the Power Spectral Density of a thermo-unpeaked (a) and of a thermo-peaked station (b). The Power Spectral Density of a complex oscillating signal returns the specific oscillation energy at different frequencies (or period of oscillation). The dominant fluctuation period is invariably 24 hours, and, as intrinsic in Fourier Spectral analysis, secondary peaks appear at sub-multiple periods of 12-8-6... hours. This characterizes both impacted and non-impacted stations (as illustrated in Figure 2.3). This evidence remarks the leading role of natural daily thermal cycle linked to solar cycle.

Thermo-peaking affects the natural daily fluctuations by adding non-natural, sub-daily anthropogenic thermal fluctuations like those displayed in Figure 2.2B; these artificial fluctuations are reflected in the corresponding Power Spectral Density of Figure 2.3B in the form of diffused small peaks with largest power for the short-time periods (i.e. below 6-8 hours).

The Power Spectral Density can be adopted as a proxy indicator for the number and relevance of sub-daily thermal fluctuations because the specific oscillation energy is proportional to the number of oscillations. To take into account all the short-scale (sub-daily) fluctuations, we integrate the Power Spectral Density for different frequency bands, from a very short scale (1 hour) to daily scale (24 hours), obtaining the averaged power of oscillation P_{av} . The choice of the appropriate frequency band is discussed in Section

2.3.3.

Formally, the averaged power P_{av} in a period T of a continuous signal in time $h(t)$ reads

$$P_{av} = \lim_{T \rightarrow \infty} \frac{1}{2T} \int_{-T}^T |h(t)|^2 dt, \quad (2.3)$$

and it can be also evaluated in the frequency domain thanks of Parseval's theorem as

$$P_{av} = \int_{-\infty}^{\infty} S(2\pi f) df, \quad (2.4)$$

where f is the frequency and S the estimate of Power Spectral Density of the root signal.

Similarly to the previous indicator, we scale the averaged power of the selected oscillation period with the daily (24h oscillation period) averaged power. Thus the indicator TP_{En} , ranging between 0 and 1, represents the ratio between the short scale and the daily scale spectral power of oscillation for the considered station:

$$TP_{En} = \frac{P_n}{P_{24}} = \frac{\int_{f_n}^{f_1} S(2\pi f) df}{\int_{f_{24}}^{f_1} S(2\pi f) df} \sim \frac{\text{sub-daily oscillation}}{\text{daily oscillation}}, \quad (2.5)$$

where n is a sub-daily frequency band with oscillating period ranging between 1 h to 24 h . Frequencies $f_{24} < f_n < f_1$ correspond to oscillating period of 24, n and 1 hour, respectively.

2.2.3 Thermopeaking thresholds

The aim of the indicators is to quantify the degree of sub-daily thermal alteration of peaked stations compared with non-peaked ones. To this purpose it is required to establish the range of variability of both indicators under non-impacted thermal regimes. In order to minimize uncertainties of the reference group (selection criteria, number of stations, etc.) we adopt an outlier approach: for a reference population of unpeaked stations, a peaked station can show an analogous behaviour to the non-impacted one if it belongs to the same population. On the other hand, a peaked station with indicator value being outlier of the reference population has to be considered as significantly thermally altered.

Among different threshold criteria, we adopt a standard non-parametric outlier definition in order to avoid a priori assumptions on the normality distribution of data. Therefore the outlier estimator for a given population Z reads

$$Lim_Z = p75(Z) + 1.5 \cdot iqr(Z), \quad (2.6)$$

where $p75$ and iqr are the 75th percentile and the interquartile range ($iqr = p75 - p25$) of population Z , respectively. For the first indicator TP_{Δ} , the population is composed by all daily i -th components $TP_{\Delta,i}$ of the reference group. The population of second indicator TP_{En} is formed by the indicator itself (23 values of the reference group), being TP_{En} an unique parameter for each station.

The thresholds Lim_{Δ} and Lim_{En} thus calculated account for a specific sub-daily thermal alteration and define two behavioural classes each. In particular, a given hydro-peaked station (parameterized with TP_{Δ} and TP_{En}) can show: i) daily maximum temperature variations statistically similar to non-peaked stations ($TP_{\Delta} < Lim_{\Delta}$) or significantly higher ($TP_{\Delta} > Lim_{\Delta}$); ii) relevant temperature fluctuation periods close to 24h (typical of non-peaked stations, $TP_{En} < Lim_{En}$), or shorter fluctuation periods (sub-daily fluctuations, $TP_{En} > Lim_{En}$).

By overlapping the two classes defined by each threshold, we can apply the following conditional rules to each investigated peaked station:

1. **Class A** - Absent or low thermal alteration: $TP_{\Delta} < Lim_{\Delta}$ and $TP_{En} < Lim_{En}$.
2. **Class B** - Moderate thermal alteration:
 - **B₁** - $TP_{\Delta} < Lim_{\Delta}$ and $TP_{En} > Lim_{En}$, or
 - **B₂** - $TP_{\Delta} > Lim_{\Delta}$ and $TP_{En} < Lim_{En}$.
3. **Class C** - High thermal alteration: $TP_{\Delta} > Lim_{\Delta}$ and $TP_{En} > Lim_{En}$.

2.2.4 Correlation analysis

In order to allow reciprocal comparisons between different stations, the designed indicators need to be uncorrelated with physiographic differences between stations. In other words, indicator values have to significantly depend only on thermal features affected by thermopeaking we illustrated in Section 2.2.2. The dependence of thermal regime on local physiographic characteristics is well-established (Caissie, 2006; Webb *et al.*, 2008) and our reference dataset is composed by stations having a broad range of station/catchment characteristics (see Table 2.1).

The proposed indicators have been designed such a way that their dependence on local physical and physiographic characteristics is filtered out. To prove that, we test the independence of both indicators TP_{Δ} and TP_{En} of the reference group to station elevation, area of the subtended catchment, mean catchment elevation, glaciation percentage of the catchment and annual mean discharge (reported in Table 2.1). To this aim we

use Spearman’s rank correlation, which is a non-parametric measure of statistical correlation between two variables. The correlation coefficient r_s is a measure of the strength of a monotonic relationship between paired data and ranges between -1 (negative correlation) and +1 (positive correlation). Absolute values of r_s greater than 0.6 mean strong correlation between the considered variables.

Reliability of the correlation coefficient has to be confirmed by p-value, which is the probability of the hypothesis of no correlation against the alternative that there is a non-zero correlation. Small values of p (e.g. $p < 0.05$) mean the corresponding correlation r_s is significantly different from zero, otherwise the hypothesis of correlation between the two variables has to be rejected.

2.3 Results

Results are organized as follows: firstly we show the capability of proposed indicators in catching thermopeaking alterations (Section 2.3.1), then the independence of the indicators from physiographic characteristics is demonstrated (Section 2.3.2). In Section 2.3.3 we motivate the choice of the adopted time intervals for the two indicators and finally in Section 2.3.4 we show how the indicators can be applied to the dataset of the peaked stations.

2.3.1 Thermo-peaked vs thermo-unpeaked stations: comparison of thermopeaking indicators

For the sake of clarity we present in detail the two indicators for some selected stations to highlight their characteristics. Figure 2.4 shows the cumulative distribution of daily indicator $TP_{\Delta,i}$ (with time interval Δ of 30 minutes) for some representative peaked (station 2033, Vorderrhein River at Ilanz CH, and station 7, Noce River at Mezzocorona IT) and unpeaked (station 2415, Glatt River at Rheinsfelden CH, and station 2161, Massa River at Blatten CH) stations. Distributions referring to peaked and unpeaked stations show two markedly different behaviours: non-impacted stations have smaller median values and variability compared to impacted stations.

In Figure 2.4, the median values of the $TP_{\Delta,i}$ distributions (according to Equation 2.2) are highlighted with filled circles and represent the TP_{Δ} indicator of the considered station. In particular, TP_{Δ} of station 2033 is around 0.6, which means that on the average the magnitude of short-scale (30 *min*) thermal variations is 60% of the daily variation magnitude. On the other hand, the amplitude of short scale temperature variations of

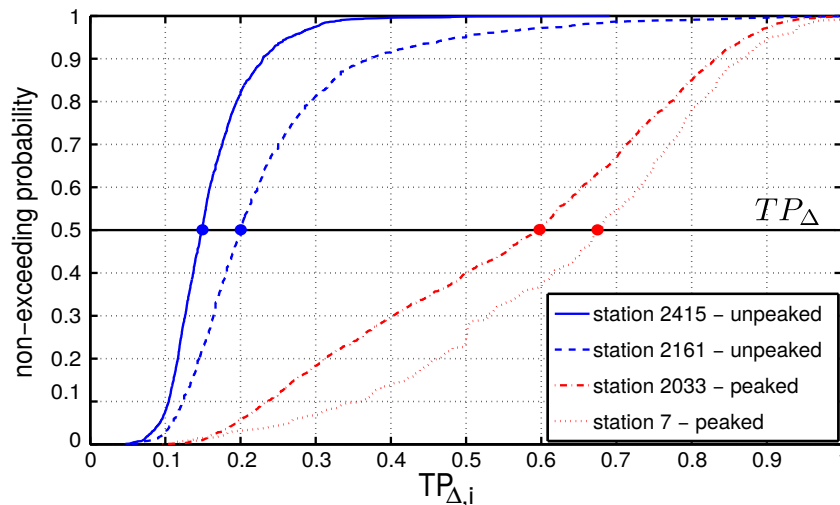


FIGURE 2.4: Cumulative distributions of $TP_{\Delta,i}$ (with time interval of 30 minutes) for selected representative peaked and unpeaked stations.

Station	River	Reach	Impacted	TP_{En}
2415	Glatt	Rheinsfelden	no	0.0044
2161	Massa	Blatten	no	0.012
2033	Vorderrhein	Ilanz	yes	0.32
7	Noce River	Mezzocorona	yes	0.093

TABLE 2.3: Example of TP_{En} (6 hour time span, $n = 6$ in Equation 2.5) for some representative peaked and unpeaked stations.

the two non-impacted stations do not exceed 20% of the daily excursion between the minimum and maximum values in the record.

The second indicator TP_{En} is a measure of the frequency of sub-daily temperature oscillations: Table 2.3 gives the values of TP_{En} referring to a Fourier period of 6 hours ($N = 6$ in Equation 2.5), for the same representative peaked and unpeaked stations of Figure 2.4. It is worth noting that indicator values of impacted and non-impacted stations differ for at least one order of magnitude. As example, TP_{En} of station 2033 is 0.32, which means that 32% of daily oscillation energy is associated with short scale oscillations having period smaller than 6 hours.

2.3.2 Correlation between physiographic station characteristics and indicators

We test the possible correlation between the physiographic and average hydrologic characteristics of the unpeaked, reference group stations and the designed indicators, as described in Section 2.2.4. In particular, the independence of each reference group indicator TP_{Δ}

Indicator	Physiographic char.	r_s	p
TP_Δ	station elevation	0.304	0.158
TP_{En}	station elevation	0.030	0.894
TP_Δ	catchment area	-0.308	0.186
TP_{En}	catchment area	0.023	0.927
TP_Δ	mean catchment elevation	0.346	0.136
TP_{En}	mean catchment elevation	0.266	0.256
TP_Δ	catchment glaciation	0.253	0.281
TP_{En}	catchment glaciation	0.393	0.086
TP_Δ	mean discharge	-0.090	0.705
TP_{En}	mean discharge	0.287	0.219

TABLE 2.4: Spearman’s correlations between proposed indicators and physiographic characteristics of the reference group stations.

and TP_{En} from station elevation, area of the subtended catchment, mean catchment elevation, glaciation percentage of the catchment and the annual mean discharge is verified. In Table 2.4 the Spearman’s correlation coefficients for each physiographic characteristics and both indicators are showed. Table 2.4 clearly demonstrates the absence of any significant correlation between the proposed indicators and the physiographic and average hydrologic characteristics of the thermal gauging stations, i.e. $p \gg 0.05$ for all cases.

Absence of a significant statistical correlation implies that a functional relationship between the considered variables is not present. Hence the designed indicators, despite thermal regimes depend on local physiographic features, allow grouping and comparing among stations with different physiographic characteristics.

It is worth underlining that the independence of TP_Δ from the physiographic characteristics is related to the normalization with daily maximum temperature variation (Equation 2.1). Without such normalization the short-scale temperature variations depend on local physiographic characteristics of the station; in particular non-normalized temperature variations show a significant correlation with the station elevation ($r_s = 0.488$ $p = 0.018$), with the catchment area ($r_s = -0.610$ $p = 0.004$) and with the mean discharge ($r_s = -0.604$ $p = 0.005$).

2.3.3 Time-interval selection and threshold calculation

The computation of both indicators TP_Δ and TP_{En} requires to choose an appropriate time interval (i.e. Δt in Equation 2.1 and n in Equation 2.5). Namely, such time span has to be tuned with the typical time-scale of thermopeaking events. The first indicator TP_Δ is linked to temperature rate of change and therefore it requires a time span scaled with the duration of sharp temperature variations (rising and falling limb) occurring during

peaking events. On the other hand, the indicator TP_{En} is linked to sub-daily temperature oscillation periods, and therefore its suitable time interval should scale with the entire duration of the peaking event.

The typical duration of discharge and temperature variations associated with hydro- and thermopeaking depends firstly on turbine capabilities and operational procedures and secondly on the distance from water release. Turbine switch on/off occur generally within the range of 15-60 minutes; for example, in Figure 2.2B, peaking temperature variations (rising and falling limb) last between 30-60 minutes. Therefore, in order to catch the largest short-scale variations, we adopt a time interval Δt of 30 minutes for TP_{Δ} calculation. On the other hand, artificial temperature fluctuation period depends on production patterns of hydropower plants and can range from some hours to daily scale according to electricity demand. The example in Figure 2.2B shows two oscillation periods of around 12h and 5h within a 48-hours record. For the second indicator TP_{En} , we adopt 6 hours of band period, assuming to be representative for hydropeaking events (see for example Figure 6 in Zolezzi *et al.* 2011).

The limits are calculated according to Equation (2.6) with the population Z referring to the stations of the reference group. The reference population of TP_{Δ} is the ensemble of daily-based distributions $TP_{\Delta,i}$ for each station, while the reference population for TP_{En} is composed by the 23 single values (one for each unpeaked station) obtained by the very definition of the indicator (Equation 2.5). Hence, for the selected time intervals $\Delta t = 30 \text{ min}$ and $n = 6 \text{ h}$, the chosen values of the thermopeaking class thresholds are $Lim_{\Delta} = 0.36$ and $Lim_{En} = 0.019$.

Once the time spans of the indicators are selected basing on typical time-scales of thermopeaking events, we test the robustness of such selection. In particular, due to the sub-daily nature of thermopeaking, the indicators are properly designed to highlight sub-daily temperature variation anomalies among impacted stations and reference group, while they invariably tend to unity at daily scale ($\Delta t = n = 24 \text{ h}$). In other words, increasing the time span for indicators calculation towards the daily scale (24 hours) causes thermal differences between unpeaked and peaked stations to progressively vanish, i.e. all peaked station indicators fall below the relative thresholds. On the contrary, decreasing the time span at sub-daily scale progressively magnifies thermal anomalies of peaked stations against the reference, unpeaked group (i.e. increment of peaked stations above thresholds). Hence the maximum statistical difference between peaked station population and reference group is reached at a specific sub-daily time scale and it is recognized by having the maximum number of peaked station above thresholds (i.e. maximum number of outliers).

Δt [h]	Lim_{Δ}	Outlier stations
10min	0.13	5
30min	0.36	5
1	0.52	4
2	0.77	0
4	1.1	0
6	1.2	0
8	1.2	0
12	1.2	0

TABLE 2.5: Threshold values of TP_{Δ} and number of peaked stations above them (outliers) for different time interval Δt .

T [h]	Lim_{En}	Outlier stations
1	0.00073	7
2	0.0023	10
4	0.0079	13
6	0.019	13
8	0.048	12
12	0.28	8

TABLE 2.6: Threshold values of TP_{En} and number of peaked stations above them (outliers) for different oscillating period band T.

Table 2.5 reports the values of thresholds Lim_{Δ} and the number of peaked stations above them (outliers) for different time spans Δt . For the selected interval (30 minutes, bold row) and for the shorter one (10 minutes), 5 stations are outlier for the specific threshold, while increasing the time span outliers tend to vanish. Hence, Table 2.5 supports the selection of 30 minutes as representative time interval for the first indicator TP_{Δ} . In the same manner, Table 2.6 collects the values of thresholds Lim_{En} and the number of peaked stations above them (outliers) for different band period n . The highest number of outliers is in the range of 4-6 hours (13 outliers), while it decreases rapidly outside this range. Therefore a 6 hours band period for the indicator TP_{En} is confirmed to be representative for the oscillating period of such thermal alterations within our dataset.

Figure 2.5 shows the space of indicators ($TP_{En} - TP_{\Delta}$) divided in four regions according to the calculated limits Lim_{Δ} and Lim_{En} . These regions (A, B_1, B_2, C) visualize the four classes of thermal alteration defined by the conditional rules presented in Section 2.2.3. Figure 2.5 also shows the population of the reference group used to calculate the limits. The reference population of TP_{Δ} is here depicted as 23 vertical boxplots (n.b. without whiskers) representing the $TP_{\Delta,i}$ distributions.

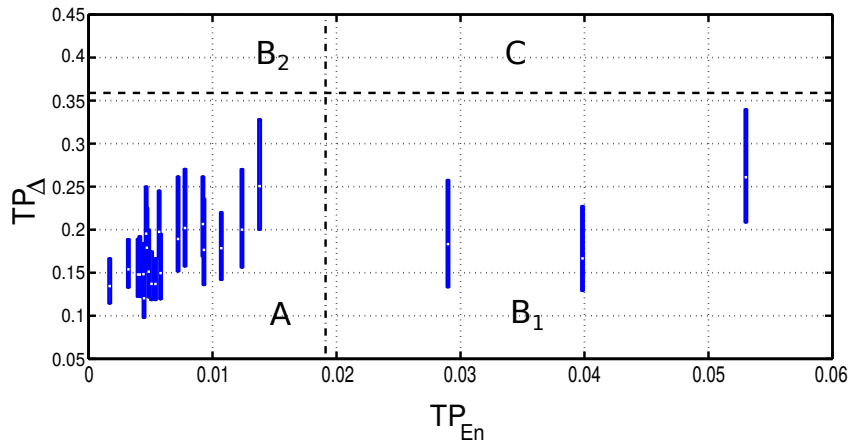


FIGURE 2.5: Indicators for the reference group and the obtained thresholds.

2.3.4 Quantification of thermopeaking alteration for the peaked stations

We finally compute the indicators for the peaked group to quantify the level of thermal alterations due to thermopeaking. Figure 2.6 shows the stations belonging to the peaked group in the space of the two indicators; stations are labelled according to Table 2.2. As a general trend, increasing values of TP_{Δ} outside region A, often correspond to higher values of also TP_{En} for the same station, i.e. there are no cases with high value of TP_{Δ} and vanishing TP_{En} or viceversa. This suggests that, despite the indicators quantify two different modes of thermal alteration, in many cases thermopeaking produces a joint effect on both of them though with different intensities.

Within the 25 peaked stations, some of them reveal no thermal alteration due to thermopeaking and lay in region A, i.e. they show short-scale temperature variations and oscillation period statistically similar to those recorded in the reference group. Some other stations fall in region B_1 but none in region B_2 : this suggests that there are cases with non-natural sub-daily thermal fluctuations of small amplitude, while large temperature variations do not occur without altering also the dominant, daily oscillation period. Finally, the most thermally altered stations lay in region C, i.e. they have magnitude and frequency of sub-daily thermal alterations different from the reference group.

2.4 Discussion

Thermal alterations at sub-daily scale due to the release of hypolimnetic water can be captured by the two indicators we propose. By their very definition (Section 2.2.2), they provide statistically average information of the sub-daily thermal behaviour of each station

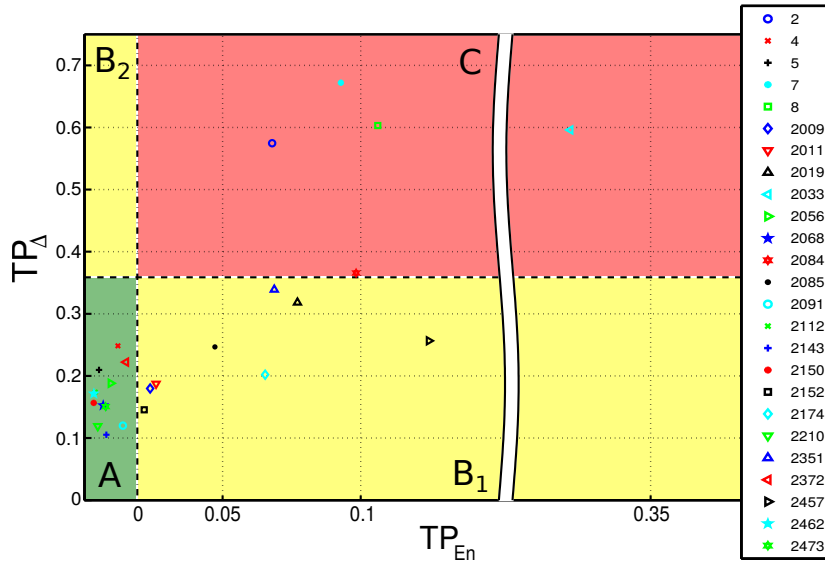


FIGURE 2.6: Indicators TP_{En} and TP_{Δ} for the peaked group stations; labels refer to Table 2.2. The graph is horizontally splitted for the sake of clarity in visualizing the most impacted station in the dataset along with the other ones.

compared with the reference (unaltered) group. Moreover, the statistical approach used in the definition of the thermopeaking thresholds provides a robust identification of the unpeaked thermal conditions for alpine reaches encompassing a broad spectrum of local physiographic characteristics.

Figure 2.6 indicates that the distribution of thermopeaking indicators is arranged along a continuum from a non-impacted region (i.e. statistically similar to unpeaked thermal regime) to an impacted condition in terms of both magnitude and frequency of sub-daily thermal alterations. Against a dataset including 25 stations affected by hydropeaking, the first remarkable evidence is that only 5 stations reveal a strong alteration due to thermopeaking (stations falling in class C of Figure 2.6). Such behaviour can be explained considering different factors. A first consideration is simply that hydropeaking does not always imply thermal alteration. Beside this, it has to be considered that at-a-station observations are affected by heat fluxes exchanged between the river water and the surrounding environment. Thermal waves generated during hydropower plant water releases, while travelling downstream with the water flow, interact continuously with several ambient thermal fluxes (e.g. solar radiation, riparian vegetation, cover, etc.). Such thermal inputs are time dependent, due to day-night and seasonal cycles, but also space-dependent: for instance, the net solar radiation acts distributedly along river reaches, while tributaries mixing occur locally (e.g. Caissie 2006). Toffolon *et al.* (2010) highlight the key-role of external fluxes in modifying the pulsing thermal waves of thermopeaking (see Figure 10 in Toffolon *et al.* 2010). The combined effect of these different factors further contribute in

Station	River	Reach	HP	TP class
1	Noce Bianco	Cogolo Pont upstream	no	A
3	Vermigliana	Vermiglio	no	A
6	Noce	Mezzocorona upstream	no	A
2	Noce Bianco	Cogolo Pont downstream	yes	C
4	Noce	Pellizzano	yes	A
5	Noce	Male	yes	A
7	Noce	Mezzocorona downstream	yes	C
8	Noce	Zambana Vecchia	yes	C

TABLE 2.7: Thermal alteration classification for the Noce catchment stations. First 3 stations have no hydropeaking (HP column) and are within the reference group (Table 2.1).

damping and re-shaping the thermal signature of hydropeaking downstream of the water release.

Such spatial dimension of thermopeaking alterations within the same catchment can be illustrated with reference to the Noce River catchment (North-East of Italy) to which the Italian station in the dataset belong. Figure 2.7 reports the pair of indicators for the Noce catchment stations (from 1 to 8) in the same space of Figure 2.6, together with a schematic visualization of the main hydrogeographic properties of the Noce river system. Stations 1, 3 and 6 lay within the reference group, not being subjected to hydropeaking (Table 2.7). In particular, station 3 refers to Vermigliana, a glacial creek with near-natural flow regime. Stations 1 and 6 are located downstream two different dams, but upstream the hydropower plant water restitutions: hence they have a regulated hydrologic regime but without hydropeaking alterations. Coherently, these stations lay in region A of the space of indicators. It is interesting to focus on the downstream changes of the thermopeaking signature between the peaked stations 2-4-5 and between the peaked stations 7-8, located downstream two different hydropower plant water releases and affected by hydropeaking (see Appendix A). The approximate distances between stations 2-4, 4-5 and 7-8 are 8, 15 and 10 kilometers, respectively. Stations 2 and 7 are the closest to water restitutions and coherently our indicators reveal a strong alteration both in term of amplitude and frequency of sub-daily thermal variations (class C). Such analogous upstream thermal alteration (stations 2 and 7) is reflected in different way in the two downstream systems. In the Upper Noce (stations 2-4-5), while hydropeaking alteration persists until station 5 (Table 2.7), thermopeaking alteration is already vanished after 8km, at station 4 (region A in Figure 2.7). On the contrary in the Lower Noce, even though stations 7-8 are farther than stations 2-4, thermopeaking is not damped within this reach (both stations 7 and 8 lay in region C).

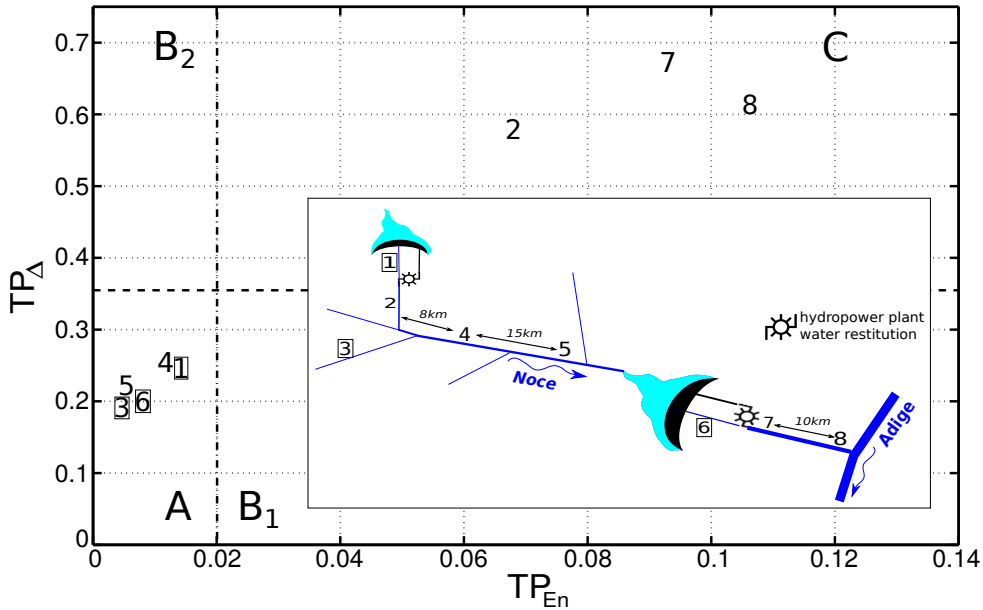


FIGURE 2.7: Thermo-peak indicators for Noce River’s stations. Boxed stations (1,3 and 6) lay within the reference group (Table 2.1). The box illustrates schematically the location of the 8 stations along the Noce River system, where the key hydropower plants and their release locations, causing hydropeaking, are reported.

The causes of such different evolution of the phenomenon have to be sought in the differences in local characteristics of the receiving river reaches. In the Upper Noce system (downstream station 2), the river meets a major tributary (Vermigliana Creek, natural regime) and some other minor creeks. The reach has mostly a simple single-thread morphology with step and pool sequences and local enlargements. Also the solar exposition varies when moving downstream the valley of Noce River (west-east oriented). The overall combination of these different thermal effects is eventually reflected into a significant damping of the thermo-peak alteration measured in station 2. A markedly different behaviour is observed in the Lower Noce reach between stations 7 and 8. Here the Noce River is channelized for most of the 10km reach length with the exception of a localized wider sub-reach of roughly 1km length. No relevant tributaries are present and heat exchanges can be expected to display small thermal source heterogeneity because of the dominant homogeneity in channel morphology and of the absence of relevant lateral tributaries. The initial thermo-peak wave recorded in section 7 therefore travels downstream almost undisturbed until station 8, which coherently falls in region C of the indicators’ space of Figure 2.7.

The indicators depicted in the space of Figure 2.6 quantify a median behaviour for each station, while for management purposes additional information might be required, particularly in consideration of the high temporal and spatial variability of both natural and altered river thermal regimes. For instance, within classification schemes of the

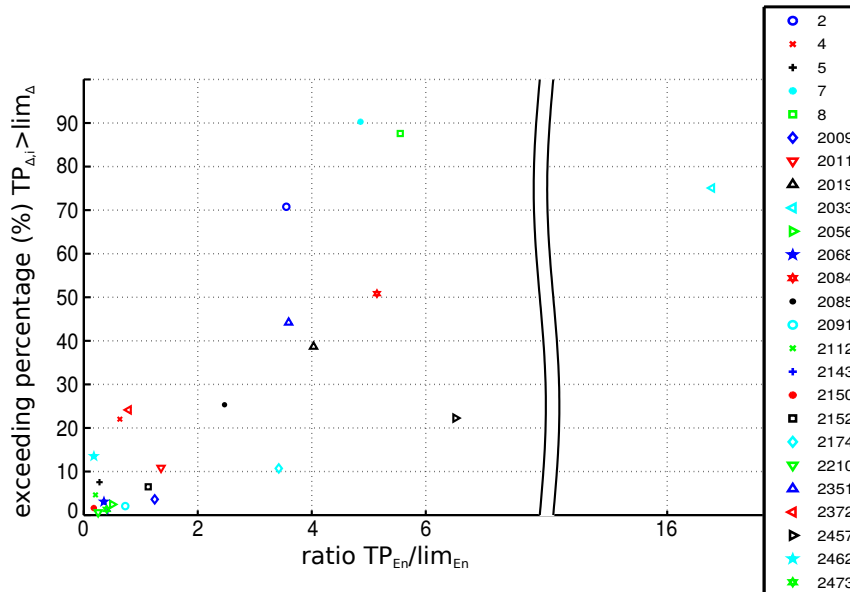


FIGURE 2.8: Recasted formulation of the indicators TP_{Δ} (exceeding probability of threshold) and TP_{E_n} scaled with threshold.

physical and ecological quality of river systems, it might often relevant to quantify *how much* or *for how long* the sub-daily thermal regime of a peaked station does differ from that of an unpeaked station. To this aim we propose a recast version of Figure 2.6 able to incorporate additional information about the variability in the sub-daily thermal regime. Figure 2.8 presents the indicators of the impacted group (Table 2.2) with modified axes. Firstly, instead of considering the indicator TP_{Δ} , which represents a median behaviour, we evaluate the percentage of $TP_{\Delta,i}$ (Equation 2.1) distribution exceeding the specific threshold $Lim_{\Delta} = 0.36$ (Y axes in Figure 2.8). Secondly, the TP_{E_n} indicator, which is an unique value for each station by its very definition (Equation 2.5), is scaled with the limit $Lim_{E_n} = 0.019$ (X axes in Figure 2.8). The practical use of the reshaped space presented in Figure 2.8 can be illustrated referring, for instance, to station 2085 (Aare River at Hagneck, CH). It shows an oscillation energy more than double (≈ 2.3 times, X axes) compared to unaltered regimes, but the magnitude of daily maximum temperature variations exceeds the unaltered limit Lim_{Δ} around 25% of time (Y axes).

In a management perspective, such reformulation of the indicator space presented in Figure 2.8 easily allows one to identify stations with altered oscillation periods (oscillation energy, X axes) and, among them, to evaluate how frequently the fluctuations are significantly stronger compared to those typical of thermally unaltered stations (magnitude of variations, Y axes).

2.5 Conclusions

The proposed indicators allow to quantify the degree of sub-daily thermal regime alteration due to thermopeaking at-a-station scale. Moreover, inasmuch as the quantification is based on a reference (non-impacted) behaviour and is independent from the physiographic characteristics of the catchment, it allows the direct comparison among different gauging stations. Such approach overcomes also the need of having temperature records both upstream and downstream each hydropower plant water restitution to evaluate the alteration of thermal regime.

In case of gauging stations located along the same river system, the spatial analysis of the indicators can also reveal information on the downstream damping scale of thermopeaking alterations, allowing the identification of more and less impacted locations. The outcomes of the present study remark also how hydro- and thermopeaking have different characteristic spatial scales of propagation, suggesting that targeted strategies have to be considered to mitigate either one or both these alterations. The methodology here presented can be adopted as first screening tool for environmental managers to identify and quantify at-a-station river thermal alterations, thus providing a powerful mapping tool to set priorities and critical locations. This relatively simple methodology for the identification of critically impacted stations allows to concentrate subsequent efforts and specific investigations to characterize particular thermal regimes at site (reach) scale.

Chapter 3

Two-dimensional numerical model of hydro- and thermo-dynamics in rivers with complex morphology

Based on: Vanzo D., A. Siviglia and E. F. Toro (*in preparation*). Hyperbolic reformulation of the shallow water advection-diffusion problem on unstructured grids.

3.1 Introduction

Numerical simulations of the advection-diffusion of a passive tracer (e.g. nutrients, pollutants, temperature etc.) in rivers are becoming increasingly useful for assessing water pollution, designing measures to improve water quality and assessing possible effects on the ecosystems (e.g. Horn *et al.*, 2004; Tsakiris and Alexakis, 2012; Rekolainen *et al.*, 2003). The shallow water equations are the usual model to describe the flows in such environments where the flows have horizontal dimensions much larger than their vertical extent. If the passive tracer is vertically well-mixed, their dynamics may be represented by a depth-averaged advection-diffusion equation. The coupling of the shallow water equations with the advection-diffusion equation results in a system of partial differential equations (PDE) of parabolic type. They govern different physical process having different scales: in the advective process small waves propagate at a finite velocity while in the diffusive process small perturbations of either the flow field or concentration of the passive tracer propagate with infinite velocity. This aspect together with the presence

of domains characterized by complex morphologies in rivers where also wetting and drying regions may appear make this problem particularly challenging from the numerical point of view. Moreover, since both the flow and passive tracer concentration may be non-smooth and contain simultaneously nonlinear hydraulic jumps, rarefaction waves and linear discontinuities, the mass preservation, which is crucial in such a context, becomes very challenging.

The aim of this chapter is to present a novel robust and accurate numerical approach for solving the shallow water advection diffusion equations over complex topographies. To this end, we follow the relaxation approach firstly proposed by Cattaneo (1949; 1958) and we transform the initial parabolic system of PDE in an hyperbolic system containing stiff source terms (Toro and Montecinos, 2014). This approach is based on a relaxation of the spatial gradients of the passive tracer concentration and does not change significantly the structure of the original system. More important it removes the unphysical phenomenon of instantaneous small perturbation wave propagation. The resulting hyperbolic relaxation system is solved numerically using a classical splitting technique, identifying two different operators. The first contains the principal part (advective operator), the topographical source terms related to bottom slopes and the stiff source terms emerging from the relaxation procedure; the second contains the remaining frictional source terms. The principal part is solved using the DOT upwind scheme developed by Dumbser and Toro (2011), which provides accurate solutions, by explicitly accounting for all the waves present in the wave pattern of the relaxation system. The first-order DOT method is extended to second-order accuracy in space and time in the ADER framework (e.g. Toro and Titarev, 2002).

The stiff source terms are handled by means of implicit ADER scheme proposed by Montecinos and Toro (2014) while topographical source terms are taking in account adopting the robust approach proposed by Duran *et al.* (2013). The frictional source terms are added to the problem solving a system of ordinary differential equations using an implicit Runge-Kutta method.

Finally, the proposed model is applied to well-established test problems with the aim of demonstrating that it is able i) to correctly treat the propagation of wetting and drying fronts preserving mass which is challenging when treating unsteady flows over complex topographies; ii) to preserve particular types of steady states, thus correctly balancing fluxes and source terms (well-balanced property); this contributes to improve the solution of steady and transient flows at any flow condition (Bermudez and Vazquez, 1994); iii) to achieve the second order of accuracy.

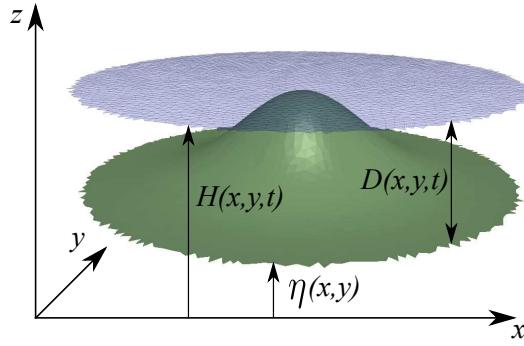


FIGURE 3.1: Sketch of water surface and channel bottom.

3.2 Governing equations

Let us consider a system of partial differential equations (PDE) composed by the shallow water equations and one advection-diffusion equation for the transport of a passive tracer in two dimensions. Introducing a Cartesian reference system $(x; y; z)$ in which the z axis is vertical and the (x, y) plane is horizontal (see Fig. 3.1), the system of governing equations can be written as:

$$\begin{cases} \frac{\partial H}{\partial t} + \frac{\partial q_x}{\partial x} + \frac{\partial q_y}{\partial y} = 0 \\ \frac{\partial q_x}{\partial t} + \frac{\partial}{\partial x} \left(\frac{q_x^2}{D} + \frac{1}{2}gH^2 - gH\eta \right) + \frac{\partial}{\partial y} \left(\frac{q_x q_y}{D} \right) + gH \frac{\partial \eta}{\partial x} + gDS_{fx} = 0 \\ \frac{\partial q_y}{\partial t} + \frac{\partial}{\partial x} \left(\frac{q_y q_x}{D} \right) + \frac{\partial}{\partial y} \left(\frac{q_y^2}{D} + \frac{1}{2}gH^2 - gH\eta \right) + gH \frac{\partial \eta}{\partial y} + gDS_{fy} = 0 \\ \frac{\partial q_c}{\partial t} + \frac{\partial}{\partial x} \left(\frac{q_x q_c}{D} - kD \frac{\partial C}{\partial x} \right) + \frac{\partial}{\partial y} \left(\frac{q_y q_c}{D} - kD \frac{\partial C}{\partial y} \right) - S_C = 0 \end{cases} \quad (3.1)$$

where H and η denote the water surface and bottom elevation respectively, $D = (H - \eta)$ is the water depth, $\vec{q} = (q_x, q_y)$ is the flow discharge per unit width, $q_c = CD$ is the mass of passive tracer per unit width and C is the depth averaged passive tracer concentration. Furthermore, g is the acceleration due to gravity, $\vec{S}_f = (S_{fx}, S_{fy})$ are the dimensionless friction terms of the hydrodynamic equations and S_C represents the external dimensionless source terms and k is the diffusion coefficient ($[m^2/s]$) for the passive tracer C , respectively. System (3.1) is of parabolic type due to the diffusive terms contained in the last equation.

In order to solve system (3.1) we need to specify the closure relations for S_{fx} , S_{fy} , S_C , and k . The module of friction $S_f = \sqrt{S_{fx}^2 + S_{fy}^2}$ is evaluated by using the Manning law as follows:

$$S_f = \frac{q^2 n_f^2}{D^{10/3}}, \quad (3.2)$$

where $q = \sqrt{q_x^2 + q_y^2}$ is the module of flow discharge and n_f is the Manning roughness coefficient. Consistently with the depth-averaged approach in which we neglect the role of three-dimensional circulations, we project (3.2) in the direction given by the flow discharge

vector \vec{q} :

$$S_{fx} = \frac{q_x q n_f^2}{D^{10/3}} \quad , \quad S_{fy} = \frac{q_y q n_f^2}{D^{10/3}} . \quad (3.3)$$

Alternatively, friction terms S_{fx} and S_{fy} are evaluated via the Chezy friction law, reading

$$S_{fx} = \frac{q_x^2}{g C_h^2 D^3} \quad , \quad S_{fy} = \frac{q_y^2}{g C_h^2 D^3} . \quad (3.4)$$

The dimensionless Chezy coefficient C_h in Equation 3.4 can be assumed as constant, typically ranging between 10 and 20, or evaluated with a logarithmic dependence from the water depth D in the form

$$C_h = 6 + 2.5 \ln \left(\frac{D}{k_{C_h} D_s} \right) , \quad (3.5)$$

where k_{C_h} is a constant (usually $k_{C_h} = 2.5$) and D_s is the median grain size characterizing the bottom.

Passive tracer dimensionless source terms S_C and diffusive coefficient k depend on the specific physical problem considered, i.e. depend on the nature of the passive tracer taken into account. In case of shallow water problems the diffusive coefficient k can be estimated (e.g. Kim and Chapra, 1997) as

$$k = C_d D U_* , \quad (3.6)$$

where U_* is the bed frictional velocity ($[m/s]$) and C_d is a constant coefficient ($C_d \approx 6$ for two-dimensional shallow water problems, Fernando, 2012). For the sake of generality S_C is not here specified while the diffusion coefficient k is assumed to be a constant if not differently specified.

When facing the specific problem of the surface water thermal transport, the source terms S_C are described by the summatory of the heat fluxes among the water column, the atmosphere and the stream bed (e.g. Caissie, 2006). Such different flux terms are available in literature and can be straight implemented in the proposed numerical model (e.g. Lai and Mooney, 2009; Siviglia and Toro, 2009; Ouellet *et al.*, 2014).

3.2.1 Hyperbolic reformulation of the equations

Following the the Cattaneo's (1949; 1958) relaxation approach, as described in Toro and Montecinos (2014), we formulate the system of governing equations (3.1) as hyperbolized system of equations with stiff source terms. Let us introduce a relaxation time ϵ , with

$\epsilon > 0$ and two auxiliary functions ψ_1 and ψ_2 such that:

$$\psi_1 \rightarrow \frac{\partial C}{\partial x}, \quad \text{as } \epsilon \rightarrow 0 \quad \psi_2 \rightarrow \frac{\partial C}{\partial y}, \quad \text{as } \epsilon \rightarrow 0. \quad (3.7)$$

Then we consider the two following additional evolution equations for ψ_1 and ψ_2 :

$$\frac{\partial \psi_1}{\partial t} + \frac{\partial}{\partial x} \left(-\frac{q_c}{D\epsilon} \right) = -\frac{\psi_1}{\epsilon}, \quad \frac{\partial \psi_2}{\partial t} + \frac{\partial}{\partial y} \left(-\frac{q_c}{D\epsilon} \right) = -\frac{\psi_2}{\epsilon}. \quad (3.8)$$

Then the following system

$$\left\{ \begin{array}{l} \frac{\partial H}{\partial t} + \frac{\partial q_x}{\partial x} + \frac{\partial q_y}{\partial y} = 0 \\ \frac{\partial q_x}{\partial t} + \frac{\partial}{\partial x} \left(\frac{q_x^2}{D} + \frac{1}{2}gH^2 - gH\eta \right) + \frac{\partial}{\partial y} \left(\frac{q_x q_y}{D} \right) + gH \frac{\partial \eta}{\partial x} + gDS_{fx} = 0 \\ \frac{\partial q_y}{\partial t} + \frac{\partial}{\partial x} \left(\frac{q_y q_x}{D} \right) + \frac{\partial}{\partial y} \left(\frac{q_y^2}{D} + \frac{1}{2}gH^2 - gH\eta \right) + gH \frac{\partial \eta}{\partial y} + gDS_{fy} = 0 \\ \frac{\partial q_c}{\partial t} + \frac{\partial}{\partial x} \left(\frac{q_x q_c}{D} - kD\psi_1 \right) + \frac{\partial}{\partial y} \left(\frac{q_y q_c}{D} - kD\psi_2 \right) - S_C = 0 \\ \frac{\partial \psi_1}{\partial t} + \frac{\partial}{\partial x} \left(-\frac{q_c}{D\epsilon} \right) + \frac{\psi_1}{\epsilon} = 0 \\ \frac{\partial \psi_2}{\partial t} + \frac{\partial}{\partial y} \left(-\frac{q_c}{D\epsilon} \right) + \frac{\psi_2}{\epsilon} = 0 \end{array} \right. \quad (3.9)$$

constitutes a relaxation system whose solutions approximate those of the original system (3.1).

System (3.9) can be written in the vectorial form as

$$\partial_t \mathbf{Q} + \partial_x \mathbf{F}_x(\mathbf{Q}) + \partial_y \mathbf{F}_y(\mathbf{Q}) = \mathbf{S}(\mathbf{Q}), \quad (3.10)$$

with

$$\mathbf{Q} = \begin{bmatrix} H \\ q_x \\ q_y \\ q_c \\ \psi_1 \\ \psi_2 \end{bmatrix}, \quad \mathbf{F}_x = \begin{bmatrix} q_x \\ \frac{q_x^2}{D} + \frac{1}{2}gH^2 - gH\eta \\ \frac{q_x q_y}{D} \\ \frac{q_x q_c}{D} - kD\psi_1 \\ -\frac{q_c}{D\epsilon} \\ 0 \end{bmatrix}, \quad \mathbf{F}_y = \begin{bmatrix} q_y \\ \frac{q_x q_y}{D} \\ \frac{q_y^2}{D} + \frac{1}{2}gH^2 - gH\eta \\ \frac{q_y q_c}{D} - kD\psi_2 \\ 0 \\ -\frac{q_c}{D\epsilon} \end{bmatrix}. \quad (3.11)$$

The different source terms can be expressed as

$$\mathbf{S}(\mathbf{Q}) = \mathbf{S}_{ft}(\mathbf{Q}) + \mathbf{S}_{rel}(\mathbf{Q}) + \mathbf{S}_{bed}(\mathbf{Q}), \quad (3.12)$$

where $\mathbf{S}_{ft}(\mathbf{Q})$ contains the bottom friction terms and the passive tracer source terms, $\mathbf{S}_{bed}(\mathbf{Q})$ are the bed-slope source terms and $\mathbf{S}_{rel}(\mathbf{Q})$ the terms arising from the relaxation procedure. They read, respectively,

$$\mathbf{S}_{ft}(\mathbf{Q}) = \begin{bmatrix} 0 \\ -g(H - \eta)S_{fx} \\ -g(H - \eta)S_{fy} \\ S_C \\ 0 \\ 0 \end{bmatrix}, \quad \mathbf{S}_{rel}(\mathbf{Q}) = \begin{bmatrix} 0 \\ 0 \\ 0 \\ 0 \\ -\frac{\psi_1}{\epsilon} \\ -\frac{\psi_2}{\epsilon} \end{bmatrix}, \quad \mathbf{S}_{bed}(\mathbf{Q}) = \begin{bmatrix} 0 \\ -gH\frac{\partial\eta}{\partial x} \\ -gH\frac{\partial\eta}{\partial y} \\ 0 \\ 0 \\ 0 \end{bmatrix} \quad (3.13)$$

Note that, due to the source terms $-\frac{\psi_1}{\epsilon}$ and $-\frac{\psi_2}{\epsilon}$, the relaxation system is stiff.

3.2.2 Hyperbolicity of the relaxation system

Let us write system (3.10) in quasi-linear form as follows:

$$\partial_t \mathbf{Q} + \mathbf{A}_x \partial_x \mathbf{Q} + \mathbf{A}_y \partial_y \mathbf{Q} = \mathbf{S}(\mathbf{Q}), \quad (3.14)$$

in which the Jacobian matrices corresponding to the flux $\mathbf{F}_x(\mathbf{Q})$ and $\mathbf{F}_y(\mathbf{Q})$ are

$$\mathbf{A}_x = \frac{\partial \mathbf{F}_x}{\partial \mathbf{Q}} = \begin{bmatrix} 0 & 1 & 0 & 0 & 0 & 0 \\ -\frac{q_x^2}{D^2} + gH - g\eta & 2\frac{q_x}{D} & 0 & 0 & 0 & 0 \\ -\frac{q_x q_y}{D^2} & \frac{q_y}{D} & \frac{q_x}{D} & 0 & 0 & 0 \\ \left(-\frac{q_x q_c}{D^2} - k\psi_1\right) & \frac{q_c}{D} & 0 & \frac{q_x}{D} & -kD & 0 \\ \frac{q_c}{D^2 \epsilon} & 0 & 0 & -\frac{1}{D\epsilon} & 0 & 0 \\ 0 & 0 & 0 & 0 & 0 & 0 \end{bmatrix}, \quad (3.15)$$

$$\mathbf{A}_y = \frac{\partial \mathbf{F}_y}{\partial \mathbf{Q}} = \begin{bmatrix} 0 & 0 & 1 & 0 & 0 & 0 \\ -\frac{q_x q_y}{D^2} & \frac{q_y}{D} & \frac{q_x}{D} & 0 & 0 & 0 \\ \left(-\frac{q_y^2}{D^2} + gH - g\eta\right) & 0 & 2\frac{q_y}{D} & 0 & 0 & 0 \\ \left(-\frac{q_y q_c}{D^2} - k\psi_2\right) & 0 & \frac{q_c}{D} & \frac{q_y}{D} & 0 & -kD \\ 0 & 0 & 0 & 0 & 0 & 0 \\ \frac{q_c}{D^2 \epsilon} & 0 & 0 & -\frac{1}{D\epsilon} & 0 & 0 \end{bmatrix}. \quad (3.16)$$

Since system (3.10) satisfies the rotational invariance property (proof omitted here) we can study the hyperbolicity of the new relaxed system considering the projected matrix obtained as

$$\mathbf{A}_{\hat{n}_{ij}} = \underline{\underline{\mathbf{A}}} \cdot \hat{n}_{ij} = (\mathbf{A}_x, \mathbf{A}_y) \cdot \hat{n}_{ij}. \quad (3.17)$$

It reads:

$$\mathbf{A}_{\hat{n}_{ij}} = \begin{bmatrix} 0 & n_{ijx} & n_{ijy} & 0 & 0 & 0 \\ n_{ijx} Dg - u\hat{U} & n_{ijx} u + \hat{U} & 0 & 0 & 0 & 0 \\ n_{ijy} Dg - v\hat{U} & n_{ijx} v & n_{ijy} v + \hat{U} & 0 & 0 & 0 \\ -C\hat{U} - k(n_{ijx}\psi_1 + n_{ijy}\psi_2) & n_{ijx} C & n_{ijy} C & \hat{U} & -n_{ijx} kD & -n_{ijy} kD \\ \frac{n_{ijx} C}{D\epsilon} & 0 & 0 & -\frac{n_{ijx}}{D\epsilon} & 0 & 0 \\ \frac{n_{ijy} C}{D\epsilon} & 0 & 0 & -\frac{n_{ijy}}{D\epsilon} & 0 & 0 \end{bmatrix}. \quad (3.18)$$

where $\hat{n}_{ij} = (n_{ijx}, n_{ijy})$, $u = \frac{q_x}{D}$ and $v = \frac{q_y}{D}$ and $\hat{U} = n_{ijx} u + n_{ijy} v$. The eigenvalues of $\mathbf{A}_{\hat{n}_{ij}}$ are the roots of the characteristic polynomial $|\mathbf{A}_{\hat{n}_{ij}} - \lambda \mathbf{I}| = 0$, where \mathbf{I} is the identity matrix and λ is a parameter. The eigenvalues are given as

$$\begin{aligned} \lambda^{(1)} &= \frac{1}{2}\hat{U} \left(1 - \sqrt{1 + \frac{4}{Pe}}\right), \quad \lambda^{(2)} = \hat{U} \left(1 - \frac{1}{Fr}\right), \quad \lambda^{(3)} = 0, \\ \lambda^{(4)} &= \hat{U}, \quad \lambda^{(5)} = \hat{U} \left(1 + \frac{1}{Fr}\right), \quad \lambda^{(6)} = \frac{1}{2}\hat{U} \left(1 + \sqrt{1 + \frac{4}{Pe}}\right), \end{aligned} \quad (3.19)$$

where we make use of the dimensionless parameters Froude $Fr = \frac{\hat{U}}{\sqrt{gD}}$ and Peclet $Pe = \frac{\epsilon \hat{U}^2}{k}$

(this parameter assess the relative importance of advection and diffusion) which are defined using the projection of the flow velocity vector \hat{U} . All the eigenvalues are real and distinct except for:

$$\begin{aligned}\lambda^1 = \lambda^2, \quad \rightarrow Pe = Pe_M = -\frac{Fr^2}{Fr - 1}, \\ \lambda^5 = \lambda^6, \quad \rightarrow Pe = Pe_P = \frac{Fr^2}{Fr + 1}.\end{aligned}\tag{3.20}$$

Finally, it is worth analyzing the behaviour of the new derived system in the limits $Pe \rightarrow 0$ (*pure diffusive* case) and $Pe \rightarrow \infty$ (*pure advective* case). In the *pure diffusive* case, the eigenvalues become:

$$\lambda^{(1)} = -\infty, \lambda^{(2)} = \hat{U} \left(1 - \frac{1}{Fr}\right), \lambda^{(3)} = 0, \lambda^{(4)} = \hat{U}, \lambda^{(5)} = \hat{U} \left(1 + \frac{1}{Fr}\right), \lambda^{(6)} = \infty,\tag{3.21}$$

and the relaxation system is no longer hyperbolic, while in *pure advective* case

$$\lambda^{(1)} = 0, \lambda^{(2)} = \hat{U} \left(1 - \frac{1}{Fr}\right), \lambda^{(3)} = 0, \lambda^{(4)} = \hat{U}, \lambda^{(5)} = \hat{U} \left(1 + \frac{1}{Fr}\right), \lambda^{(6)} = \hat{U},\tag{3.22}$$

the relaxation system is hyperbolic but not strictly.

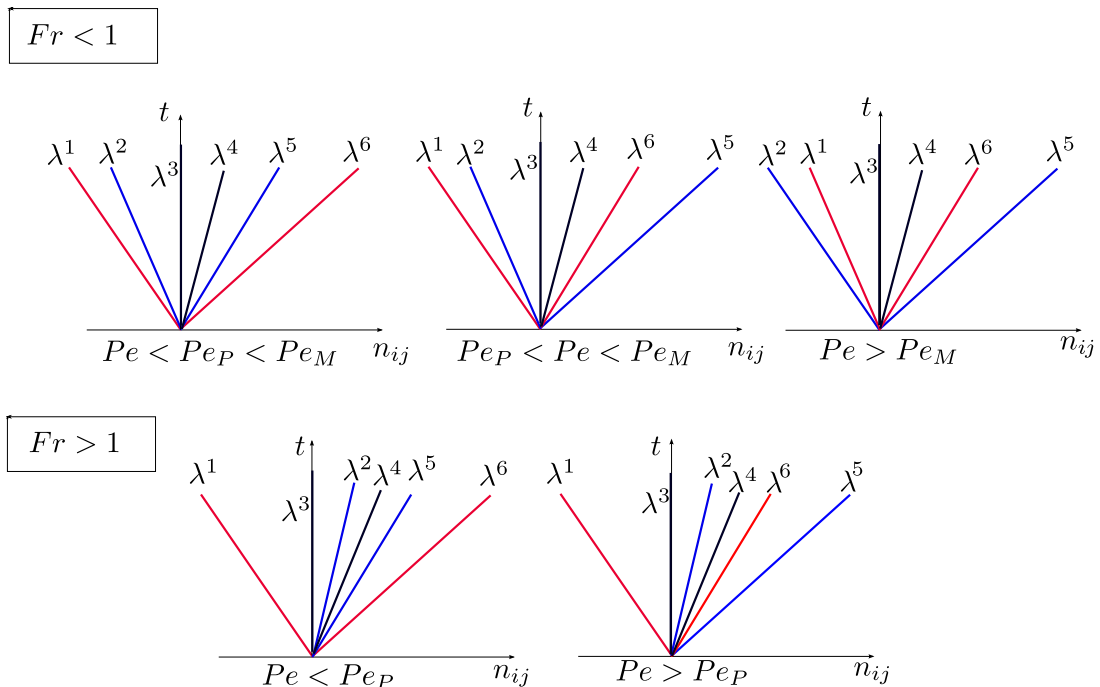
3.2.3 Relaxation system versus the original system

According to the relaxation philosophy, as the relaxation time $\epsilon \rightarrow 0$ the relaxation system (3.9) tends to the original system of equations (3.1). Therefore, exact solutions of the two systems are different for any finite value $\epsilon > 0$ and their differences increases as ϵ increases. The error of the new system is inherent with its relaxation formulation. Moreover, when numerical solutions of the relaxation system are seek, an additional error is committed, a numerical error, that depends on the grid size and the order of accuracy of the numerical method used. Then it is clear that a key ingredient for obtaining accurate results solving the relaxation system is the choice of the relaxation parameter ϵ . Montecinos *et al.* (2014) demonstrate that the optimal value for the relaxation parameter is

$$\epsilon_r = \frac{O(1)\rho_*^r}{\beta(r)},\tag{3.23}$$

with $O(1) = 15$, r order of accuracy of the method and

$$\beta(r) = \frac{1 - 2^{-\frac{1}{2}}}{2^{r-\frac{1}{2}} - 1}.\tag{3.24}$$


 FIGURE 3.2: Possible wave patterns in space (n - t) for the relaxation system.

As representative mesh spacing ρ_* we adopt the minimum radius of the inscribed circle among all triangular cells T_i of the domain ($\rho_* = \min(\rho_i)$). This criterion (3.23) provides a practical and robust way of choosing the relaxation parameter. For $\epsilon > \epsilon_r$ the formulation error is prevailing over the numerical error then increasing the order of accuracy or refining the mesh will not help much in recovering the exact solution of the original system. On the contrary, when $\epsilon \leq \epsilon_r$ the numerical error prevails over the formulation error and increasing the order of accuracy or decreasing the grid size should ensure convergence to the exact solution of the original system (Toro and Montecinos, 2014).

3.2.4 Wave patterns and maximum eigenvalue

Let us assume $\hat{U} > 0$ and exploit the range of variations of the six eigenvalues (3.19) in the limits of $Pe \rightarrow 0$, $Pe \rightarrow \infty$ and $Fr \rightarrow 0$, $Fr \rightarrow \infty$. It results that

$$-\infty < \lambda^{(1)} \leq 0, \quad -\infty < \lambda^{(2)} \leq \hat{U}, \quad \lambda^3 = 0, \quad \lambda^4 = \hat{U}, \quad \hat{U} \leq (\lambda^{(5)}, \lambda^{(6)}) < \infty. \quad (3.25)$$

According to relations (3.20) and (3.25) the possible wave patterns are three for the subcritical case ($Fr < 1$) and two for the supercritical case ($Fr > 1$). They are given in Fig. 3.2.

From the analysis of the eigenvalues it emerges that the largest eigenvalue in absolute value can be λ^5 or λ^6 depending of the values assumed by the Peclet number. λ^5 corresponds to the largest eigenvalue of the shallow water equations and then it can be view as the eigenvalue related to the advective part, while λ^6 is a function of the relaxation time parameter and the diffusion coefficient through the Peclet number. Then we can identified two cases: *advection dominated case* in which $\lambda^5 > \lambda^6$ ($Pe > Pe_P$) and a *diffusive dominated case* in which $\lambda^6 > \lambda^5$ ($Pe < Pe_P$). When numerical solutions of the relaxation system are seek, the adoption of explicit methods requires that the stability condition of Courant must be satisfied. The stability conditions poses some restriction on the choice of the time step used for marching the solution in time. In particular the time step Δt is inversely proportional to the maximum eigenvalue of the system. Therefore in the *advection dominated case* we can integrate the relaxation system using a time step which depends on λ^5 , the largest hydrodynamic eigenvalue. From a computational time perspective this means that the relaxation system is equivalent to the pure hydrodynamic system governed by the shallow water equations. While, in the *diffusive dominated case*, the time marching solution depends on the Peclet number and it advances with smaller time steps which approaches the null values as $Pe \rightarrow 0$.

In order to highlight the implications in the context of real-world applications, let us discuss the order of magnitude of the parameters involved for real rivers.

Reformulating the condition $Pe = Pe_P$ in terms of dimensional variables it is easy to derive the condition

$$k < g(1 + Fr)\epsilon D. \quad (3.26)$$

Substituting Equation (3.6) into (3.26) we obtain

$$C_d < g(1 + Fr)\frac{\epsilon}{U_*}. \quad (3.27)$$

In real-world Froude number is in the range $[0, 2]$, hence $g(1 + Fr) \approx 10 \cdot [1, 3]$. Bottom shear velocity U_* has order of magnitude of $O(-1)$ (e.g. Wilcock, 1996). The relaxation parameter ϵ depends on the mesh characteristic length ρ_* and for real-scale applications has order of magnitude between $O(-1, 0)$. Hence condition (3.27) reads

$$C_d < g(1 + Fr) \cdot O(0, 1) \approx [1, 3] \cdot O(1, 2)). \quad (3.28)$$

Recalling that C_d has order of magnitude $O(0)$ (Fernando, 2012) for real-scale river applications, the condition (3.26) is usually satisfied and therefore the reformulated hyperbolic system lies in the *advection dominated case*.

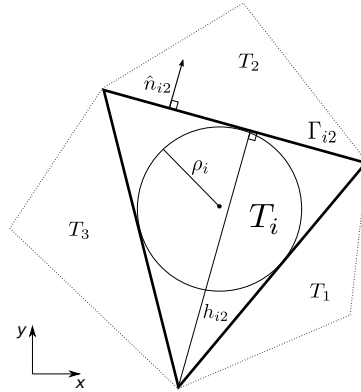


FIGURE 3.3: Sketch of the triangular mesh with the adopted notation.

3.3 Numerical solution

The problem is discretized adopting a finite volume approach over unstructured triangular meshes. A conforming triangulation \mathcal{T}_Ω of the computational domain $\Omega \subset R^2$ by elements T_i such that

$$\mathcal{T}_\Omega = \bigcup T_i, \quad (3.29)$$

is assumed. Each element T_i has 3 edges Γ_{ij} of length S_{ij} , with associated outward pointing face-normal vectors $\hat{n}_{ij} = (n_{ijx}, n_{ijy})$ (Figure 3.3). Data are represented by cell averages \mathbf{Q}_i^n and the numerical solution sought at time $t^{n+1} = t^n + \Delta t$, is denoted with \mathbf{Q}_i^{n+1} .

3.3.1 Splitting procedure

We handle the inhomogeneous character of system (3.10) due to the presence of source terms by a splitting technique. We initially consider the following initial value problem (IVP)

$$\mathcal{C}(\mathbf{Q}) = \mathbf{S}(\mathbf{Q}), \quad (3.30)$$

where \mathcal{C} represents the advective operator

$$\partial_t \mathbf{Q} + \partial_x \mathbf{F}_x(\mathbf{Q}) + \partial_y \mathbf{F}_y(\mathbf{Q}) = 0. \quad (3.31)$$

The solution is found by solving the following initial value problem (IVP):

$$\left. \begin{array}{l} PDE : \quad \mathcal{C}(\mathbf{Q}) = \mathbf{S}(\mathbf{Q}) = \mathbf{S}_{ft}(\mathbf{Q}) + \mathbf{S}_{rel}(\mathbf{Q}) + \mathbf{S}_{bed}(\mathbf{Q}) \\ IC : \quad \mathbf{Q}(x, y, 0) = \mathbf{Q}_i^n \end{array} \right\} \text{IVP}. \quad (3.32)$$

The complete IVP (3.32) is then splitted into three different IVPs as:

$$\left. \begin{aligned} ODEs : \quad \frac{d\mathbf{Q}}{dt} &= \mathbf{S}_{ft}(\mathbf{Q}) \\ ICs : \quad \mathbf{Q}(x, y, 0) &= \mathbf{Q}_i^n \end{aligned} \right\} \xrightarrow{\frac{1}{2}\Delta t} \overline{\mathbf{Q}}_i \quad \text{IVP1}, \quad (3.33)$$

$$\left. \begin{aligned} PDEs : \quad \mathcal{C}(\mathbf{Q}) &= \mathbf{S}_{rel}(\mathbf{Q}) + \mathbf{S}_{bed}(\mathbf{Q}) \\ ICs : \quad \mathbf{Q}(x, y, 0) &= \overline{\mathbf{Q}}_i \end{aligned} \right\} \xrightarrow{\Delta t} \overline{\overline{\mathbf{Q}}}_i \quad \text{IVP2}, \quad (3.34)$$

$$\left. \begin{aligned} ODEs : \quad \frac{d\mathbf{Q}}{dt} &= \mathbf{S}_{ft}(\mathbf{Q}) \\ ICs : \quad \mathbf{Q}(x, y, 0) &= \overline{\overline{\mathbf{Q}}}_i \end{aligned} \right\} \xrightarrow{\frac{1}{2}\Delta t} \mathbf{Q}_i^{n+1} \quad \text{IVP3}. \quad (3.35)$$

3.3.1.1 Solution of IVP1 and IVP3

In the following the solution for IVP1 is illustrated. Analogous procedure can be implemented for solving IVP3. The right-hand side of ODE (3.33) is evaluated at time $t = \frac{1}{2}\Delta t$ making use of a time Taylor expansion. After a straightforward manipulation IVP1 can be written as:

$$\frac{d\mathbf{Q}}{dt} = \left(\mathbf{I} - \frac{1}{2}\Delta t \left[\frac{\partial \mathbf{S}_{ft}}{\partial \mathbf{Q}} \right]_{\mathbf{Q}_i^n} \right)^{-1} \mathbf{S}_{ft}(\mathbf{Q}|_{\mathbf{Q}_i^n}), \quad (3.36)$$

where \mathbf{I} represents the 6×6 identity matrix and $[\frac{\partial \mathbf{S}_{ft}}{\partial \mathbf{Q}}]$ is the matrix containing the derivatives of friction source terms and external forcing S_C in the advection-diffusion equation with respect to conserved variables. Finally, Equation (3.36) is suitable for time integration using the well-established second-order accurate Runge-Kutta scheme (e.g. Butcher, 1987). Adopting this splitting procedure allows to retain the adaptability of the numerical model to different kind of passive tracer problems, indeed any kind of source terms (i.e. both conservative and non-conservative terms) can be straight implemented.

3.3.1.2 Solution of IVP2

We seek for a solution of the PDEs

$$\partial_t \mathbf{Q} + \partial_x \mathbf{F}_x(\mathbf{Q}) + \partial_y \mathbf{F}_y(\mathbf{Q}) = \mathbf{S}_{rel}(\mathbf{Q}) + \mathbf{S}_{bed}(\mathbf{Q}). \quad (3.37)$$

By integrating (3.37) in the control volume $V = [T_i] \times [t^n, t^{n+1}]$ we obtain

$$\mathbf{Q}_i^{n+1} = \mathbf{Q}_i^n - \frac{\Delta t}{|T_i|} \sum_{j=1}^3 [S_{ij} \mathbf{F}_{\hat{n}_{ij}}] + \Delta t \mathbf{S}_{rel,i} + \Delta t \mathbf{S}_{bed,i} \quad (3.38)$$

where $\mathbf{F}_{\hat{n}_{ij}}$ represents the outward pointing orthogonal interface flux of cell i through its edge j . With \mathbf{Q}_j we denote the neighbour states associated to the cell i .

Fluxes $\mathbf{F}_{\hat{n}_{ij}}$ are evaluated according to Dumbser-Osher-Toro (DOT) solver (Dumbser and Toro, 2011) as

$$\mathbf{F}_{\hat{n}_{ij}} = \frac{1}{2} (\mathbf{F}_{\hat{n}_{ij}}(\mathbf{Q}_0) + \mathbf{F}_{\hat{n}_{ij}}(\mathbf{Q}_1)) - \left(\frac{1}{2} \left(\sum_{k=1}^G \omega_k |\mathbf{A}_{\hat{n}_{ij}}(\psi(s_k))| \right) (\mathbf{Q}_1 - \mathbf{Q}_0) \right) \quad (3.39)$$

where

- $\mathbf{F}_{\hat{n}_{ij}}(\mathbf{Q}) = (\mathbf{F}_x, \mathbf{F}_y) \cdot \hat{n}_{ij}$;
- $|\mathbf{A}_{\hat{n}_{ij}}| = \mathbf{R}_{\hat{n}} |\mathbf{\Lambda}_{\hat{n}}| \mathbf{R}_{\hat{n}}^{-1}$, with $\mathbf{\Lambda}_{\hat{n}}$, $\mathbf{R}_{\hat{n}}$ and $\mathbf{R}_{\hat{n}}^{-1}$ diagonal matrix of the eigenvalues $\lambda_{\hat{n}}^{(i)}$, the right eigenvectors and its inverse, respectively;
- \mathbf{Q}_0 and \mathbf{Q}_1 are the left and the right state in phase-space, respectively;
- $\psi(s) = \mathbf{Q}_0 + s(\mathbf{Q}_1 - \mathbf{Q}_0)$ with $0 \leq s \leq 1$, is straight-line integration path;
- G number of points s_k (with associated weights ω_k) used for Gauss-Legendre quadrature.

The stiff source terms emerging from the relaxation system $\mathbf{S}_{rel}(\mathbf{Q})$ are included in the solution using a local implicit ADER scheme (Montecinos and Toro, 2014) while the topographical source terms $\mathbf{S}_{bed}(\mathbf{Q})$ are solved adopting the strategy of modified state proposed by Duran *et al.* (2013). This approach is very robust and allow to easy handle complex topographies as well as wetting and drying problems.

3.3.1.3 Second order extension

Second order accuracy for the IVP2 is achieved using the ADER-TVD framework adopted in Siviglia *et al.* (2013). The procedure can be summarized as follows:

- *Reconstruction procedure*

We seek for a reconstruction polynomial of degree one in the TVD framework. For each element T_i we identify a stencil of four cells composed of T_i itself and of its three neighbouring cells T_j , $j = 1, 2, 3$:

$$\mathcal{S}_i = T_i \cup T_{j=1} \cup T_{j=2} \cup T_{j=3} . \quad (3.40)$$

We define with $\mathbf{w}_i = \mathbf{w}_i^0 + \mathbf{a}_{i1}(x - x_i) + \mathbf{a}_{i2}(y - y_i)$ the linear reconstruction polynomial in cell T_i , where \mathbf{a}_{i1} and \mathbf{a}_{i2} are slopes and (x_i, y_i) are the coordinates of the

cell barycentre \mathbf{G}_i . We initially compute the values of \mathbf{w}_i^0 , \mathbf{a}_{i1} and \mathbf{a}_{i2} by requiring integral conservation all over \mathcal{S}_i , i. e.:

$$\frac{1}{|T_k|} \int_{T_k} \mathbf{w}_i(\vec{x}) \, d\vec{x} = \overline{\mathbf{Q}}_k \quad \forall T_k \in \mathcal{S}_i . \quad (3.41)$$

The reconstruction Equation (3.41) is solved using a constrained least-squares method in order to guarantee that it is exactly satisfied at least inside element T_i .

In order to avoid spurious oscillations in the vicinity of large gradients, for each conserved variable we apply a TVD limiter to the linear reconstruction. In practise we use the limited reconstruction polynomial:

$$\hat{\mathbf{w}}_i = \overline{\mathbf{Q}}_i + \hat{\mathbf{a}}_{i1} (x - x_i) + \hat{\mathbf{a}}_{i2} (y - y_i) , \quad (3.42)$$

being $\hat{\mathbf{a}}_{i1} = \phi_i \mathbf{a}_{i1}$ and $\hat{\mathbf{a}}_{i2} = \phi_i \mathbf{a}_{i2}$ the limited reconstruction slopes, where the monoslope limiter proposed by Buffard and Clain (2010) is applied component-wise to each variable.

- *Second order accurate one-step time discretisation*

We still need to compute the temporal evolution of the reconstructed polynomial (3.42) in order to be able to construct our final second-order accurate one-step finite volume scheme. The key idea in the ADER approach is to solve high-order Riemann problems at the element boundaries. This is achieved by using a Taylor series expansion in time:

$$\mathbf{Q}_i(x, y, t) = \mathbf{Q}_i(x_i, y_i, t^n) + (x - x_i) \partial_x \mathbf{Q} + (y - y_i) \partial_y \mathbf{Q} + (t - t^n) \partial_t \mathbf{Q} + \mathcal{O}(x^2, y^2, t^2) . \quad (3.43)$$

Then we use the Cauchy-Kowalevski procedure in order to substitute time derivatives with space derivatives in (3.43). For second-order accuracy it suffices to rewrite the system (3.37) as follows:

$$\partial_t \mathbf{Q} = -(\mathbf{A}_x \partial_x \mathbf{Q} + \mathbf{A}_y \partial_y \mathbf{Q}) + \mathbf{S}_{rel} + \mathbf{S}_{bed} . \quad (3.44)$$

The value of $\mathbf{Q}_i(x_i, y_i, t)$ and its spatial derivatives are obtained from the reconstruction polynomial (3.42). In the Cauchy-Kowalevski procedure of Equation (3.44) the term \mathbf{S}_{rel} is here neglected since its included into the fluxes calculation as explained in Section 3.3.1.5.

- *Second-order accurate one-step scheme*

The TVD reconstruction and the Cauchy-Kowalevski procedure gives the boundary-extrapolated value $\overline{\mathbf{Q}}_{ij}$ for each cell i and edge (neighbour) j , hence the final second-order accurate one-step scheme can be written as follows:

$$\mathbf{Q}_i^{n+1} = \mathbf{Q}_i^n - \frac{\Delta t}{|T_i|} \sum_{j=1}^3 \left[S_j \mathbf{F}_{\hat{n},ij}(\overline{\mathbf{Q}}_{ij}^+, \overline{\mathbf{Q}}_{ij}^-) \right] + \Delta t \mathbf{S}_{rel,i} + \Delta t \mathbf{S}_{bed,i}, \quad (3.45)$$

where $\overline{\mathbf{Q}}_{ij}^+$ denotes the boundary-extrapolated data from within element T_i and $\overline{\mathbf{Q}}_{ij}^-$ denotes the boundary-extrapolated data from the neighbour cell associated with edge j , respectively.

3.3.1.4 Second order locally implicit ADER scheme for relaxation source terms

The source terms $\mathbf{S}_{rel,i}$, which arise from the relaxation procedure, are evaluated according to Montecinos and Toro (2014) as

$$\mathbf{S}_{rel,i} = \mathbf{B} \left(\mathbf{I} - \frac{\Delta t}{2} \mathbf{B} \right)^{-1} \left[\mathbf{Q}_i^n - \frac{\Delta t}{2} \mathbf{A}_{\hat{n}} \left(\mathbf{I} - \frac{\Delta t}{2} \mathbf{B} \right)^{-1} \hat{\mathbf{a}}_i \right], \quad (3.46)$$

where $\hat{\mathbf{a}}_i = (\hat{\mathbf{a}}_{i1}, \hat{\mathbf{a}}_{i2})$ are the limited reconstruction slopes of Equation (3.42) and $\mathbf{B} = \frac{\partial \mathbf{S}_{rel}}{\partial \mathbf{Q}}$ the derivatives of the source terms \mathbf{S}_{rel} with respect to the unknowns \mathbf{Q} .

3.3.1.5 Numerical treatment of the bed topography

Bed topography source terms \mathbf{S}_{bed} are treated following the approach of Duran *et al.* (2013), based on a modification of the left (\mathbf{Q}_0) and right (\mathbf{Q}_1) Riemann states at the edges Γ_{ij} . Such method preserves the motionless steady states and allow the occurrence of dry states. In case of non-zero bed topography interface fluxes have to account also for bed elevation η , therefore interface fluxes read

$$\mathbf{F}_{\hat{n}_{ij}} = \mathbf{F}_{\hat{n}_{ij}}(\mathbf{Q}_0, \mathbf{Q}_1, \eta_0, \eta_1), \quad (3.47)$$

where η_0 and η_1 are the bottom elevation at the left and right Riemann state, respectively. Interface states are modified with a non negative reconstruction of water depth D^* and of the free surface H^* , hence

$$\mathbf{Q}_0^* = \mathbf{Q}_0(H_0^*, D_0^*), \quad \mathbf{Q}_1^* = \mathbf{Q}_1(H_1^*, D_1^*). \quad (3.48)$$

Source term $\mathbf{S}_{bed}(\mathbf{Q}_i)$ is conveniently discretized introducing \hat{H}_{ij} and $\bar{\eta}_{ij}$, an approximation of water surface H and bottom elevation η at the interface Γ_{ij} , respectively:

$$\mathbf{S}_{bed}(\mathbf{Q}_i) = \sum_{j=1}^3 S_{ij} \mathbf{S}_{bed_{ij}} = \sum_{j=1}^3 S_{ij} \begin{bmatrix} 0 \\ -g\hat{H}_{ij}(\eta_i - \bar{\eta}_{ij})\hat{n}_{ij,x} \\ -g\hat{H}_{ij}(\eta_i - \bar{\eta}_{ij})\hat{n}_{ij,y} \\ 0 \\ 0 \\ 0 \end{bmatrix}. \quad (3.49)$$

Adopting the modified states of Equation (3.48) and the source terms approximation for Equation (3.49), interface fluxes of Equation (3.47) are recast as

$$\mathbf{F}_{\hat{n}_{ij}}^* = \mathbf{F}_{\hat{n}_{ij}}(\mathbf{Q}_0^*, \mathbf{Q}_1^*, \eta_0, \eta_1) = \mathbf{F}_{\hat{n}_{ij}}(\mathbf{Q}_0^*, \mathbf{Q}_1^*, \bar{\eta}_{ij}, \bar{\eta}_{ij}) - \mathbf{S}_{bed_{ij}}. \quad (3.50)$$

Therefore, inserting Equation (3.50) into the update formula (3.45) gives the final update formula

$$\mathbf{Q}_i^{n+1} = \mathbf{Q}_i^n - \frac{\Delta t}{|T_i|} \sum_{j=1}^3 \left[S_{ij} \mathbf{F}_{\hat{n}_{ij}}^* \right] + \Delta t \mathbf{S}_{rel,i} \quad (3.51)$$

Using an appropriate interpolation of the bottom elevation the approach formally reaches the second-order of accuracy. Further details are given in Duran *et al.* (2013).

3.4 Numerical tests

Here we apply the second order version of the method proposed in this chapter to three established test problems. The aim of the first test is to verify that the scheme adopted is well-balanced up to machine precision while the second test aims at verifying that the expected theoretical order is achieved. In the third test the robustness of the approach is assessed for a dam-break problem over a complex topography showing that the model is capable of preserve mass. Finally a test has been performed considering a river characterized by a complex morphology. If not specified, the tests are performed setting the CFL number to 0.9 and the relaxation parameter is fixed to $\epsilon = 0.9 \epsilon_r$ where ϵ_r is given by relation (3.23).

3.4.1 Extended C-property

The extended C-property represents the capability of a numerical model to correctly preserve the motionless steady state in presence of non-flat bottom and occurrence of

	first order			second order		
	H	$q = \sqrt{q_x^2 + q_y^2}$	q_c	H	$q = \sqrt{q_x^2 + q_y^2}$	q_c
L_1	1.07E-015	7.39E-014	5.33E-015	8.44E-015	3.37E-013	7.11E-013
L_2	4.37E-016	8.72E-014	2.85E-015	5.17E-015	2.05E-013	1.18E-013
L_∞	9.99E-016	2.26E-013	3.33E-015	1.32E-014	4.05E-013	3.86E-014

TABLE 3.1: Numerical verification of the extended C-property. Error norms at time $t = 60$ s for H , $q = \sqrt{q_x^2 + q_y^2}$ and q_c .

emerging topography (Castro *et al.*, 2005). The consistency and well-balancing of the implemented method for the treatment of bed slope source terms is analytically showed in Duran *et al.* (2013).

We test here the numerical extended C-property both for the hydrodynamic and passive tracer components. For a given constant water surface elevation H_0 and constant concentration C_0 , the exact steady state solution of the system (3.9) reads

$$\begin{cases} H(x, y, t) = \max(H_0, \eta(x, y)) \\ q_x(x, y, t) = q_y(x, y, t) = 0 \\ q_c(x, y, t) = q_c(x, y, 0) = D(x, y, 0)C_0 \\ \psi_1(x, y, t) = \psi_2(x, y, t) = 0 \end{cases} \quad \forall x, y, t. \quad (3.52)$$

The square computational domain $[-5; 5] \times [-5; 5]$ m is discretized by 2784 triangular cells. Reflective boundary conditions are set at the domain edges and the bottom is described by the following expression:

$$\eta(x, y) = \exp(-(x + 1.5)^2 - (y + 1.5)^2) - \exp(-(x - 1.5)^2 - (y - 1.5)^2). \quad (3.53)$$

Equation (3.53) describes a hump and pothole which are symmetric along diagonal direction with respect of the domain center, as shown in Figure 3.4. The initial conditions are $H_0 = 0.5$ m and $C_0 = 2$, with diffusion coefficient $k = 1$ m²/s. The test is inviscid ($S_{fx} = S_{fy} = S_C = 0$ in Equation 3.9) and simulation time out is set to $t = 60$ s. The extended C-property is tested for both first and second order of accuracy. Error norms of the numerical solution with respect to the exact solution given by Equation (3.52) are shown in Table 3.1 for the water elevation H , the magnitude of liquid discharge $q = \sqrt{q_x^2 + q_y^2}$ and the passive tracer mass q_c . From Table 3.1 we observe the motionless state is conserved up to machine precision for both first and second order solver. The slight increment of the error norms for the second-order case have to be ascribed to round-off errors in the TVD reconstruction procedure.

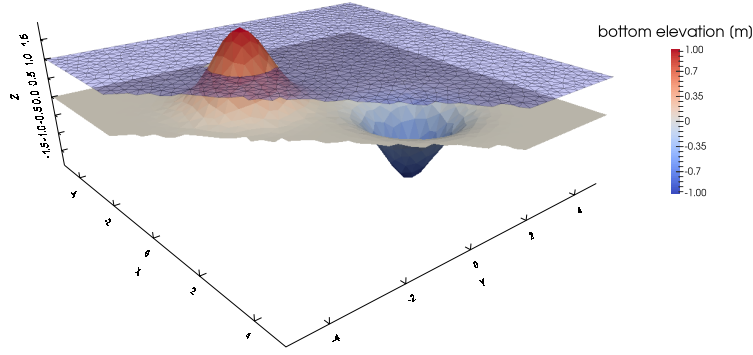


FIGURE 3.4: Extended C-property test: 3D snapshot of water and bottom elevation at $t = 60$ s.

3.4.2 Second-order experimental convergence: 2D advection-diffusion test

Being interested in high order solution for the contaminant advection-diffusion problem, we test the numerical convergence of the model to the second-order of accuracy by means of a numerical test with known analytical solution. The test consists on the motion of a 2D Gaussian concentration pulse (Noye and Tan, 1989; Croisille and Greff, 2005), initially centered at $x_0 = y_0 = 0.5$ m. A uniform, steady and frictionless flow is imposed as initial condition and for upstream boundary condition, with water depth $D = 1$ m and velocity $u = v = 0.8$ m/s. Transparent boundary conditions are set downstream. For a given constant diffusive coefficient $k = 0.01$ m²/s the exact solution of the problem reads

$$\tilde{C}(x, y, t) = \frac{C_p}{4t + 1} \exp \left[-\frac{(x - ut - x_0)^2}{k(4t + 1)} - \frac{(y - vt - y_0)^2}{k(4t + 1)} \right], \quad (3.54)$$

where C_p is the initial height of the gaussian pulse. We set $C_p = 1$ and the initial concentration pulse C_0 can be trivially obtained from Equation (3.54) at the initial time ($C_0 = \tilde{C}(x, y, 0)$). The computational domain is a square $[0; 2] \times [0; 2]$ m discretized with a number of cell ranging between 226 and 31920. For each mesh refinement we adopt the maximum value $\rho_{max} = \max(\rho_i)$ of the radius of the inscribed circles in the triangular cells. Error norms are evaluated at output time $t = 1$ s and rate of convergence is calculate using ρ_{max} as characteristic cell length of the mesh.

During the simulation the initial concentration pulse travels in diagonal direction carried by the uniform flow, meanwhile it spreads and flattens due to the diffusive contribution. Figure 3.5 shows jointly the initial ($t = 0$ s) and final configuration ($t = 1$ s) of the concentration pulse.

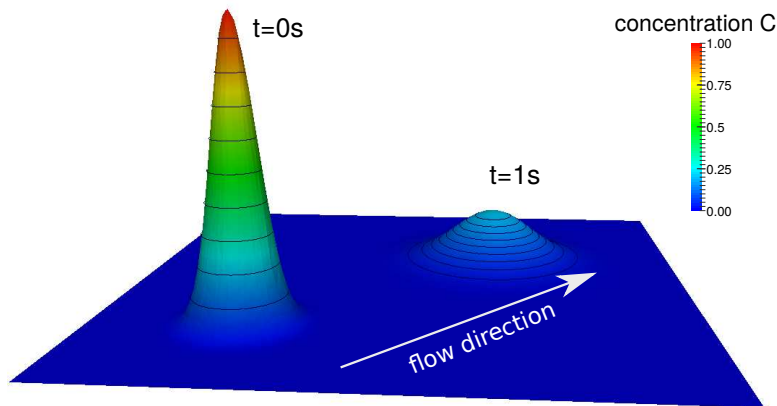


FIGURE 3.5: 3D snapshot of advection-diffusion test: initial condition ($t = 0$ s) and final configuration at $t = 1$ s. The exact solution is given by the surface while blue rings represent the exact solution.

N cell	ρ_{max} [m]	L_1	$O(L_1)$	L_2	$O(L_2)$	L_∞	$O(L_\infty)$
226	0.071	2.94E-03		8.51E-03		6.29E-02	
898	0.039	2.01E-03	0.63	5.39E-03	0.76	3.51E-02	0.97
1522	0.030	1.21E-03	2.01	3.41E-03	1.80	2.68E-02	1.07
3970	0.020	5.53E-04	1.87	1.42E-03	2.10	1.07E-02	2.19
8382	0.014	2.55E-04	2.09	6.39E-04	2.17	4.40E-03	2.41
15988	0.010	1.33E-04	2.19	3.15E-04	2.38	2.32E-03	2.16
31920	0.007	6.75E-05	1.91	1.55E-04	2.00	9.24E-04	2.59

TABLE 3.2: 2D advection-diffusion test: error norms and experimental convergence rates at final time $t = 1$ s.

Table 3.2 collects error norms and convergence rates for each mesh refinement. It is seen as the convergence rates correctly tend to value 2 in each norm.

3.4.3 Long term evolution of a squared wave: 1D advection-diffusion test

We test the performance of the model in reproducing the advection-diffusion of a initial discontinuous concentration square wave for a long term simulation (e.g. Croisille and Greff, 2005; Siviglia and Toro, 2009). The test is performed for both first and second order and using two different values of the diffusion coefficient. The numerical domain consists in a long and flat channel ($[0; 1000] \times [-5; 5]$ m) discretized with 12218 cells. A uniform, one dimensional, steady and frictionless flow is imposed as initial and upstream boundary conditions, with water depth $D = 1$ m and velocity $u = 0.8$ m/s, $v = 0$ m/s; downstream boundary conditions are imposed to be transparent.

The initial condition for the concentration is

$$\begin{cases} C_0 = 1 & \text{if } x_L < x < x_R \\ C_0 = 0 & \text{otherwise} \end{cases} \quad (3.55)$$

with $x_L = 50$ and $x_R = 100$. The exact solution of the problem is given by the following expression:

$$\tilde{C}(x, t) = \frac{C_0}{2} \left[\operatorname{erf} \left(\frac{x - x_L - ut}{\sqrt{4kt}} \right) - \operatorname{erf} \left(\frac{x - x_R - ut}{\sqrt{4kt}} \right) \right]. \quad (3.56)$$

The simulation time out is $t = 1000$ s. In the first set of numerical runs the coefficient diffusion is $k = 10^{-4}$ m²/s while in the second is $k = 1$ m²/s. For both cases we compare the performance of first and second order schemes. Figure 3.6 jointly shows the concentration longitudinal profiles at different output times ($t = 300$ s; 600 s; 1000 s): black line represents exact solutions while blue diamonds and red circles represent first and second order solutions, respectively. In the first run (Figure 3.6A) the passive tracer transport is fully dominated by advection terms and the exact solution preserves the initial discontinuity for all the simulation time. The spreading of the numerical solutions in Figure 3.6A is due to the numerical diffusion which ensure the stability of the method. Comparing first and second order schemes in the final time configuration, the concentration peak is underestimated by 28% and 6.5% respectively.

Increasing the value of diffusion coefficient k (Figure 3.6B) the concentration wave rapidly spreads travelling downstream and the exact solution is smooth. In such configuration the performance of the model significantly increases for both first and second order schemes. At final time $t = 1000$ s the concentration peak is underestimated by 12% and 1.7% for the first and second order scheme, respectively.

3.4.4 2D dam break over a complex domain

The dam break test over three humps, originally proposed by Kawahara and Umetsu (1986), is widely adopted as benchmark test for shallow water solvers (e.g. Brufau *et al.*, 2002; Nikolos and Delis, 2009; Liang and Borthwick, 2009; Liang, 2010). It is a severe test as it includes discontinuous flow variables and repeating wetting and drying processes over a complex domain topography. The computational domain is rectangular $[0; 75] \times [-15; 15]$ m and discretized with 11742 triangular cells. The bottom topography is described by

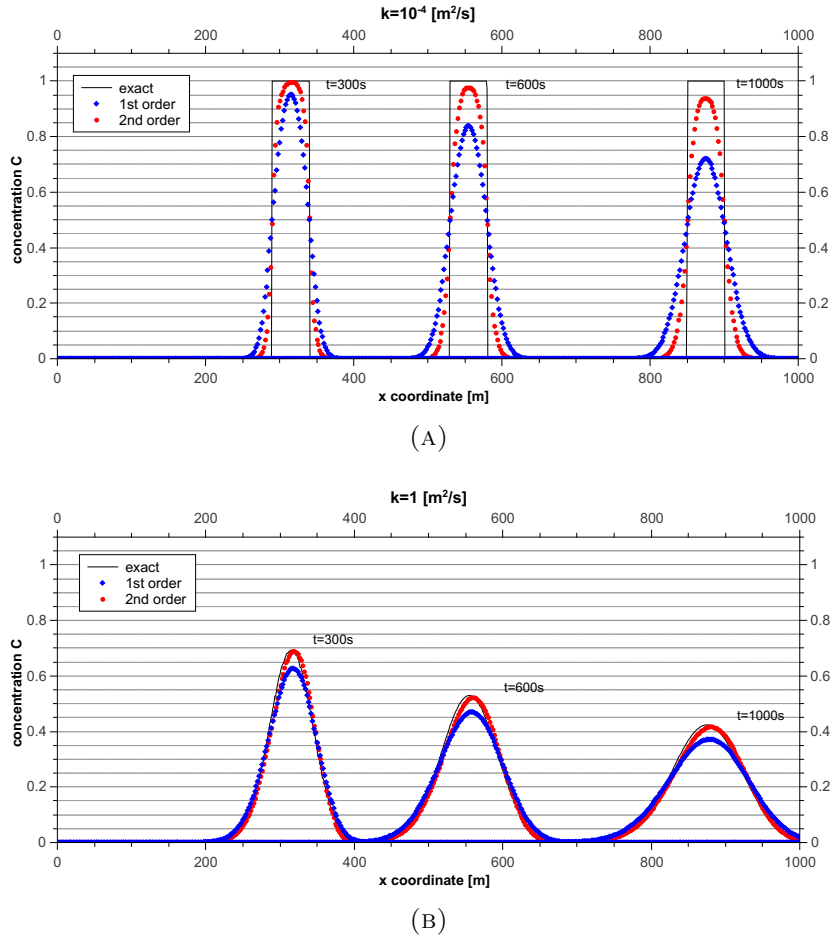


FIGURE 3.6: Concentration longitudinal profiles at different output times ($t = 300 \text{ s}; 600 \text{ s}; 1000 \text{ s}$): black line represents the exact solution while blue diamonds and red circles represent first and order scheme, respectively. (A) $k = 10^{-4} \text{ m}^2/\text{s}$, (B) $k = 1 \text{ m}^2/\text{s}$.

$$\eta(x, y) = \max \left[0, 1 - \frac{1}{8} \sqrt{(x - 30)^2 + (y + 9)^2}, \right. \\ \left. 1 - \frac{1}{8} \sqrt{(x - 30)^2 + (y - 9)^2}, 3 - \frac{3}{10} \sqrt{(x - 47.5)^2 + y^2} \right]. \quad (3.57)$$

Initially, an infinitely thin dam is located at $x = 16 \text{ m}$ and still water with constant pollutant concentration is imposed upstream. The initial conditions read

$$\begin{cases} D_0 = 1.875 \text{ m} \text{ and } C_0 = 1 & \text{if } x < 16 \text{ m} \\ D_0 = 0 \text{ m} \text{ and } C_0 = 0 & \text{otherwise} \\ q_x = q_y = 0 \quad \forall x, y. \end{cases} \quad (3.58)$$

Reflective boundary conditions are applied for all the lateral edges of the domain and the

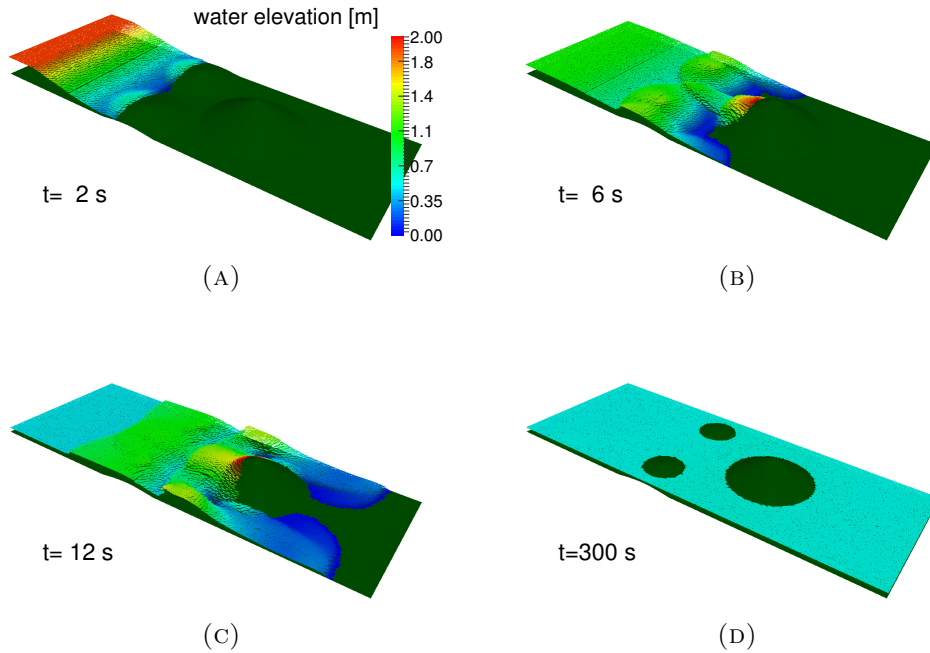


FIGURE 3.7: Dam break test over three humps: 3D snapshots of water elevation at different times.

Manning coefficient is set to $n_f = 0.018 \text{ s}/\text{m}^{1/3}$. The diffusion coefficient $k = 0.1 \text{ m}^2/\text{s}$ and the simulation is performed with the second order scheme.

At $t = 0 \text{ s}$, the dam collapses instantaneously and water inundates the domain. Figures 3.7 and 3.8 illustrate the inundation of the floodplain at different times. At $t = 2 \text{ s}$ the water front reaches the first two small humps starting to overcome them. Two curved reflection waves arise and start propagating upstream. By $t = 6 \text{ s}$ small humps are fully submerged and the wet/dry front partially runs up the large central hump and bypasses it laterally. At $t = 12 \text{ s}$ water is flooding the lee side of the big hump while upstream reflection bores generated by the humps and the side walls continuously interact. After a continuous crossing interactions among waves, topography and side walls, flow slows down and start reaching the steady state due to energy dissipation generated by bottom friction. By $t = 300 \text{ s}$ the steady state is achieved with flow velocity gently tends to zero, and the peaks of the small humps are no longer submerged.

Figure 3.9 shows the evolution of the pollutant concentration front during the simulation. The concentration is correctly driven by hydraulic waves and the final steady configuration show a constant concentration in the wet domain. In all the different output times the results are predicted to be similar to those proposed in literature (e.g. Brufau *et al.*, 2002; Nikolos and Delis, 2009; Liang and Borthwick, 2009; Liang, 2010).

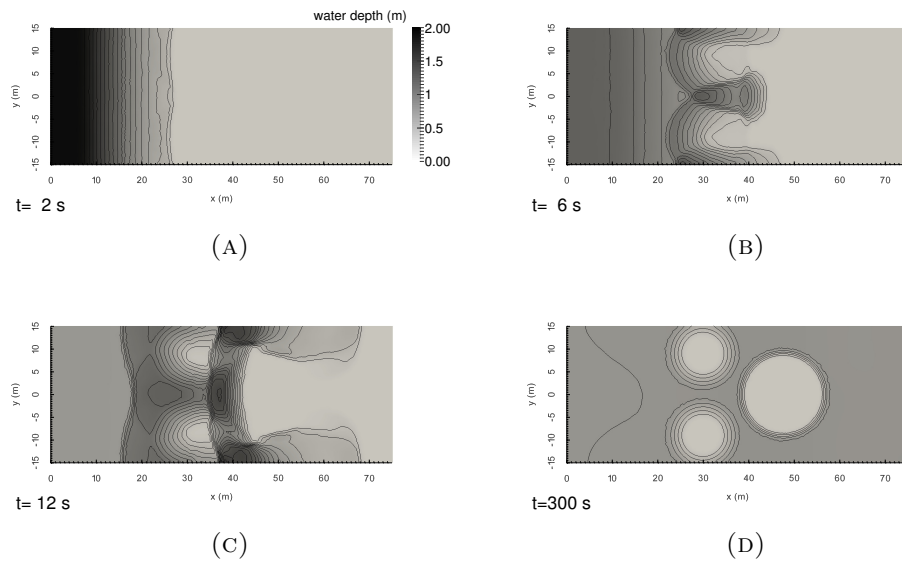


FIGURE 3.8: Dam break test over three humps: 2D contour plots of water depth at different times.

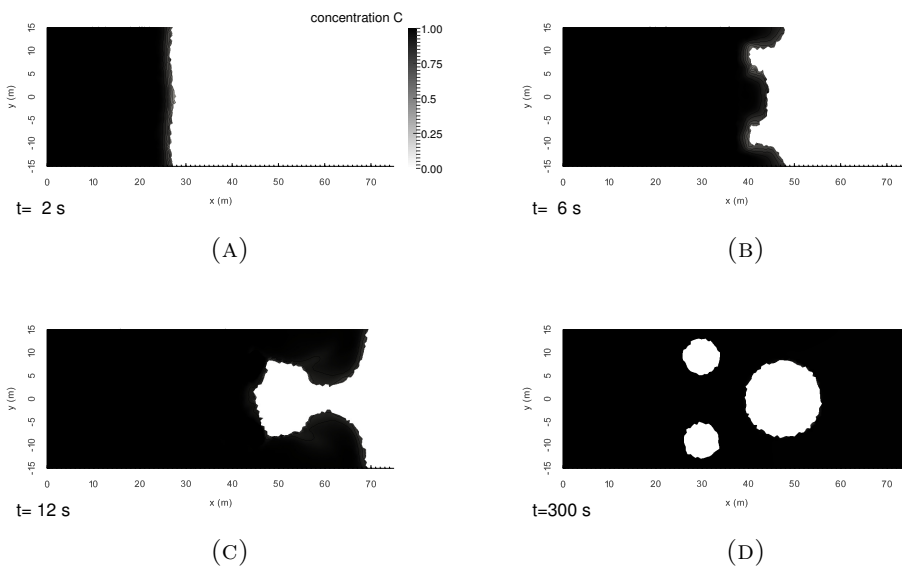


FIGURE 3.9: Dam break test over three humps: 2D contour plots of pollutant concentration at different times.

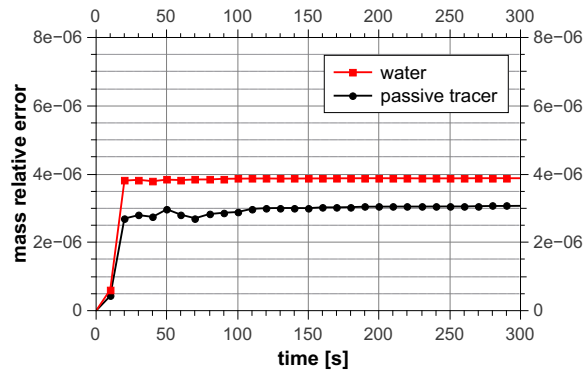


FIGURE 3.10: Time evolution of the relative errors of water and passive tracer mass.

Finally, in Figure 3.10 we plot the time evolution of the relative error of water and passive tracer mass. It is shown as these errors are of order $O(-6)$.

3.4.5 Advection-diffusion of a passive tracer in a complex morphology

The aim of this test is to assess the capability of the proposed numerical approach to simulate the propagation of a passive tracer in a reach of a wandering river characterized by a very complex morphology with main channel with a series of smaller side channels (morphology 4 in Section 4.2.2 and Table 4.1). The reach is 1495 m long has total mean width of 80 m mean longitudinal slope of 0.005 m/m and has been discretized by 81581 triangular cells. All the calculations are performed using a roughness coefficient n_f equal to 0.033 $s/m^{1/3}$. At the inlet a constant water discharge $Q = 20 m^3/s$ and uniform flow depth are imposed for all the duration of the simulations while the concentration of the passive tracer change in time as depicted in Figure 3.11. It is characterized by a rising (falling) limb of concentration from $C = 0$ to $C = 1$ ($C = 1$ to $C = 0$) which last 900 s . The maximum concentration $C = 1$ is kept constant from $t = 2100 s$ to $t = 3900 s$. The CFL number is fixed to 0.95. At the downstream end transparent conditions are imposed. Initial conditions are obtained solving the system of governing equations until a steady solution is obtained. We consider two different configurations one with vanishing diffusion coefficient $k = 10^{-9} m^2/s$ (pure advection, only water molecular diffusion) and the other characterized by a constant diffusion coefficient $k = 0.1 m^2/s$.

The hydrodynamic configuration is shown in Figure 3.12 which illustrates the distribution of water depth and flow velocity in the domain. Figure 3.12 show the high variability of both the hydrodynamic variables, with alternation of shallow water-rapid flow areas and deep-slow flow pools typical of braided river patterns.

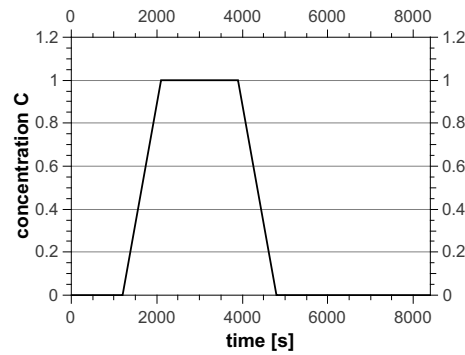
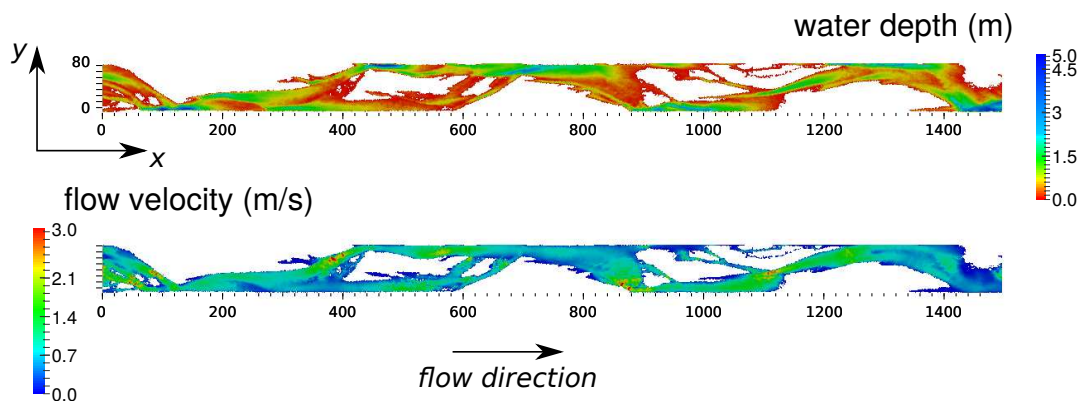
FIGURE 3.11: Pollutant concentration (C) wave input in time.

FIGURE 3.12: Distribution of simulated water depth and flow velocity for the real-scale test.

The distribution of pollutant concentration is shown in Figure 3.13 for different times; the y -axis is magnified of a factor 2 for the sake of legibility. Figure 3.13 illustrates the distribution of the pure advection ($k = 10^{-9} \text{ m}^2/\text{s}$) and advection-diffusion ($k = 0.1 \text{ m}^2/\text{s}$) tests when input wave concentration already reach its maximum ($t = 2700 \text{ s}$), during the falling limb of the input wave ($t = 4500 \text{ s}$) and in the final part when pollutant wave is expiring ($t = 6000 \text{ s}$).

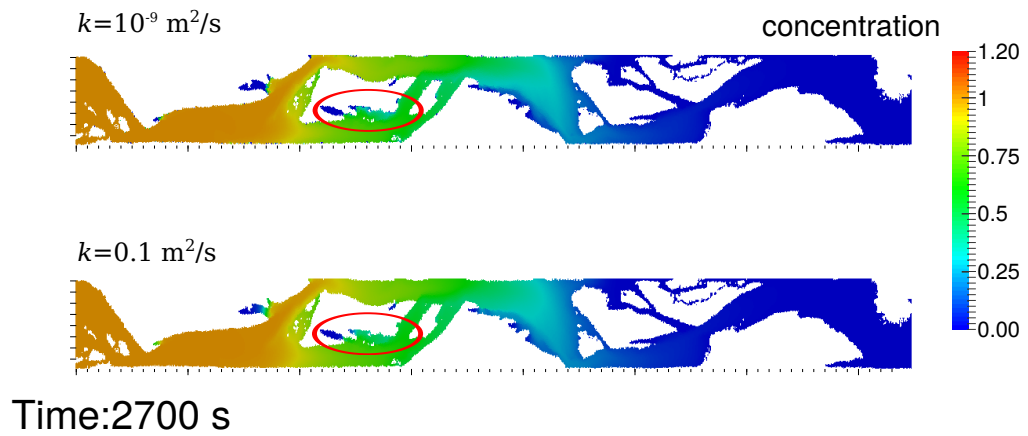
The pollutant wave enters, passes through and leaves progressively the domain conveyed by the constant water flow. In the main channel the dominant pollutant transport mechanism is the advection due to the higher momentum of the water flow. Observing the principal channel in the different timeshots of Figure 3.13 there are no sensible differences between pure advection and advection-diffusion cases.

The differences in concentration distributions arise in side, lateral and backwater channels. In order to help the comparison of these locations, some of them are highlighted in Figure 3.13 with red circles. In such areas, where flow momentum decreases, the relative magnitude of diffusive mechanisms arises, further conveying the pollutant. Here it is

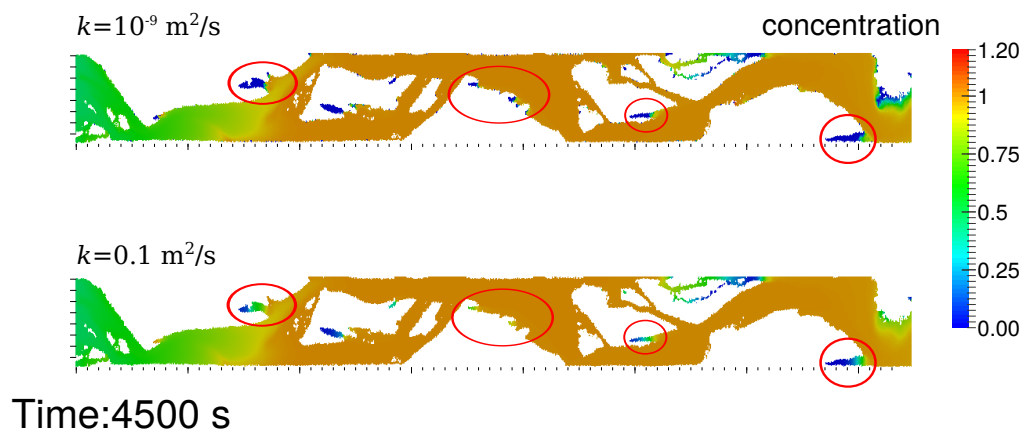
worth notice the double effects of diffusion: during the rising phase of the pollutant wave ($t = 2700 s$ and $t = 4500 s$) concentration increases more with respect to the pure advection test. On the contrary, during the recession phase of the wave, pollutant is trapped in lateral side channel and slowly decreases due to concentration gradients.

3.5 Conclusions

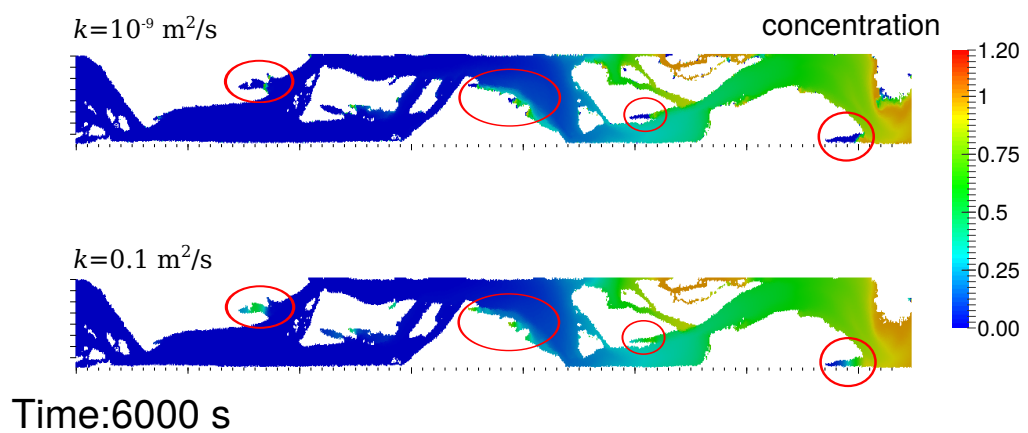
In this chapter we have reformulated the two- dimensional shallow water advection-diffusion model in the form of a hyperbolic system with stiff source terms, via the Cattaneo's relaxation approach. We analyse the eigenstructure and the possible wave patterns associated with the new relaxation system deriving the conditions under which hyperbolicity and strictly hyperbolicity are lost. Furthermore we derived the conditions under which the relaxation system is advection dominated: i.e. the maximum eigenvalue is the one associated to the shallow water system. We discuss that many rivers are in the advection dominated case and then modeling the advection-diffusion of a passive tracer does not require extra computational costs compare to the pure hydrodynamic case. Finally we test the robustness of the new developed model performing four different test cases showing its capability in dealing with complex morphologies and preserving mass.



(A)



(B)



(C)

FIGURE 3.13: Pollutant concentration C distribution for pure advection ($k = 10^{-9} \text{ m}^2/\text{s}$) and advection-diffusion ($k = 0.1 \text{ m}^2/\text{s}$) tests; y direction is magnified for the sake of legibility.

Chapter 4

An eco-hydraulic modeling of the interactions between hydropeaking and river morphology

Based on: Vanzo D., G. Zolezzi and A. Siviglia (under review). Eco-hydraulic modeling of the interactions between hydropeaking and river morphology. Submitted to Ecohydrology (Wiley & Sons).

4.1 Introduction

Hydropeaking related to hydropower operations produces adverse ecological effects that depend on its interaction with the channel morphology. This chapter proposes a first quantitative attempt to investigate the eco-hydraulic response of different river morphologies to hydropeaking waves based on a 2D hydraulic modeling approach. As mentioned in Chapter 1, the management of the downstream river channel represents one of the possible mitigation options to reduce negative effects hydropower plant releases. In particular, among morphological improvements, local widenings of channelized river reaches are increasingly carried out also in alpine areas where the availability of public land in valley floodplains is limited (Rohde *et al.*, 2005). The rationale behind these measures is that giving “more room to the river” (Rohde *et al.*, 2006) is normally expected to improve the health of river systems at least locally, because channel width represents a fundamental control on river morphodynamics (e.g. Siviglia *et al.*, 2008; Crosato and Mosselman, 2009). Widening is then expected to promote self-formed morphodynamics, leading to enhanced

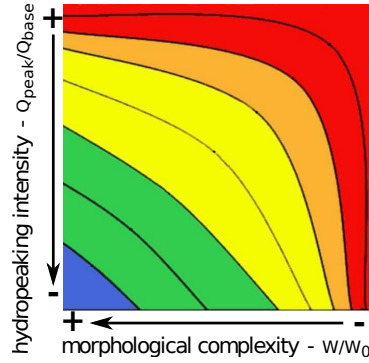


FIGURE 4.1: Hydro-morphological alteration space: qualitative ecological response to interaction between hydropeaking pressure (vertical axis) and morphological complexity (horizontal axis) of receiving river reach, inspired by Baumann *et al.*, 2012. Downward vertical shifts in the plot correspond to reducing hydropeaking intensities, while horizontal shifts correspond to increasing morphological complexity (right to left). Red and blue regions represent the expected worst and best state from ecological point of view, respectively.

morphological diversity, and turn into more local hydraulic diversity (e.g. in water depth and flow velocity patterns). Such hydro-morphological diversity is often expected to give rise to improved ecosystem health (e.g. Elozegi *et al.*, 2010).

When the target river reach is subjected to hydropeaking, however, evidence from monitoring of river widening programs has shown little ecological improvements in restored reaches despite the increase in morphological diversity (e.g. Muhar *et al.*, 2007). In a recent assessment of hydropeaking mitigation measures, Person *et al.* (2013) indicate that increasing morphological complexity generally offers the best habitat condition, but they also suggest that at the same time this condition may maximize the stranding risk for fish species. The review of Harby and Noack (2013) points out the relevance of the interactions among hydropeaking and morphological diversity, further remarking the relevance of their better understanding as well as that such assessment is difficult also because often site-specific. This interaction has been so far only qualitatively predicted, i.e. within a hydro-morphological alteration space originally inspired by Baumann *et al.* (2012), which has the merit of trying to overcome the site-specificity of the problem. Figure 4.1 shows how the best expected ecological response (blue region) should occur in the combination of high morphological complexity and vanishing hydropeaking intensity. Moreover it indicates that ecological improvements can be reached both through “horizontal” strategies, which act on morphological complexity, as well as through “vertical” strategies, which modify the hydropeaking intensity, or through a combination of both (e.g. “diagonal” strategies).

In the present study we aim at quantitatively exploring ecologically-relevant hydraulic interactions between different hydropeaking scenarios and different channel morphologies, through the use of 2D hydraulic modeling. More specifically we aim at developing a

modeling approach able to: (i) quantify two-dimensional eco-hydraulic effects of different channel morphologies on the propagation of hydropeaking waves of different intensities; (ii) compare the response of different Ecologically-Relevant Hydraulic Parameters (hereinafter EHRPs) to changes in the morphological pattern of the riverbed and in the base flow; (iii) support the analysis of tradeoffs between operational (i.e. increase in base flow) and constructional (i.e. channel widening/narrowing) mitigation measures. The results allow to quantify the variability of well-recognized, Ecologically-Relevant Hydraulic Parameters when “horizontal”, “vertical”, or “diagonal” mitigation measures (Figure 4.1) are implemented on a hydropeaked river reach. Though not pretending to achieve a complete generality, we try to cover a representative set of combinations of realistic hydropeaking scenarios and realistic morphological patterns that can be found in alpine areas.

The potential of hydraulic numerical modeling has been already exploited in recent years with the aim of evaluating reach scale hydro-ecological effects, also in relation to hydropeaking. Hauer *et al.* (2013a) used a 1D numerical model to investigate the longitudinal damping of hydropeaking waves due to the characteristics of the downstream channel, while Gostner *et al.* (2013b) focus on the quantification of morphological variability at different flow discharges in some specific sites using a 2D model. Casas-Mulet *et al.* (2014a) test and explore the capability of a 1D numerical model to quantify fish-stranding areas on rivers subject to hydropeaking. Differently from previous studies, our focus here is on modeling the interaction between reach self-formed morphology and hydropeaking events at reach scale through a 2D depth averaged numerical model.

4.2 Methods

The modeling approach to investigate the eco-hydraulic interaction between hydropeaking and channel morphology can be summarized in three main steps: firstly we set a suite of hydropeaking scenarios and river bed patterns (Sections 4.2.1, 4.2.2 and 4.2.3), which represent the inputs for the numerical simulations; secondly we perform the numerical simulations (Section 4.2.4) using GIAMT2D, a 2D (x-y) shallow-water numerical model (Siviglia *et al.*, 2013); thirdly the hydraulic numerical variables (e.g. flow velocity, water depth) resulting from the simulations are summarized in a single parameter which accounts for a specific ecological effect (Section 4.2.5).

In more detail, a series of 36 numerical runs under steady flow conditions have been performed, simulating three different hydropeaking scenarios in combination with six different channel morphologies. All the simulated hydropeaking-morphological combinations have been designed with the aim to reproduce realistic conditions of medium-large alpine

river reaches subject to hydropeaking. A full generalization, and a rigorous scaling approach able to quantitatively consider all possible real configurations is out of the scope of the present work.

The research design has therefore foreseen three basic choices, which respectively set the input discharge, the topographical domain and the outcomes of the hydraulic model simulations that are relevant for the scope of the work. The input discharge is associated with the peak and base values of a representative hydropeaking scenario. The topographical domain is constructed starting from six different experimental channel morphologies obtained in mobile-bed flume experiments by Garcia Lugo (2014). In particular, the different channel morphologies are obtained by varying the externally imposed channel width and keeping the same flow rate, sediment size and longitudinal slope; they cover a suite of representative channel patterns that include nearly flat bed without relevant bedforms, alternate bars, wandering and braiding configurations.

The simulation outcomes are analysed in terms of a suite of quantifiable Ecologically-Relevant Hydraulic Parameters (Section 4.2.5) assumed as representative of three eco-hydraulic phenomena chosen because they are of typical concern under hydropeaking conditions: physical habitat or hydro-morphological diversity, macroinvertebrate drift and fish stranding. Such ERHPs allow to measure the effects of hydropeaking interaction with different channel morphologies, hence to quantitatively compare different configurations in the hydro-morphological alteration space. Results are then analysed in terms of the spatial distributions of each ERHP at the reach scale and discussed comparatively.

4.2.1 Hydropeaking events

For the sake of simplicity, we consider a single hydropeaking event schematized as a rectangular wave, characterized by a base discharge Q_{base} and a peak discharge Q_{peak} (Figure 4.2). In real cases the base flow could correspond to the minimum environmental flow, constantly released from the upstream dam, while the peak discharge is obtained by adding the discharge released by the hydropower plant (Q_{prod} , for electricity production) to the base flow. For the sake of simplification, we adopt an hydropeaking wave as in the “worst” possible ecological scenario, whereby discharge instantaneously varies from base to peak and viceversa.

Three different hydropeaking patterns (A, B and C) are considered in the study (Table 4.1): they are built by varying the base flow Q_{base} and keeping the same discharge value used for electricity production Q_{prod} . The selected range of the ratio Q_{peak}/Q_{base} can

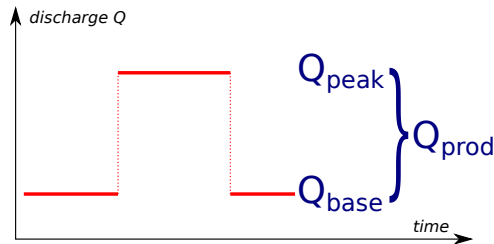


FIGURE 4.2: The hydropeaking event is schematized as a rectangular wave, varying from a base (Q_{base}) and a peak (Q_{peak}) discharge.

Prod. pattern	A	B	C
Q_{prod} [m^3/s]	45	45	45
Q_{peak} [m^3/s]	50	55	65
Q_{base} [m^3/s]	5	10	20
Q_{peak}/Q_{base}	10	5.5	3.25
Morphology number	Total width [m]	Equilibrium pattern	Widening ratio W/W_0
1	15	flat bed	1
2	20	alternate bars	1.33
3	30	alternate bars	2
4	80	wandering	5.33
5	100	braiding	6.66
6	150	braiding	10

TABLE 4.1: Hydro-morphological configurations: three different hydropeaking patterns (column A, B and C of upper panel) characterized by same electricity production Q_{prod} but different ratio of Q_{peak}/Q_{base} . Six self-formed morphologies (row 1 to 6 of lower panel) upscaled from experimental runs; widening ratio refers to the first morphology of 15 m width.

be often found in alpine and piedmont scenarios. Changes in Q_{base} may correspond to different imposed environmental flows from the dam or in the subcatchments that contribute in the reach located between the dam and the water release section.

4.2.2 Channel morphologies

The bed morphologies used in the present work are based on detailed topographic scans of simulated river bed patterns in a series of laboratory flume experiments performed by Garcia Lugo (2014). Namely, the considered topographies result from six experiments in a mobile bed laboratory flume with fixed banks and the same values of water discharge, initial mean bed slope and sediment size. Each experiment differs only for the imposed channel width (ranging from 0.15 m to 1.5 m). The system freely develops from an initial flat bed towards a morphodynamic equilibrium state, characterized by constantly changing bed morphologies whose configuration is statistically different among different runs.

Experiments show how, increasing only the available channel width, the bottom pattern shifts from flat bed (narrow channel) to braiding network (wide channels), passing through transitional configurations characterized by alternate bars and wandering morphologies. These original flume reaches are 14.5 *m* long and the provided scans of equilibrium pattern have a spatial resolution of 50 *mm* and 5 *mm* in longitudinal and transverse direction respectively. Then a total of 290 cross sections are available for each configuration.

In order to get realistic bathymetries resembling to alpine river reaches we have scaled the flume topographies using a simple geometrical similarity. Therefore the bottom scans of the six original experiments and the mean sediment grain size have been multiplied by a factor $\lambda = 100$. The upscaled morphologies that have been used in our analysis thus span a channel width range between (15 *m* ÷ 150 *m*), are 1450 *m* long and have a uniform grain size ($D_s \approx 0.1$ *m*). The main geometrical characteristics of the adopted morphologies are given in Table 4.1. In particular, morphology 1 has almost flat bed, 2 and 3 show an alternate bar pattern with different bar amplitude (larger for case 3) while pattern 4 is characterized by a transitional wandering channel. Finally, morphologies 5 and 6 show different braiding patterns. Figure 4.3 reports a planar view (x-y, with magnified y axis for the sake of clearer visualization) and one illustrative cross section (y-z) of the channel for three sample morphologies: flat bed (1), alternate bars (3) and braiding (5). Figure 4.3 clearly shows the key role of the channel width in driving different morphological patterns.

4.2.3 Hydro-morphological configurations

The designed three hydropower production patterns (A, B, C in Table 4.1) and six self-formed morphological patterns (from 1 to 6 in Table 4.1) provide 18 possible configurations that can be visualized in the hydro-morphological alteration space of Figure 4.1. In this diagram unaltered hydro-morphological configurations are those laying close to axis origin, while hydrological (y axis) and morphological (x axis) alterations can be thought to increase when moving away from the origin. We parameterized hydrological alteration, i.e. hydropeaking intensity, through the ratio Q_{peak}/Q_{base} , which therefore decreases moving downwards; note that this corresponds to increase base (or environmental) flow. On the other hand, morphological complexity is parameterized with the widening ratio W/W_0 computed with respect to smallest width value of all the upscaled morphologies ($W_0 = 15$ *m*) and it increases when moving from right to left. For the sake of clarity, each configuration is labelled in the form “WK”, where W denotes the hydropeaking pattern (A, B o C in Table 4.1), K is the analysed upscaled morphology (from 1 to 6, Table 4.1). For example, A3 corresponds to release pattern A ($Q_{peak} = 50$ m^3/s , $Q_{base} = 5$ m^3/s) and morphology 3 (alternate bars).

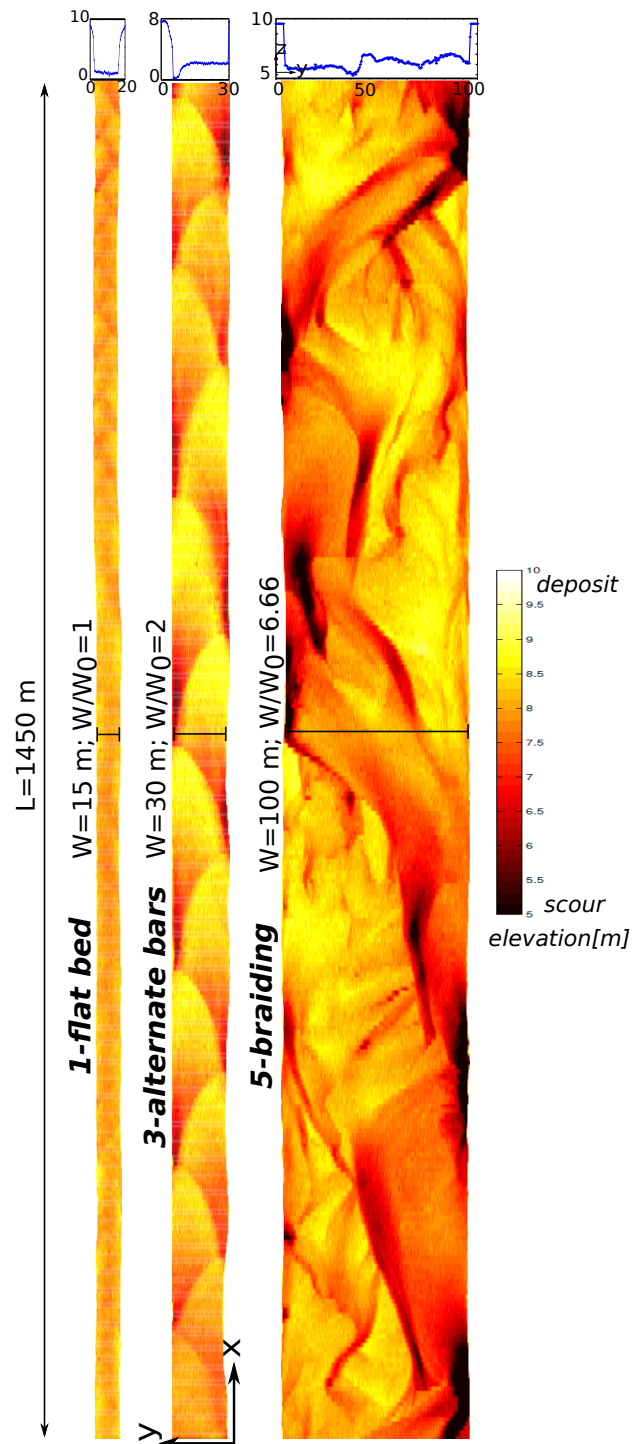


FIGURE 4.3: Example of (y-z) cross section (on the top) and (x-y) planar view for three different morphologies: flat bed (1), alternate bars (3) and braiding network (5), with a widening ratio W/W_0 of 1, 2 and 6.66 respectively.

Each hydromorphological configuration is also characterized by a longitudinal reach-averaged bed slope that has been chosen equal to 0.003 m/m , a realistic value for alpine and piedmont river reaches with channel width in the range ($15 \text{ m} \div 150 \text{ m}$). It is worth mentioning that our hydromorphological configurations have been set up with the aim of being realistic representations of hydropower-regulated alpine/piedmont streams: therefore the upscaled experimental scans are used only as topographic representation of different channel patterns. For the same reason, neither the chosen slope nor the base/peak discharge values need to match the corresponding values in the laboratory experiments. In other words, the channel bed morphology and the chosen hydropeaking discharges are independent variables. This would not be the case if aiming at closely reproducing the experimental runs with the numerical hydraulic model, when the discharge value is the channel-forming one, i.e. the one that generates the examined morphologies.

4.2.4 Hydraulic modeling

Hydraulic simulations have been conducted with GIAMT2D (Siviglia *et al.*, 2013), a non-stationary 2D (x-y) shallow water numerical model build on unstructured triangular grids. A robust wet-and-dry algorithm is implemented, allowing the correct simulation of emerging topography. The different computational domains are built on the upscaled bathymetries of lab experiments (see Table 4.1) and have number of cells ranging from 94810 (morphology 1) to 163528 (morphology 6) with mean cell area equal to 0.4 m^2 and 1.6 m^2 , respectively. For the reasons explained in Section 4.2.3, there is no need for a calibration of the roughness coefficient with water level data from the laboratory runs, and therefore for all the numerical runs we set bed roughness (Strickler coefficient k_s) equal to $30 \text{ m}^{1/3} \text{ s}^{-1}$. The value is estimated from the well-known Strickler formula $k_s = 21.1/D_s^{1/6}$ ($k_s = 1/n_f$, where n_f is the Manning coefficient), where D_s is the upscaled mean grain size. Simulations are performed with fixed bed, imposing a constant inflow discharge at upstream boundary (see data in Table 4.1) and uniform flow as downstream boundary condition. Each of the 36 numerical runs (18 configurations for 2 discharge stages) reach steady conditions roughly within 1-2 hours of simulated time. The simulated local values of flow depth and velocity are then statistically analysed over all the wet cells.

4.2.5 Ecologically Relevant Hydraulic Parameters

Three relevant eco-hydraulic effects have been considered: the variation of physical habitat diversity between high and low discharge stages (e.g. Gostner *et al.*, 2013b), the catastrophic drift of benthic organisms during the rising limb (e.g. Bruno *et al.*, 2010, 2013) and

the fish stranding during the rapid recession phases (e.g. Halleraker *et al.*, 2003). Each of these ecological effect has been associated with one measurable Ecologically-Relevant Hydraulic Parameters. It must be noted that the choice of these three ERHPs can not be considered as exhaustive: the investigated ecological effects are driven also by other biotic and physical parameters that are not considered here (e.g. Nagrodski *et al.*, 2012; Irvine *et al.*, 2014).

As quantitative indicators (ERHP) related to each examined ecological effect, we choose: i) a measure of spatial heterogeneity of water depth and velocity, which reflects habitat diversity availability; ii) the magnitude of the near-bed shear stress as primary cause of macroinvertebrate drift; and iii) the variation of wetted area between high and low stage which is associated with fish stranding. It is worth mentioning that different choices for the velocity are available in order to compute the first and the second ERHP. Among them one can choose the velocity U along the longitudinal direction or the magnitude $|U| = \sqrt{U^2 + V^2}$ where V is the velocity along the transversal direction. Our analyses, not presented here, show that the results are slightly affected by this choice. Therefore we decide to compute the two ERHPs using U because this would allow an immediate comparison with the data obtained from one-dimensional modeling approaches.

4.2.5.1 Hydro-Morphological Index of Diversity

Habitat heterogeneity has been recognized to be a key-point for ecosystem integrity (e.g. Elosegi *et al.*, 2010) and the variability of water depth and flow velocity distributions reflects the river spatial complexity and heterogeneity. Gostner *et al.* (2013a) developed an Hydro-Morphological Index of Diversity (HMID) at reach scale based on the variability of flow velocity and water depth spatial statistic distributions for a given flow discharge. The HMID index reads

$$HMID = \left(1 + \frac{\sigma_U}{\mu_U}\right)^2 \cdot \left(1 + \frac{\sigma_D}{\mu_D}\right)^2, \quad (4.1)$$

where σ_U and μ_U are depth-averaged flow velocity in longitudinal direction (U) standard deviation and mean value, respectively. Similarly, σ_D and μ_D are water depth (D) standard deviation and mean value, respectively. Ratio σ/μ is the coefficient of variation (CV) and it represents the extent of variability in relation to the mean value of the distribution.

For simple morphologies (i.e. straight channelized reach with almost flat bed) flow velocity and water depth tend to have uniform values ($\sigma \rightarrow 0$), so in Equation (4.1) HMID is a small value close to one. On the other hand, high morphological complexity causes heterogeneous distributions of the hydraulic variable (larger ratios σ/μ), with a

consequent increase of the HMID value. Gostner *et al.* (2013a) tune the HMID values for a set of representative Swiss pre-alpine sites and identify three hydro-morphological categories:

1. $HMID < 5$: occurs in case of channelized and morphologically heavily altered reaches;
2. $5 < HMID < 9$: transitional range from heavily modified to almost natural morphology;
3. $HMID > 9$: morphologically natural reaches.

4.2.5.2 Macroinvertebrate drift

Macroinvertebrate communities are naturally subjected to catastrophic and behavioural drift in unaltered flow regime reaches but this process has been shown increasing in presence of hydropeaking (e.g. Bruno *et al.*, 2010; C er eghino *et al.*, 2004). Being the flow velocity close to the bottom the driver of macroinvertebrate drift, we evaluate it in terms of bottom shear stress (τ). Choosing the Strickler parametrization for roughness, the bottom shear stress in each cell is evaluated as:

$$\tau = \rho g \frac{U^2}{k_s^2 D^{1/3}} \left[\frac{N}{m^2} \right], \quad (4.2)$$

where ρ is water density and g gravity acceleration.

Even though different macroinvertebrate species are characterized by different drift resistance depending also on their ability to hiding and sheltering, we assume a unique threshold value for the onset of all macroinvertebrate drift as presented by Hauer *et al.* (2012). This value is set to $\tau_{drift} = 10 \text{ N/m}^2$. The threshold approach is useful to quantitatively discriminates two opposite behaviour for macroinvertebrate communities: with low bottom flow velocity ($\tau < \tau_{drift}$) individuals are able to settle down and colonize the river bed, while with high flow velocity ($\tau > \tau_{drift}$) they tend to be drifted away. From the food chain perspective, the former case can be defined as *sink* behaviour, representing areas with macroinvertebrate biomass accumulation, while the latter case can be defined as *source* behaviour, being the drifted biomass available for fish feeding.

We have chosen to evaluate the shear stress only in the reach bed portion which is submerged both at high and low stages, because daily or even subdaily emergence of bedforms can not allow the settling of stable macroinvertebrate communities.

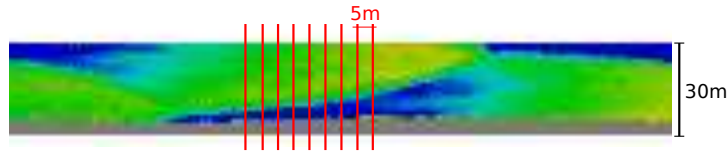


FIGURE 4.4: Example of the transversal slices used for the local evaluation of the wetted area variation; morphology No. 3 ($W = 30\text{ m}$).

4.2.5.3 Fish stranding

Fish stranding could be a serious hazard for fish communities (especially for early-life stages) and it may occur under different circumstances (e.g. Irvine *et al.*, 2014). Under hydropeaking conditions rapid flow fluctuations may alternately wet and dry river bed areas (Nagrodski *et al.*, 2012). During high flow stages fishes can move and occupy available lateral shallow water regions for feeding, sheltering and spawning but, depending on extension of dried areas and rate of change of water level, they can be stranded during the falling limb of hydropeaking event. In this chapter we take into account only the variation of wetted area during an hydropeaking event as ERHP, not considering the water level rate of change. This second element is taken into account in Chapter 5, where a further investigation of fish stranding phenomena is proposed. Moreover it is worth noting that the daily drying of spawning areas, which can increase eggs and juvenile fish mortality, strongly depends on the magnitude of the variation of wetted area rather than water level rate of change (e.g. Casas-Mulet *et al.*, 2014c).

The variation ΔA_w of wetted area A_w during hydropeaking event is evaluated according to the Swiss protocol (Baumann *et al.*, 2012) as

$$\Delta A_w = \frac{A_w^{peak} - A_w^{base}}{A_w^{peak}} \cdot 100 \text{ [%]}, \quad (4.3)$$

where the superscript indicates the discharge stage (peak or base). Referring to the Swiss protocol, cross sections with $\Delta A_w < 30\%$ can be considered in “good” status, so with low risk of stranding.

Wetted area variation has to be evaluated locally at cross section scale, as suggested also by Baumann *et al.* (2012). Hence ΔA_w (Equation 4.3) is computed slicing each river reach (1450 m long) along the transversal direction, as shown in Figure 4.4. We use slices 5 meters wide obtaining a total of 290 subareas. For each subarea we evaluated the variation of wetted area (calculated with Equation 4.3) and compute the statistics over the 290 subareas of each reach.

4.2.5.4 Overall comparison of different ERHPs

In order to set up a comparative analysis among all the three examined eco-hydraulic phenomena a unique metric is needed for each ERHP, able to account for the difference between base and peak flow conditions. We have therefore chosen the loss of the HMID from base to peak for habitat diversity, the percentage loss of macroinvertebrate sink area for drift and the percentage of wetted area in good status in relation to the adopted fish stranding criterion. Such comparison is deliberately simplified and it assumes that intermittent hydropeaking waves always fluctuate between the same two discharge values.

Furthermore, an ensemble measure of the overall eco-hydraulic response of each analysed channel morphology to hydropeaks with different base flow conditions has been developed. Conceptually such measure is based on recognizing that the continuous shift between base and peak flows determines an extremely harsh environment. The worst of the two states, in ecological terms, has to be viewed as the most limiting state and therefore the most representative of the system eco-hydraulics conditions on long terms.

More specifically, for each of the 18 examined configurations, the following three steps have been followed. i) We have sought a normalized score within the same range 1 to 4 (1: worst; 4: best) for each of the three eco-hydraulic phenomena, to ensure inter-phenomena comparability. ii) For the case of habitat diversity and invertebrate drift, we have assigned such score to every combination, both for peak and for base flow, and then we have chosen the lowest value, corresponding to the most limiting condition, as the unique representative of each combination. In the case of stranding risk, a unique score could be immediately given, being the phenomenon already defined by both base and peak flow. iii) The ensemble eco-hydraulic response for each of the 18 examined hydromorphological configuration was evaluated as the average of the representative scores for habitat diversity, drift and stranding risk. Under step i), for every ERHP, the maximum score (4) has been assigned to every combination in the best eco-hydraulic status, i.e. every combination found in the blue areas of the diagram representing the ERHP behaviour in the hydromorphological space of Figure 4.1, and viceversa for the minimum score (1), which has been assigned to every combination found in the red parts of the same diagrams. Intermediate scores have been given to combinations found in the green and yellow areas on the basis of linear interpolation between the maximum and minimum values.

4.3 Results

The results of numerical simulations are discussed in term of reach-scale metrics based on spatial statistics of the selected ERHPs. This allow us to highlight and quantify the role

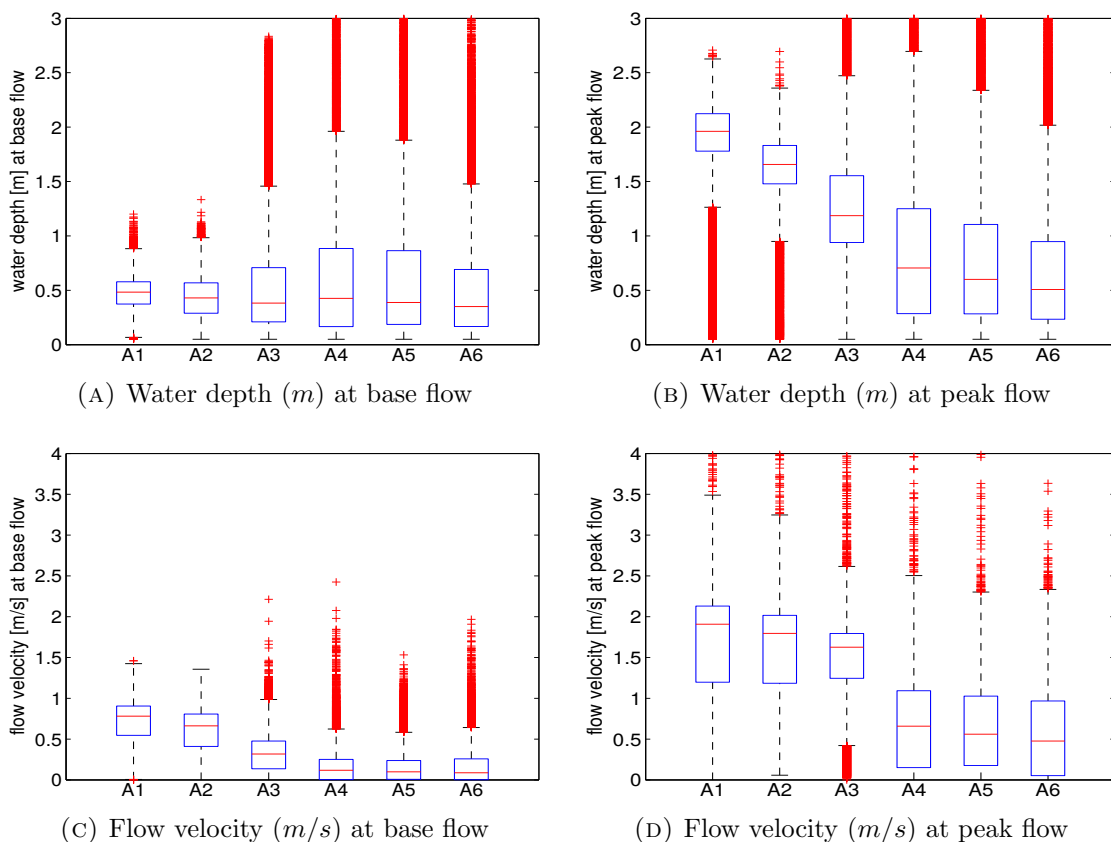


FIGURE 4.5: Box and whiskers plot for the distributions of water depth (A and B) and of longitudinal flow velocity (C and D) of the considered six morphologies (from 1 to 6) for the production pattern A, both for base (A and C) and peak flow conditions (B and D).

of reach-scale morphology in defining ERHP distributions. We first discuss the numerical results in terms of the fundamental hydraulic quantities (flow velocity and water depth) and use this as a reference to present the results related to each ERHP.

4.3.1 Spatial distribution of flow depth and velocity

The statistical distributions of simulated water depth and longitudinal flow velocity are represented in the form of a box and whiskers plot in Figure 4.5. The plots show the distribution for the production pattern A ($Q_{peak}/Q_{base} = 10$), which corresponds to the strongest hydropeaking intensity among the three examined in the present work, and the six morphologies (1 to 6). Results are displayed for base (Figure 4.5A,C) and peak flow (Figure 4.5B,D).

As it can be expected, the median values of the depth and velocity distributions (center line of each box) generally increase from base to peak flow and decrease for increasing morphological complexity (i.e. by increasing widening ratio, from A1 to A6), though those

relations are non-linear and characterized by the presence of thresholds where different behaviours can be detected. For instance, median values of the depth and velocity distributions almost do not change when morphological complexity increases in the case of the multi-thread morphological configurations (A4-A5-A6). In these channel morphologies median values also show very little increase when passing from base (Figure 4.5A,C) to peak flow conditions (Figure 4.5B,D), compared with “simpler” morphologies corresponding to nearly flat bed without bedforms or alternate bars (A1-A2-A3).

Besides changes in median values among the examined configurations, for the purpose of the present work the variability of local flow depth and velocity values is particularly important, because they reflect the hydraulic heterogeneity of local conditions for a given hydro-morphological configuration. In Figure 4.5 the overall spatial variability is represented by the extension of the box (interquartile range) and of the whiskers for the different morphologies. For the same discharge value, water depth is highly variable in complex morphological configurations (A4-A5-A6), especially in comparison with the simpler morphological patterns (A1-A2-A3) (Figure 4.5A,B). The same behaviour does not apply for flow velocity, for which the variability is comparable among the examined morphological categories, and differences are much less evident.

The invariance of the median values from base to peak discharge and the higher variability of the local values may be related with the higher resilience of the morphologically complex systems (A4-A5-A6) to discharge variations and matches the common perception that greater morphological complexity should ensure higher ecological functionalities (e.g. Elozegi *et al.*, 2010).

4.3.2 Hydro-Morphological Index of Diversity

As a quantitative, species-independent quantification of the physical habitat variability among the examined hydro-morphological configurations we have computed the hydro-morphological index of diversity HMID (Section 4.2.5.1). In Figure 4.6 the HMID value is plotted against the six considered widening ratios W/W_0 that have been related with the considered morphologies. Each continuous line refers to a different discharge, namely corresponding to the “base” and “peak” values under the three considered hydropeaking scenarios (Table 4.1).

The dependency of the HMID on the widening ratio is clearly non-linear and is qualitatively similar for all the chosen hydropeaking patterns. Regardless of the chosen discharge value, the HMID invariably increases with morphological complexity. For instance, the Bbase series refer to $Q = 10 \text{ m}^3/\text{s}$ and show low HMID values ($HMID < 5$) for the two simplest morphologies characterized by nearly flat bed or alternate bars ($W/W_0 = 1, 1.33$,

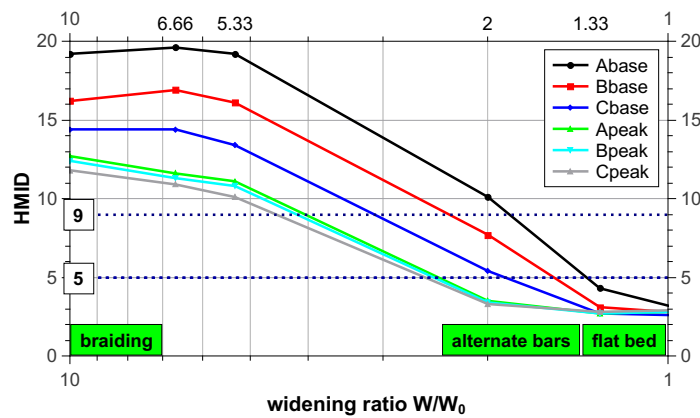


FIGURE 4.6: HMID index versus six widening ratios. Series represent the different release patterns (A,B and C) both for peak and base flow; dotted lines represent category thresholds proposed by Gostner *et al.* (2013a).

right side of the plot). For higher widening ratios the HMID value grows more rapidly and attains moderate values ($5 < HMID < 9$) for the alternate bars configuration associated with $W/W_0 = 2$. The growth of the HMID with the widening ratio is eventually reduced and tends to stop around an approximately constant value of $HMID \approx 20$ for the most complex, multi-thread morphologies ($W/W_0 = 5.33, 6.66, 10$). This means that channel widening beyond $W/W_0 = 5.33$ cannot determine further increase of the diversity of physical habitat conditions, measured through the HMID.

Nonlinearity is also evident in the effect of flow discharge, because the vertical spacings between the curves referring to base flow are much larger compared to those at peak flows (Figure 4.6). Under peak flow conditions (A,B,Cpeak) the bed morphologies are almost fully submerged, and the different trends are almost overlapped. This suggests that the peak discharges associated with nearly complete wetting conditions of the active channel bed do not significantly affect the HMID. It turns out that it is basically dependent on channel morphology under these conditions.

Comparing the values from Figure 4.6 with the HMID categories proposed by Gostner *et al.* (2013a) it is possible to highlight that the braiding configurations ($W/W_0 = 5.33, 6.66, 10$) lay always in category 3 ($HMID > 9$, morphologically natural) while the simple morphologies ($W/W_0 = 1$ - flat bed and $W/W_0 = 1.33$ - small alternate bars) are always within category 1, no matter the choice of discharge pattern. On the other hand, for the morphology number 3 ($W/W_0 = 2$ - alternate bars) the HMID values lay in different categories depending on the chosen hydropeaking series (so for different discharge stages).

The quantitative information reported in Figure 4.6 can be used to build the hydro-morphological alteration space as in Figure 4.1. Thus we can plot the quali-quantitative

spaces in Figure 4.7, which show the hydro-morphological tradeoffs for HMID index. Black dots represent the 18 configurations, labelled (in blue) with the obtained value of HMID. The space is divided in three regions by the locus of points having HMID equal to 9 and 5, qualitatively defined by linear interpolation of values in Figure 4.6. With this view, blue region gathers configurations with $HMID > 9$, green area with $5 < HMID < 9$ and red region with $HMID < 5$. Figure 4.7A refers to base flow while Figure 4.7B to peak flow conditions. The HMID is strongly dependent on morphology (thresholds are predominantly vertical) while it smoothly changes with increases in the base flow (Figure 4.7A). Moreover, the comparing between the base and peak configurations show a sensible temporal variability of HMID for morphologies between alternate bars and transitional ($W/W_0 = 2$ to 4), while the HMID almost shows no base-to-peak change of class for the other channel morphologies (Figure 4.7).

4.3.3 Macroinvertebrate drift

For this ERHP we analysed the statistical distributions focusing both on the variation from base to peak conditions (temporal variability) and on the variation linked to different morphologies (spatial variability). In Figure 4.8A mean values of the bottom shear stress are plotted for six widening ratios W/W_0 corresponding to the different morphologies. The data series represent the different release patterns (A,B and C) both for peak and base flow. Mean values are useful to understand general trends for this ERHP: the bottom shear stress decreases non linearly as the widening ratio increases. It is worth noting how, for more complex morphologies ($W/W_0 = 5.33, 6.66, 10$), the ERHP tends to flatten, suggesting the type of self-formed morphology strongly influence ERHP's distribution.

We then apply the hydraulic threshold criteria ($\tau_{drift} = 10 \text{ N/m}^2$, Hauer *et al.*, 2012) and plot the percentage of area with bottom shear stress lower than the drift threshold (τ_{drift}). In Figure 4.8B is shown how increasing the widening ratio, so varying the reach morphology, makes mean shear stress decreasing, with reach that tends invariantly to increase the areas where macroinvertebrate communities can settle (shear stress under the threshold, sink behaviour). However in Figure 4.8B is possible to quantify how the most relevant differences of the series occur for low discharge stages (base discharge) and simple morphologies ($W/W_0 = 1, 1.33, 2$). On the other hand, once bed morphologies are almost fully submerged (peak discharge stages) there are no relevant differences between series A, B and C.

Figure 4.9 reports the hydro-morphological alteration space for the macroinvertebrate drift (with the values of Figure 4.8B) for base flow (Figure 4.9A) and peak flow (Figure 4.9B) conditions. Blue labels are the percentages of area with sink behaviour

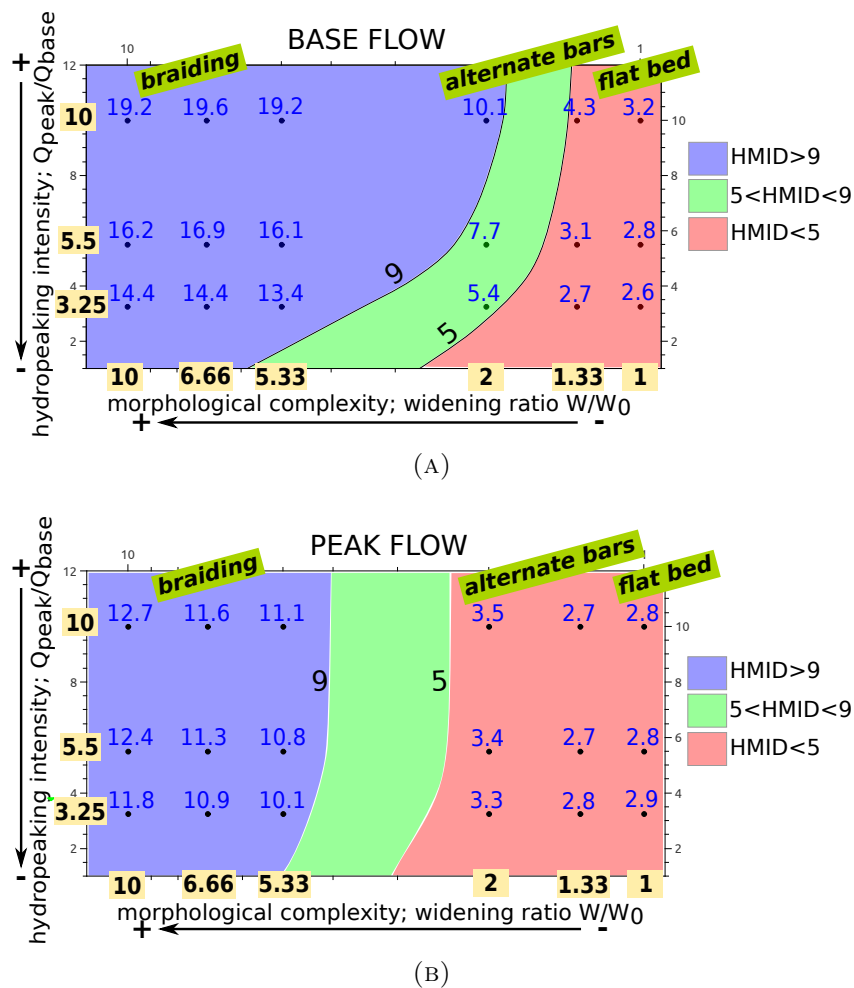


FIGURE 4.7: Hydro-morphological alteration space of HMID for base (A) and peak flow (B). Blue regions represent configuration with $HMID > 9$ (morphologically natural), red regions with $HMID < 5$ (morphologically heavily altered) while intermediate green regions represent transitional configurations. Black dots correspond to configurations of the numerical runs while blue labels are the obtained HMID values.

($\tau < \tau_{drift}$). Blue regions represent configurations with dominant (more than 75%) settling of macroinvertebrate communities while, on the opposite, red regions represent scenarios dominated by macroinvertebrate drifting. At base flow condition (Figure 4.9A), the sink/source behaviour is determined by both base flow variability (i.e. Q_{peak}/Q_{base}) and by channel pattern for the less complex morphologies (small widening ratios). On the other hand, channel morphology becomes the dominant control on the sink/source behaviour, compared to base flow variability, when moving to braided systems (left part of the space). Moreover, in the case of peak flow, we observe a strong reduction of sink behaviour (absent blue region).

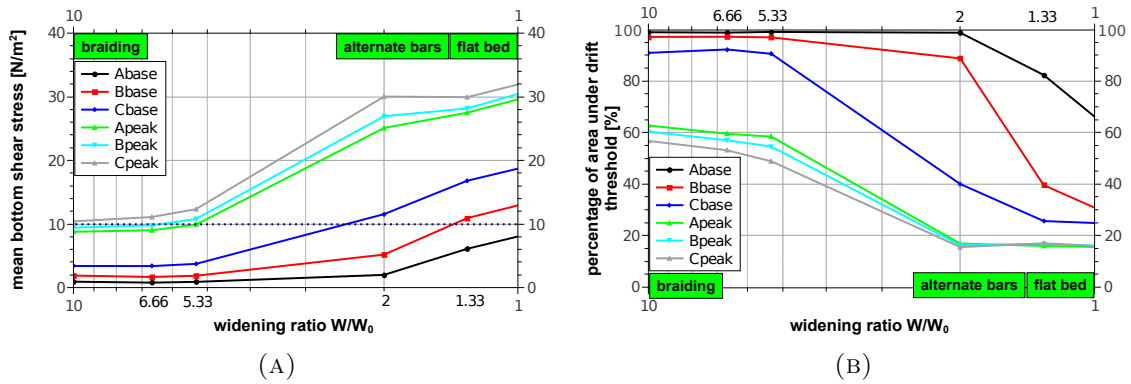


FIGURE 4.8: Panel A: mean of the bottom shear stress versus six widening ratios corresponding to the different morphologies; the dotted line denotes the drift threshold $\tau_{drift} = 10 \text{ N/m}^2$ (Hauer *et al.*, 2012). Panel B: percentage of area with bottom shear stress lower than the drift threshold τ_{drift} versus six widening ratios. In both panels the series represent the different release patterns (A,B and C) both for peak and base flow.

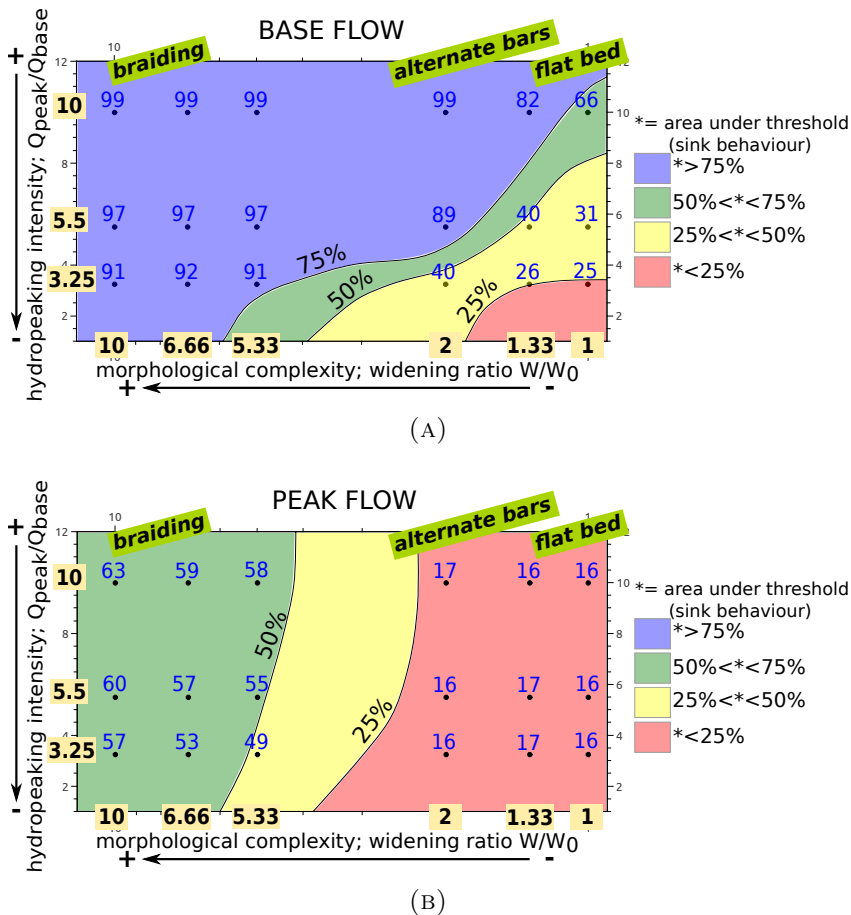


FIGURE 4.9: Hydro-morphological alteration space of macroinvertebrate drift for base (A) and peak flow (B). Blue regions represent configurations with dominant (more than 75%) settling of macroinvertebrate communities (sink areas) while red ones represent scenarios dominated by macroinvertebrate drifting (source areas). Black dots correspond to configurations of the numerical runs while blue labels are the percentages of area with sink behaviour.

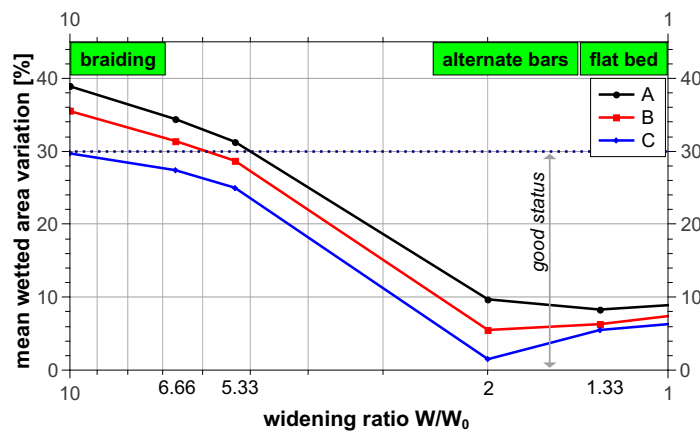


FIGURE 4.10: Mean wetted area variation versus six widening ratios; dotted line is the threshold proposed in Swiss protocol (Baumann *et al.*, 2012) to discriminate the low stranding risk (good status).

4.3.4 Fish stranding

Results for the mean wetted area variation, plotted versus the widening ratio W/W_0 are given in Figure 4.10. As first consideration the trend of this ERHP is depending on the type of reach morphology with a great increment passing from alternate bar pattern ($W/W_0 = 2$) to braiding system ($W/W_0 = 5.33$) but the variation keeps increasing also with an established braiding system (left part of the plot, $W/W_0 = 6.66, 10$).

In order to highlight the percentage of area that can be considered in a good status (so with low risk of stranding, according to Baumann *et al.*, 2012), we show on Figure 4.11C the area in a good status (with wetted area variation lower than 30%) versus the widening ratio W/W_0 . The hydro-morphological alteration space for stranding risk in Figure 4.11C has been obtained firstly by determining, for each of the 18 hydropeaking-morphology configurations, the percentage of area satisfying the criteria $\Delta A_w < 30\%$ (blue labels in Figure 4.11C). Afterwards, the same procedure leading i.e., from Figure 4.8B to Figure 4.9, has been adopted. The three extrapolated threshold curves represent the locus of points with 25%, 50% and 75% of wetted areas in a good status, respectively. The thresholds divide the space into 4 regions with an increasing risk of stranding moving from blue to red region.

In Figure 4.11C it can be easily seen that the area with low stranding risk invariably decreases when the widening ratio (channel width) increases, showing a non-linear trend associated to the different effects of the reach morphology. Overall, stranding risk is dependent both on reach morphology and on hydropeaking intensity. However, it is almost independent from flow discharge in morphologies with a less degree of morphological complexity (i.e. $W/W_0 = 1, 1.33, 2$, right part of the space). Opposite to the ensemble

ecological response suggested by the initial Figure 4.1, this ERHP reveals the worst ecological situation (i.e. highest stranding risk) in correspondence of high morphological complexity ($W/W_0 = 5.33, 6.66, 10$).

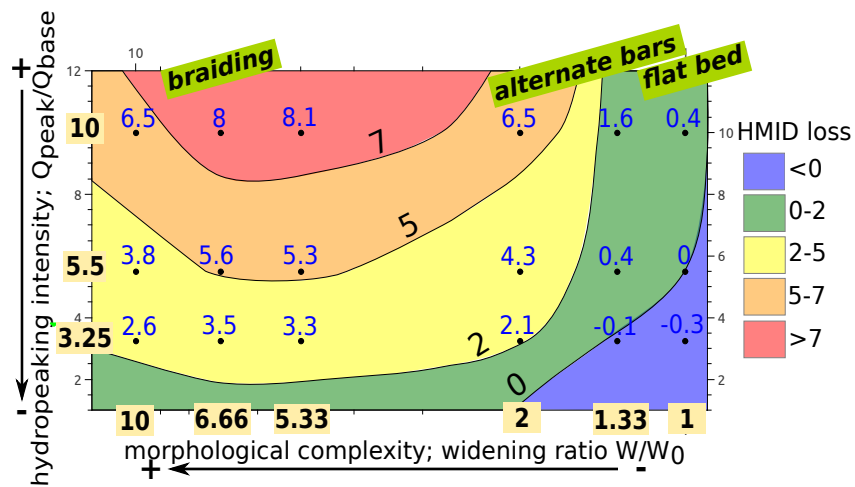
4.3.5 Comparative analysis of ERHPs response to hydropeaking for different morphologies

The present work has focused on the analysis of one single hydropeaking wave. In real cases, the presence of hydropeaking intrinsically implies that the affected river reach is subject to a repeated daily or sub-daily switch from base to peak flow conditions, and may therefore be viewed as “two rivers in one”, as recently pointed out by Jones (2014). The inherent intermittency of the hydropeaking phenomenon is accounted for in Figures 4.11 and 4.12 that are an attempt to synthetically quantify the hydropeaking effect of for each ERHP separately (Figure 4.11) and jointly (Figure 4.12).

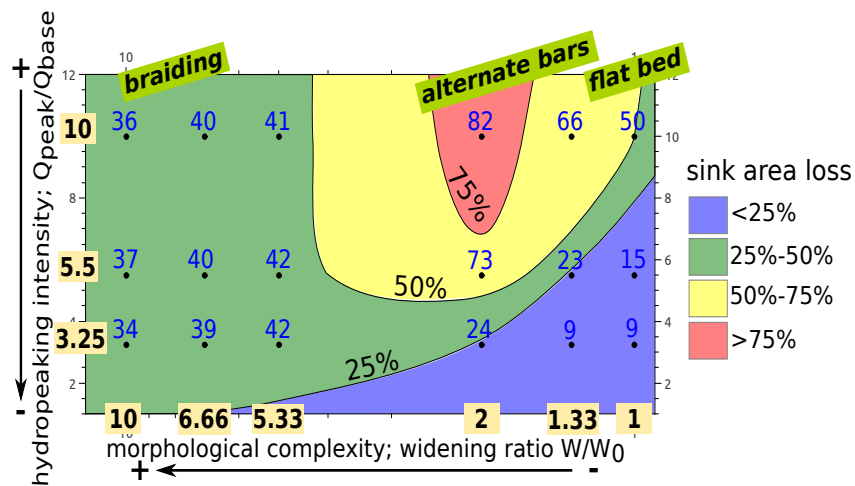
Figure 4.11 reports the quantitative behaviour of habitat diversity loss (Figure 4.11A), of drift sink area loss (Figure 4.11B) and of the percentage of wet area in good status with respect to stranding risk (Figure 4.11C), in the form of the hydromorphological space introduced in Figure 4.1. Each of these diagrams is representative of the response of each ERHP to one hydropeaking wave as a whole, while Figures 4.7 and 4.9 refer to the behaviour of the ERHP under either base or peak flow conditions.

Comparing Figure 4.7, 4.9 and 4.11 allows to quantify how different is the role of hydropeaking for the three phenomena of drift, stranding and habitat diversity across the range of examined bed morphologies. A prevalent horizontal gradient from red to blue areas in the hydromorphological spaces indicates a dominant morphological control on the ERHP behaviour, regardless of the hydropeaking intensity (or base flow increase). This is the case of hydro-morphological diversity at base (Figure 4.7A) and peak (Figure 4.7B) flow conditions and of the percentage of wet areas in good status with respect to the stranding risk (Figure 4.11C).

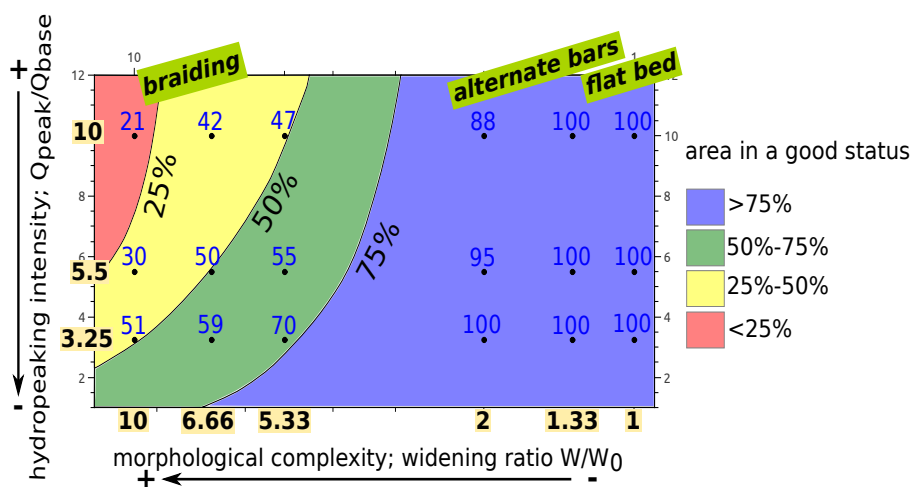
In contrast, the base to peak loss of habitat diversity, expressed in Figure 4.11A through the HMID difference between base and peak flow conditions, seems to be fundamentally controlled by hydropeaking intensity almost regardless of the channel pattern. The location of the red region around $W/W_0 = 5.33$ also suggests that transitional morphologies between single and multi-thread are the most sensitive to intense hydropeaking because they determine a higher loss of hydromorphological diversity compared both to alternate bars and braided channel patterns for a given hydropeaking intensity. An exception to such behaviour is related to the simplest morphological configurations (widening ratio smaller than 1.33), where the loss of diversity is much more limited and almost



(A)



(B)



(C)

FIGURE 4.11: Hydro-morphological alteration space of ERHPs variation passing from Q_{base} to Q_{peak} : (A) variation of HMID index; (B) variation of area with sink behaviour; (C) percentage of area with low risk of stranding.

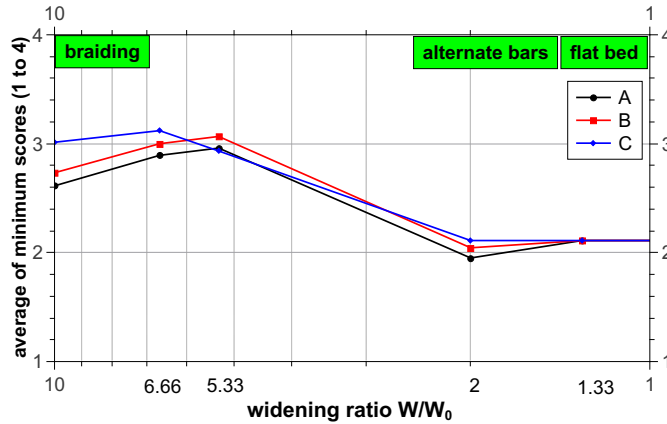


FIGURE 4.12: Classes of hydro-morphological quality for the three ERHPs under repeated hydropeaking.

independent from the hydropeaking intensity, though the limiting factor here is the low absolute HMID value under base flow condition, due to the poorly developed bed topography.

The response of macroinvertebrate sink areas does not show clear trends with either channel morphology or hydropeaking intensity like the other two ERHPs do, with the two hydromorphological controls being more balanced and nonlinear trends being more distinctive of the ERHP at both base and high flow, and also of its base-to-peak loss. Such loss of sink areas is strongly sensitive to hydropeaking in alternate-bar channel patterns, and is nearly unaffected by base flow increase for wandering or braided morphologies, which correspond to an almost constant loss of 40% (nearly homogeneously green left portion of Figure 4.11B).

The performance of each ERHP is finally aggregated in Figure 4.12, as described in Section 4.2.5.4, to obtain an overall eco-hydraulic comparison among the examined 18 hydropeaking - channel morphology combinations. Figure 4.12 suggests how morphologies from wandering to low braiding seem to provide the optimal eco-hydraulic conditions, while a further increase of the braiding intensity corresponds to a reduction of the representative score because of the high associated increase in stranding risk. The lowest scores are found for widening ratios corresponding to alternate bars or smaller. The strongest variability in the eco-hydraulic response to hydropeaking is found when the river pattern transitions from alternate bars to wandering. Such response does not seem to vary considerably in the range of examined hydropeaking intensities, from about 1:3 to 1:10.

4.4 Discussion

4.4.1 Morphological controls on hydropeaking effects

The proposed modeling approach allows to highlight trends in the eco-hydraulic response of a river reach along a gradient of different channel morphologies, from almost flat bed to braiding. Overall the eco-hydraulic response shows a high degree of nonlinearities in behaviour, in qualitative agreement with the findings of Hauer *et al.* (2014).

Braided reaches appear as the most resilient to hydropeaking in terms of the absolute high availability of habitat diversity (HMID > 9), of the very limited loss of invertebrates sink areas and of habitat diversity, especially if compared to wandering morphologies. The major concern with a braided river reach subject to hydropeaking lies in its high risk of stranding. Braided river reaches are very uncommon in the contemporary landscape of hydropower-regulated river systems, at least in the alpine region of Europe. Among the few ones recognized as “near-natural”, the braided Tagliamento River (Bertoldi *et al.*, 2009) is subjected to hydropeaking characterized by a rather limited intensity in all seasons of the year, which is not causing any relevant threat to the fish population.

When moving to single-thread morphologies, alternate bars are predicted to be extremely sensitive environment to macroinvertebrate drift, to offer safer regions from stranding and also are not affected by relevant diversity loss, though their diversity is never particularly valuable in ecological terms (HMID usually < 9). In a recent study, Hauer *et al.* (2014) analysed the stranding risk associated with different types of gravel bars, by combining information on peak-to-base change in wetted area, on shallow habitat availability and on substrate grain size composition to develop and apply a conceptual stranding risk model. They simulated almost identical hydropeaking intensities (1:3, 1:5 and 1:10) to the present analysis, occurring over several sites with different bar morphologies in regulated Austrian rivers. The outcome of the stranding risk model of Hauer *et al.* (2014) highlights a qualitatively analogous contrasting effect of gravel bar morphology with respect to the one emerging from the present analysis: simpler morphologies, found in more regulated reaches, featured the smallest reduction in wetted area, coherently with the blue region in our Figure 4.11C. However the same morphologies are also characterized by the absence of minimum suitable habitats, as it also emerges from our Figure 4.7A,B at both base and peak flow.

Moreover, Hauer *et al.* (2014) emphasize the role of bar morphology on stranding risk. They point out a difference in behaviour between point bars, which occur at the inner side of river bends, alternate bars, which develop in straightened river reaches, and mid-channel bars. Point bars feature a smaller variability in wetted area compared to

alternate bars, and thus display less sensitivity to hydropeaking, in some way analogously to mid-channel bars. The point bar tails are characterized by smaller-scale topographical structures that create suitable habitats at both peak and base flow and also the overall morphology of the two types of bars is quite different. In our work, widening determines an analogous increasing morphological complexity, with less regular bar pattern and superimposed smaller scale heterogeneities (Figure 4.3). For instance, when moving from $W/W_0 = 2$ to $W/W_0 = 5.33$, secondary channels develop alongside alternate bars and progressively become more relevant in the whole reach morphology, before this becomes fully braided.

The outcomes of our study suggests that transitional morphologies between single and multi-thread offer the most interesting and less trivial behaviour, because they offer the best tradeoff between sink area loss and percentage of dewatering-safe areas (see the corresponding green areas in Figure 4.11B) among the non-trivial morphological configurations. This is reflected by the overall eco-hydraulic “optimum” as it emerges from the score reported in Figure 4.12, which has been obtained by averaging each ERHP-specific score. Interestingly, such result is only morphology-dependent and does not seem to be affected by hydropeaking intensity. The relevant role of the transitional morphologies is coherent with the findings of Person *et al.* (2013), who performed a comparative analysis of several hydropeaking mitigation measures. Person *et al.* (2013) noted that “braided reaches provided the richest in-stream structure”, i.e. habitat diversity and availability, though “braided” there refers to a reach with a main channel and one single secondary, smaller channel, separated by a gravel bar with superimposed smaller-scale irregularities, thus resembling an actually wandering or transitional morphology. While Hauer *et al.* (2014) indicate that no “optimal” river topography for hydropeaking mitigation could be found among the examined 16 bar reaches in their study, our analysis suggest that at least the best tradeoff, if not optimal conditions, are actually provided by such transitional patterns. This type of channel morphology is increasingly dominating the regulated fluvial landscape since the last decades, at least in Europe and in other pre-alpine contexts in the industrialized world (e.g. Surian and Rinaldi, 2003; Habersack and Piegay, 2007), because of channel adjustments of formerly braided reaches caused by altered flow and sediment regimes, as well as by gravel mining. The occurrence of hydropeaking over transitional channel morphologies may therefore be already frequent in alpine areas with strong hydropower development, may characterize morphologically restored (locally widened) river reaches and may also increasingly occur in the future in alpine-piedmont areas with yet unexploited hydropower potential.

The topographic differences between the different types of bars observed by Hauer *et al.*

(2014) are qualitatively consistent with theoretical and experimental findings in river morphodynamics, which suggest that alternating, point and mid-channel bars are related to fundamentally different physical processes, which lead to different topographic expressions. Point bars are forced by a curved channel geometry (Blondeaux and Seminara, 1985), and alternate bars mostly develop as a result of a free instability mechanism of the riverbed topography (Tubino *et al.*, 1999). In our work, when moving from morphologies 1 to 6, generated by a progressive widening under analogous hydraulic conditions (formative discharge, channel slope, sediment size) similar topographic differences are found. Future research shall concentrate on the relations between the topographic expressions of such bar units and the underlying morphodynamic processes.

4.4.2 Implications for restoration of hydropeaking rivers

A central question related to “giving more room” to channelized rivers is whether morphological/structural measures alone would be effective when the river reach to be restored also suffers from hydrological alteration, and namely from hydropeaking (Fette *et al.*, 2007). Harby and Noack (2013) suggest that “morphological restoration might be able to achieve the same mitigation effect than by adjusting hydro operations”. Also Tuhtan *et al.* (2012) conclude that it may be possible to create fish shelters or, more in general to design instream refugia in addition to flow regime modifications. Paetzold *et al.* (2008) indicate that the combined conditions of hydropeaking inundation and gravel bar morphology are crucial for providing suitable habitats for the riparian arthropods, and that morphological river rehabilitation (e.g. channel widening) can benefit riparian arthropods, particularly in rivers that are affected by hydropeaking. Muhar *et al.* (2007) report that, contrary to expectations, little or no ecological improvements have been documented in some widened reaches subject to hydropeaking, indicating the need for a deeper quantitative investigation of hydropeaking-channel morphology interactions.

The mutual interplay between channel morphology and hydropeaking is agreed to represent a key phenomenon, but so far quantitative indications on its dynamics and eco-hydraulic effects have not been provided. In this respect, the proposed modeling approach can be used as a template for a quantitative analysis of the most effective tradeoffs between two different strategies aiming to achieve the same ecological target or between two different ecological targets that pose contrasting hydro-morphological requirements. For instance the hydro-morphological alteration space originally proposed by Baumann *et al.* (2012) suggests how the same eco-hydraulic effect can often be obtained through both vertical and horizontal strategies. As an illustrative example, Figure 4.11C suggests that the same reduction in stranding risk corresponding to a wandering channel pattern

($W/W_0 = 5.33$) under the most intense hydropeaking scenario (A: $Q_{peak}/Q_{base} = 10$) can be obtained either by increasing the base flow from 5 to 20 m^3/s and keeping the same morphology or by reducing the active river corridor width of roughly 1.5 times (down to $W/W_0 \simeq 3.5$) without any variation of the hydropeaking intensity. Under the conditions of our simulations, both actions are predicted to achieve an increase of the area with low stranding risk from 47% to 70% of the total wetted area. Analogously, the same mitigation of sink area loss can be achieved in a channel with alternating bars by either a three-fold base flow increase or by widening the channel up to 2.5 times its initial width (Figure 4.11B). Also, the paradox posed by the contrasting trends of hydromorphological diversity (increases with morphological complexity) and of the percentage of stranding safe areas (which instead decreases with morphological complexity) can be given a quantitative answer. Channelization below morphological instability to occur should not be preferred to avoid stranding risk because of its overall poor eco-hydraulic functioning (see for example the overall score in Figure 4.12).

Besides providing a representation of the effects of base flow increase as a hydropeaking mitigation measure, moving along the vertical axis of the hydromorphological spaces like Figure 4.1 is also a way to account for the seasonal variability of the base flow typical of alpine rivers, where the combined effect of snowmelt and, in some cases of glacier melt, naturally increase base flow conditions even within hydropower-regulated river reaches. Our analysis suggests that the effects of base flow increase are morphology-dependent, because: (1) it maximizes the benefits for habitat diversity for transitional/wandering channel morphologies; (2) it minimizes the loss of invertebrate drift areas in channels with alternate bars and (3) it reduces stranding risk in braiding morphologies. Increasing base flow alone might be thought to lead to decreasing available habitats, but our work suggests that this effect is morphology-dependent and definitely not the case under transitional patterns. This reiterates the interaction with morphological mitigation especially when based on a design channel width for which a wandering morphology is expected.

A final consideration related to legal requirements on hydropeaking intensities can be made from looking at the three panels composing Figure 4.11. Regardless of the channel morphology, the worst ecological scenarios (red areas) appear to develop only for base to peak flow ratios smaller than 1:5, with larger ratios (smaller hydropeaking intensities) invariably producing milder effects for all the examined ERHPs. This quantitatively substantiates legal requirements on minimum base to peak flow ratios that are prescribed at 1:3 (Switzerland) or also 1:5 (Austria) (Hauer *et al.*, 2014).

River - Country	Widening ratio	Channelized width [m]	Widening length [m]	Reference
Rio Mareta - I	2-3	20	2000	Trentini <i>et al.</i> (2012)
Aurino - I	2-3	50	1000+800	Campana <i>et al.</i> (2014)
Thur - CH	2-3	50	1500	www.rivermanagement.ch
Kander - CH	6	20	500	www.rivermanagement.ch
Mur - A	2-3	70	2500	Gosdorf Project - Mur River
Drau - A	1.5-2	50	450	LIFE-Project Upper Drau River
Isar - D	2	50	9000	www.rivermanagement.ch

TABLE 4.2: Some examples of European river widening projects.

4.4.3 Applicability and limitations of the proposed approach

Though our analysis has not been developed referring to actual specific cases, it is relevant to note that the hydromorphological conditions under which our modeling experiments have been designed are quite realistic. First, the considered ranges of widening ratios W/W_0 and of reach length (normalized with the channelized width W_0) are in good correspondence with those typical of river widening projects in alpine streams. Examples taken from selected river widening projects in the alpine region of Europe are reported in Table 4.2. It appears that the allowed width of the restored reach may be in the range of 1.5 to 6 times the channelized river width (vs. 1.3 to 10 of our study), while the typical length of widened reaches may range from 10 up to 100 times the same initial river width, an identical range to that employed in our analysis. Second, the considered range of hydropeaking intensities (1:3, 1:5, 1:10) is representative of many actual situations in Alpine streams (Hauer *et al.*, 2014).

Another relevant factor for the applicability of our results to real hydropeaking streams is the simulated degree of inundation of the examined morphologies under base and peak flow conditions. Alternate bars ($W/W_0 = 2$) are overtopped by peak flows, which only partially inundate (70 to 80%) transitional and braiding morphologies. This is consistent with the few reported data for some Austrian rivers, indicating that gravel bars in the Alpine environment may only be overtopped in terms of hydropeaking, while the braided sections may not be fully overtopped in terms of (theoretical) artificial fluctuating flows like in the Austrian Lech River (Auer, 2012).

The presented approach has therefore been developed referring to idealized though realistic combinations of hydropeaking waves of different intensities and of channel morphologies of varying complexity. In order to be applied to a given specific case the availability of the following data is required: the actual discharge time series of the reach, roughness and river bed topography data of the investigated reach. Channel morphology should be known at sufficient spatial resolution, i.e. a resolution which allows mapping

the main two-dimensional riverbed features, like bars, bifurcations, secondary channels. Should only sparse cross-sections be available, a numerical morphodynamic model could be used to develop scenarios of the potential future morphological patterns of the reach. This might be used to choose the optimal channel width value when designing a local river widening project.

It is finally useful to review the main limitations of the present study. The chosen ERHPs are only some possible choices that cannot be considered exhaustively representative of the related eco-hydraulic process. For instance, the criterion used to quantify the variability in stranding risk (equation 4.3) is purely based on existing regulation, namely from the Swiss water protection guidelines (Baumann *et al.*, 2012). Analogous plots could be derived using other specific regulations adopted in other countries, like Norway or Austria. In Norway a dewatering threshold has been suggested (Saltveit *et al.*, 2001; Halleraker *et al.*, 2003; Irvine *et al.*, 2009; Tuhtan *et al.*, 2012), which is based on the vertical flow level variation rather than on the wetted area variation. In Austria an analogous criterion (besides those on hydropeaking magnitude) of the Swiss one is used though with a 20% rather than an 30% threshold. More specific criteria are needed to predict more in detail the actual response of the eco-hydraulic process to different morphologies under hydropeaking. For instance in the case of stranding, Hauer *et al.* (2014) account for the relevant role of the substrate size, which is not considered in this analysis. Moreover, the worst possible scenario of ramping rate has been considered, by assuming an instantaneous shift from base to peak flow and viceversa. Therefore the stranding risk maps (Figure 4.11C) have to be viewed as an upper limit for that ERHP. More in general, the present approach is not able to predict the actual biological response of a reach to hydropeaking, but only its response in terms of the physical conditions that can be of relevance for a specific biotic element.

On the other hand, the potential of the proposed approach also lies in its capability to incorporate other Ecologically-Relevant Hydraulic Parameters that have not been examined within this work like, e.g. the physical habitat availability of a target species, which can be obtained by integrating the outcomes of the hydraulic model with the specific hydraulic preference information or habitat rating curves. This would lead to a tailored version of the hydro-morphological alteration space of Figure 4.1 for the design case.

Finally it must be noted that the assumed biunique relation between channel widening (i.e. the parameter W/W_0) and the developed riverbed morphology holds only when adequate sources of sediment supply are connected with the target river reach; therefore an implicit assumption of our study has been that of enough availability of upstream sediment supply, which may not always be the same in regulated alpine streams.

4.5 Conclusions

The present work consists of a first quantitative attempt to investigate the eco-hydraulic response of river reaches with different channel morphologies to hydropeaking waves. It is based on a hydraulic modeling approach and it focuses on three eco-hydraulic phenomena with well known relevance under hydropeaking conditions: habitat diversity, macroinvertebrate drift and fish stranding. A series of 18 combinations of 3 hydropeaking waves having different intensity (ratio Q_{peak}/Q_{base}) with 6 channel morphologies of increasing complexity (from nearly flat bed to alternate bars, wandering and braiding) are investigated in terms of Ecologically Relevant Hydraulic Parameters (ERHPs) chosen to measure the target eco-hydraulic phenomena. Under the assumptions and simplifications described in Section 4.2 we performed steady hydraulic simulations via a 2D numerical model for both base and peak flow conditions for each of the 18 combinations, which can be viewed as realistic replicates of actual scenarios occurring in Alpine region.

Non-linear trends are predicted for the chosen ERHPs with both hydropeaking intensity and morphological complexity. Habitat diversity and fish stranding risk are mostly controlled by channel morphology and show contrasting behaviours with increasing morphological complexity. Braided reaches are the most resilient to hydropeaking offering the highest habitat diversity, very limited base-to-peak loss of sink areas of drifting invertebrates and also of habitat diversity, while alternate bars are extremely sensitive environments to drift and offer safer regions from stranding. Transitional morphologies between single- and multi-thread, which have increasingly replaced formerly braided reaches in the regulated river landscape, offer the best eco-hydraulic tradeoffs. The proposed approach can be applied to a specific case to support the choice of the most effective river restoration strategy leading to the optimal eco-hydraulic conditions for the ecological targets of primary interest.

Chapter 5

Unsteady modeling of fish stranding risk under hydropeaking conditions

This chapter focuses on a modeling approach to investigate the fish stranding risk. For the sake of simplification, in the previous chapter each of the three different eco-hydraulic assets (habitat diversity, macroinvertebrate drift and fish stranding) has been quantified through one single representative Ecologically-Relevant Hydraulic Parameter (Section 4.2.5). However the fish stranding phenomenon, as well as the others two assets, is known to be related to several complex abiotic and biotic processes (Nagrodski *et al.*, 2012; Irvine *et al.*, 2014).

The general aim of this chapter is to put a step forward in understanding the hydro-morphological controls on fish stranding risk and especially to quantitatively investigate the implications of existing legal requirements for stranding risk under different conditions of hydropeaking intensity and channel morphology. To this aim this chapter models the water depth rate of change (or *dewatering rate*), which represents a critical and triggering feature for stranding (e.g. Young *et al.*, 2011), together with the variation of the wetted area, such to investigate and compare two different ERHPs related to the same eco-hydraulic asset.

The chapter consists of two main parts. In the first part (Section 5.1) the aim is to investigate and quantify the tradeoffs between dewatering rate and wetted area variation for different self-formed river morphologies. The analysis is conducted with the same methodology of the Chapter 4. The second part (Section 5.2) is dedicated to the fish stranding risk modeling in Lundesokna River, a Norwegian river subjected to hydropeaking.

5.1 Fish stranding risk and river morphology: unsteady numerical modeling

Modeling and quantifying the stranding risk accounting for the role of river morphology is still an open topic which fosters a lively debate at both scientific and managerial level (e.g. Person *et al.*, 2013; Harby and Noack, 2013). Research findings from field and laboratory experiences underline how stranding risk reduces with mild dewatering rates (e.g. Halleraker *et al.*, 2003; Irvine *et al.*, 2009); some river management guidelines include such outcomes and concurrently suggest different ranges of wetted area variations to mitigate stranding risk (e.g. Baumann *et al.*, 2012).

Both wetted area variation and dewatering rate depend, albeit differently, on hydro-morphological configurations: the variation of wetted area from peak to base flow can be seen as “steady” feature, because it only depends on the two extreme discharge stages and on the river morphology. On the other hand, the dewatering rate depends also on the “unsteady” hydropeaking characteristics, i.e. on the discharge rate of change. Thus hydro-morphological configurations with potential high (or low) stranding risk arise from the combination of such two features.

The numerical investigation here proposed builds on the analysis of the previous chapter (Section 4.2) and is based on the same set of river morphologies (Section 4.2.2), though introducing the fundamental element of hydrodynamic unsteadiness associated with hydropeaking. The workflow and the results of the unsteady modeling of fish stranding risk are given in the following sections.

5.1.1 Methods

The modeling approach to investigate the fish stranding risk follows the workflow presented in the previous chapter, Section 4.2. In particular we adopt the same suite of river bed patterns (Section 4.2.2) and recast the hydropeaking scenarios of Section 4.2.1, now accounting for the transient discharge rising and falling limbs (Section 5.1.1.1). Similarly, the hydro-morphological configurations is that described in Section 4.2.3, while the employed hydraulic numerical model is described in Chapter 3. Finally, the hydraulic variables (e.g. flow velocity, water depth) resulting from the numerical simulations are summarized into two additional ERHPs which are particularly relevant for fish stranding.

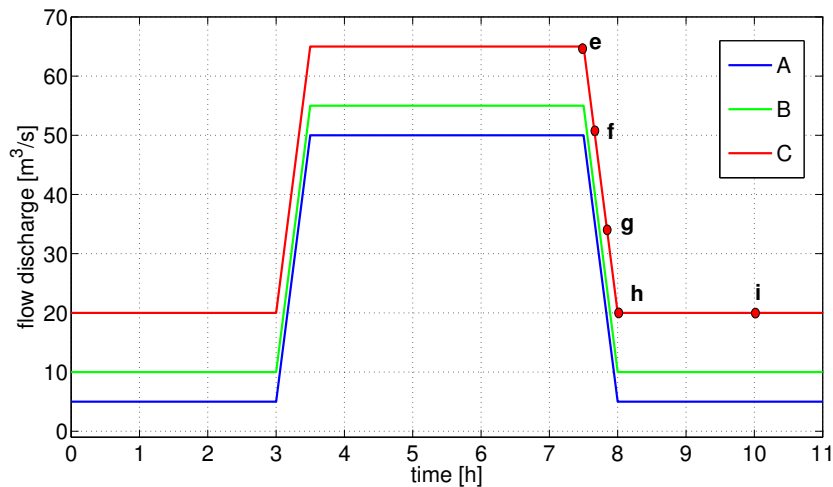


FIGURE 5.1: Simplified hydropeaking waves for the unsteady stranding risk modeling. In lowercase letters the output points for the dewatering rate evaluation are reported.

5.1.1.1 Hydropeaking events

The simplified hydropeaking waves presented in Section 4.2.1 are employed by fully considering the transient rising and falling limbs. In particular, the three hydropeaking patterns A, B and C, have peak (Q_{peak}) and base (Q_{base}) discharge as in Table 4.1, and a rising and falling limb lasting 30 *min* each. The recast hydropeaking patterns are shown in Figure 5.1.

It is worth noting the entire set of numerical simulations starts from and ends to hydrodynamic steady configurations of base flow discharge. The duration of the input peak discharge is set on 2 hours for all the simulations. Such duration has been then verified to allow the system reaching the steady conditions also for the peak stages, before the dewatering event starts.

In order to describe and quantify the temporal variations of the outcomes of the numerical simulations we select a series of specific timings during the unsteady simulation when dewaterings rate are evaluated and discussed. In particular, Figure 5.1 shows these different characteristic timings (lowercase letters, from *e* to *i*) in relation to hydropeaking pattern C. Points *e*, *f*, *g* and *h* are taken every 10 minutes from the beginning (*e*) to the end (*h*) of the inlet discharge falling limb. Then point *i* is taken 2 hours after the end of hydropeaking wave (*h*). It is worth to underline that both point *e* and *i* correspond to steady peak and base flow conditions, respectively.

status	class	wetted area variation [%]
<i>very good</i>	blue	< 10%
<i>good</i>	green	10 ÷ 30%
<i>moderate-bad</i>	red	> 30%

TABLE 5.1: Swiss threshold on wetted area variation for stranding risk quantification (Baumann *et al.*, 2012).

5.1.1.2 Ecologically Relevant Hydraulic Parameters for fish stranding

The first Ecologically Relevant Hydraulic Parameter for fish stranding is the variation of wetted area, as widely discussed in previous chapter (Section 4.2.5.3 and 4.3.4). Therefore in this study the wetted area variation, similarly to Equation (4.3), reads

$$\Delta A_w = \frac{A_w^e - A_w^i}{A_w^e} \cdot 100 \text{ [%]}, \quad (5.1)$$

where superscripts e and i coherently refer to the specific timings of Figure 5.1.

The second ERHP is the maximum dewatering rate during the discharge falling limb. The water depth rate of change (or dewatering rate) is evaluated discretely for each computational cell as $\Delta D/\Delta t$ (where D and t are water depth and time values, respectively) among the intervals $e-f$, $f-g$, $g-h$ and $h-i$ (Figure 5.1). Hence, for each cell of the computational domain four dewatering rates are evaluated during each simulation. Among such four values, we then selected the maximum one as unique proxy for the local stranding risk. It is relevant to underline that the maximum dewatering rate is taken into account in the final results only when water depth decreases below 20 *cm*. This choice is based on evidence that fish escapes potential stranding areas for vanishing water depth (Saltveit *et al.*, 2001). For the sake of clarity, the dewatering rate is here expressed as a positive quantity, hence as magnitude of water depth rate of change.

Different criteria are currently adopted in existing national regulations for both the considered ERHPs. In particular, several dewatering thresholds have been proposed, based on experimental findings (e.g. Saltveit *et al.*, 2001; Halleraker *et al.*, 2003; Irvine *et al.*, 2009; Tuhtan *et al.*, 2012). Similarly, both Swiss and Austrian regulations take into account the wetted area variation as stranding risk indicators, but adopting different threshold values. In this study we deliberately quantify and discuss our results according to the criteria stated in the Swiss water protection guidelines (Baumann *et al.*, 2012). In particular, each ERHP defines three ecological status for stranding risk; Tables 5.1 and 5.2 give the status classification with respect to wetted area variation and dewatering rate, respectively.

status	class	dewatering rate [cm/h]
<i>very good</i>	blue	< 18
<i>good</i>	green	$18 \div 30$
<i>moderate-bad</i>	red	> 30

TABLE 5.2: Swiss threshold on dewatering rate for stranding risk quantification (Baumann *et al.*, 2012).

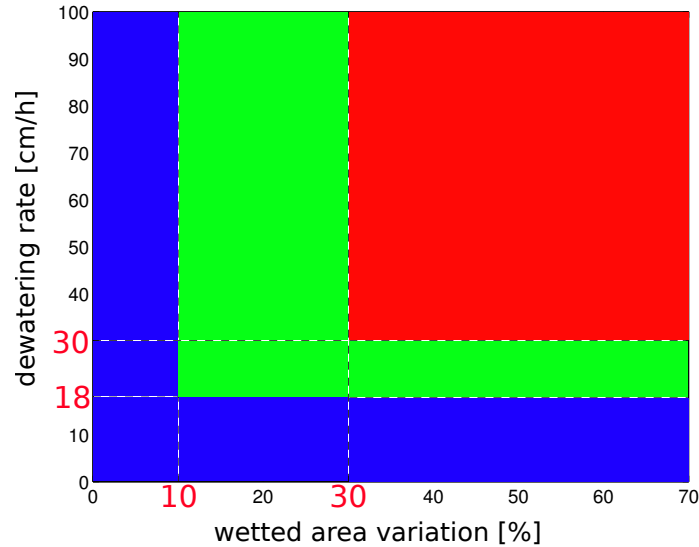


FIGURE 5.2: Stranding risk classification space based on both criteria of the Swiss water protection guidelines (Baumann *et al.*, 2012). Coloured region represent status classification: blue, green and red represent *very good*, *good* and *moderate-bad* status, respectively.

In order to shed light on the mutual tradeoffs of the two ERHPs and the role of river morphology on such tradeoffs, we plot the space in Figure 5.2 to jointly discuss the simulation results. The space is depicted on the base of the chosen Swiss thresholds, given in Tables 5.1 and 5.2. The joint classification in the space of the two ERHPs shown in Figure 5.2 responds to specific physical considerations: in case of very slow dewatering rates, stranding risk tends to minimize, whatever is the wetted area variation, thanks of fish capability of moving and sheltering. On the other hand, if the wetted area variation tends to vanish, stranding potential areas reduce whatever the magnitude of dewatering rate. Therefore, following such considerations, the joint classification of Figure 5.2 is built as follows: for each of the 9 possible combinations obtained by the intersection between the 3 classes of the two ERHPs (Tables 5.1 and 5.2), we assign the best status (i.e. blue, green, red) between the two single classes.

It is worth remarking that the results for the two considered ERHPs are evaluated at reach-scale, i.e. considering the frequency distributions over the overall reach, to discuss

their general behaviour, but also at local scale, i.e. at cross-section scale. Initially we use 5 meters wide transversal slices, for a total of 290 subareas, as already discussed in Section 4.2.5.3 (see Figure 4.4). Then, during result post-processing, we discard the first (upstream) and the last (downstream) 5 subareas, in order to avoid considering local effects associated with the unsteady numerical boundary conditions.

For the sake of clarity, as local proxy indicator of the maximum dewatering rate for each subarea, we calculate the median value of the single-cell maximum rates in the subarea which dried during the event. Finally, in order to investigate the influence of the chosen size of the local scale (i.e. of the width of the analysed transverse slices), we first evaluate the two ERHPs in 280 subareas of 5 *m* length, and then repeat the analysis slicing the reach domain each 10, 20, 50 and 100 *m*, for a total of 140, 70, 28 and 14 subareas, respectively.

5.1.2 Results

In this section the simulations results for the unsteady modeling of fish stranding are given. Firstly global distributions of the simulated hydraulic variable (i.e. flow depth and velocity) are presented. In the second part the distributions of the two selected ERHPs are reported and discussed. It is important to remark that, for the scope of this analysis, we are interested on the dewatering process from peak to base flow, which drives the potential fish stranding along the reach. Therefore only the second part of hydropeaking waves (Figure 5.1), i.e. the transition from steady peak to steady base flow conditions, is shown in the results, although numerical simulations have been performed for all the hydropeaking events in Figure 5.1.

5.1.2.1 Spatial distribution of flow depth, velocity and rate of change

The numerical simulations compute flow depth and velocity for each cell of the computational domain. As illustrative example, Figure 5.3A shows the spatial distributions of the flow velocity at base and peak flow stages of dewatering pattern A (Figure 5.1) for three different morphologies. In particular, according to the nomenclature introduced in previous chapter (Section 4.2.3), the depicted morphologies correspond to flat bed (No. 1, $W/W_0 = 1$), alternate bars (No. 3, $W/W_0 = 2$) and braiding network (No. 5, $W/W_0 = 6.66$). Similarly, Figure 5.3B shows the water depth distributions for the same aforementioned configurations.

Quantitative insights on the reach-scale distributions of the hydraulic variables (flow depth and velocity) are given by means of box and whiskers plots in Figures 5.4 and 5.5. For the sake of brevity, analogously to previous figures, only dewatering pattern

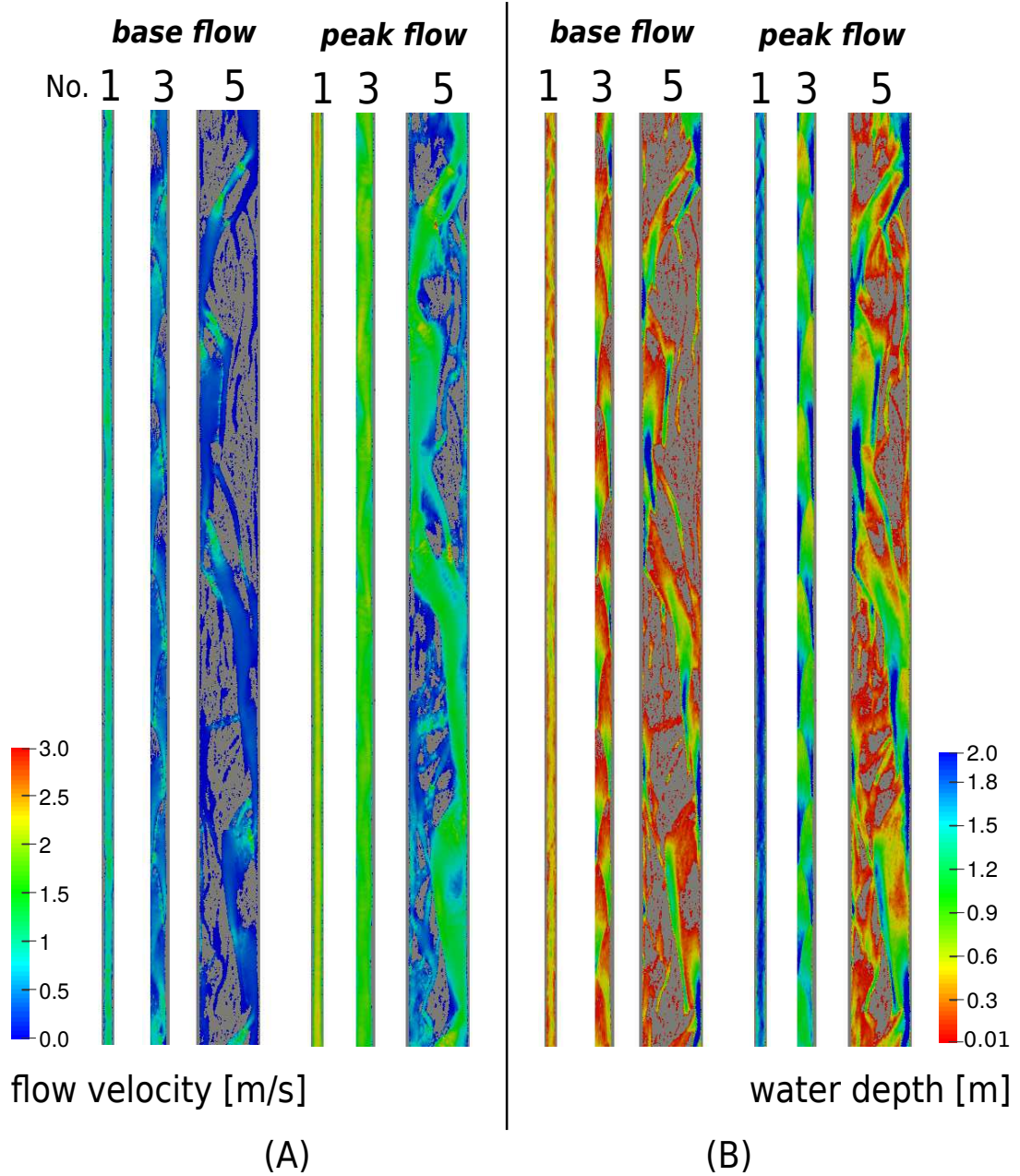


FIGURE 5.3: Flow velocity (A) and water depth (B) distributions at base ($Q_{base} = 5 \text{ m}^3/\text{s}$) and peak ($Q_{peak} = 50 \text{ m}^3/\text{s}$) flow stage of the dewatering pattern A. Morphologies 1, 3, and 5 correspond to flat bed ($W/W_0 = 1$), alternate bars ($W/W_0 = 2$) and braiding network ($W/W_0 = 6.66$), respectively.

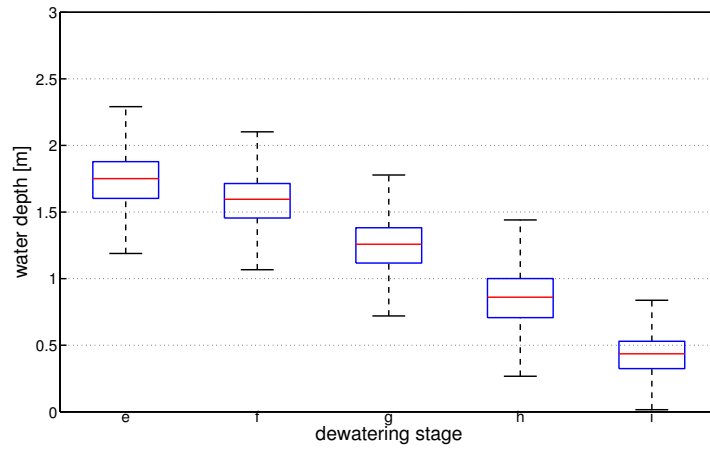
A for morphologies 1,3 and 5 are depicted. The largest variation of water depth, when passing from peak to base flow, occurs in case of flat bed configuration (Figure 5.4A), while the braiding network (Figure 5.4C) shows the greatest water depth variability (i.e. box extension) together with a significant resilience to sudden discharge variation.

Similar behaviours are noticeable also for longitudinal flow velocity distributions in Figure 5.5. A sensible reduction of flow velocity median values constantly occurs when moving from narrow, flat morphologies (No. 1, Figure 5.5A) to wider, braiding patterns (No. 5, Figure 5.5C). It is worth remarking that the aforementioned flow depth and velocity distributions illustrate the transient state between peak and base flow conditions, with the same hydro-morphological configurations of previous chapter. Therefore please note that results and implications on peak-to-base variations have been already discussed in Sections 4.3 and 4.4.

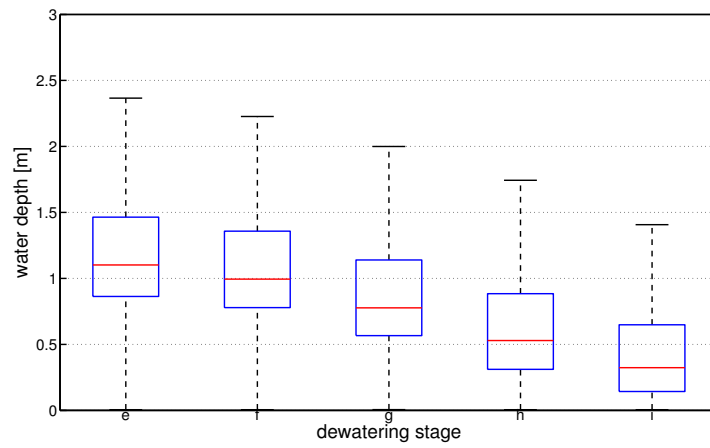
The estimation of the dewatering rate is performed in four intervals during and after the discharge falling limb. In particular the water rate of change is calculated between dewatering stages *e-f*, *f-g*, *g-h* and *h-i* (Figure 5.1). Figure 5.6 shows the distributions of the dewatering rate for same configurations of the above figures during the dewatering process. The greatest variations and magnitudes are those associated with the flat bed case (Figure 5.6A), underlining the small resilience to hydrodynamic variation of such configuration. The maximum median value passes from about 260 *cm/h* for morphology 1 (A), to 150 *cm/h* for alternate bars (B), to less than 50 *cm/h* for the braiding system (C). All the maximum values of dewatering rate, evaluated over all the computational domain, occur within the *g-h* interval, hence in the final tail of the inlet discharge wave, reflecting the inherent unsteadiness of the phenomenon. The travelling time of the negative hydraulic wave along the entire domain ranges between 3 to 10 minutes, according to the different hydro-morphological configurations. Therefore, the inlet maximum dewatering rate, which occurs in the middle point of the falling limb (dewatering interval *f-g*), reaches the outlet boundaries within 10 minutes: such delay causes the maximum dewatering rate at reach-scale being shifted in time at interval *g-h*.

5.1.2.2 Longitudinal distribution of wetted area variation and maximum dewatering rate

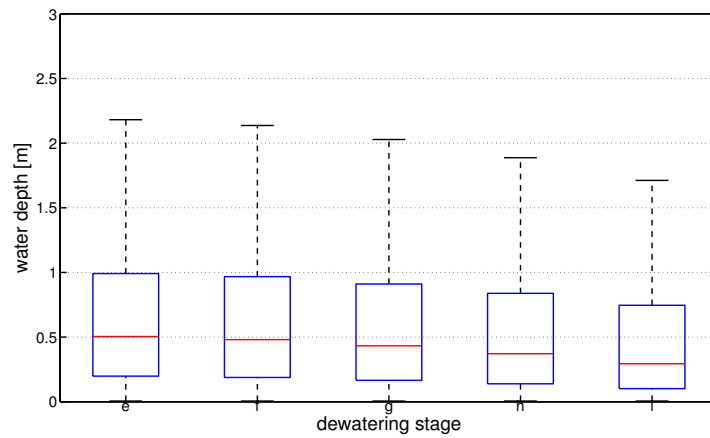
Results can be visualized at local scale plotting the considered ERHPs for each subarea of the domain, as mentioned in Section 5.1.1.2. Similarly to previous section, for the sake of readability only three of the six investigated morphologies are shown in the following plot. In particular, we focus on the simplest bed pattern (flat bed, No. 1), the alternate



(A) Morphology 1 ($W/W_0 = 1$), flat bed.

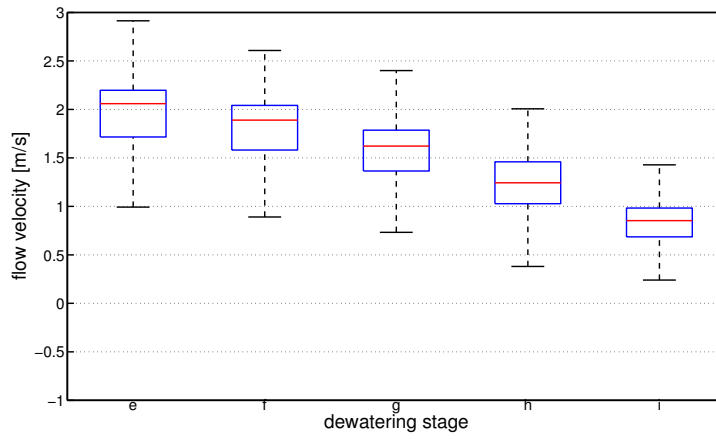


(B) Morphology 3 ($W/W_0 = 2$), alternate bars.

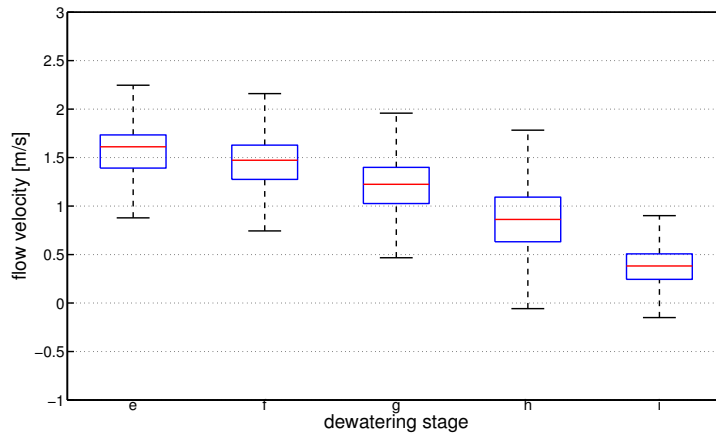


(C) Morphology 5 ($W/W_0 = 6.66$), braiding network.

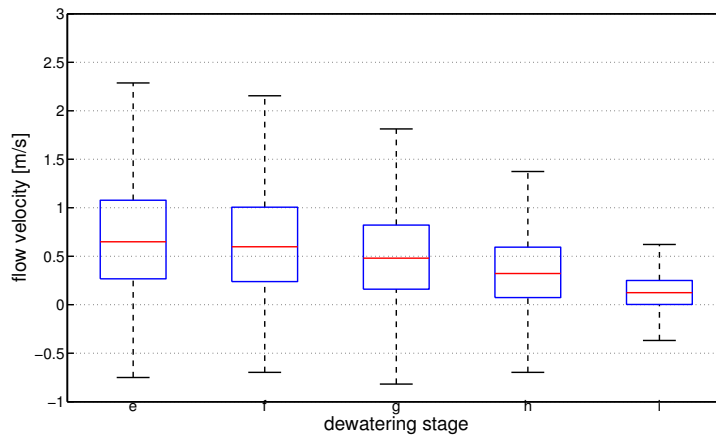
FIGURE 5.4: Box and whiskers plot of water depth distributions during dewatering pattern A (from 50 to 5 m^3/s) for three different morphologies.



(A) Morphology 1, flat bed.

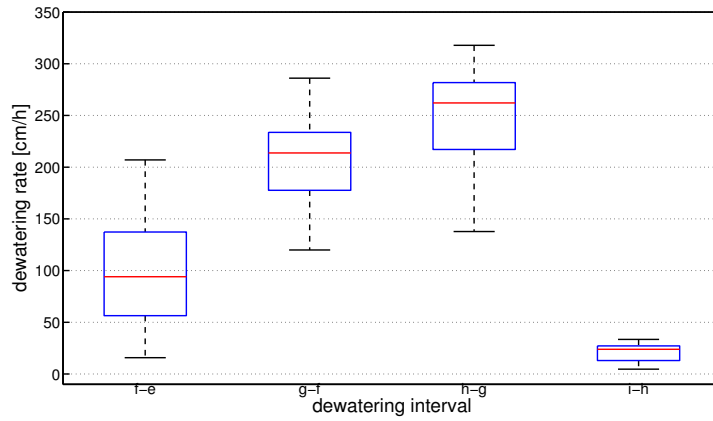


(B) Morphology 3, alternate bars.

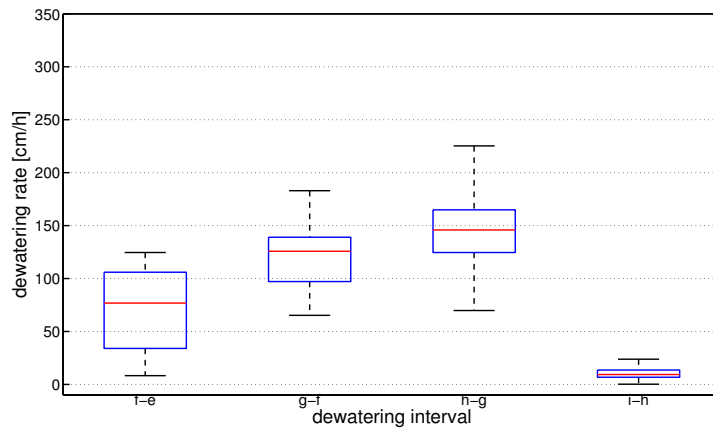


(C) Morphology 5, braiding network.

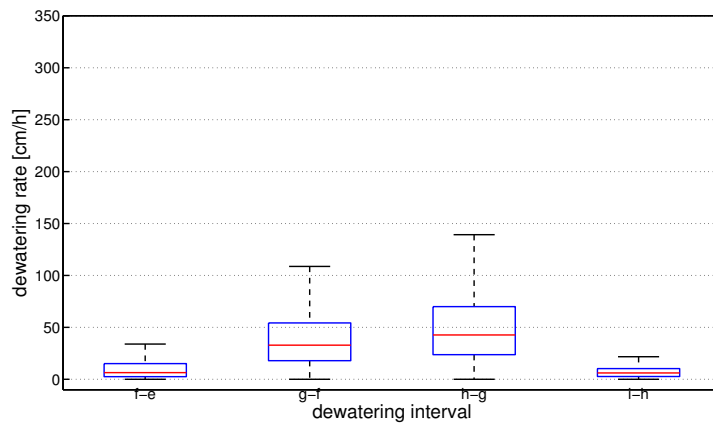
FIGURE 5.5: Box and whiskers plot of longitudinal flow velocity distributions during dewatering pattern A (from 50 to 5 m^3/s) for three different morphologies.



(A) Morphology 1, flat bed.

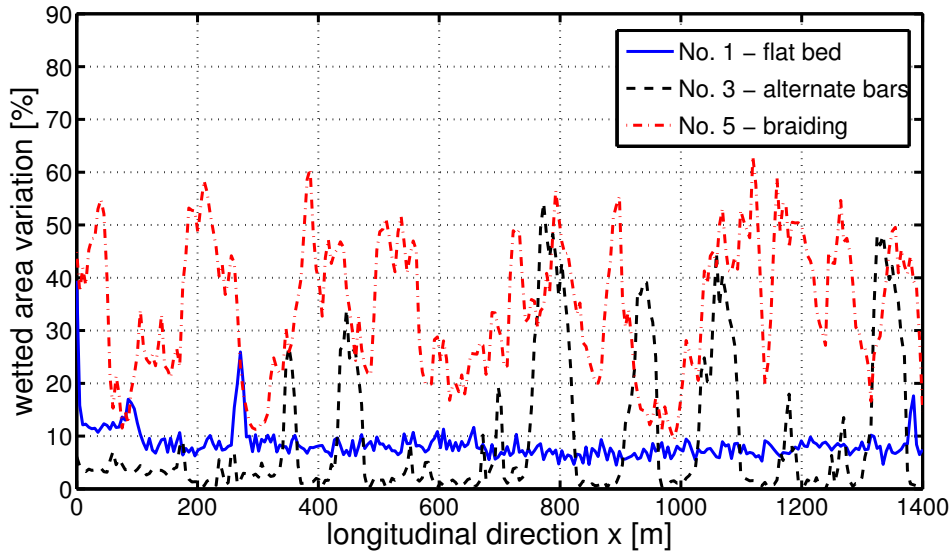


(B) Morphology 3, alternate bars.

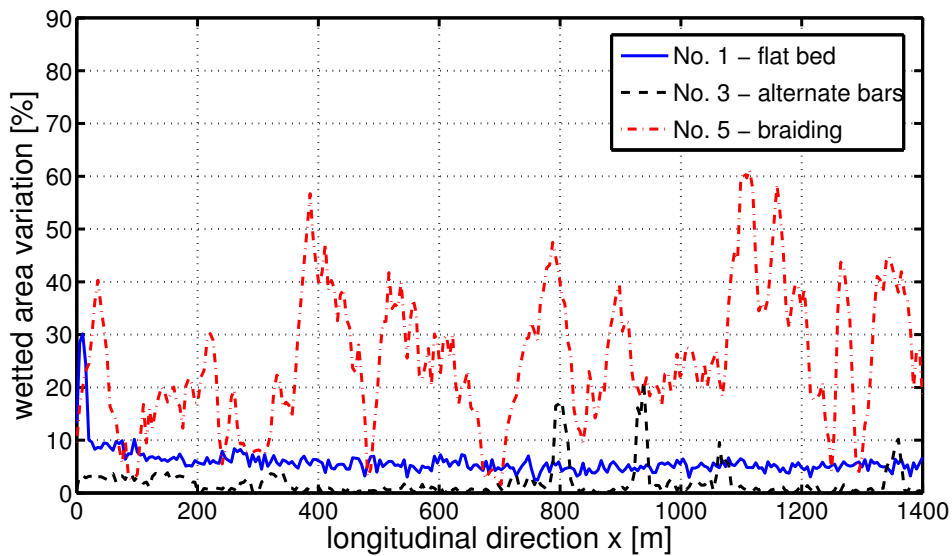


(C) Morphology 5, braiding network.

FIGURE 5.6: Box and whiskers plot of dewatering rate distributions during dewatering pattern A (from 50 to 5 m^3/s) for three different morphologies.



(A) Dewatering pattern A ($Q_{peak}/Q_{base} = 10$).



(B) Dewatering pattern C ($Q_{peak}/Q_{base} = 3.25$).

FIGURE 5.7: Wetted area variation along longitudinal direction x for three different morphological configurations: flat bed (No. 1), alternate bars (No. 3) and braiding network (No. 5). Panels A and B show the dewatering pattern A ($Q_{peak}/Q_{base} = 10$) and C ($Q_{peak}/Q_{base} = 3.25$), respectively.

bars (No. 3) and the braiding system (No. 5). For the same reason above, the most and least intense dewatering pattern (A and C respectively) are compared in this section.

Figure 5.7 shows the longitudinal distribution of the wetted area variation for three different morphologies (1, 3 and 5) during dewatering pattern A (panel A) and C (panel B). As already underlined in the previous chapter, wetted area variation increases with the channel width, thus with the morphological complexity: braiding pattern (No. 5,

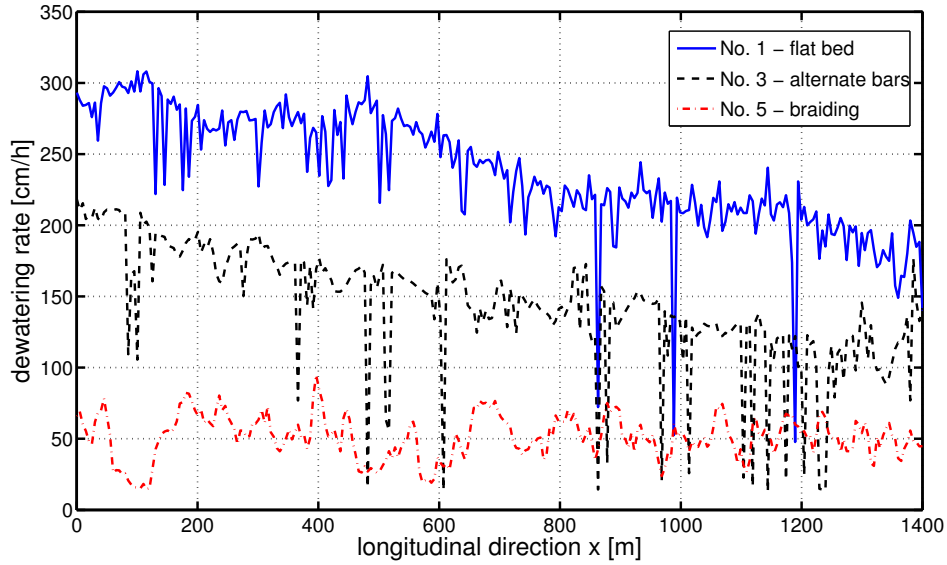
$W/W_0 = 6.66$) shows an overall high variability of the wetted area variation, which fluctuates between 10% and 60%; on the other hand, the smallest variability is associated with the flat bed case (No. 1, $W/W_0 = 1$). For the case of alternate bars (No. 3, $W/W_0 = 2$), the wetted area variation results in sharp, almost equidistant peaks which can reach magnitudes of about 50%: such behaviour arises due to the intrinsic regularity of alternate bars morphology.

When moving from the most intense dewatering pattern A to the mildest one C, by means of increasing the base flow discharge (from 5 to 20 m^3/s), the wetted area variation invariably decreases, as point out in the previous chapter. The reduction is particularly noticeable for the alternate bars pattern, reflecting the progressive overtopping of the alternate bars when increasing the base flow.

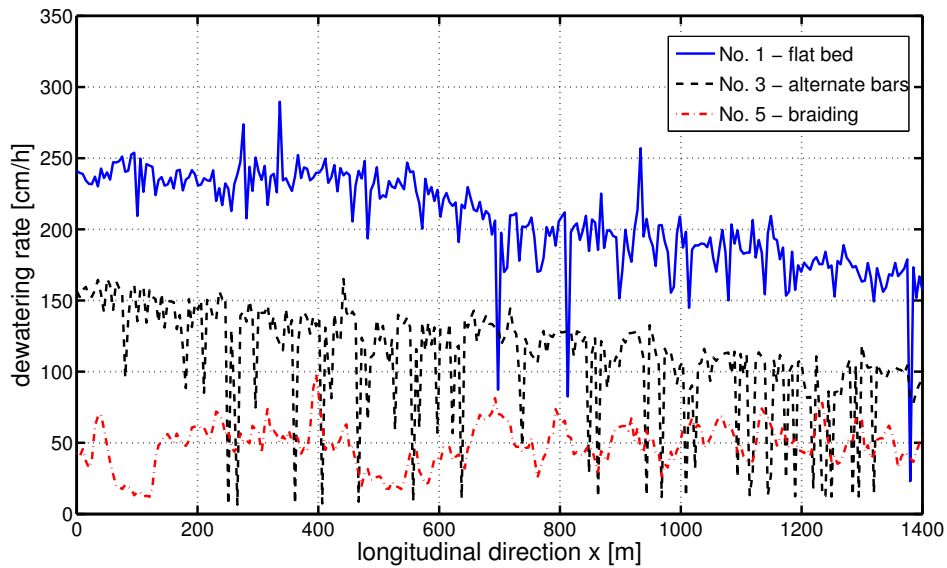
Figure 5.8 shows the longitudinal distribution of the maximum dewatering rate for three different morphologies (1, 3 and 5) during dewatering pattern A (panel A) and C (panel B). In both dewatering patterns the dewatering rate is generally maximum for the flat bed case (No. 1) and minimum for the braiding case (No. 5), with intermediate values for the alternate bars pattern (No. 3). The spikes shown in some subareas, particularly for morphologies 1 and 3, occur when locally little area is dried: in such cases the median value of dewatering rate is calculated among few computational cells (or even on a single cell) hence the median tends invariably to the very local values of dewatering rate.

Comparing panel A and B of Figure 5.8, it can be highlighted that the maximum rate of change decreases when increasing the base flow (i.e. moving from pattern A to C) but with different magnitudes: flat bed and alternate bars experience a sensible reduction while little variations can be found for the braiding pattern, remarking the high resilience of complex morphologies.

It is worth noting how the maximum dewatering rate damps when moving downstream of the channel, for all the cases but the braiding network. In particular damping of the maximum rate is caused by the hydraulic wave smoothing when moving downstream and it is evident in case of narrow channel and small morphological variability (No. 1, flat bed). The resilience to rapid hydraulic variations by the braiding network (No. 5) can be observed in both panel A and B, having the maximum rate of change constantly fluctuating among 50 and 100 cm/h , whatever accounting for upstream or downstream part (no longitudinal damping) or considering different dewatering pattern (panel A or B).



(A) Dewatering pattern A ($Q_{peak}/Q_{base} = 10$).



(B) Dewatering pattern C ($Q_{peak}/Q_{base} = 3.25$).

FIGURE 5.8: Maximum dewatering rate along longitudinal direction x for three different morphological configurations: flat bed (No. 1), alternate bars (No. 3) and braiding network (No. 5). Panel A and B shows the dewatering pattern A ($Q_{peak}/Q_{base} = 10$) and C ($Q_{peak}/Q_{base} = 3.25$), respectively.

5.1.2.3 Tradeoffs between wetted area variation and dewatering rate

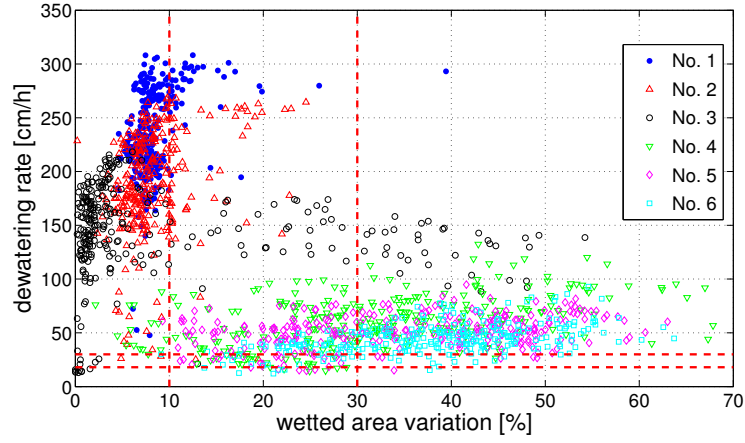
The local values (i.e. for each subarea) of wetted area variation and maximum dewatering rate are jointly shown in Figure 5.9, as proposed in Section 5.1.1.2 (Figure 5.2). In particular, different panels of Figure 5.9 refers to the different dewatering scenarios A, B and C, respectively. In each scatter plot series refer to the different morphologies (Table 4.1), from flat bed (No. 1) to braiding pattern (No. 6). The chosen thresholds (Section 5.1.1.2), from Swiss criteria (Baumann *et al.*, 2012), are depicted in red dashed lines.

All the dewatering patterns (panel A, B and C of Figure 5.9) show common features in point displacement: clouds of points referring to the first two morphologies (1 and 2) invariably lay in the left-top part of the space, i.e. having high values ($> 150 \text{ cm/h}$) of dewatering rate with small values of wetted area variation ($< 20\%$). Moreover, clouds referring to complex morphologies (4, 5 and 6) are clearly separated from the aforementioned ones and are spread in horizontal direction (i.e. large range of area variation) with reduced dewatering rate ($< 100 \text{ cm/h}$). The alternate bars pattern (No. 3) shows a particular behaviour: its cloud has intermediate values of dewatering rate (between morphologies 1, 2 and 4,5,6), but the horizontal spreading is non-homogeneous, with large part of points having very small wetted area variation.

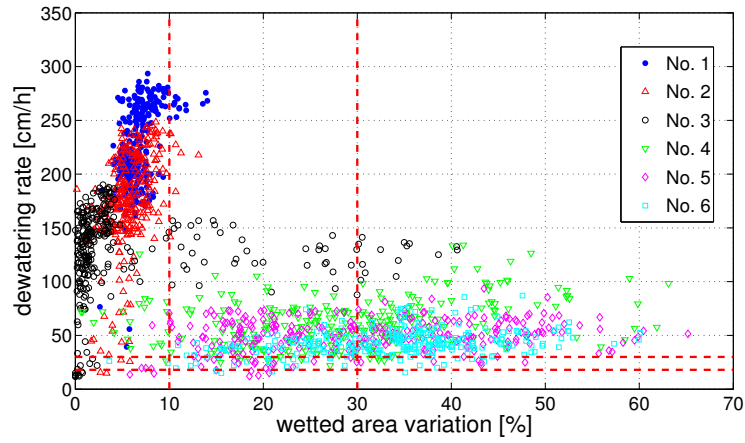
Comparing the clouds displacement among the different patterns (panel A, B and C of Figure 5.9) it is also possible to underline some particular trends: varying the dewatering pattern (from A to C), i.e. increasing the base flow, results in a mild reduction of dewatering rate values for morphologies 1, 2 and 3, as also shown in Figure 5.8. Moreover, always moving from pattern A to C, wetted area variation mildly reduces for all the morphologies.

The results in the space of parameters of Figure 5.9 can be then classified according to the reference space of Figure 5.2, built on the aforementioned Swiss criteria. The resulting class percentages are shown in the stacked column chart of Figure 5.10. For the sake of clarity, Figure 5.10 shows the percentages of subareas (i.e. points in Figure 5.9) laying in the different stranding risk classes plotted in Figure 5.2, for all the morphological (column 1 to 6) scenarios and all the dewatering pattern (panel A to C). The same colours are used in Figures 5.2 and 5.10 for the sake of readability.

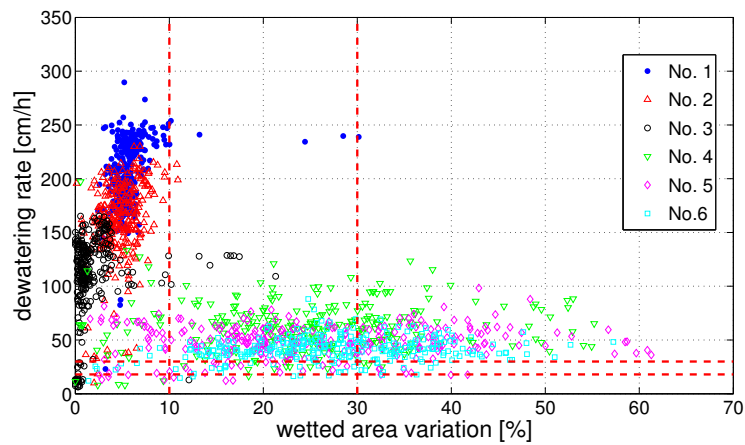
According to the joint criteria proposed in Section 5.1.1.2, the first three morphologies (1, 2 and 3) show almost no stranding risk. For such configurations the high percentage of areas in *very good* or *good* status is mainly due to the small values of wetted area variation (see Figure 5.9). On the contrary, when reaching morphology 4 (wandering pattern), areas in *moderate-bad* status (red colour) considerably increase, with values



(A) Dewatering pattern A ($Q_{peak}/Q_{base} = 10$).



(B) Dewatering pattern B ($Q_{peak}/Q_{base} = 5.5$).



(C) Dewatering pattern C ($Q_{peak}/Q_{base} = 3.25$).

FIGURE 5.9: Maximum dewatering rate vs. wetted area variation for the six investigated morphologies (from No. 1 to No. 6). Each panel corresponds to a different dewatering pattern (A, B and C).

between 30 and 70% according to the different hydro-morphological configurations. For the complex morphologies (4, 5 and 6) it is worth noting how stranding risk invariably increases (red class) when passing from 4 (wandering pattern) to 6 (braiding network). However such increment rate and the magnitude of red class percentage both depend on the dewatering pattern and decrease when increasing the base flow, i.e. from panel A to C of Figure 5.10.

5.1.2.4 Subarea length sensitivity analysis

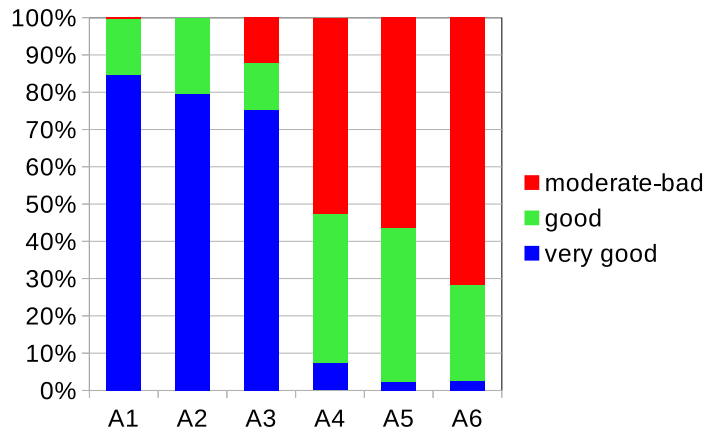
We test the robustness of the outcomes presented in the previous section when varying the extension of the local scale (i.e. the length of the considered subareas), as introduced in Section 5.1.1.2. The goal is to verify to which extent the trends highlighted in Figure 5.9 are driven by the morphological characteristics of each configuration rather than the choice of the length of each local transverse slice. Figures 5.11, 5.12 and 5.13 show the same stranding risk classification of Figure 5.10 varying the subarea lengths, for dewatering pattern A, B and C, respectively.

For all the dewatering patterns (Figures 5.11, 5.12 and 5.13) the classification shows similar behaviours, with little or moderate variations with respect to the percentages obtained with 5 *m*-long subareas (Figure 5.10). In particular, when choosing lengths of 10 *m* (panels A) and 20 *m* (panels B), very little variations (less than 5%) are found for all the three dewatering patterns. Discrepancies of less than 10% are instead found for subarea lengths of 50 *m* and about 15% when choosing slice lengths of 100 *m*.

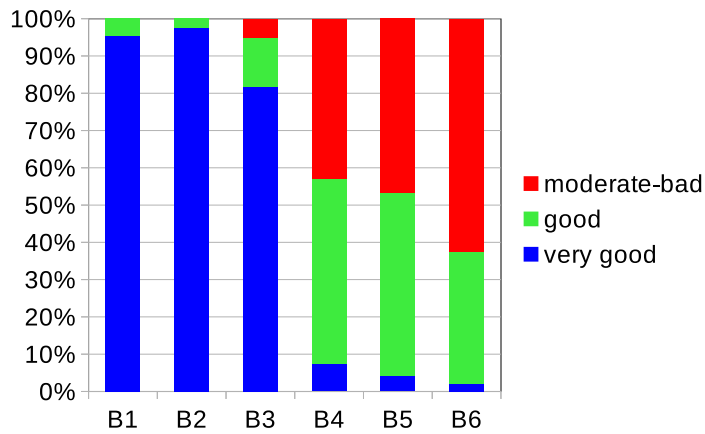
5.1.3 Discussion

The analysis proposed in this chapter extends and integrates the outcomes of the previous one (Section 4.4) in relation to the eco-hydraulic asset of fish stranding risk. In particular, the tradeoffs between two Ecologically Relevant Hydraulic Parameters linked to fish stranding, namely dewatering rate and wetted area variation, have been investigated. The global statistics of the flow depth and velocity evaluated during the dewatering process (Figure 5.4 and 5.5, respectively) remark the resilience of configurations with higher morphological complexity; such resilience is particularly evident when considering the reduction of dewatering rate for the braiding morphology in Figure 5.6C.

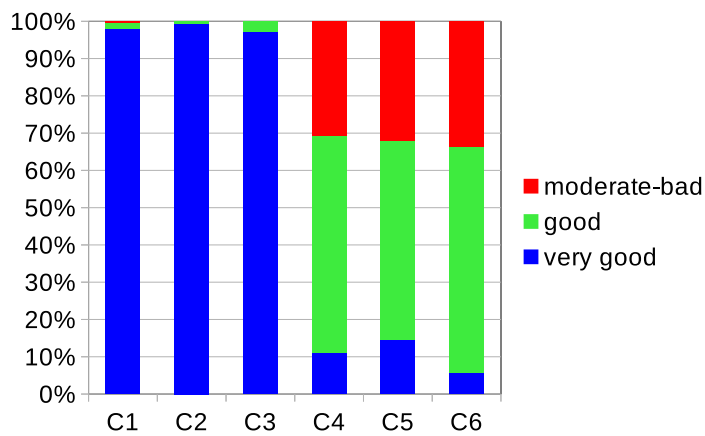
The different behaviours and tradeoffs highlighted so far (Section 5.1.2) can be jointly reviewed and discussed by means of Figure 5.14: it shows the mean displacement of all the 18 investigated hydro-morphological configurations in the space of the considered Ecologically Relevant Hydraulic Parameters. In particular each symbol of Figure 5.14 represents



(A) Dewatering pattern A ($Q_{peak}/Q_{base} = 10$).



(B) Dewatering pattern B ($Q_{peak}/Q_{base} = 5.5$).



(C) Dewatering pattern C ($Q_{peak}/Q_{base} = 3.25$).

FIGURE 5.10: Stacked column chart of the stranding risk for the six considered morphologies (column 1 to 6) and the three dewatering pattern (panel A to C).

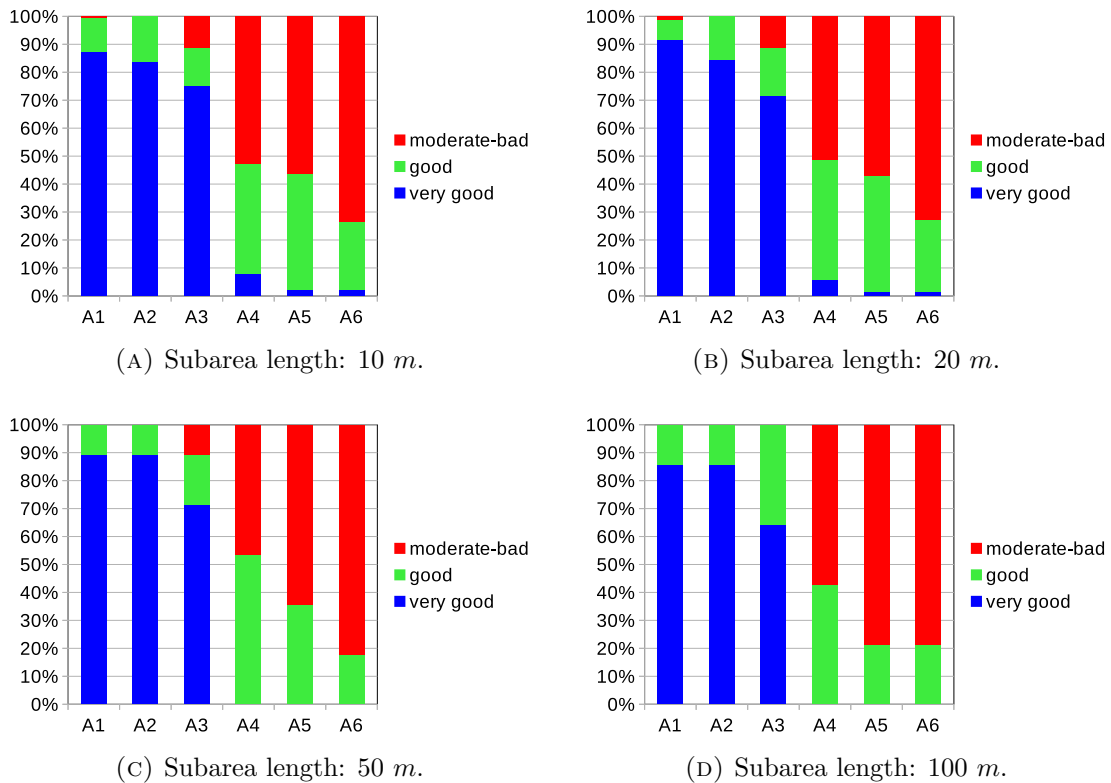


FIGURE 5.11: Stacked column chart of the stranding risk for the six considered morphologies (column 1 to 6) and dewatering pattern A ($Q_{peak}/Q_{base} = 10$). Different panels (A to D) refer to different choice of subarea (i.e. transverse slice) length.

the geometric mean of each different cloud of points depicted in Figure 5.9. The symbol shape identifies the dewatering pattern: triangle, circle and square represent pattern A ($Q_{peak}/Q_{base} = 10$), B ($Q_{peak}/Q_{base} = 5.5$) and C ($Q_{peak}/Q_{base} = 3.25$), respectively. Instead the six different colours refer to the six considered morphologies (see Table 4.1).

Reviewing the evidences of Section 5.1.2 with the support of Figure 5.14, the different behaviours of the six investigated morphologies can be grouped into two main ecohydraulic responses. The first group contains the first three morphologies, namely flat bed (No. 1, $W/W_0 = 1$) and alternate bars (No. 2, $W/W_0 = 1.33$ and No. 3, $W/W_0 = 2$), respectively. They are characterized by relatively narrow and single thread channels with small percentage of dried areas for all the investigated dewatering patterns. The variation of wetted area is small (left side in Figure 5.14) because of the little morphological diversity, while the maximum dewatering rate for such morphologies is always relatively high ($> 100 \text{ cm/h}$). This group is sensitive to different hydropeaking intensities and different hydrodynamic configurations: hence maximum dewatering rates decrease when increasing the base flow (curved continuous line trajectory in Figure 5.14).

The second group includes morphology 4 (wandering pattern, $W/W_0 = 5.33$) and the

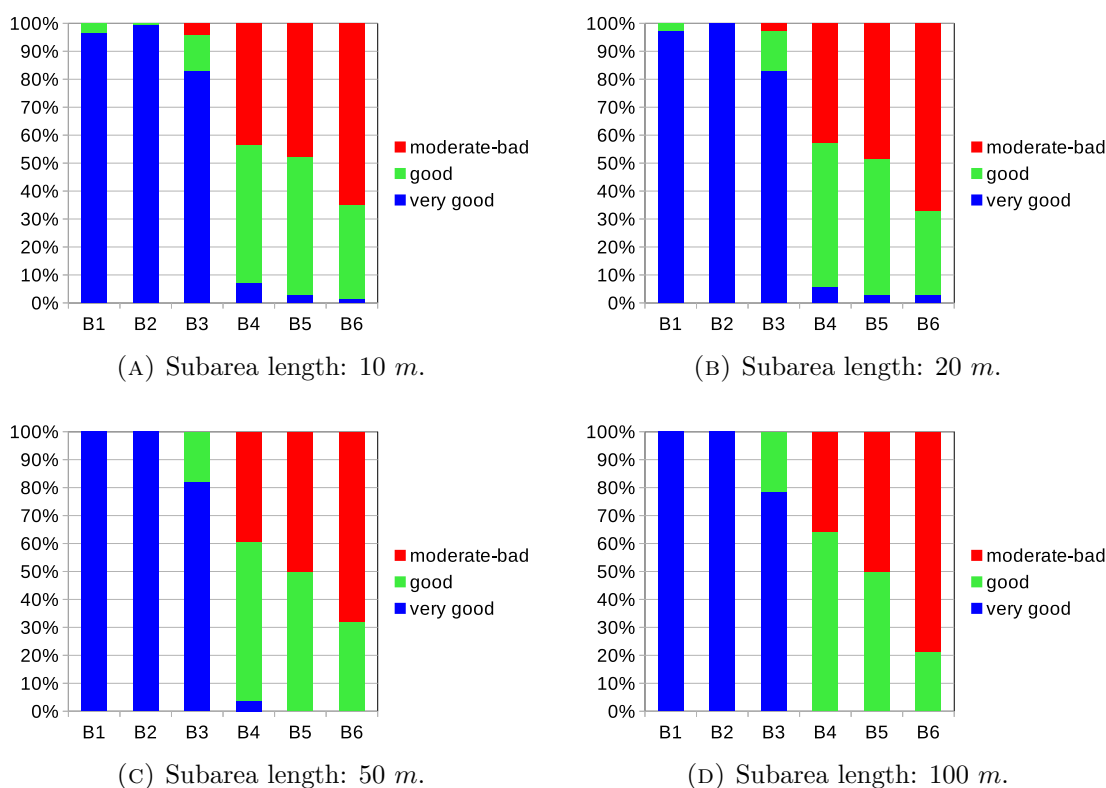


FIGURE 5.12: Stacked column chart of the stranding risk for the six considered morphologies (column 1 to 6) and dewatering pattern B ($Q_{peak}/Q_{base} = 5.5$). Different panels (A to D) refer to different choice of subarea (i.e. transverse slice) length.

two braiding patterns 5 ($W/W_0 = 6.66$) and 6 ($W/W_0 = 10$). In the space of Figure 5.14 this group is clearly separated from the previous one. Such morphologies are characterized by large channel widths, with a pronounced diversity of bars which generates several secondary channels (e.g. Figure 5.3B). The variety of morphological structures results in a more variegate distributions of the bed elevation: because of that, varying the base flow turns into an hydro-morphological interaction with morphological structures at different elevations. As a matter of fact, the base flow increase (from pattern A to C) causes a progressively overtopping of lowest bed structures and results in a sensible reduction of wetted area variation (straight continuous line trajectory in Figure 5.14). The resilience of the second group to hydrodynamic variations, as highlighted in Figure 5.8, can be marked also in Figure 5.14: base flow variations (i.e. from hydropeaking A to C) result in negligible variations of the maximum dewatering rates.

The proposed modeling analysis suggests the possible existence of rather “general” trajectories in the stranding risk parameter space of Figure 5.14; dewatering rate non-linearly decreases when increasing the channel width; similarly, the variation of wetted area is positively related to channel width, i.e. to morphological complexity, as widely

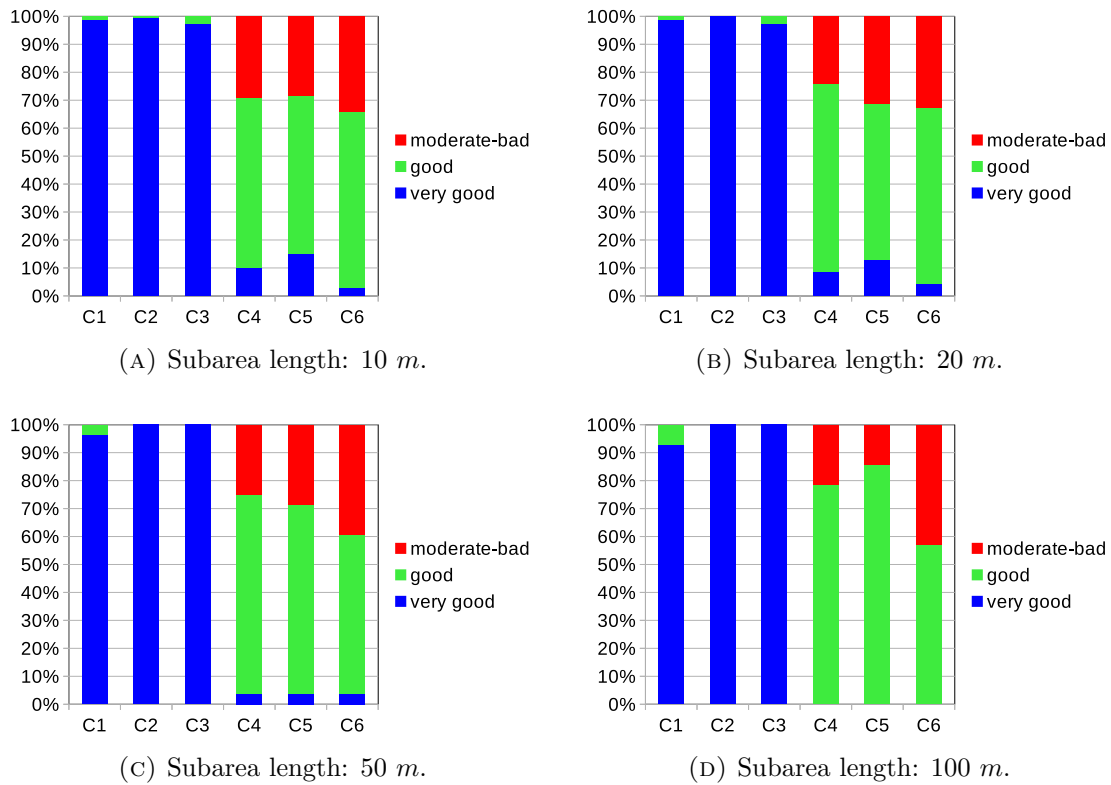


FIGURE 5.13: Stacked column chart of the stranding risk for the six considered morphologies (column 1 to 6) and dewatering pattern C ($Q_{peak}/Q_{base} = 3.25$). Different panels (A to D) refer to different choice of subarea (i.e. transverse slice) length.

discussed in previous chapter. These two concurrent trends are highlighted in Figure 5.14 by the dashed line trajectory. As already remarked in Section 4.4, also in Figure 5.14 alternate bars pattern shows its peculiar behaviour, having little wetted area variations with respect to other configurations.

Figures 5.10 and 5.14 suggest a further consideration: none of the designed three dewatering patterns, which differ for the peak-to-base flow ratio (see Figure 5.1), is able to significantly reduce the potential stranding risk in case of complex morphologies (4, 5 and 6). This fact suggests the benefits of only increasing the base flow might be limited for some morphological configurations, where the bottleneck is the relevant wetted area variation (morphologies 4, 5 and 6 in Figure 5.14). For such cases a different modification of the pattern productions, i.e. a discharge falling limb slowdown, might further smooth maximum dewatering rates and shift the representative points (i.e. the geometric means of Figure 5.14) towards the green-blue region. This option has not been evaluated in the present study, although the proposed approach can be replicated to quantify the tradeoffs of alternative dewatering scenarios.

Another relevant outcome is given by the sensitivity analysis of results presented in

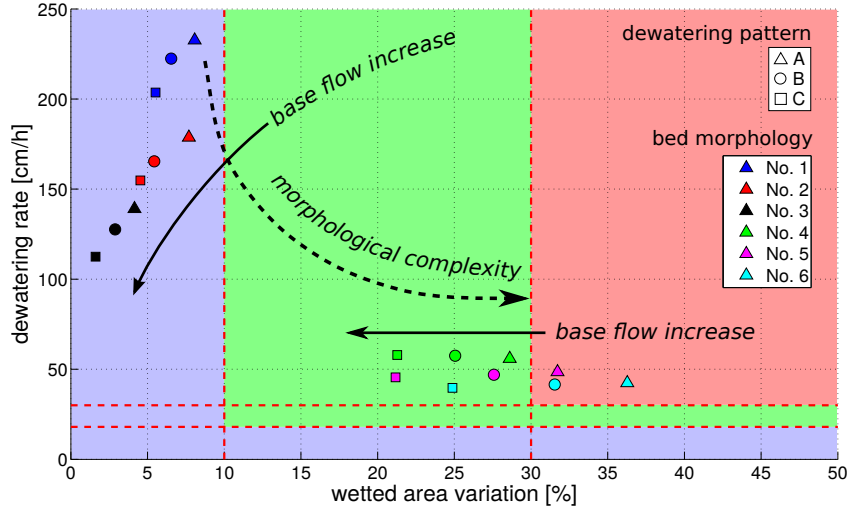


FIGURE 5.14: Maximum dewatering rate vs. wetted area variation for the 18 simulated hydro-morphological configurations. Triangles, circles and squares represent dewatering pattern A, B and C, respectively; colours identify the six investigated morphologies.

Section 5.1.2.4. The local tradeoffs between the considered ERHPs do not markedly depend on the subarea length, with very little discrepancies when such length ranges between 5 and 20 m (compare Figures 5.10, 5.11, 5.11 and 5.11). This suggests two crucial considerations: firstly, the proposed ERHPs analysis effectively measures meso-scale morphological features and not micro-scale localized phenomena. Secondly, such awareness positively supports and indicates that a spatial scale up to 20 m (or even to 50 m) is adequate for practical evaluation of stranding risk.

Finally, it is worth remarking the present study proposed a quantitative modeling of the potential stranding risk purely based on a selection of Ecologically Relevant Hydraulic Parameters. Moreover the quantification given in Figure 5.10 is obviously dependent on the chosen thresholds, but all the remaining considerations have general applicability. In this analysis we deliberately adopted the Swiss criteria for the stranding risk evaluation (Baumann *et al.*, 2012). We then combine the two single criterion for the dewatering rate and the wetted area variation as shown in Figure 5.2. The reviewed classification hence concurrently accounts for the two ERHPs and allow to quantify their tradeoffs with the different morphological patterns. The gap of the eco-hydraulic response between simple (1, 2 and 3) and complex (4, 5 and 6) morphologies is remarked in Figure 5.10, whatever the chosen dewatering pattern. This confirms the transitional morphologies (i.e. from roughly 3 to 4) to be the morphological watershed for the investigated ecological response.

5.2 Dewatering scenario modeling in Lundesokna River

In this section the numerical modeling of hydropeaking in Lundesokna River is presented. In particular the aim is to quantify and locate potential fish stranding areas via a two-dimensional numerical modeling. This is achieved adopting the approaches presented in the previous section, i.e. evaluating and quantifying two Ecologically-Relevant Hydraulic Parameters connected to fish stranding both at reach and local scale. Differently from Chapter 4, where we investigate the tradeoffs between different river morphologies and hydropeaking waves, here the river morphology is given while the inlet hydropeaking wave is changed according to different scenarios.

Being interested in the specific process of fish stranding, the study focuses only on the falling limb of the typical hydropeaking wave, i.e. in the dewatering phase (or *recession phase*). Similarly to the previous section, the investigated Ecologically-Relevant Hydraulic Parameters are the dewatering rate (or *water depth rate of change*) and the variation of wetted area, which are ones of the major abiotic factors influencing fish stranding (e.g. Nagrodski *et al.*, 2012).

Stranding is not equal to mortality (Saltveit *et al.*, 2001), despite it can have lethal or sub-lethal effects on fish (Nagrodski *et al.*, 2012). Therefore in this study we account also for the duration of river bed dry conditions, which influence the mortality rate of stranded fish. In particular, early life stages of fish are the most vulnerable. Egg incubation and embryo development are highly sensible to local environmental alteration while exposure to dry condition can represent an harmful stress (Young *et al.*, 2011) possibly altering their mortality rate (e.g. Casas-Mulet *et al.*, 2014c). In a broader view, duration of bed dry conditions affects also the survival of benthic species (e.g. Richards *et al.*, 2013).

It is worth mentioning that all field and raw data of Lundesokna River have been provided by the Department of Hydraulic and Environmental Engineering of the Norwegian University of Science and Technology-NTNU and the Centre for Environmental Design of Renewable Energy-CEDREN (Norway). If not differently specified, the information on Lundesokna River and its hydraulic system are taken from Casas-Mulet (2014).

5.2.1 Study-site description

Lundesokna River, Sor Trondelag, is located in central Norway (Figure 5.15b). The Lundesokna River is a tributary of the Gaula River, the biggest river in central Norway and one among the best Atlantic salmon fishing rivers in Norway (*Knut Alfredsen, personal communication*). The Lundesokna hydropower system has a total catchment area of 395 km^2 and consists of three regulated reservoirs and three power plants (Figure 5.15a).

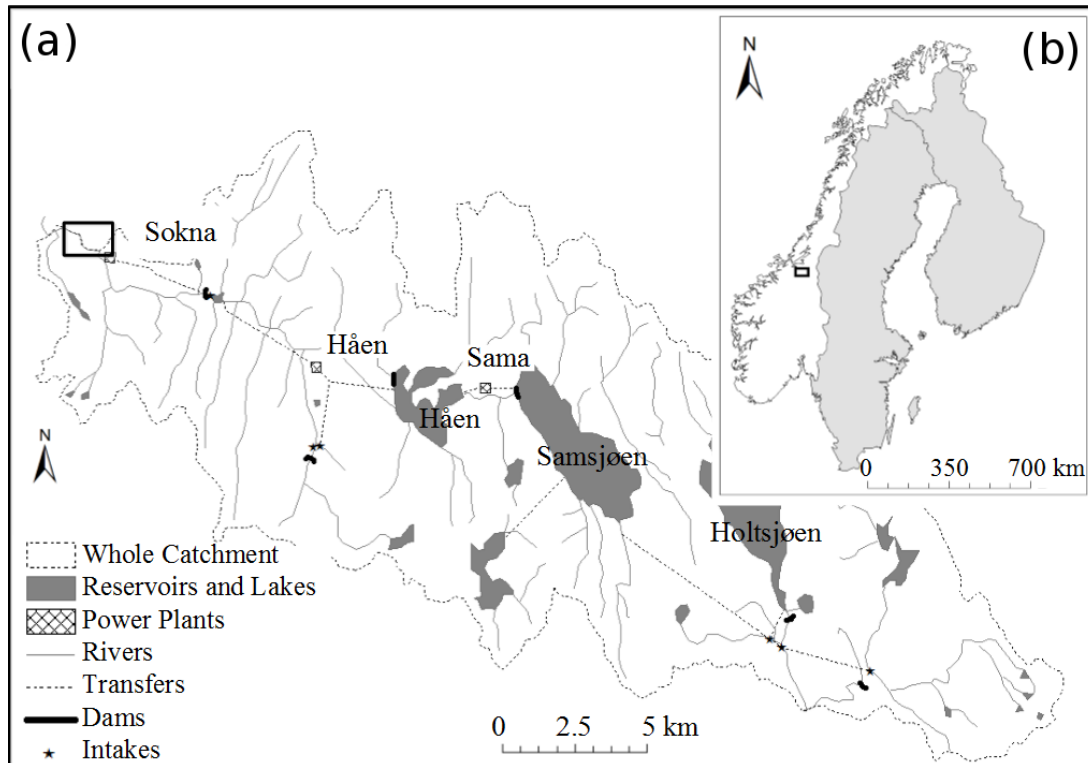


FIGURE 5.15: (a) Illustration of the Lundesokna hydropower system and (b) its location in Norway, from Casas-Mulet *et al.* (2014a).

The installed capacity is about 61 MW with an average production of 278 GWh per year (Casas-Mulet *et al.*, 2014c).

The study reach is about 2 km long, starting immediately downstream the water restitution of the lowermost power plant (Sokna in Figure 5.15a) and ending about 1 km before the confluence with the main Gaula River. The total width ranges between 15 m and 25 m in the considered reach, with a mean longitudinal slope of 0.002 m/m. The reach is a single thread channel with a relatively uniform bed topography in the straight parts, while varying configurations of side bars are present in correspondence of the bends.

The Sokna station operates according to market electricity price fluctuations and the water availability in the reservoirs. The resulting hydropeaking is characterized by abrupt flow fluctuations that typically range from 20 m³/s to 0.45 m³/s in less than 20 minutes (Casas-Mulet *et al.*, 2014c), as shown in Figure 5.16. Energy market price variability results in very irregular hydropower production patterns. The production stops range from few hours to several days, with almost dry river bed during such periods.

Figure 5.17 shows the study reach downstream the Sokna outlet. The study-site of Figure 5.17 is the same already investigated by Casas-Mulet *et al.* (2014a). For this reach a detailed topography description is available (for details refers to Casas-Mulet *et al.*, 2014a).

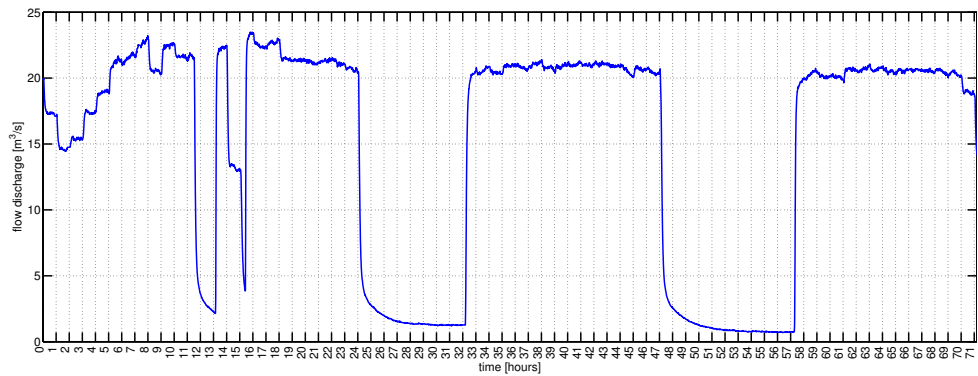


FIGURE 5.16: Example of flow discharge fluctuations in Lundesokna River due to hydropowering. Hydrograph shows the days from 16th (00:00 am) to 18th (11:00 pm) of December 2011.



FIGURE 5.17: Map of the lowermost 2km of Lundesokna River with location of some study-site from Casas-Mulet *et al.* (2014a).

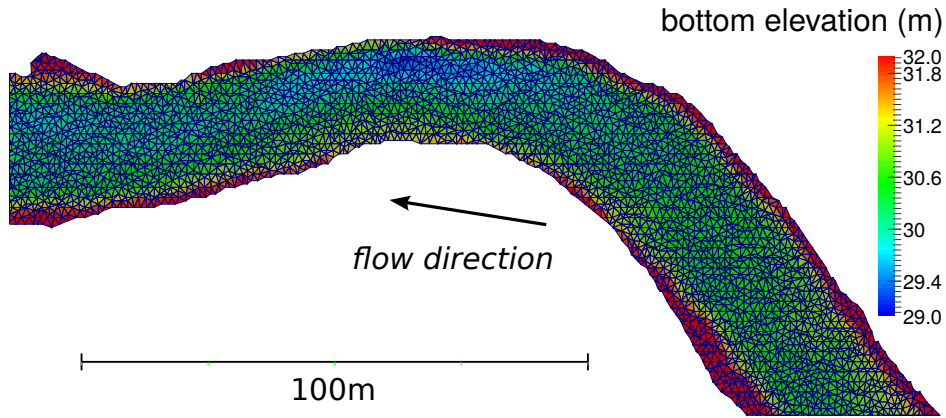


FIGURE 5.18: Sketch of the computational domain in correspondence of the Site 2 of Casas-Mulet *et al.* (2014a).

5.2.2 Model setup

The entire length of the Lundesokna river under consideration is ...Km and is depicted in Figure 5.17. For numerical purposes it is discretized with 63492 triangular cells. The mean cell area is 0.81 m^2 , ranging between a maximum of 1.55 m^2 and a minimum of 0.20 m^2 . The cell elevations have been interpolated linearly from different set of available topographic measures. In particular, the selected sites of Figure 5.17 are scanned at high-resolution, with average sampling point distance between 0.03 m (laser scanner) and 2 m (real-time kinematic gps), as described in Casas-Mulet *et al.* (2014a). The rest of the reach topography is mapped at 40 different cross-sections with a resolution of about 1 m along the transect. The mean longitudinal distance between the surveyed cross-sections is about 50 m . In other to increase the number of topographic measures in some side bars, about one hundred of additional points have been mapped. Figure 5.18 shows a sketch of the computational domain in correspondence of the Site 1 and Site 2.

For the unsteady numerical simulations of different dewatering scenarios (described in Section 5.2.3) the flow discharge is imposed at the upstream boundary condition, while uniform flow is imposed at the downstream boundary of the numerical domain. Hydraulic simulations have been conducted with the non-stationary 2D (x-y) shallow water numerical model described in Chapter 3.

5.2.2.1 Roughness calibration

A collection of water elevation measures has been used for the roughness calibration of the numerical model. In particular four set of measures are available at four different different discharge stages. The water elevation surveys have been conducted for flow discharge of $Q = 0.45 \text{ m}^3/\text{s}$, $10.58 \text{ m}^3/\text{s}$, $16.44 \text{ m}^3/\text{s}$ and $20.63 \text{ m}^3/\text{s}$. For each stage (from lowest

Mean	0.12	Standard deviation	0.088
25th percentile	0.042	75th percentile	0.16
Minimum	0.00	Maximum	0.37

TABLE 5.3: Roughness calibration: descriptive statistics (all in m) for the water level absolute error.

to highest) 24, 18, 25 and 28 water level sampling points are available along the reach, respectively. It is worth noting that the lowest and highest values of flow discharge closely represent the full-production and zero-production stages imposed by the Sokna outlet.

Aiming at perform a series of unsteady simulations, the roughness has to be jointly calibrated for all the available discharges, i.e. an unique roughness value for varying flow discharge is sought. Hence the calibration is performed evaluating the error between simulated and measured water level for all the available data (i.e. 95 measured points). We set about 20 different configurations for the roughness closure using both Strickler closure (Equation 3.3), with coefficients ranging between $20 m^{1/3}s^{-1}$ and $35 m^{1/3}s^{-1}$, and also Chezy closure (Equation 3.4), with mean sediment diameter ranging between $0.02 m$ and $0.1 m$. Such diameter values roughly corresponds to the 50th and the 95th percentile of the actual sediment size distribution. We then perform 20×4 steady simulations, one for each configuration and discharge stage. Comparing the residual sum of squares (RSS) for each of the 20 roughness configurations, the best one (minimum RSS) results to be with Strickler closure and coefficient $K_s = 25 m^{1/3}s^{-1}$. The selected roughness configuration gives, among all the four discharge stages, a mean absolute error of $0.12 m$ and a standard deviation of $0.088 m$; further descriptive statistics of the absolute error are given in Table 5.3.

The calibrated roughness configuration is given also by means of linear regression analysis. In particular the Figure 5.19 shows the simulated water levels against the measured ones for chosen roughness coefficient, together with the linear regression of the two quantities (red continuous line). The linear regression analysis returns a slope of $s = 0.9846$, with 95% interval of confidence of 0.97000-0.9991. The coefficient of determination R^2 is equal to 0.9948.

5.2.3 Dewatering scenarios

A series of different dewatering scenarios have been designed in order to simulate and quantify the stranding risk areas. The different dewatering sequences are sketched starting from the actual release options of the Sokna hydropower plant. In particular, the Sokna hydropower plant has an optimal intake capacity of $20 m^3/s$ while the minimum

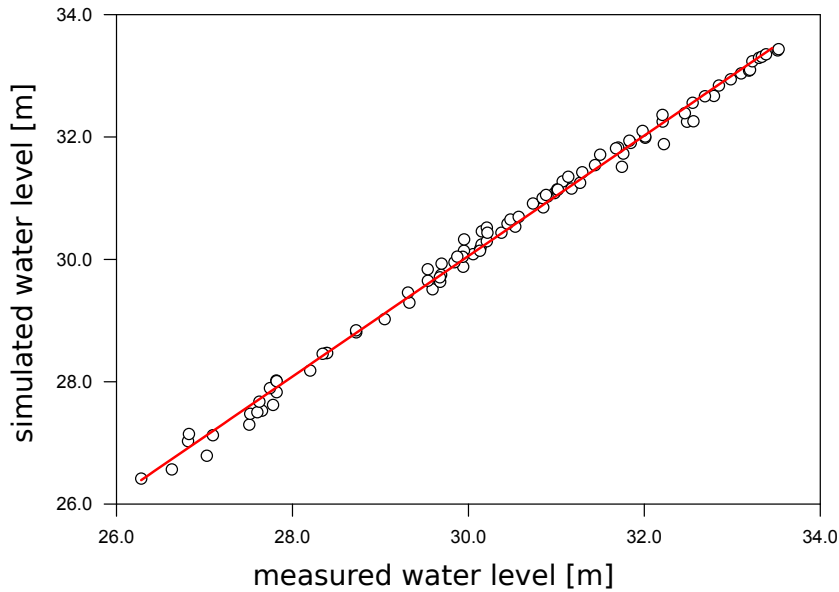


FIGURE 5.19: Roughness calibration: simulated against measured water levels; red continuous line represents the linear regression.

production flow is $8 \text{ m}^3/\text{s}$. Below such minimum flow the hydropower system might experience poor efficiency and cavitation problems (Casas-Mulet *et al.*, 2014b). A representative base flow of $0.5 \text{ m}^3/\text{s}$ (Knut Alfredsen, *personal communication*) is set for the no production option. Sokna plant has an additional operational option which allows to bypass up to $3.5 \text{ m}^3/\text{s}$.

Currently the typical dewatering scenario is that having a sudden discharge decrease from $20 \text{ m}^3/\text{s}$ to $0.5 \text{ m}^3/\text{s}$ in about 15 minutes (see Figure 5.16). Therefore such configuration represents the Scenario 0, that we want to compare with other possible dewatering procedures.

We design six possible alternatives (S1-S6) to the current scenario S0, as shown in Figure 5.20. The involved discharge stages are given by the hydropower plant operation options, while we chose arbitrarily a set of suitable durations of such operations. Similarly to the current zero scenario S0, the duration of all the falling limbs in scenarios S1, S2 and S6 is fixed to 15 minutes each. Moreover, for these scenarios the steady limbs (constant flow discharge) last 30 minutes each.

In Scenario S1 the power plant decreases the production until the minimum ($8 \text{ m}^3/\text{s}$), and subsequently stops the production after 30 minutes. Scenario S2 differs from the previous for an additional discharge stage step: after stopping the production, the discharge is kept constant at the maximum value allowed by the bypass ($3.5 \text{ m}^3/\text{s}$) before falling to the base flow stage. In scenarios S3, S4 and S5 discharge firstly falls from the production stage ($20 \text{ m}^3/\text{s}$) to the maximum bypass stage ($3.5 \text{ m}^3/\text{s}$) in 15 minutes, then

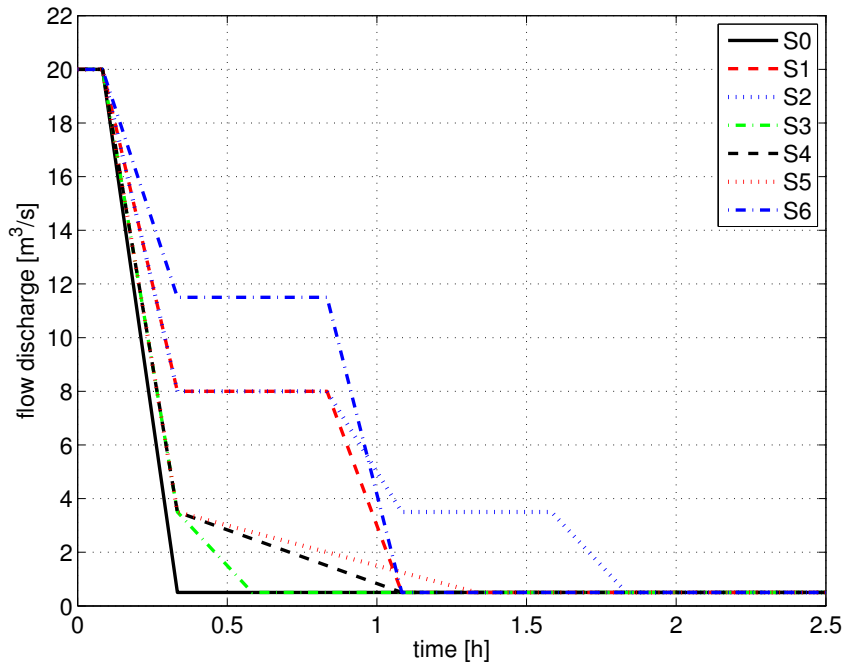


FIGURE 5.20: Dewatering scenarios for stranding risk modeling in Lundesokna River.

it is reduced down to the base flow ($0.5 \text{ m}^3/\text{s}$) in 15, 45, and 60 minutes respectively. Finally, in Scenario S6 we simulate a partial reduction of the production at $11.5 \text{ m}^3/\text{s}$, then the production is stopped and discharge falls to the base flow stage.

It is worth underlining that all the simulations start from and end to the same steady conditions characterized by flow discharge of $20 \text{ m}^3/\text{s}$ and $0.5 \text{ m}^3/\text{s}$, respectively. For the sake of clarity, all the dewatering operations start at time $t = 5 \text{ min}$ and the final configurations refer to $t = 3.5 \text{ h}$, when steady hydraulic configuration is achieved for all the scenarios.

5.2.4 Results

The results of dewatering simulations are presented in this section emphasizing different aspects of the fish stranding phenomena. Firstly, reach-scale statistics (i.e. on the entire domain) are given as a primary characterization of the differences among the different scenarios (Section 5.2.4.1). Then the focus is switched to the local scale, and the spatial distribution of simulations results are shown, with a particular attention to the sites 1,2 and 3 identified in Figure 5.17). In particular in Section 5.2.4.2 the total variation of wetted area is discussed, while Section 5.2.4.3 accounts for the differences in dewatering rate for the simulated scenarios. Finally, an analysis of the duration of dry conditions is shown in Section 5.2.4.4.

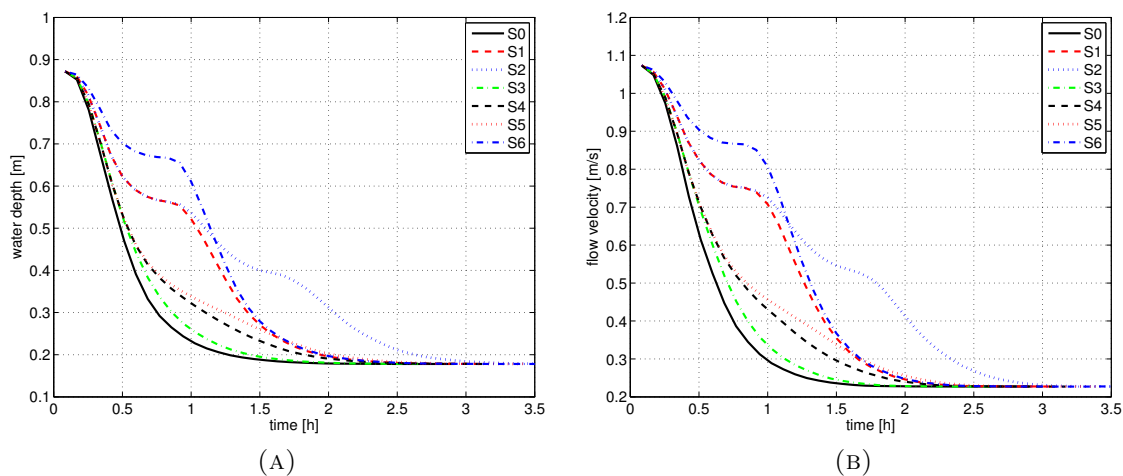


FIGURE 5.21: Reach-scale statistics: water depth (A) and flow velocity (B) median values during dewatering phase for each simulated scenario.

5.2.4.1 Reach-scale statistics

Numerical simulations return the local value of water depth and flow velocity for each computational cell. In this section the reach-scale statistics of the hydraulic variable distributions are shown. It is worth underline that hereinafter with *flow velocity* we refer to the magnitude of the velocity vector having two components in the plane (x-y). Moreover, the statistics are computed on the wet cells every 5 minutes for the entire duration of the simulations (3.5 hours) and dry conditions are defined when water depth is smaller than 1 cm.

The median values of water depth and flow velocity are shown in Figure 5.21. The water depth median value ranges from about 0.85 m for the full production stage ($20 \text{ m}^3/\text{s}$) to 0.2 m for the base flow ($0.5 \text{ m}^3/\text{s}$), as in Figure 5.21A. Water depth decreases accordingly to the release scenarios of Figure 5.20, with S0 and S2 being the fastest and the slowest scenario in reaching the base flow steady condition, respectively. The flow velocity median value shows a similar behaviour and decreases from about 1.1 m/s (full production) to about 0.25 m/s (base flow).

The total variation of the wetted area, evaluated according to Equation (4.3), is about 52% when passing from full production to base flow discharge (Figure 5.22A). Figure 5.22B shows the median dewatering rate in time for all the simulated scenarios. The dewatering rate is evaluated with a timespan of 5 minutes and then expressed in (cm/h) for a easily comparison with available literature (e.g. Halleraker *et al.*, 2003). For the sake of clarity, the dewatering rate is expressed as positive value, i.e. the absolute value of the water depth rate of change which is formally negative during the dewatering. Moreover, we

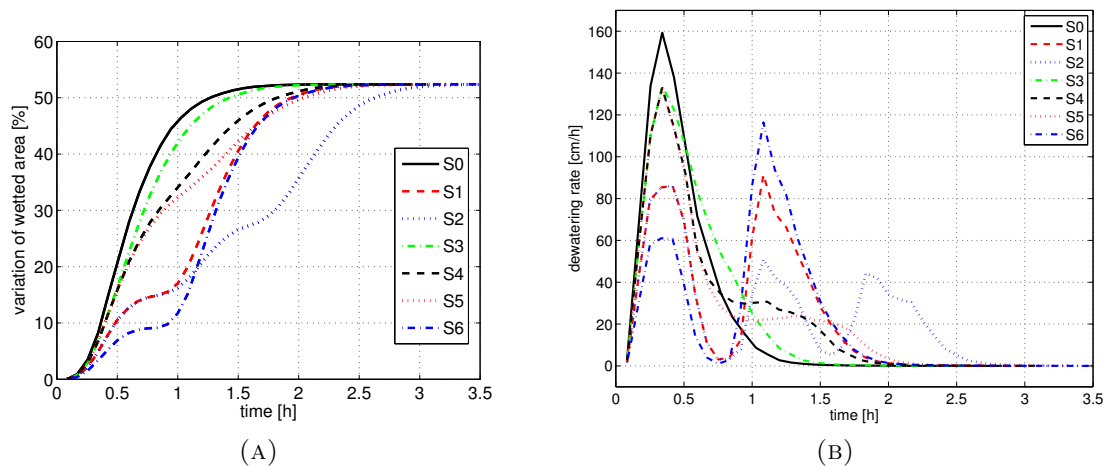


FIGURE 5.22: Reach-scale statistics: wetted area variation (A) and dewatering rate median value (B) during dewatering phase for each simulated scenario.

account for the dewatering rate when water depth is below 20 *cm*, inasmuch fish escape from drying areas has been observed for vanishing water depth (Saltveit *et al.*, 2001).

The current scenario S0 has the greatest value of dewatering rate, about 160 *cm/h* (Figure 5.22B), occurring during the rapid discharge falling limb. In scenario S1, S2 and S6 the first peak reduces and secondary peaks arise according to the discharge falling limbs of Figure 5.20. Scenarios S3, S4 and S5 show a slightly reduction of the dewatering rate peak with a subsequent increase of it in the right tail-end.

As discussed in Section 5.1, the stranding risk critically depends on the concurrent presence of high dewatering rate and drying morphology. Hence the highest risk of stranding is expected to occur during the high dewatering rate periods (i.e. peaks in Figure 5.22B) with concurrent high wetted are variation (i.e. vertical variation in Figure 5.22A). For example, scenario S0 experience the dewatering peak in the interval $t \approx 0.2; 0.5$ *h* (Figure 5.22B): within such interval the total wetted area variation is about 18% (Figure 5.22A). On the other hand, the main dewatering peak of scenario S6 occurs around $t \approx 1; 1.2$ *h*, with a relative wetted area variation of about 8%.

The results presented so far in term of global statistics offer an overview of the potential stranding risk at a reach scale. The unsteady two-dimensional simulations allow to go a step further having the capability to investigate the problem at a local scale. This approach allows to draw local maps of the areas characterized by a different degree of stranding risk combining both information on dewatering rate and wetted area variation. Therefore the aim of the following sections is to obtain a local spatial distribution of the results, with a specific focus for sites 1, 2 and 3 reported in Figure 5.17.

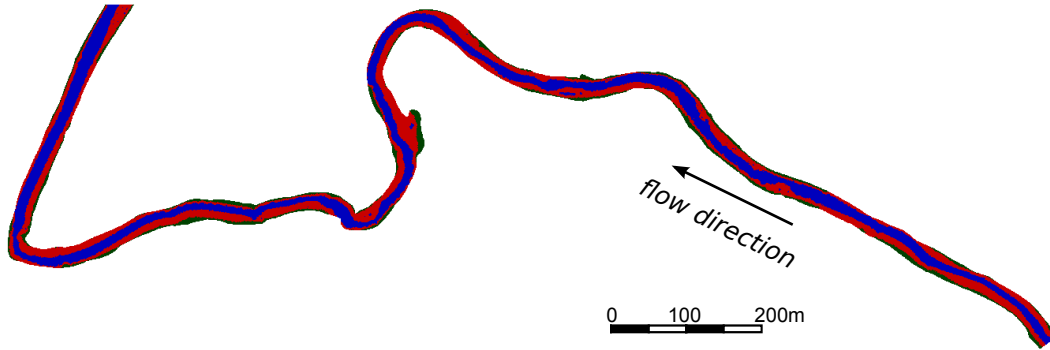


FIGURE 5.23: Variation of wetted area: in blue the wetted area at base flow, in red the area dried passing from production stage ($20 \text{ m}^3/\text{s}$) to base flow ($0.5 \text{ m}^3/\text{s}$).

5.2.4.2 Local variation of wetted area

The maximum potential stranding area is that gets dry when passing from high to low flow. In the investigated reach our simulations return a wetted area of 44548 m^2 under full production conditions against 21577 m^2 under base flow conditions. Therefore the dried area, obtained as the difference between the cases, is 22971 m^2 , which represents a total variation of wetted area (Equation 4.3) of 52%. This result is clearly depicted in Figure 5.23 where the wetted area for the base flow stage is depicted in blue while the dried area obtained passing from full production ($20 \text{ m}^3/\text{s}$) to base flow ($0.5 \text{ m}^3/\text{s}$) is depicted in red. Dark green areas represent cells never get wet during simulations. The asymmetric distribution of the dried areas (red) between left and right riverside is evident within and nearby channel bends, underlining the presence of side bars.

Figure 5.24 shows a magnification in correspondence of Site 1 and 2 (A) and Site 3 (B). Particularly, Site 1 and 2 have an overall wetted area of 7475 m^2 and 4110 m^2 for high and low flow conditions, respectively. This corresponds to a variation of wetted area of 45%. Site 3, which is visualized in the bottom-left part of Figure 5.24B, has a wetted area variation of 33%, passing from 1058 m^2 to 349 m^2 in the dewatering event.

5.2.4.3 Local maximum dewatering rate

The maximum dewatering rate is evaluated with a timespan of 5 minutes and is computed only if water depth is below 20 cm and the cell get dried during the dewatering process, i.e. the red area in Figure 5.23. For the sake of clarity the obtained values are reclassified into 5 intervals, partially inspired by the different literature suggestions (e.g. Halleraker *et al.*, 2003; Saltveit *et al.*, 2001). In particular, maximum dewatering rates ranging between 0-10 (blue), 10-30 (cyan) and 30-60 (green) cm/h are classified as slow, gentle and moderate

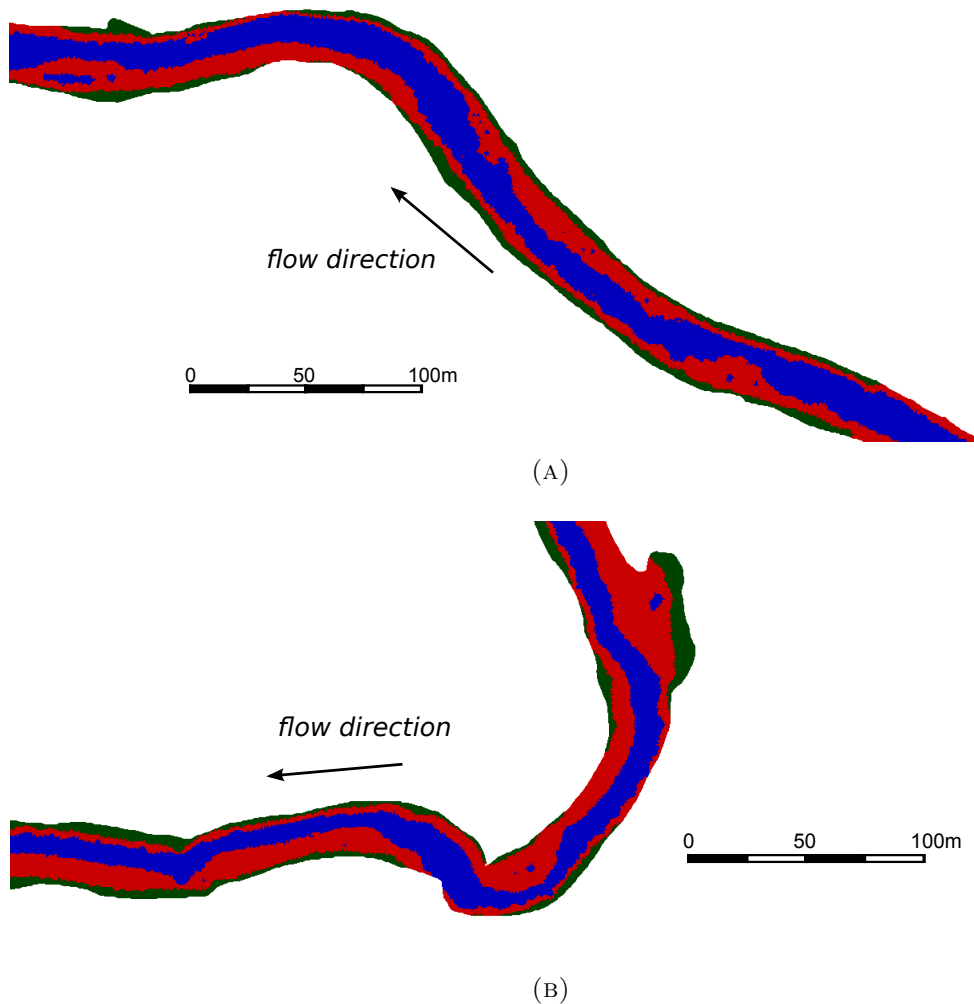


FIGURE 5.24: Variation of wetted area: in blue the wetted area at base flow, in red the area dried passing from production stage ($20 \text{ m}^3/\text{s}$) to base flow ($0.5 \text{ m}^3/\text{s}$). Particular of Site 1 and 2 (A) and Site 3 (B).

processes, respectively. Higher dewatering rates, 60-120 (yellow) and greater than 120 cm/h are classified as rapid and very rapid events, respectively. Please note that in Figures 5.25, 5.26 and 5.27 only areas that get dried during the dewatering process are classified; dark green areas correspond to numerical domain always dry or wet.

Figure 5.25 shows the maximum dewatering rate according to the classification described above. For scenarios S0 (Figure 5.25A) and S6 (Figure 5.25B). It appears clearly that the investigated Lundesokna reach experiences almost only very rapid (red areas) dewatering processes under the current scenario (Figure 5.25A). For example, Figure 5.25B shows the dewatering rate for the scenario S6: in such configuration an overall reduction of the maximum values occurs, but still the reach is characterized by rapid (yellow) and very rapid (red) dewatering areas. It is worth noting (Figure 5.25B), the maximum dewatering rate progressively reduces moving downstream, according to the progressively

damping of the hydraulic wave (e.g. Hauer *et al.*, 2013a).

Figures 5.26 and 5.27 show results for Site 1 and 2, and Site 3 respectively. Comparing the different scenarios of Figure 5.26, it appears that scenarios S1 and S2 slightly reduces the dewatering rates in some portions of the Site (yellow areas), but do not provide noticeable improvements. Scenario S5, characterized by an initial abrupt discharge decrease (as in S0) but with a slow final tail-end (see Figure 5.20), does not reduces at all the maximum dewatering rates in last 20 *cm* (red areas). A timid reduction is provided by Scenario S6, where yellow areas appears along the entire length of Site 1 and 2. Coherently with the discharge pattern (Figure 5.20), reduced dewatering rates appear in initial dried areas (i.e. external part of dried portions), having Scenario 6 a initial reduced falling limb from 20 to 11.5 m^3/s and a subsequent variation down to the base flow condition.

The reduction of maximum dewatering rates is more evident in Site 3, as shown in Figure 5.27. In Scenarios S1, S2 and S6 major portions of dried area turn from very rapid (red) to rapid (yellow) dewatering magnitude with respect to reference scenario S0. Moreover little areas with moderate dewatering magnitudes appear in external part of dried corridor, although neither Site 3 shows relevant dewatering rates reduction with the investigated scenarios.

The overall comparisons of the maximum dewatering rates for all the seven simulated scenarios for the entire studied reach are given in Figure 5.28, which reports the percentage of dried areas classified with the different dewatering rate intervals for all the considered scenarios. In all cases, areas showing a slow (blue) or gentle (cyan) dewatering magnitude are almost irrelevant: overall they account for only about 1.5% of the total area indeed. Moderate dewatering (green) occurs with percentages ranging between 2.4% (S0) and 4.5% (S6). All the scenarios are strongly characterized by rapid and very rapid dewatering processes. It is worth underlining that the Scenario S0 actually represents the worst one in terms of dewatering rate, having about 84% of area in red class. Scenario S1 and S2, despite a relevant difference in discharge pattern (Figure 5.20), result in having similar classes distribution, with about 40% and 55% of area in very rapid (red) and rapid (yellow) class, respectively. The differences of tail-end duration which characterized scenarios S3, S4 and S5 (Figure 5.20), appear to have negligible benefits comparing to Scenario S0. In such cases the very rapid area (red) slightly reduces to about 79% indeed. The greatest benefits in terms of dewatering rates are obtained with the scenario S6, where 6% of area shows maximum dewatering rates below 60 *cm/h* and the very rapid conditions occur in 34% of the dried area.

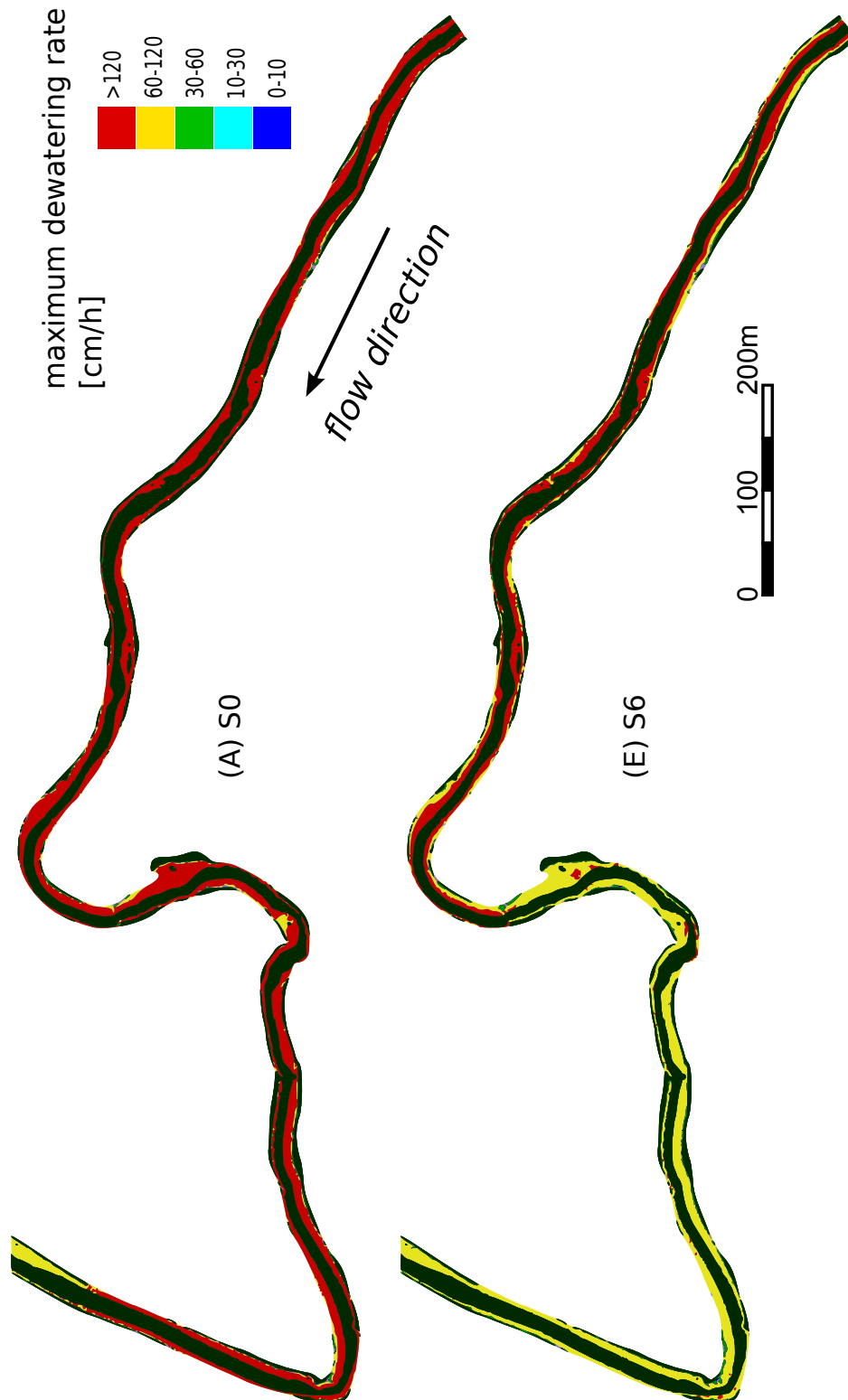


FIGURE 5.25: Maximum dewatering rate in last 20 cm of water column for scenarios S0 and S6.

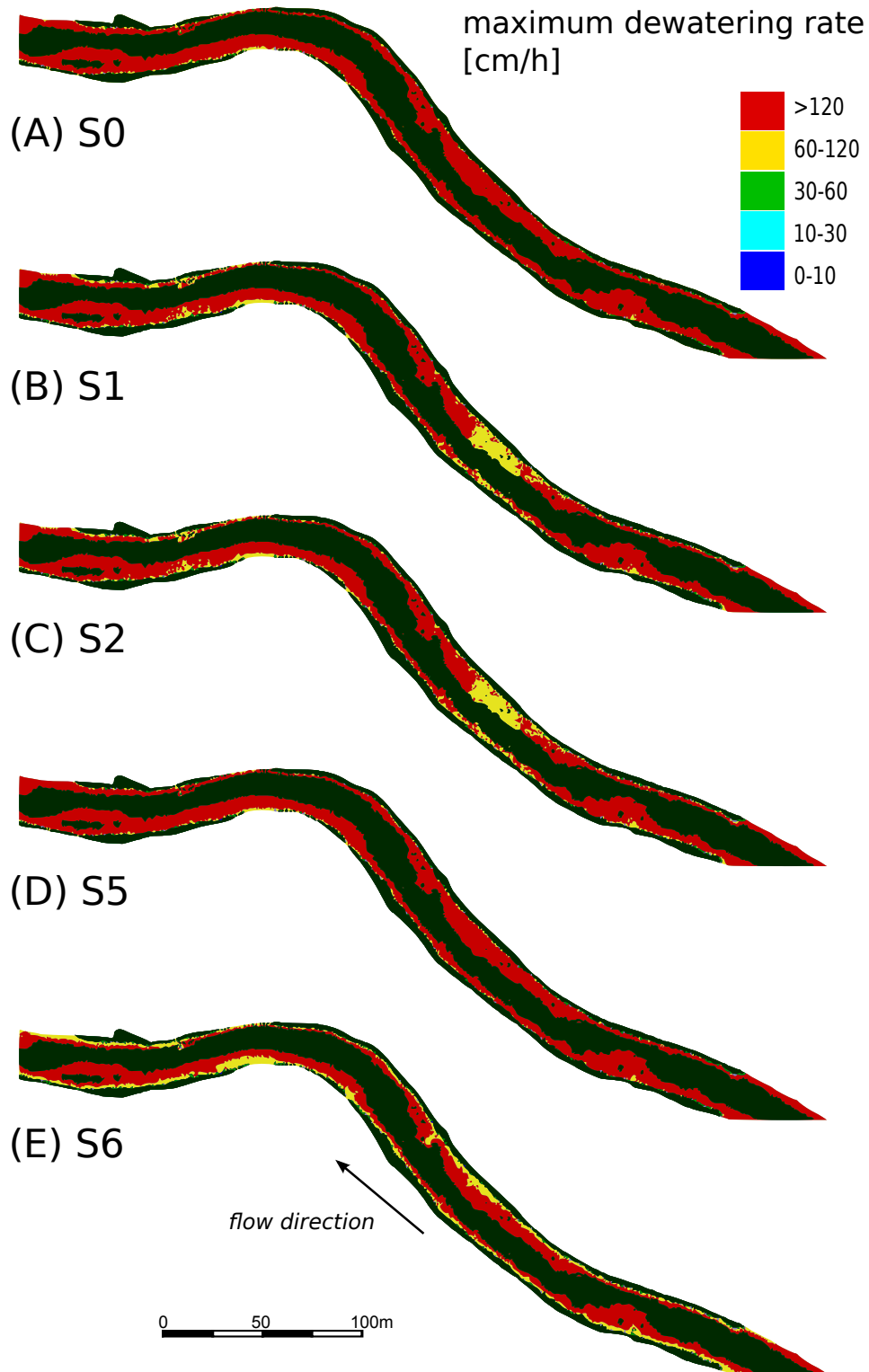


FIGURE 5.26: Maximum dewatering rate in last 20 cm of water column for scenarios S0, S1, S2, S5 and S6; particular of Site 1 and 2.

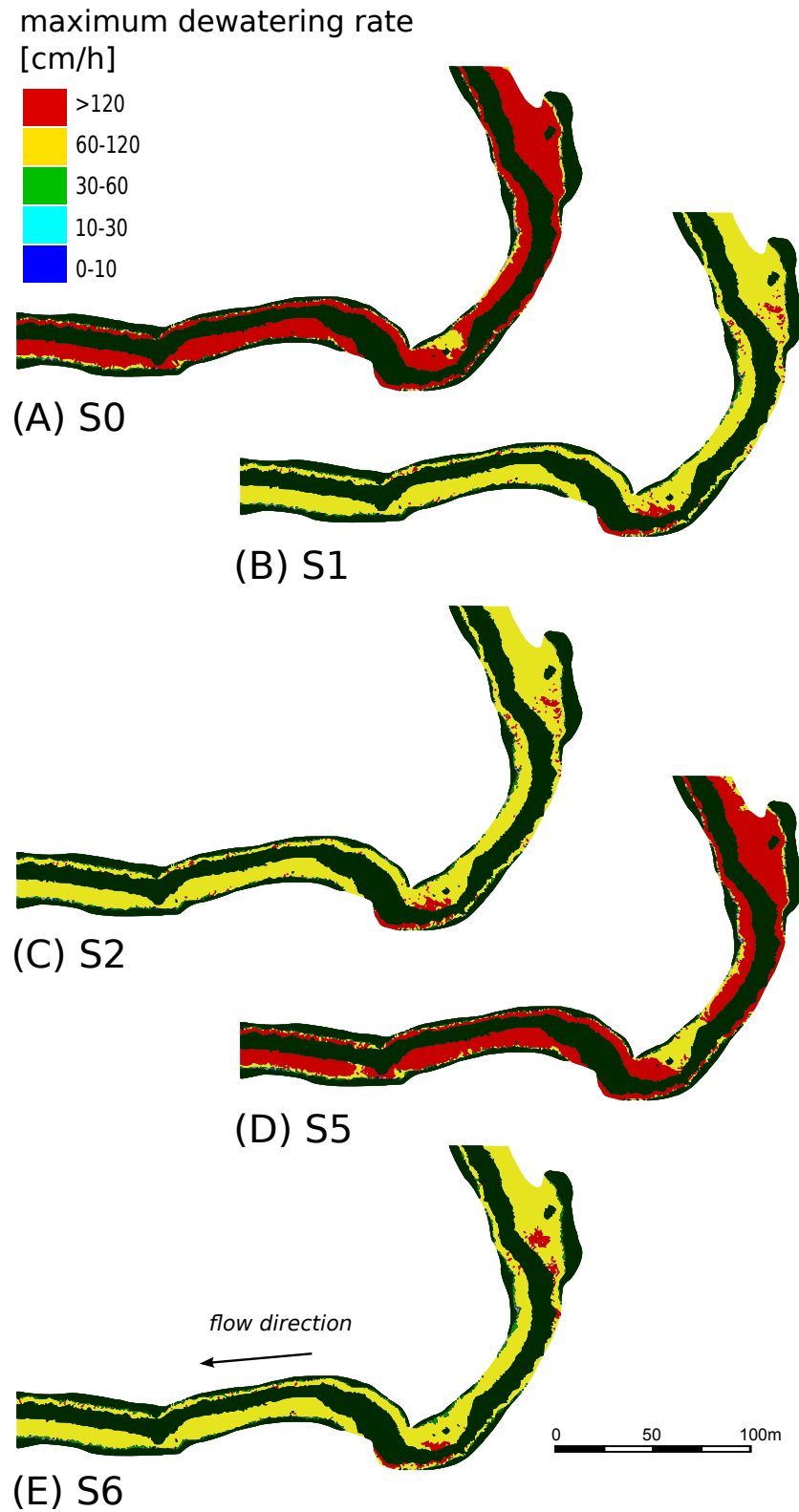


FIGURE 5.27: Maximum dewatering rate in last 20 *cm* of water column for scenarios S0, S1, S2, S5 and S6; particular of Site 3.

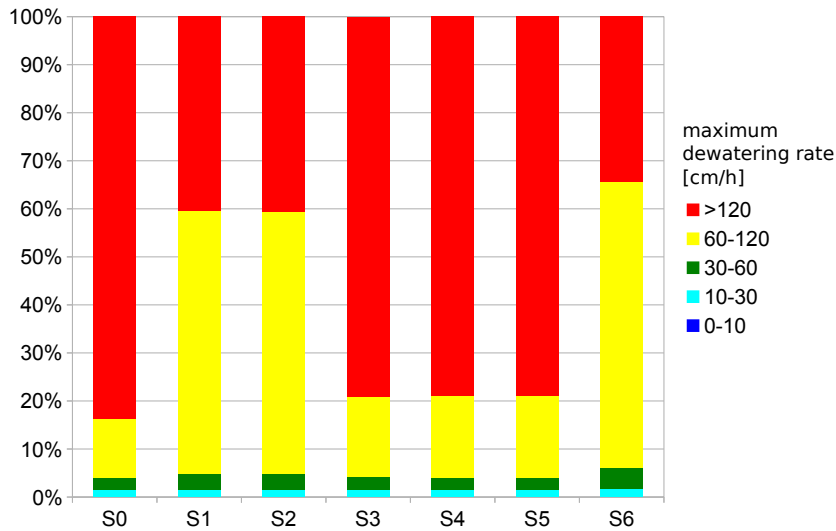


FIGURE 5.28: Percentages of maximum dewatering rate in last 20 *cm* of water column for the entire domain and for all the simulated scenarios.

5.2.4.4 Local duration of dry conditions

A novel aspect investigated in this work is the duration of dry conditions. These strongly depends on duration of production stops, but also can vary according to different dewatering patterns. In this work all the simulations reach the base flow steady conditions within 3.5 *h*, thus this represents our reference time interval. For the sake of clarity, the maximum duration of dry conditions can be 3.5 *h* = 210 *min* if the cell is never wet. Similarly to previous section, in Figures 5.29, and 5.30 only areas that get dried during the dewatering process are classified; dark green areas correspond to numerical domain always dry or wet.

Stranding phenomena does not always imply lethal consequences (e.g. Nagrodski *et al.*, 2012), but the tolerance to dry conditions is specie-specific and highly depends on local habitat features (i.e. substrate characteristics, presence of pools and refugia). Evidences of fish and benthic organism survival to dry conditions range from hours (Saltveit *et al.*, 2001; Casas-Mulet *et al.*, 2014c) to even days (Richards *et al.*, 2013), but a rationale parametrization of lethal exposure duration can hardly be set. Therefore the dry condition duration is deliberately classified in intervals of 60 *min*, as shown in the legend of Figures 5.29 and 5.30, which show the gravel bed exposure duration for Site 1 and 2, and for Site 3, respectively. In Figure 5.29 long dry conditions (red areas) occur only for scenarios S0 and S5, with others having reduced exposure duration. Scenario S2 returns the shortest durations, coherently with being the scenario with the longest discharge pattern (Figure 5.20). Moreover Site 1 and 2 show almost no areas having dry condition duration within 60 *min*.

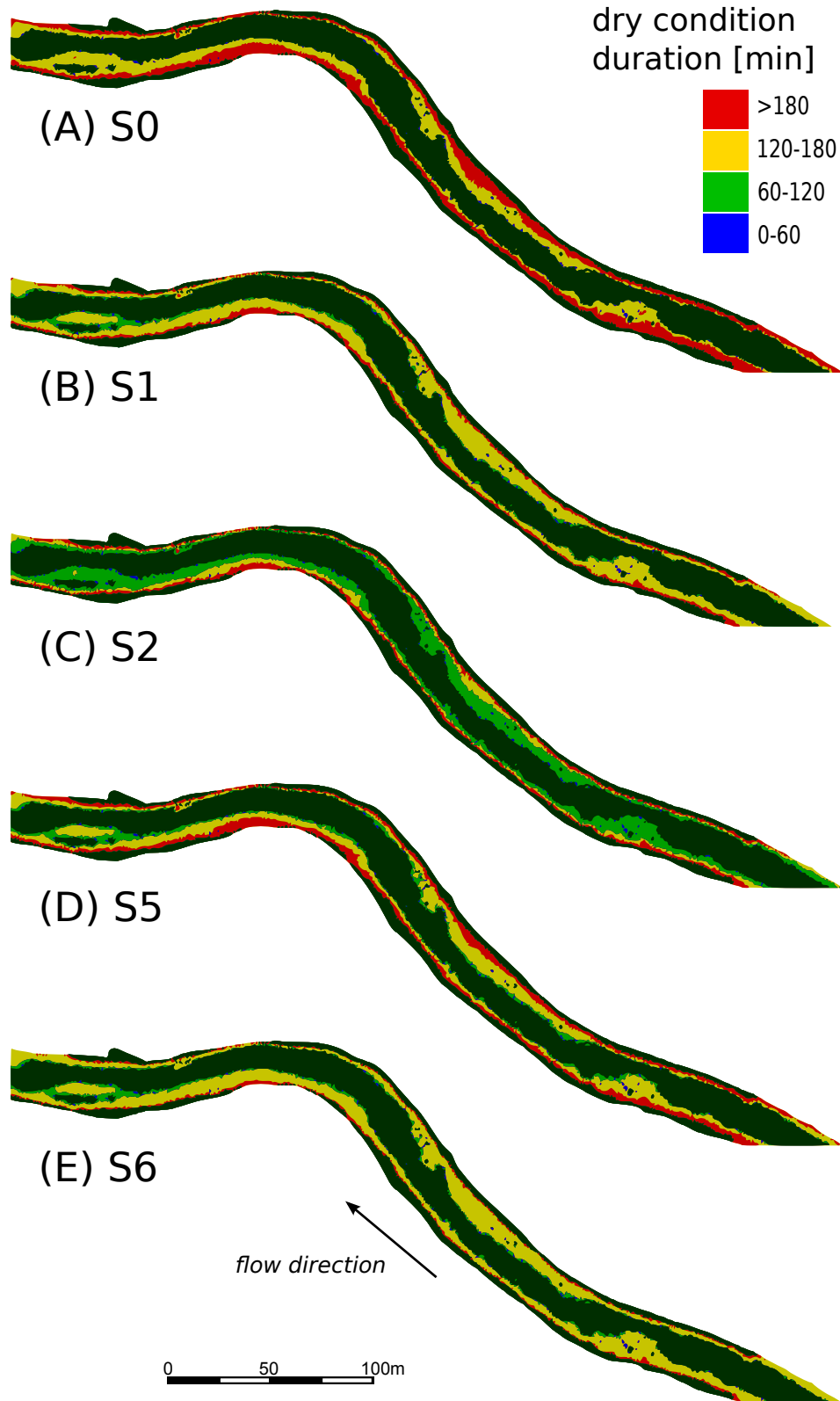


FIGURE 5.29: Duration of dry conditions (in minutes) for scenarios S0, S1, S2, S5 and S6; particular of Site 1 and 2.

In Site 3 (Figure 5.30) exposure durations are generally smaller with respect to Site 1 and 2. This fact has to be ascribed mainly to the different travel time of the hydraulic wave along the river reach. Reference scenario S0 mostly lays in yellow class, with dry conditions within 2 and 3 hours. Scenarios S1, S5 and S6, despite significant differences in discharge patterns (Figure 5.20), result in having similar distribution of duration classes, with an evident decrease (increase of green areas) with respect to reference scenario. Similarly to what happens in Site 1 and 2, also in Site 3, Scenario S2 returns the shortest exposure durations, even within 60 *min* (blue areas).

In order to quantify the dry condition durations in the entire reach, Figure 5.31 shows the percentages for each duration class for all the simulated scenarios. As expected, all the scenario have shorter exposure duration with respect to Scenario S0: the reference case has about 97% of dried area lasting for more than 120 *min*. The greatest exposure reduction is provided by Scenario S2, having half of total dried area exposed for less than 120 *min*. Extending the tail-end of the dewatering patterns in scenarios S3, S4 and S5 (Figure 5.20) progressively reduces the exposure duration in some areas of the domain, with evident increase of green class. However for the same scenarios there is no benefit for such areas get dried at the beginning of dewatering ramping, turning into an almost constant percentage (about 30%) of area in red class. Finally, Scenario 6 returns the smallest percentage of long exposure time (red class, about 12%), with about 28% of area dried for less than 120 *min*.

5.2.5 Discussion

The numerical simulations we conducted confirm the relevant hydropeaking pressure in Lundesokna River. The total variation of wetted area passing from full production discharge to base flow is of 52%, therefore large portion of areas are potentially subjected to fish stranding and dewatering of fish redds. Moreover, the current typical dewatering scenario (S0 in Figure 5.20) is characterized by having about 95% of exposed areas with maximum dewatering rate in last 20 *cm* depth greater than 60 *cm/h*, which means relevant stranding risk conditions (e.g. Halleraker *et al.*, 2003).

All the designed alternative dewatering scenarios (S1-S6 in Figure 5.20) appear to differently improve the reference condition. Accounting for the dewatering rates, Scenario 6 provides the greatest rate reductions (Figure 5.28), however the harmful conditions still persist for all the investigated scenarios.

Comparing Figures 5.22 and 5.28 it is possible to investigate and understand the role of reach morphology during the dewatering dynamics. The greatest amount of drying area occurs in the first stages of dewatering process (percent variation in Figure 5.22A),

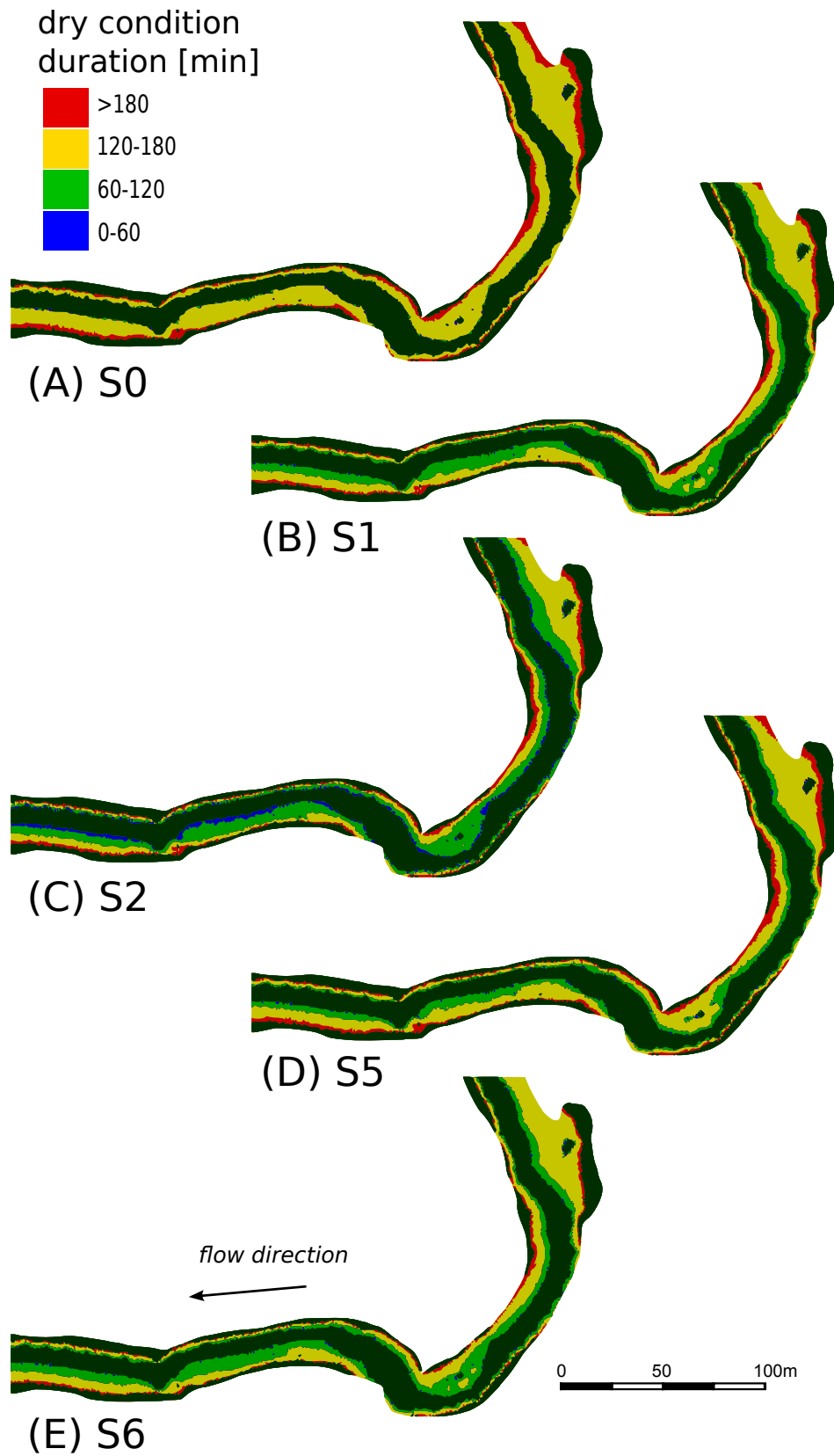


FIGURE 5.30: Duration of dry conditions (in minutes) for scenarios S0, S1, S2, S5 and S6; particular of Site 3.

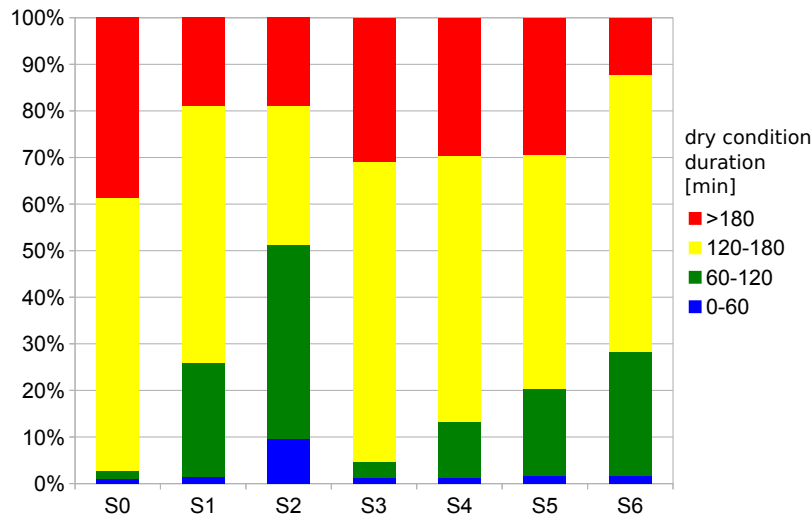


FIGURE 5.31: Percentages of dry condition duration for the entire domain and for all the simulated scenarios.

when side bars and other morphological features start to be exposed, i.e. drying of the upper portion of morphological structures (where *upper* refers to local bed elevation). On the other hand, last part of dewatering transient shows little variations of wetted area, i.e. little drying of the lower portion of morphological structures (where *lower* refers to local bed elevation), being the water way already confined in the center parts of the reach thalweg. If dewatering greatest peaks occur concurrently to the greatest wetted area variations (Figures 5.22), the stranding risk is maximized. For example, scenarios S3, S4 and S5 have been designed having a gentle tail-end of the dewatering curve, however such alternatives bring almost no benefits (see Figure 5.28) with respect to reference scenario, because they do not modify the initial dewatering dynamics.

Scenario S1 and S2 are designed having one and two subsequent discharge plateaux during dewatering, respectively (Figure 5.20), hence they strongly differ in terms of released flow and dewatering duration. However, final percentages in Figure 5.28 shows that the two scenarios provide similar benefits, despite their release pattern differences. Such evidence remarks how the critical temporal interval in the dewatering process is the initial one, which is then responsible of most of the stranding risk. As a matter of fact, the key successful element of scenario S6 is that it reduces the first dewatering rate peak by delaying the second highest peak (Figure 5.20), hence partially offsetting dewatering from area variation. Eventually such configuration results in producing the greatest benefits, as shown in Figure 5.28.

The reference scenario S0 represents the worst case also in terms of duration of dry conditions, having 97% of area in dry conditions lasting more than 120 *min* during the 3.5

hours of simulation (Figure 5.31). The crucial role of the upper portion of bed structures is also reflected on the duration of dry conditions. Scenarios S3, S4 and S5 reduce the exposure time in lower parts of the river bathymetry, i.e. in areas which get dried during the tail of dewatering, hence increasing the size of blue and green classes in Figure 5.31. However, for such scenarios there is no percentage reduction of red class (dry condition longer than 180 *min*), which refers to upper parts of the bed morphologies that are dried at the beginning of the dewatering process. As expected, the best performance in terms of dry condition duration is provided by Scenario S2, having the longest discharge pattern duration (Figure 5.20). It is also worth noting that Scenario S6 provides also significant benefits with respect to the reference scenario.

Comparing the outcomes of the simulated scenarios, i.e. accounting both for reducing areas with rapid dewatering and dry exposure duration, scenarios S2 and S6 are predicted to providing the best benefits. It is important to remark that such conclusions are merely based on the quantification of the Ecologically-Relevant Hydraulic Parameters as proxy indicators for the stranding risk and the embryo survival. Each designed alternative scenario entails variations in Sokna dam operations, with different magnitudes of additional released water and economical losses due to the decrease of electricity production. Within such perspective Scenario S6 is expected to be more economically feasible than Scenario S2: the former requires indeed a partial reduction of electricity production and no additional bypassed water release, while the latter implies a production reduction to the minimum efficiency stage and also additional bypassed water release.

The collection of proposed scenarios can not be exhaustive of all possible release options: for example, it is worth remarking that the duration of discharge plateaux in the different scenarios has been deliberately set to 30 *min*, so further dewatering scenarios can be tuned also modifying such release option. However the present results provide relevant indications on the effectiveness of the studied different dewatering patterns. Starting from the considerations on the successful components of Scenario 6, other options can be tested in other to find out the one which minimize the potential ecological impacts.

Adopting a two-dimensional modeling approach allows to properly investigate and quantify hydraulic and ecological features, especially in presence of non-trivial bed morphologies, like side or central bars. However the exploitation of a two-dimensional approach can be limited in case of scarce available topographic scans. For the present study detailed topographic information were available in specific sites (see Figure 5.17), while the remaining two-dimensional domain has been reconstructed from the interpolation of available topographic measures. Increasing the topographic resolution in the reach may help further testing the robustness and reliability of the given outcomes.

The typical hydropeaking event occurring in Lundesokna River results in very rapid variations of the hydraulic quantities, as shown in Figure 5.21. Such severe variations raise a crucial issue about the unsteadiness of the investigated phenomenon and hence on the choice of the modeling approach. The present dewatering scenario entails a discharge falling limb which lasts about 15 *min*: such input negative hydraulic wave propagates downstream and reaches the downstream boundary (about 2 *km* downstream) with a delay of about 30 *min*. This means that the reach experiences rapid transitory hydraulic configurations that therefore can not be correctly described if a steady modeling approach is adopted. Thus a coherent evaluation of the dewatering rate requires the adoption of unsteady numerical modeling. The unsteadiness of the modeled events is reflected also in the spatial distribution of both dewatering rates and duration of dry conditions. In particular, maximum dewatering rates constantly decrease moving downstream due to the damping of the transitory negative hydraulic wave. Analogously, the durations of dry condition are invariantly shorter moving downstream due to the travel time of the wave. According to such outcomes, unsteady modeling seems to be unavoidable when targeting to quantify dewatering rates in highly peaked rivers.

5.3 Conclusions

The study proposed in this chapter provides insights on the stranding risk modeling. In particular we focus on investigating and quantifying the tradeoffs between dewatering rate and wetted area variation, which represent two concurrent hydro-morphological features having a crucial role in triggering fish stranding. The first part follows the workflow proposed in Chapter 4, and particularly deals with the interaction between hydropeaking and self-formed river morphology. The outcomes reported in Section 5.1.3 underline the influence of river bed morphology in final distributions of the selected ERHPs and remark the crucial role and critical behaviour of the transitional morphologies between single and multi-thread channel morphologies. Within the proposed approach we then quantify the potential stranding risk with a recast classification directly inspired to existing national regulations (Baumann *et al.*, 2012), however the proposed approach is suitable to be exploited with different classification criteria.

The second part (Section 5.2) is devoted to modeling of fish stranding in Ludesokna River, a Norwegian hydropeaked river. In such context the main focus shifts to quantify the stranding risk when varying the transitory dewatering phase. Among the tested scenarios we identify which ones provide the greatest benefits in terms of eco-hydraulic response. Without claiming for definitive and exhaustive solutions, the outcomes discussed

in Section 5.2.5 might provide a useful background for analysis of critical impacts of hydropeaking in Lundesokna.

It is worth recalling both the findings of Section 5.1 and 5.2 underline the marked unsteadiness of the investigated phenomena. When aiming at modeling hydro-morphological configurations that experience severe hydropeaking events, the choice of an adequate numerical modeling strategy becomes crucial. As an example, the inherent unsteadiness that characterizes the hydraulic negative wave of dewatering process results in longitudinal damping of maximum dewatering rates, as pointed out in Section 5.1.2.2 (Figure 5.8) and in Section 5.2.5. These evidences remark the need of fully unsteady numerical approaches when aiming to reliably estimate dewatering intensities. Furthermore, the use of two-dimensional numerical approaches in eco-hydraulic modeling is progressively growing (e.g. Gostner *et al.*, 2013b; Hauer *et al.*, 2014), hence the present study might represent a useful contribution in exploiting, debating and benchmarking eco-hydraulic modeling strategies.

After all, both the reported studies provide quantitative suggestions and operative approaches that can be exploited to put a step forward in fish stranding modeling, but more in general in habitat modeling. Namely, the quantitative outcomes of the present chapter can be useful for an effective quantification of the ecological tradeoffs of different dewatering strategies. However, further investigations are required in order to tune those release operations which can provide the best ecological-economical tradeoffs. Accomplishing this task within the proposed approach will provide practical management alternatives for hydropower production in rivers subjected to stranding risk issues such as the Lundesokna in Norway.

Chapter 6

Conclusions

In this chapter a summary of the relevant conclusions arising from each of the previous chapters is given. Furthermore, the particular conclusions are jointly reviewed to answer the specific research questions posed in Chapter 1 of the thesis. Finally, some recommendations for further research are given.

6.1 Summary of chapter conclusions

Chapter 2 presents the development of two dimensionless at-a-station indicators for the assessment of river sub-daily thermal alterations. The indicators quantify the sub-daily thermal rate of change and oscillation frequencies contained in the thermal signal. These characteristics can be potentially affected by thermopeaking. The two indicators eventually allow to identify three different sub-daily thermal alteration classes: absent or low, medium and high. The methodology presented in Chapter 2 can be adopted as first screening tool for environmental managers to identify and quantify at-a-station river thermal alterations at sub-daily scales, as those related to hydropeaking, thus providing a powerful mapping tool to set priorities and critical locations. This relatively simple methodology for the identification of critically impacted stations allows to concentrate subsequent efforts and specific investigations to characterize particular thermal regimes at site (reach) scale.

In *Chapter 3* we develop a numerical model for surface water temperature transport. Water temperature can be considered as a passive tracer, therefore the model simulates the advection-diffusion of a generic passive tracer. We reformulate the two-dimensional shallow water advection-diffusion model in the form of a hyperbolic system with stiff source terms, using a relaxation approach. This approach is based on a relaxation of

the spatial gradients of the passive tracer concentration and does not change significantly the structure of the original system. More importantly it removes the unphysical phenomenon of instantaneous small perturbation wave propagation of the original system. We derive the conditions under which the relaxation system is advective dominated: i.e. the maximum eigenvalue is the one associated to the shallow water system. We discuss that many rivers are in the advection dominated case and conclude that modeling the advection-diffusion of a passive tracer does not require extra computational costs compare to the pure hydrodynamic case. Finally we test the robustness of the new developed model performing four different test cases showing its capability in dealing with complex morphologies and preserving mass.

Chapter 4 proposes a first quantitative attempt to investigate the eco-hydraulic response of different river morphologies to hydropeaking waves based on a 2D hydraulic modeling approach. Physical habitat diversity, macroinvertebrate drift and fish stranding risk are quantitatively investigated with reference to realistic hydro-morphological conditions of regulated alpine streams. The study underlines how habitat diversity and fish stranding have the strongest dependency on channel morphology and show nearly opposite behaviours with increasing morphological complexity. Moreover, braided reaches result to be the most resilient to hydropeaking by offering the highest habitat diversity and very limited base-to-peak variation of macroinvertebrate drift. While alternate bars are extremely sensitive environments to drift and offer safer regions from stranding. Finally, transitional morphologies between single- and multi-thread offer the best eco-hydraulic tradeoffs. The proposed approach allows to quantify to which extent the same eco-hydraulic targets can be achieved by either morphological restorations or base flow increases: such quantification of the eco-hydraulic effectiveness of complementary management strategies offers a powerful tool to support design of restoration measures in hydropeaking rivers.

Chapter 5 proposes a quantitative attempt to investigate the stranding risk using 2D unsteady simulations. In particular we focus on the quantification of the tradeoffs between dewatering rate and wetted area variation, that are commonly used in existing national regulations to assess fish stranding risk, though little quantification of their meaning for different channel morphologies was provided so far. Our investigations reveal the crucial influence of river bed morphology on the stranding risk and confirm the particular behaviour of the alternate bars and the transitional morphologies, as resulting in Chapter 4. The second part of the chapter presents an application of the above fish stranding risk

modeling to the Ludesokna River, a Norwegian hydropeaked river. The study quantifies the potential eco-hydraulic benefits of a suite of dewatering scenarios. The outcomes might provide a useful background for analysis of critical impacts of hydropeaking on the Ludesokna river. Overall, the analysis underlines the relevant unsteadiness of the investigated phenomena and the need to use fully unsteady, 2D hydraulic modeling approaches in the quantification of the stranding risk under hydropeaking conditions.

Appendix A provides a methodology to quantify hydropeaking alterations, which is easy to apply, requires stream flow data at a readily available resolution, and allows for the comparison of hydropeaking flow alteration among several gauged stations. Hydropeaking flow alteration is quantified by designing two indicators related to flow magnitude and rate of change. The classification methodology proposed in *Appendix A* is broadly applicable to procedures for the evaluation of flow regime alterations and classification of river hydromorphological quality, and may help to guide river restoration actions.

6.2 Synthesis of the research questions

This doctoral thesis is built on three main research elements, as introduced in Chapter 1. Each chapter and the *Appendix A* faced the proposed research challenges adopting different strategies, i.e. statistical tools as well as numerical modeling. Jointly reviewing the main findings of each particular study it is possible to answer the particular research questions (*i-iii*) posed in Chapter 1.

1. Characterization of hydropeaking and thermopeaking alterations:

we developed *i*) two different procedures (Chapter 2 and *Appendix A*) which allow the identification and classification of hydrological and thermal alterations from at-a-station temperature (and flow) time series. The designed dimensionless indicators account for the sub-daily fluctuations of water temperature (and flow) and *ii*) identifies suitable temporal scales to discriminate altered from near-natural thermal regimes. In particular (Chapter 2) we find that 30 minutes and 6 hours are the most adequate temporal scales to mark the alteration of thermal signature in terms of short-scale maximum variations and sub-daily oscillation frequencies. With respect to hydrological alterations (*Appendix A*) we find that a resolution of 1 hour of the flow dataset it is sufficient for the evaluation of the short-scale flow variations induced by hydropeaking. By means of a statistical outlier definition *iii*) we outline the range of variability of the designed indicators for a reference dataset

of alpine near-natural reach stations, which therefore represent the reference, unaltered behaviour with respect to thermopeaking and hydropeaking alterations.

It is worth mentioning that the procedure for the quantification of hydropeaking alterations presented in Appendix A have been included as screening tool in Italian national guideline on river hydromorphological quality assessment (Carolli *et al.*, 2014).

2. Modeling the surface water thermal transport:

using a relaxation technique, we develop *i)* a new numerical approach that solves the shallow water advection-diffusion equations over complex topographies. We demonstrate that this approach is robust and accurate. Moreover we show that in many rivers modeling the advection-diffusion of a passive tracer using the modeling approach developed in Chapter 3, does not require extra computational costs compare to the pure hydrodynamic case. After all, these features are particularly attractive for real world computations of river thermal regime.

3. Investigation of the role of river morphology under hydropeaking conditions:

we systematically investigate the interaction between hydropeaking waves and river morphology in a two-dimensional numerical modeling framework. In particular *i)* we first identify a series of measurable Ecologically Relevant Hydraulic Parameters which are proxies of some ecological assets linked to hydropeaking. Hence we quantify the eco-hydraulic response of a suite of representative river morphologies evaluating those selected ERHPs. *ii)* Both Chapters 4 and 5 underline the resilience of the braiding network to hydropeaking events and the high sensitivity of alternate bars pattern which results providing the poorest eco-hydraulic tradeoffs. Moreover transitional morphologies offer the best eco-hydraulic response to hydropeaking alteration. *iii)* The modeling approach proposed in Chapter 4 and 5 provides a direct quantification of the ERHPs within the available national regulations, but also represents a supporting tool to test and review presently adopted eco-hydraulic thresholds. The study on Lundesokna River, which provides useful indications on the tradeoffs between dewatering events and stranding risk, represents an exploitable support to design further mitigation strategies in the Lundesokna basin and can easily be extended to other hydropeaking river reaches.

6.3 Main conclusions

This thesis faces some crucial aspects in the understanding of the eco-hydraulic effects of hydropeaking and thermopeaking. The lively and challenging research gaps and, in

the other hand, the growing requests by river management agencies for usable supporting tools, push this work in exploring different approaches having the common aim of developing modeling and assessment tools.

A crucial need in river management policies is the identification and quantification of those anthropogenic alterations which threaten the river ecological quality. The developed methodologies, based on a statistical classification of the near-natural hydrological and thermal regimes, might provide two valuable screening procedures for supporting environmental policies.

Shifting to the research context, the lively interdisciplinary commingling of eco-hydraulics and the continuous improvements in numerical computing offer novel challenges and opportunities to environmental modelers. The numerical model for the shallow-water advection-diffusion problem provides an effective tool in environmental applications which can be exploit for thermal, as well as pollutant transport modeling.

Eventually, the proposed investigation of the interaction between hydropeaking and river morphology provides a flexible approach that can usefully increase present understanding of ecological implications of hydropeaking. Moreover the application presented in Chapter 5 underlines the potential exploitation in supporting ecologically, target-oriented, river restoration strategies.

6.4 Recommendations for further research

The different paths explored in this thesis result in novel modeling and assessment tools for hydropeaking and thermopeaking rivers. However such outcomes have no claims of exhaustiveness, likewise they might pave the way for further research questions and efforts. To this aim, I give a short recommendation list, supported by experiences and results of my doctoral work.

- i)* The crucial role of river morphology in determining the ecological response to anthropogenic flow alterations deserves deeper investigation. In particular this thesis accounts for the role of self-formed river morphologies triggered by channel width in unlimited sediment supply configurations. This is often not the case in river reaches downstream dam and hydropower plant systems. Hence the morphodynamic responses to channel widening with limited sediment supply and its subsequent eco-hydraulic response is yet an unquestioned topic;
- ii)* the developed numerical model provides an useful tool to investigate the thermal transport in rivers. Further efforts might be dedicated to investigate the influence

of river morphology in the thermodynamic processes (e.g. transport, damping, heat exchanges) that rivers experience when subjected to thermopeaking;

iii) the proposed approach which jointly combined two dimensional hydro- and thermodynamic simulations can be further exploited integrating other eco-hydraulic features adopted in the meso-scale habitat modeling (e.g. bed substrate, species suitability curves), hence offering a powerful tool for environmental modeling.

Bibliography

- Alpine Convention (2009). Water and water management issues. Report on the State of the Alps. Technical report, Permanent Secretary of the Alpine Convention, Innsbruck.
- Anonymous (2012). Retningslinjer for revisjon av konsesjonsvilkår for vassdragsreguleringer (English: Guidelines for revision of hydropower licenses). Technical report, Ministry of Petroleum and Energy.
- Arismendi I., Johnson S. L., Dunham J. B., Haggerty R. and Hockman-Wert D. (2012). The paradox of cooling streams in a warming world: Regional climate trends do not parallel variable local trends in stream temperature in the Pacific continental United States. *Geophysical Research Letters*, 39:1–7.
- Auer H. (2012). Flussmorphologische Grundlagenuntersuchungen am Lech zur Bewertung des Schwalleinflusses bei unterschiedlichen Flusstypen.
- Baumann P., Kirchhofer A. and Schälchli U. (2012). Risanamento deflussi discontinui - Pianificazione strategica. Un modulo dell'aiuto all'esecuzione Rinaturazione delle acque. Technical report, Ufficio federale dell'ambiente, Bern, CH.
- Bermudez A. and Vazquez M. E. (1994). Upwind methods for hyperbolic conservation laws with source terms. *Computers & Fluids*, 23(8):1049–1071.
- Bertoldi W., Gurnell A., Surian N., Tockner K., Zanoni L., Ziliani L. and Zolezzi G. (2009). Understanding reference processes: Linkages between river flows, sediment dynamics and vegetated landforms along the Tagliamento River, Italy. *River Research and Applications*, 25(February):501–516.
- Bevelhimer M. S., McManamay R. A. and O'Connor B. (2014). Characterizing sub-daily flow regimes: implications of hydrologic resolution on Ecohydrology studies. *River Research and Applications*, pages n/a–n/a.
- Blondeaux P. and Seminara G. (1985). A unified bar–bend theory of river meanders. *Journal of Fluid Mechanics*, 157:449.
- Boano F., Revelli R. and Ridolfi L. (2007). Bedform-induced hyporheic exchange with unsteady flows. *Advances in Water Resources*, 30(1):148–156.
- Bonacci O., Trninić D. and Roje-Bonacci T. (2008). Analysis of the water temperature regime of the Danube and its tributaries in Croatia. *Hydrological Processes*, 22(7): 1014–1021.

-
- Brufau P., Vázquez-Cendón M. and García-Navarro P. (2002). A numerical model for the flooding and drying of irregular domains. *International Journal for Numerical Methods in Fluids*, 39(3):247–275.
- Bruno M. C., Maiolini B., Carolli M. and Silveri L. (2009). Impact of hydropeaking on hyporheic invertebrates in an Alpine stream (Trentino, Italy). *Ann. Limnol.-Int. J. Lim.*, 45(3):157–170.
- Bruno M. C., Maiolini B., Carolli M. and Silveri L. (2010). Short time-scale impacts of hydropeaking on benthic invertebrates in an Alpine stream (Trentino, Italy). *Limnologica - Ecology and Management of Inland Waters*, 40(4):281–290.
- Bruno M. C., Siviglia A., Carolli M. and Maiolini B. (2013). Multiple drift responses of benthic invertebrates to interacting hydropeaking and thermopeaking waves. *Ecohydrology*, 6(4):511–522.
- Buffard T. and Clain S. (2010). Monoslope and multislope muscl methods for unstructured meshes. *Journal of Computational Physics*, 229(10):3745–3776.
- Bunt C. M., Cooke S. J., Katopodis C. and Mckinley R. S. (1999). Movement and summer habitat of brown trout (*Salmo trutta*) below a pulsed discharge hydroelectric generating station. *Regul River*, 15(5):395–403.
- Butcher J. C. (1987). *The Numerical Analysis of Ordinary Differential Equations: Runge-Kutta and General Linear Methods*. Wiley-Interscience, New York, NY, USA.
- Caissie D. (2006). The thermal regime of rivers: a review. *Freshwater Biology*, 51(8):1389–1406.
- Campana D., Marchese E., Theule J. I. and Comiti F. (2014). Geomorphology Channel degradation and restoration of an Alpine river and related morphological changes. *Geomorphology*, 221:230–241.
- Carolli M., Bruno M. C., Siviglia A. and Maiolini B. (2012). Responses of benthic invertebrates to abrupt changes of temperature in flume simulations. *River Research and Applications*, 28(6):678–691.
- Carolli M., Vanzo D., Zolezzi G., Siviglia A. and Bruno M. C. (2014). Metodo per la quantificazione della pressione da hydropeaking. Technical report, Istituto Superiore per la Protezione e la Ricerca Ambientale, ISPRA, Rome, I. In: *IDRAIM: sistema di valutazione idromorfologica, analisi e monitoraggio dei corsi d'acqua*. http://www.isprambiente.gov.it/files/pubblicazioni/manuali-lineeguida/Metodo_Hydropeaking_CAROLLI_ET_AL2014.pdf.
- Carron J. and Rajaram H. (2001). Impact of variable reservoir releases on management of downstream water temperatures. *Water Resources Research*, 37(6):1733–1743.
- Casas-Mulet R. (2014). *Dynamics of Dewatering and Flooding during Hydropeaking*. PhD thesis, Norwegian University of Science and Technology, Department of Hydraulic and Environmental Engineering.

- Casas-Mulet R., Alfredsen K., Boissy T., Sundt H. and R  ther N. (2014a). Performance of a one-dimensional hydraulic model for the calculation of stranding areas in hydropeaking rivers. *River Research and Applications*, pages n/a–n/a.
- Casas-Mulet R., Alfredsen K. and Killingtveit A. (2014b). Modelling of environmental flow options for optimal Atlantic salmon, *Salmo salar*, embryo survival during hydropeaking. *Fisheries Management and Ecology*, 21:480–490.
- Casas-Mulet R., Saltveit S. J. and Alfredsen K. (2014c). The survival of atlantic salmon (*Salmo salar*) eggs during dewatering in a river subjected to hydropeaking. *River Research and Applications*, 7:n/a–n/a.
- Castro M. J., Ferreiro A. F., Garc  a-Rodr  guez J. A., Gonz  lez-Vida J. M., Mac  as J., Par  s C. and V  zquez-Cend  n M. E. (2005). The numerical treatment of wet/dry fronts in shallow flows: application to one-layer and two-layer systems. *Mathematical and computer modelling*, 42(3):419–439.
- Catrinu-Renstrom M. D. and Knudsen J. K. (2011). Perspectives on hydropower’s role to balance non-regulated renewable power production in Northern Europe. Technical report, Norway.
- Cattaneo C. (1949). Sulla conduzione del calore. *Atti Semin. Mat. Fis. Univ. Modena*, 3: 83–101.
- Cattaneo C. (1958). A form of heat conduction equation which eliminates the paradox of instantaneous propagation. *Compte Rendus*, 247(4):431–433.
- C  r  ghino R., Cugny P. and Lavandier P. (2002). Influence of Intermittent Hydropeaking on the Longitudinal Zonation Patterns of Benthic Invertebrates in a Mountain Stream. *International Review of Hydrobiology*, 87(1):47.
- C  r  ghino R., Legalle M. and Lavandier P. (2004). Drift and benthic population structure of the mayfly *Rhithrogena semicolorata* (Heptageniidae) under natural and hydropeaking conditions. *Hydrobiologia*, 519(1-3):127–133.
- Charmasson J. and Zinke P. (2011). Mitigation Measures Against Hydropeaking Effects. Technical report, SINTEF Energy Research.
- Croisille J.-P. and Greff I. (2005). An efficient box-scheme for convection–diffusion equations with sharp contrast in the diffusion coefficients. *Computers & fluids*, 34(4):461–489.
- Crosato A. and Mosselman E. (2009). Simple physics-based predictor for the number of river bars and the transition between meandering and braiding. *Water Resources Research*, 45(3):n/a–n/a.
- Dickson N. E., Carrivick J. L. and Brown L. E. (2012). Flow regulation alters alpine river thermal regimes. *Journal of Hydrology*, 464-465:505–516.
- Dumbser M. and Toro E. F. (2011). On universal osher-type schemes for general nonlinear hyperbolic conservation laws. *Communications in Computational Physics*, 10(3):635–671.

-
- Duran A., Liang Q. and Marche F. (2013). On the well-balanced numerical discretization of shallow water equations on unstructured meshes. *Journal of Computational Physics*, 235:565–586.
- Elosegi A., Díez J. and Mutz M. (2010). Effects of hydromorphological integrity on biodiversity and functioning of river ecosystems. *Hydrobiologia*, 657(1):199–215.
- European Commission (2000). Directive 2000/60/EC of the European Parliament and of the Council of 23 October 2000: establishing a framework for Community action in the field of water policy.
- European Commission (2009). Directive 2009/28/EC of the European Parliament and of the Council of 23 April 2009: on the promotion of the use of energy from renewable sources and amending and subsequently repealing Directives 2001/77/EC and 2003/30/EC.
- Fernando H. (2012). *Handbook of Environmental Fluid Dynamics, Volume Two: Systems, Pollution, Modeling, and Measurements*. Environmental science and engineering / [CRC press]. Taylor & Francis.
- Fette M. (2005). *Tracer Studies of River-Groundwater Interaction under Hydropeaking Conditions*. PhD thesis, ETH, Zürich.
- Fette M., Weber C., Peter a. and Wehrli B. (2007). Hydropower production and river rehabilitation: A case study on an alpine river. *Environmental Modeling & Assessment*, 12(4):257–267.
- Finch C., Pine W. E. and Limburg K. E. (2014). Do hydropeaking flows alter juvenile fish growth rates? A test with juvenile humpback chub in the Colorado river.
- Fleckenstein J. H., Krause S., Hannah D. M. and Boano F. (2010). Groundwater-surface water interactions: New methods and models to improve understanding of processes and dynamics. *Advances in Water Resources*, 33(11):1291–1295.
- Flodmark L. E. W., Vøllestad L. A. and Forseth T. (2004). Performance of juvenile brown trout exposed to fluctuating water level and temperature. *Journal of Fish Biology*, 65(2):460–470.
- FOEN (2011). Water protection legislation. *Federal office for the environment*.
- Formann E., Habersack H. and Schober S. (2007). Morphodynamic river processes and techniques for assessment of channel evolution in Alpine gravel bed rivers. *Geomorphology*, 90(3-4):340–355.
- Frutiger A. (2004). Ecological impacts of hydroelectric power production on the River Ticino. Part 1: Thermal effects. *Archiv für Hydrobiologie*, 159(1):43–56.
- Gao Y., Vogel R. M., Kroll C. N., Poff N. L. and Olden J. D. (2009). Development of representative indicators of hydrologic alteration. *Journal of Hydrology*, 374(1-2): 136–147.

- Garcia Lugo G. A. (2014). *Braided rivers: an exploratory study combining flume experiments and the analysis of remotely-sensed data*. PhD thesis, Queen Mary University of London.
- Gebre S., Alfredsen K., Lia L., Stickler M. and Tesaker E. (2013). Review of Ice Effects on Hydropower Systems. *Journal of Cold Regions Engineering*, 27(4):196–222.
- Gebre S., Timalina N. and Alfredsen K. (2014). Some Aspects of Ice-Hydropower Interaction in a Changing Climate. *Energies*, 7(3):1641–1655.
- Gore J. A. and Petts G. E. (1989). *Alternatives in Regulated River Management*. Taylor & Francis.
- Gorla L., Signarbieux C., Turberg P., Buttler A. and Perona P. (2015). Effects of hydropeaking waves' offsets on growth performances of juvenile *Salix* species. *Ecological Engineering*, 77:297–306.
- Gostner W., Alp M., Schleiss A. J. and Robinson C. T. (2013a). The hydro-morphological index of diversity: a tool for describing habitat heterogeneity in river engineering projects. *Hydrobiologia*, 712(1):43–60.
- Gostner W., Parasiewicz P. and Schleiss a. J. (2013b). A case study on spatial and temporal hydraulic variability in an alpine gravel-bed stream based on the hydromorphological index of diversity. *Ecohydrology*, 6(4):652–667.
- Graf W. L. (2006). Downstream hydrologic and geomorphic effects of large dams on American rivers. *Geomorphology*, 79(3-4):336–360.
- Grant G., Schmidt J. and Lewis S. (2003). *A Peculiar River*, volume 7.
- G.S.E. (2012). Rapporto statistico impianti a fonti rinnovabili. Technical report, Gestore dei Servizi Energetici – GSE S.p.A., Roma.
- Habersack H. M. and Piegay H. (2007). Challenges in river restoration in the Alps and their surrounding areas. In Habersack, Helmut; Piégay, Hervé; Rinaldi M., editor, *Gravel Bed Rivers 6: From Process Understanding to River Restoration*, pages 703–737. Elsevier.
- Halleraker J. H., Saltveit S. J., Harby A., Arnekleiv J. V., Fjeldstad H.-P. H.-P. and Kohler B. (2003). Factors influencing stranding of wild juvenile brown trout (*Salmo trutta*) during rapid and frequent flow decreases in an artificial stream. *River Research and Applications*, 19(5-6):589–603.
- Harby A. and Noack M. (2013). *Ecohydraulics*. John Wiley & Sons.
- Hari R. E., Livingstone D. M., Siber R., Burkhardt-Holm P. and Guttinger H. (2006). Consequences of climatic change for water temperature and brown trout populations in Alpine rivers and streams. *Global Change Biology*, 12(1):10–26.
- Hauer C., Unfer G., Graf W., Leitner P., Zeiringer B. and Habersack H. (2012). Hydro-morphologically related variance in benthic drift and its importance for numerical habitat modelling. *Hydrobiologia*, 683(1):83–108.

-
- Hauer C., Schober B. and Habersack H. (2013a). Impact analysis of river morphology and roughness variability on hydropeaking based on numerical modelling. *Hydrological Processes*, 27(15):2209–2224.
- Hauer C., Unfer G., Holzmann H., Schmutz S. and Habersack H. (2013b). The impact of discharge change on physical instream habitats and its response to river morphology. *Climatic Change*, 116:827–850.
- Hauer C., Unfer G., Holzapfel P., Haimann M. and Habersack H. (2014). Impact of channel bar form and grain size variability on estimated stranding risk of juvenile brown trout during hydropeaking. *Earth Surface Processes and Landforms*, 1641(March):n/a–n/a.
- Holland S. P. and Mansur E. T. (2008). Is Real-Time Pricing Green? The Environmental Impacts of Electricity Demand Variance. *Review of Economics and Statistics*, 90(3): 550–561.
- Horn A. L., Rueda F. J., Hörmann G. and Fohrer N. (2004). Implementing river water quality modelling issues in mesoscale watershed models for water policy demands—an overview on current concepts, deficits, and future tasks. *Physics and Chemistry of the Earth, Parts A/B/C*, 29(11):725–737.
- Horne B. D., Rutherford E. S. and Wehrly K. E. (2004). Simulating effects of hydrodam alteration on thermal regime and wild steelhead recruitment in a stable-flow Lake Michigan tributary. *River Research and Applications*, 20(2):185–203.
- Irvine R. L., Oussoren T., Baxter J. S. and Schmidt D. C. (2009). The effects of flow reduction rates on fish stranding in British Columbia, Canada. *River Research and Applications*, 25(4):405–415.
- Irvine R. L., Thorley J. L., Westcott R., Schmidt D. and DeRosa D. (2014). Why do fish strand? An analysis of ten years of flow reduction monitoring data from the Columbia and Kootenay rivers, Canada. *River Research and Applications*, 7(4):n/a–n/a.
- Jager H. I. and Smith B. T. (2008). Sustainable reservoir operation: Can we generate hydropower and preserve ecosystem values?
- Jiang L., Ban X., Wang X. and Cai X. (2014). Assessment of Hydrologic Alterations Caused by the Three Gorges Dam in the Middle and Lower Reaches of Yangtze River, China. *Water*, 6(5):1419–1434.
- Jones N. E. (2013). Spatial patterns of benthic invertebrates in regulated and natural rivers. *River Res Appl*, 29(3):343–351.
- Jones N. E. (2014). The dual nature of hydropeaking rivers: is ecopeaking possible? *River Research and Applications*, 30(4):521–526.
- Jordan F. (2007). *Modèle de prévision et de gestion des crues: optimisation des opérations des aménagements hydroélectriques à accumulation pour la réduction des débits de crue*. PhD thesis, Ecole polytechnique fédérale de Lausanne, Lausanne, Switzerland.

- Kaushal S. S., Likens G. E., Jaworski N. A., Pace M. L., Sides A. M., Seekell D., Belt K. T., Secor D. H. and Wingate R. L. (2010). Rising stream and river temperatures in the United States. *Frontiers in Ecology and the Environment*, 8(9):461–466.
- Kawahara M. and Umetsu T. (1986). Finite element method for moving boundary problems in river flow. *International Journal for Numerical Methods in Fluids*, 6(6):365–386.
- Kim K. S. and Chapra S. C. (1997). Temperature model for highly transient shallow streams. *Journal of Hydraulic Engineering*, 123(1):30–40.
- Kinouchi T. (2007). Impact of long-term water and energy consumption in Tokyo on wastewater effluent: implications for the thermal degradation of urban streams. *Hydrological Processes*, 21(9):1207–1216.
- Kottek M., Grieser J., Beck C., Rudolf B. and Rubel F. (2006). World Map of the Köppen-Geiger climate classification updated. *Meteorol Z*, 15(3):259–263.
- Lai Y. and Mooney D. (2009). On a Two-Dimensional Temperature Model: Development and Verification. In *World Environmental and Water Resources Congress 2009*, pages 1–14, Kansas City, Missouri, US.
- Liang Q. (2010). A well-balanced and non-negative numerical scheme for solving the integrated shallow water and solute transport equations. *Communications in Computational Physics*, 7(5):1049.
- Liang Q. and Borthwick A. G. (2009). Adaptive quadtree simulation of shallow flows with wet–dry fronts over complex topography. *Computers & Fluids*, 38(2):221–234.
- Lundquist J. D. and Cayan D. R. (2002). Seasonal and spatial patterns in diurnal cycles in streamflow in the western United States. *J Hydrometeorol*, 3(5):591–603.
- Lytle D. A. and Poff N. L. (2004). Adaptation to natural flow regimes. *Trends in Ecology and Evolution*, 19(2):94–100.
- Meile T., Boillat J.-L. and Schleiss A. (2008). Reduction of Hydropeaking in Rivers by Bank Macro Roughness. *Wasserwirtschaft*, 98(12):18–24.
- Meile T., Boillat J. L. and Schleiss a. J. (2011). Hydropeaking indicators for characterization of the Upper-Rhone River in Switzerland. *Aquatic Sciences*, 73(1):171–182.
- Montecinos G. I. and Toro E. F. (2014). Reformulations for general advection–diffusion–reaction equations and locally implicit aders schemes. *Journal of Computational Physics*, 275:415–442.
- Montecinos G. I., Müller L. O. and Toro E. F. (2014). Hyperbolic reformulation of a 1d viscoelastic blood flow model and aders finite volume schemes. *Journal of Computational Physics*, 266:101–123.
- Muhar S., Jungwirth M., Wiesner C., Poppe M., Schmutz S., Hohennsinner S. and Habersack H. (2007). Restoring riverine landscapes at Drau River: successes and deficits in the context of ecological integrity. In *Gravel-Bed Rivers VI: From Process Understanding to River Restoration*, volume 2025, pages 779–803.

-
- Nagrodski A., Raby G. D., Hasler C. T., Taylor M. K. and Cooke S. J. (2012). Fish stranding in freshwater systems: sources, consequences, and mitigation. *Journal of environmental management*, 103:133–41.
- Nikolos I. and Delis A. (2009). An unstructured node-centered finite volume scheme for shallow water flows with wet/dry fronts over complex topography. *Computer Methods in Applied Mechanics and Engineering*, 198(47):3723–3750.
- Norwegian Ministry of Petroleum and Energy (2012). Retningslinjer for revisjon av konsesjonsvilkår for vassdragsreguleringer (English: Guidelines for revision of hydropower licenses). Technical report, Norwegian Ministry of Petroleum and Energy, Oslo.
- Noye B. and Tan H. (1989). Finite difference methods for solving the two-dimensional advection–diffusion equation. *International Journal for Numerical Methods in Fluids*, 9(1):75–98.
- Olden J. D. and Naiman R. J. (2010). Incorporating thermal regimes into environmental flows assessments: modifying dam operations to restore freshwater ecosystem integrity. *Freshwater Biology*, 55(1):86–107.
- Ouellet V., Secretan Y., St-Hilaire A. and Morin J. (2014). Water temperature modelling in a controlled environment: comparative study of heat budget equations. *Hydrological Processes*, 28(2):279–292.
- Paetzold A., Yoshimura C. and Tockner K. (2008). Riparian arthropod responses to flow regulation and river channelization. *Journal of Applied Ecology*, 45:894–903.
- Pekárová P., Miklánek P., Halmová D., Onderka M., Pekár J., Kučárová K., Liová S. and Škoda P. (2011). Long-term trend and multi-annual variability of water temperature in the pristine Bela River basin (Slovakia). *Journal of Hydrology*, 400(3-4):333–340.
- Person E., Bieri M., Peter A. and Schleiss A. J. (2013). Mitigation measures for fish habitat improvement in Alpine rivers affected by hydropower operations. *Ecohydrology*, pages n/a–n/a.
- Petts G. E. and Gurnell A. M. (2005). Dams and geomorphology: Research progress and future directions. *Geomorphology*, 71(1-2):27–47.
- Poff N. L. and Zimmerman J. K. H. (2010). Ecological responses to altered flow regimes: a literature review to inform the science and management of environmental flows. *Freshwater Biol.*, 55(1):194–205.
- Poff N. L., Allan J. D., Bain M. B., Karr J. R., Prestegard K. L., Richter B. D., Sparks R. E. and Stromberg J. C. (1997). The natural flow regime. *BioScience*, pages 769–784.
- Prats J., Val R., Armengol J. and Dolz J. (2010). Temporal variability in the thermal regime of the lower Ebro River (Spain) and alteration due to anthropogenic factors. *Journal of Hydrology*, 387(1-2):105–118.
- Puffer M., Berg O. K., Huusko A., Vehanen T., Forseth T. and Einum S. (2014). Seasonal effects of hydropeaking on growth, energetics and movement of juvenile atlantic salmon (*Salmo salar*). *River Research and Applications*, 7:n/a–n/a.

- Rekolainen S., Kämäri J., Hiltunen M. and Saloranta T. M. (2003). A conceptual framework for identifying the need and role of models in the implementation of the water framework directive. *International Journal of River Basin Management*, 1(4):347–352.
- Rheinheimer D. E. and Viers J. H. (2014). Combined effects of reservoir operations and climate warming on the flow regime of hydropower bypass reaches of California's Sierra Nevada.
- Rheinheimer D. E., Null S. E. and Lund J. R. (2011). Optimizing Selective Withdrawal from Reservoirs to Manage Downstream Temperatures with Climate Warming. *Journal of Water Resources Planning and Management*, pages 1–9.
- Richards R. R., Gates K. K. and Kerans B. L. (2013). Effects of simulated rapid water level fluctuations (hydropeaking) on survival of sensitive benthic species.
- Richter B. D., Baumgartner J. V., Powell J. and Braun D. P. (1996). A Method for Assessing Hydrologic Alteration within Ecosystems. *Conserv Biol*, 10(4):1163–1174.
- Rinaldi M., Surian N., Comiti F. and Bussettini M. (2013). A method for the assessment and analysis of the hydromorphological condition of Italian streams: The Morphological Quality Index (MQI). *Geomorphology*, 180-181:96–108.
- Rohde S., Schütz M., Kienast F. and Englmaier P. (2005). River widening: an approach to restoring riparian habitats and plant species. *River Research and Applications*, 21(10):1075–1094.
- Rohde S., Hostmann M., Peter A. and Ewald K. (2006). Room for rivers: An integrative search strategy for floodplain restoration. *Landscape and Urban Planning*, 78(1-2): 50–70.
- Saltveit S. J., Halleraker J. H., Arnekleiv J. V. and Harby A. (2001). Field experiments on stranding in juvenile Atlantic salmon (*Salmo salar*) and brown trout (*Salmo trutta*) during rapid flow decreases caused by hydropeaking. *Regul. River*, 17(4-5):609–622.
- Sauterleute J. F. and Charmasson J. (2014). A computational tool for the characterisation of rapid fluctuations in flow and stage in rivers caused by hydropeaking. *Environ Modell Softw*, 55:266–278.
- Sawyer A. H., Cardenas M. B., Bomar A. and Mackey M. (2009). Impact of dam operations on hyporheic exchange in the riparian zone of a regulated river. *Hydrological Processes*, 23:2129–2137.
- Schmidt J. C. and Wilcock P. R. (2008). Metrics for assessing the downstream effects of dams. *Water Resources Research*, 44(4):n/a–n/a.
- Schmutz S., Bakken T. H., Friedrich T., Greimel F., Harby A., Jungwirth M., Melcher A., Unfer G. and Zeiringer B. (2014). Response of fish communities to hydrological and morphological alterations in hydropeaking rivers of Austria. *River Research and Applications*, 28(6):n/a–n/a.

-
- Scruton D. A., Ollerhead L. M. N., Clarke K. D., Pennell C., Alfredsen K., Harby A. and Kelley D. (2003). The behavioural response of juvenile Atlantic salmon (*Salmo salar*) and brook trout (*Salvelinus fontinalis*) to experimental hydropeaking on a Newfoundland (Canada) River. *River Research and Applications*, 19(5-6):577–587.
- Shen Y. and Diplas P. (2010). Modeling Unsteady Flow Characteristics of Hydropeaking Operations and Their Implications on Fish Habitat. *Journal of Hydraulic Engineering*, 136(12):1053–1066.
- Shuster W. D., Zhang Y., Roy A. H., Daniel F. B. and Troyer M. (2008). Characterizing storm hydrograph rise and fall dynamics with stream stage data. *J Am Water Resour Assoc*, 44(6):1431–1440.
- Siviglia A. and Toro E. F. (2009). Waf method and splitting procedure for simulating hydro-and thermal-peaking waves in open-channel flows. *Journal of Hydraulic Engineering*, 135(8):651–662.
- Siviglia A., Repetto R., Zolezzi G. and Tubino M. (2008). River bed evolution due to channel expansion: general behaviour and application to a case study (Kugart River, Kyrgyz Republic). *River Research and Applications*, 24(9):1271–1287.
- Siviglia A., Stecca G., Vanzo D., Zolezzi G., Toro E. F. and Tubino M. (2013). Numerical modelling of two-dimensional morphodynamics with applications to river bars and bifurcations. *Advances in Water Resources*, 52:243–260.
- Surian N. and Rinaldi M. (2003). Morphological response to river engineering and management in alluvial channels in Italy. *Geomorphology*, 50(4):307–326.
- Swiss Federal Office of Energy (2013). Energieperspektiven 2050: Zusammenfassung. Technical report, Swiss Federal Office of Energy.
- Tealdi S., Camporeale C. and Ridolfi L. (2011). Long-term morphological river response to hydrological changes. *Advances in Water Resources*, 34(12):1643–1655.
- Thompson L. C., Cocherell S. a., Chun S. N., Cech J. J. and Klimley a. P. (2010). Longitudinal movement of fish in response to a single-day flow pulse. *Environmental Biology of Fishes*, 90(3):253–261.
- Toffolon M., Siviglia A. and Zolezzi G. (2010). Thermal wave dynamics in rivers affected by hydropeaking. *Water Resources Research*, 46(8):n/a–n/a.
- Toro E. and Titarev V. (2002). Solution of the generalized riemann problem for advection–reaction equations. *Proceedings of the Royal Society of London. Series A: Mathematical, Physical and Engineering Sciences*, 458(2018):271–281.
- Toro E. F. and Montecinos G. I. (2014). Advection-diffusion-reaction equations: Hyperbolization and high-order ader discretizations. *SIAM Journal on Scientific Computing*, 36(5):A2423–A2457.
- Trentini G., Monaci M., Goltera A., Comiti F., Gallmetzer W. and Mazzorana B., editors (2012). *Riqualficazione del Rio Mareta: pianificazione e prime fasi di attuazione*. bu.press, Bolzano.

- Tsakiris G. and Alexakis D. (2012). Water quality models: an overview.
- Tubino M., Repetto R. and Zolezzi G. (1999). Free bars in rivers. *Journal of Hydraulic Research*, 37(6):759–775.
- Tuhtan J. a., Noack M. and Wieprecht S. (2012). Estimating stranding risk due to hydropeaking for juvenile European grayling considering river morphology. *KSCE Journal of Civil Engineering*, 16(2):197–206.
- Tukey J. W. (1977). *Exploratory data analysis*. Addison-Wesley Publishing company, Reading, Mass.
- Valentin S., Lauters F., Sabaton C., Breil P. and Souchon Y. (1996). Modelling temporal variations of physical habitat for brown trout (*Salmo trutta*) in hydropeaking conditions. *Regul River*, 12(2-3):317–330.
- Vehanen T., Jurvelius J. and Lahti M. (2005). Habitat utilisation by fish community in a short-term regulated river reservoir. *Hydrobiologia*, 545(1):257–270.
- Wang J. N., Li C., Duan X. B., Luo H. H., Feng S. X., Peng Q. D. and Liao W. G. (2013a). The relationship between thermal regime alteration and spawning delay of the four major chinese carps in the yangtze river below the three gorges dam.
- Wang Q., Li S., Jia P., Qi C. and Ding F. (2013b). A review of surface water quality models. *The Scientific World Journal*, 2013.
- Ward J. V. and Stanford J. A. (1979). *The ecology of regulated streams*. Plenum Press.
- Webb B. W. and Nobilis F. (2007). Long-term changes in river temperature and the influence of climatic and hydrological factors. *Hydrological Sciences Journal*, 52(1): 74–85.
- Webb B. W., Hannah D. M., Moore R. D., Brown L. E. and Nobilis F. (2008). Recent advances in stream and river temperature research. *Hydrological Processes*, 22(7):902–918.
- Wilcock P. R. (1996). Estimating local bed shear stress from velocity observations. *Water Resources Research*, 32(11):3361–3366.
- Young P. S., Cech J. J. and Thompson L. C. (2011). Hydropower-related pulsed-flow impacts on stream fishes: a brief review, conceptual model, knowledge gaps, and research needs. *Reviews in Fish Biology and Fisheries*, 21(4):713–731.
- Zhong Y. and Power G. (1996). Environmental impacts of hydroelectric projects on fish resources in China. *Regulated Rivers: Research & Management*, 12(1):81–98.
- Zimmerman J. K. H., Letcher B. H., Nislow K. H., Lutz K. A. and Magilligan F. J. (2010). Determining the effects of dams on subdaily variation in river flows at a whole-basin scale. *River Research and Applications*, 26(10):1246–1260.
- Zolezzi G., Bellin A., Bruno M. C., Maiolini B. and Siviglia A. (2009). Assessing hydrological alterations at multiple temporal scales: Adige River, Italy. *Water Resources Research*, 45(12):1–15.

Zolezzi G., Siviglia A., Toffolon M. and Maiolini B. (2011). Thermopeaking in Alpine streams: event characterization and time scales. *Ecohydrology*, 4(4):564–576.

Appendix A

Based on: Carolli M., D. Vanzo, G. Zolezzi, A. Siviglia, M. C. Bruno and K. Alfredsen. A simple procedure for the assessment of hydropeaking flow alterations applied to several European streams. Aquatic Sciences, accepted for publication.

Release of water from storage hydropower plants generates rapid flow and stage fluctuations (hydropeaking) in the receiving water bodies at a variety of sub-daily time-scales. In this paper we present an approach to quantify such variations, which is easy to apply, requires stream flow data at a readily available resolution, and allows for the comparison of hydropeaking flow alteration amongst several gauged stations. Hydropeaking flow alteration is quantified by adopting a rigorous statistical approach and using two indicators related to flow magnitude and rate of change. We utilised a comprehensive stream-flow dataset of 105 gauging stations from Italy, Switzerland and Norway to develop our method.

Firstly, we used a GIS approach to objectively label the stations in two groups: gauges with an upstream water release from hydropower plants (peaked group) and without upstream releases (unpeaked group). Secondly, we used the datasets of the unpeaked group to calculate one threshold for each of the two indicators. Thresholds defined three different classes: absent or low pressure, medium, and high pressure, and all stations were classified according to these pressure levels. Thirdly, we showed that the thresholds can change, depending on the country dataset, the year chosen for the analysis, the number of gauging stations, and the temporal resolution of the dataset, but the outcome of the classification remains the same. Hence, the classification method we propose can be considered very robust since it is almost insensitive to the hydropeaking thresholds variability. Therefore, the method is broadly applicable to procedures for the evaluation of flow regime alterations and classification of river hydromorphological quality, and may help to guide river restoration actions.

A.1 Introduction

Flow variability is recognized as a key driver to sustain the biodiversity and the functionality of river ecosystems. This variability acts over a large spectrum of temporal scales ranging from hours to seasons, and is important for maintaining hydraulic complexity, sediment transport, hyporheic exchanges, floodplain connections and habitat structure and complexity (Poff *et al.*, 1997; Poff and Zimmerman, 2010). A major role is played by sub-daily variations that may induce heavy hydro-morphological alterations in a water course. These short-time scale variations can result from natural events such as strong

snowmelt and rainfall events, or from human activities as water releases from storage hydropower plants. The magnitude of natural events results in diel variations in flow of about 10% of the daily mean flow (Lundquist and Cayan, 2002; Shuster *et al.*, 2008), while anthropogenic water releases can cause much more severe variations (Zolezzi *et al.*, 2009). The occurrence of natural events is limited to few days (precipitations) and few months (snowmelt) during the year, while anthropogenic releases can persist each day of the year.

The present work focuses on hydropeaking, the rapid variations of the flow regime induced by power production from hydroelectric plants at the sub-daily scale. Hydropeaking has several known effects on the river biota: it causes alteration of abundance and faunal composition of fish, benthic and hyporheic communities (Bruno *et al.*, 2009, 2010; Jones, 2013; Tuhtan *et al.*, 2012; Young *et al.*, 2011), increases fish and invertebrates stranding (Scruton *et al.*, 2003) reduces nearshore-riparian habitats (Fette *et al.*, 2007).

Because of its relevance, quantification of sub-daily alterations is becoming increasingly important in legislation at a regional, national and international level, as, for instance, in relation to the Water Framework Directive (European Commission, 2000), in the Swiss Water Protection Act (FOEN, 2011), in the implementation of Italian national methodology for hydromorphological assessment of rivers (Rinaldi *et al.*, 2013) and in the Norwegian regulations on the renewal of hydropower licensing (Anonymous, 2012).

Hydrological alterations are usually quantified using daily discharge data (Richter *et al.*, 1996), thus ignoring sub-daily variations, and few methods adopt flow data at the higher resolution necessary for the quantification of hydropeaking-induced alterations (Meile *et al.*, 2011; Zimmerman *et al.*, 2010; Bevelhimer *et al.*, 2014; Sauterleute and Charmasson, 2014). For instance, Meile *et al.* (2011) proposed a set of three indicators and performed an analysis on different gauging stations along the Upper Rhone river. The authors used these indicators to define regulated and unregulated water courses. Zimmerman *et al.* (2010) developed a predictive method based on four “flashiness indices” that can be computed from hourly discharge data, and applied it to 30 gauging stations in the Connecticut River basin (USA) to compare the potential impacts of different types of dam operations. Recently, Sauterleute and Charmasson (2014) proposed an assessment tool based on eighteen hydropeaking parameters, grouped by magnitude, time and frequency. Their analysis provides detailed information that can be particularly useful for the assessment of hydrological impacts and potential mitigation measures in relation to hydropeaking. Bevelhimer *et al.* (2014) divided a set of streams in three different groups: without alterations, with peaking and run of the river hydropower plants and compared the respective flow regimes using different indicators that quantify magnitude, variation, frequency and rate of change of flow events at sub-daily (hourly) and daily scale.

The indicators proposed by Meile *et al.* (2011) and by Sauterleute and Charmasson (2014) can potentially be used to compare different levels of hydropeaking pressure among different streams but in both cases their application was limited to only one water course. Moreover, their methodology might not be broadly applicable, as the method proposed by Meile *et al.* (2011) requires long-term data of the same river watershed, which may not always be available. The large number of parameters adopted in the methodology of Sauterleute and Charmasson (2014) does not allow to make straightforward comparison among streams. The method proposed by Zimmerman *et al.* (2010) focuses on a single watershed and requires detailed data collection of the basin in order to assess the hydrological alterations induced by a different set of dam operations. The method proposed by

Bevelhimer *et al.* (2014) aims to compare different streams but requires the calculation of a large set of indicators. Thus, a new easy-to-use methodology based on few indicators, calculated from a temporally short, but spatially wide dataset is needed to classify the “hydropeaking pressure” that we define here as the physical alteration of flow regime due to hydropeaking. In particular, we select two largely independent hydrological variables to measure pressure of hydropeaking, discharge magnitude and rate of change (Richter *et al.*, 1996; Meile *et al.*, 2011; Sauterleute and Charmasson, 2014). The classification of hydropeaking pressure resulting from the application of the proposed methodology is purely hydrological and has no direct significance for the assessment of the effects on river ecology. The use of thresholds differs from the most commonly used methods (e.g. Richter *et al.*, 1996; Sauterleute and Charmasson, 2014) which usually compare before-after impacts data series.

Most of the large storage hydropower plants were built around the half of the past century in all three investigated countries, and discharge data at sub-daily resolution are available only for much more recent times. Therefore, we could not use a classical pre- and post-regulation comparison for each gauged station. Instead, our approach uses a space-for-time proxy to allow detecting hydrological alterations even if historical data are not available. Specifically, we sought to develop a methodology to classify levels of “hydropeaking pressure” with the following requirements: i) it is easily implementable by using the smallest possible number of indicators, which are based on short time datasets that are commonly available at sub-daily sampling resolution; ii) it allows comparison among different gauged stations in the same area; iii) it distinguishes between types of hydropeaking pressure; iv) it is statistically robust.

The methodology can effectively be used as a first screening to prioritize sites for the implementation of river restoration. Such sites would, however, need further investigation of the biotic effects of the same hydropeaking pressure which can vary from reach to reach, depending on a variety of local and non-local factors, such as channel morphology, bed sediment composition, water quality, presence of other hydro-morphological stressors (Valentin *et al.*, 1996; Bunt *et al.*, 1999; Hauer *et al.*, 2013a).

A.2 Methods

A.2.1 Flow data selection

We used discharge data from 105 gauging stations located in Italy, Switzerland and Norway (Table A.1), collected from public rivers monitoring agencies. Based on available GIS informations, and/or the analysis of the streamflow time series, we identified two different groups of gauges: the first group is characterized by the presence of an upstream water release from a storage hydropower plants (peaked stations) and the second one without any release (unpeaked stations).

The first dataset was based on 28 gauges (16 peaked and 12 unpeaked) in the NE part of Italy (Trentino region, see Fig. A.1 a). These stations are well-distributed on the entire regional area. We used a 1-year dataset (2012) at a resolution of 15 minutes. The second dataset included flow data from 36 gauging stations located in Switzerland, 18 of such stations are peaked and 18 unpeaked (see Fig. A.1 b). The dataset is 6 years long (2007-2012) with a resolution of 15 minutes. Finally, the third dataset is from Norway (see Fig. A.1 c), where we considered 14 peaked and 27 unpeaked gauges. The dataset

	Italy (IT)	Switzerland (CH)	Norway (NO)
Total stations	28	36	41
Peaked stations	16	18	14
Unpeaked stations	12	18	27
Data breakdown time [min]	15	15	60
Length of data record (available years)	1 year (2012)	6 years (2007-2012)	6 years (2007-2012)
Size of the equivalent yearly dataset (peaked and unpeaked stations)	28	216	246
Size of the equivalent yearly dataset (peaked stations)	16	108	84
Size of the equivalent yearly dataset (unpeaked stations)	12	108	162
Latitude Limits	45°-46°30'	45°-48°	57°-71°
Longitude limits	10°-11°50'	5°-11°	5°-31°
Climate (Kotttek <i>et al.</i> , 2006)	Polar tundra, snow fully humid cool summer, snow fully humid warm summer	Polar tundra, continentally fully humid cool summer, continentally fully humid warm summer	Polar tundra, snow fully humid cool summer, continentally fully humid cool summer

TABLE A.1: Summary of features of the three datasets.

is 6 years long (2007-2012) and the data resolution is 1 hour. Stream gauges were chosen in order to cover different river types: glacial, snow-fed, rain-fed, lake emissary, regulated rivers not affected by hydropeaking.

The size of equivalent yearly datasets was calculated by multiplying the available number of years by the number of gauging stations, for a total of 490 data series, with 282 unpeaked and 208 peaked equivalent yearly datasets. The main characteristics of the datasets and of the climate of each country are presented in Table A.1, and the list of the stations used for the analysis is given in Tables A.2, A.3, A.4.

A.2.2 Indicators

As a starting point we considered two of the three indicators proposed by Meile *et al.* (2011) and we conveniently modified them in order to provide a single indicator for an easy classification of the data series. Namely, the first indicator, *HP1*, is a dimensionless

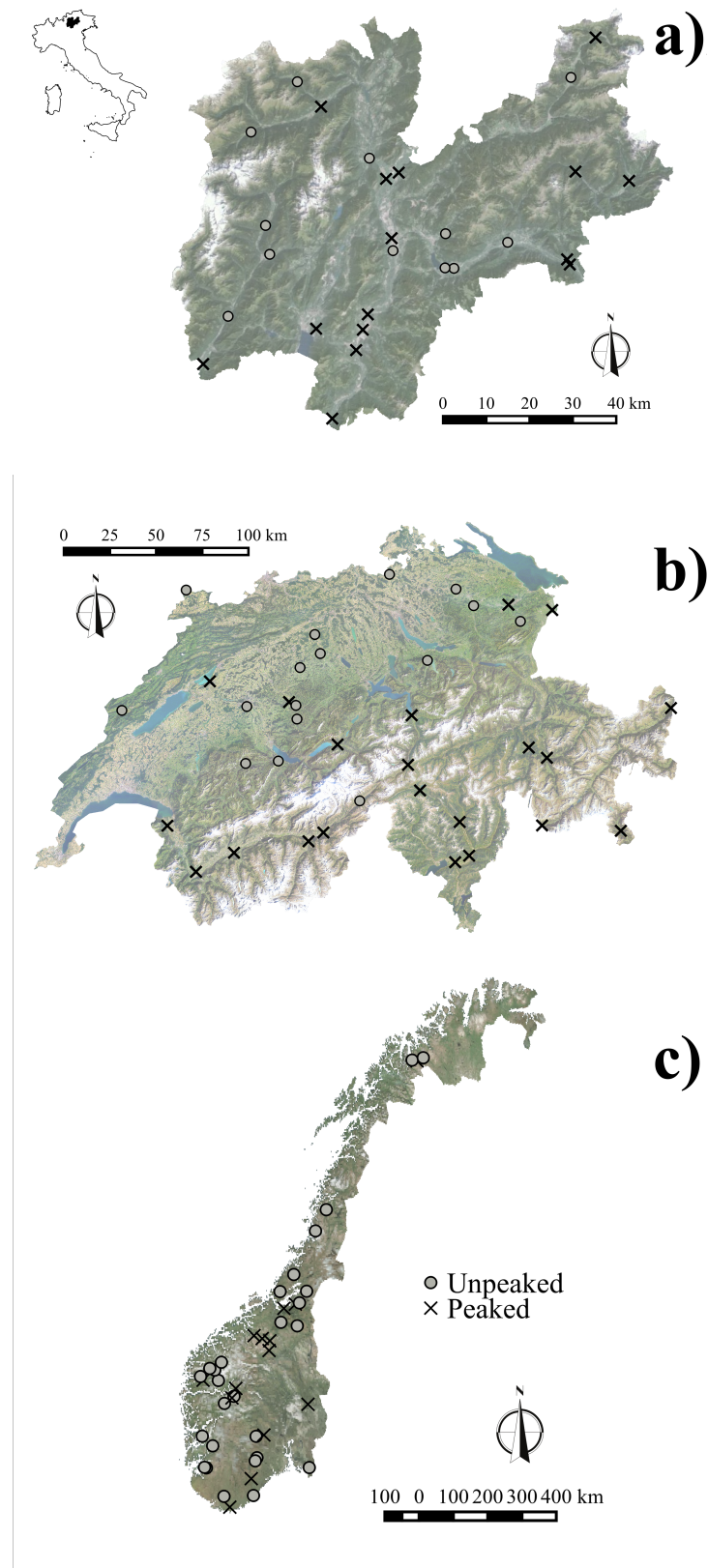


FIGURE A.1: Geographic distribution of the a) Italian gauging stations, b) Swiss gauging stations, and c) Norwegian gauging stations. Circles represent the unpeaked stations, and crosses the peaked stations.

measure of the magnitude of hydropeaking and is defined as follows:

$$HP1_i = \frac{Q_{max,i} - Q_{min,i}}{Q_{mean,i}}, i \in [1, 365]; \quad (A.1)$$

$$HP1 = median(HP1_i). \quad (A.2)$$

where subscript i denotes the day of the year. $HP1$ is defined as the annual median of daily values of $HP1_i$, calculated as the difference between the maximum and the minimum discharge value ($Q_{max,i}$ and $Q_{min,i}$, respectively) over the i^{th} day, normalized by the discharge daily mean value ($Q_{mean,i}$). The second indicator, $HP2$, measures the temporal rate of discharge changes and is defined as follows:

$$(HP2_k)_i = \left(\frac{\Delta Q_k}{\Delta t_k} \right)_i = \left(\frac{Q_k - Q_{k-1}}{t_k - t_{k-1}} \right)_i, i \in [1, 365] \quad (A.3)$$

$$HP2_i = P_{90} |(HP2_k)_i|; \quad (A.4)$$

$$HP2 = median(HP2_i). \quad (A.5)$$

where Q_k refers to each available discharge datum (e.g. $[1 \leq k \leq 24]$ for data sampled every 60 minutes). $HP2$ is compute as the annual median of daily values of $HP2_i$, which is the 90th percentile (P_{90}) of the discretized time derivative of the instantaneous stream-flow series. $HP2$ is a dimensional parameter and it is expressed in $m^3s^{-1}h^{-1}$. The ninetieth percentile P_{90} was arbitrarily chosen as a measure of the daily rate of change because it is a conservative estimation of the cutoff value for extreme high flow events and allows excluding possible error measurements. We used the absolute value of P_{90} , this taking into account ramping rates of the hydrographs in both directions, i.e. the increasing and falling limb. Finally, we used annual median values to characterize each gauged station with a distinctive yearly value for both indicators. The median value is used, for instance, as the measure of central tendency for the non-parametric approach for the hydrological alteration parameters of IHA7 (Richter *et al.*, 1996).

A.2.3 Hydropeaking thresholds and hydropeaking pressure classes

For the quantification of the hydropeaking pressure we identified a threshold for each indicator: TR_{HP1} and TR_{HP2} . The thresholds are calculated from the 282 unpeaked datasets using a non-parametric method (Tukey, 1977), in order to avoid a priori assumptions on normality in data distribution. The values of the two thresholds correspond to the values of the two estimators which separate the outliers from the rest of the unpeaked distribution. The chosen outlier estimators which correspond to the thresholds' values are:

$$TR_{HP1} = P_{75}(HP1_i^{unp}) + 1.5(P_{75} - P_{25})(HP1_i^{unp}), \quad (A.6)$$

$$TR_{HP2} = P_{75}(HP2_i^{unp}) + 1.5(P_{75} - P_{25})(HP2_i^{unp}), \quad (A.7)$$

where $HP1_i^{unp}$ and $HP2_i^{unp}$ are the daily values of the two indicators for unpeaked stream gauges and P_{75} and P_{25} are the 75th and the 25th percentile of the distribution, respectively.

Once the thresholds (A.6) and (A.7) are identified, the following conditional rules are applied to each station to identify three different classes of hydropeaking pressure:

Watershed	Gauged station	Group	HP1	HP2	Class
Vanoi	Caoria	Peaked	1.12	1.14	2a
Avisio	Cavalese	Peaked	1.13	2.39	3
Cismon	Fiera di Primiero	Peaked	0.82	0.81	2a
Noce	Malè	Peaked	0.59	2.15	2b
Noce	Marco	Peaked	0.43	3.60	2b
Noce	Mezzolombardo	Peaked	1.62	17.25	3
Noce	Pellizzano	Peaked	0.81	3.02	3
Brenta	Ponte Filippini	Peaked	0.39	1.16	1
Adige	Ponte San Lorenzo	Peaked	0.39	17.21	2b
Chiese	Ponte Tedeschi	Peaked	2.16	7.44	3
Leno	Rovereto	Peaked	1.26	1.29	3
Adige	San Michele all' Adige	Peaked	0.36	8.25	2b
Sarca	Torbole	Peaked	0.18	0.34	1
Fersina	Trento	Peaked	1.60	0.70	2a
Adige	Villalagarina	Peaked	0.38	13.55	2b
Adige	Vo Destro	Peaked	0.47	13.19	2b
Brenta	Borgo Valsugana	Unpeaked	0.16	0.22	1
Brenta	Caldonazzo	Unpeaked	0.80	0.34	2a
Avisio	Campitello	Unpeaked	0.29	0.26	1
Fersina	Canezza	Unpeaked	0.43	0.16	1
Chiese	Cimego	Unpeaked	0.10	0.18	1
Brenta	Levico	Unpeaked	0.12	0.12	1
Sarca	Preore	Unpeaked	0.29	0.59	1
Rabbies	Rabbies	Unpeaked	0.25	0.17	1
Avisio	Soraga	Unpeaked	0.21	0.34	1
Sarca	Spiazzo	Unpeaked	0.28	0.36	1
Sporeggio	Sporeggio	Unpeaked	0.21	0.36	1
Noce	Vermigliana	Unpeaked	0.24	0.16	1

TABLE A.2: Italian gauged stations grouped by the values of the hydropeaking indicators $HP1$ and $HP2$, and relative hydropeaking pressure class (calculated from a one year data record).

1. **Class 1:** *Absent or low pressure.* $HP1 < TR_{HP1}$ and $HP2 < TR_{HP2}$. The gauged station is statistically similar to an unpeaked gauged station.
2. **Class 2a:** *Medium pressure.* $HP1 > TR_{HP1}$ and $HP2 < TR_{HP2}$. $HP1$ indicator is above threshold and the gauged station is an outlier in hydropeaking magnitude compared to unpeaked group.
3. **Class 2b:** *Medium pressure.* $HP2 > TR_{HP2}$ and $HP1 < TR_{HP1}$. $HP2$ indicator is above threshold and the gauged station is an outlier in temporal rate of discharge variations compared to unpeaked group.
4. **Class 3:** *High pressure.* $HP1 > TR_{HP1}$ and $HP2 > TR_{HP2}$. Both indicators are above thresholds.

Watershed	Gauged station	Group	HP1		HP2		Class
			Min	Max	Min	Max	
Ticino	Bellinzona	Peaked	0.60	1.28	10.39	15.00	2b-3
Rhone	Branson	Peaked	0.39	0.64	10.17	16.60	2b
Aare	Brienzwiler	Peaked	0.68	0.97	8.44	10.57	2b-3
Saltina	Brig	Peaked	0.39	0.54	0.12	0.15	1
Rhein	Diepoldsau, Rietbrucke	Peaked	0.46	0.58	20.01	24.95	2b
Hintherrhein	Fursteanu	Peaked	0.91	1.66	14.22	18.30	3
Aare	Hagneck	Peaked	0.49	0.72	21.94	34.09	2b
Poschiavino	Le Prese	Peaked	0.41	0.75	0.66	1.00	1-2a
Inn	Martina	Peaked	1.63	1.89	20.12	25.87	3
Ticino	Polleggio, Campagna	Peaked	0.93	2.55	5.49	12.99	3
Rhone	Porte du Scèx	Peaked	0.34	0.55	12.39	16.53	2b
Ticino	Riazzino	Peaked	0.60	1.28	11.63	16.79	2b-3
Reuss	Seedorf	Peaked	0.51	0.63	6.16	9.19	2b
Rhone	Sion	Peaked	0.38	0.61	6.39	8.84	2b
Mera	Soglio	Peaked	0.18	0.32	0.17	0.34	1
Sitter	St. Gallen, Bruggen	Peaked	1.26	1.70	2.80	5.11	3
Albula	Tiefencastel	Peaked	0.67	1.23	3.74	4.87	2b-3
Vispa	Visp	Peaked	0.75	1.23	4.12	5.66	3
Reuss	Andermatt	Unpeaked	0.18	0.27	0.16	0.26	1
Sitter	Appenzell	Unpeaked	0.34	0.47	0.14	0.18	1
Aare	Bern-Schonau	Unpeaked	0.06	0.08	0.81	1.47	1-2b
Allaine	Boncourt, Frontiere	Unpeaked	0.16	0.33	0.03	0.07	1
Emme	Eggiwil, Heidbuel	Unpeaked	0.38	0.46	0.06	0.13	1
Alp	Einsiedeln	Unpeaked	0.31	0.45	0.05	0.12	1
Emme	Emmenmatt	Unpeaked	0.26	0.30	0.24	0.41	1
Kander	Hondrich	Unpeaked	0.15	0.22	0.35	0.56	1
Langeten	Huttwill, Haberenbad	Unpeaked	0.16	0.20	0.04	0.07	1
Thur	Jonschwil, Muhlau	Unpeaked	0.28	0.42	0.65	1.12	1-2b
Ilfis	Langnau	Unpeaked	0.22	0.28	0.15	0.21	1
Luthern	Nebikon	Unpeaked	0.20	0.25	0.03	0.05	1
Simme	Oberwil	Unpeaked	0.14	0.22	0.15	0.26	1
Rhone	Reckingen	Unpeaked	0.13	0.20	0.09	0.22	1
Glatt	Rheinsfelden	Unpeaked	0.08	0.09	0.06	0.10	1
Areuse	St. Sulpice	Unpeaked	0.12	0.24	0.02	0.10	1
Murg	Wangi	Unpeaked	0.22	0.56	0.07	0.23	1
Wigger	Zofingen	Unpeaked	0.14	0.18	0.10	0.14	1

TABLE A.3: Swiss gauged stations grouped by corresponding maximum and minimum value of hydropeaking indicators $HP1$ and $HP2$ and hydropeaking pressure class changes (calculated based on six year data record).

Watershed	Gauged station	Group	HP1		HP2		Class
			Min	Max	Min	Max	
Numedalslagen	Bruhaug	Peaked	0.27	1.54	1.36	5.80	1-2b
Driva	Driva power plant	Peaked	0.20	0.71	6.08	16.54	2b
Driva	Driva v/Elverhøy bru	Peaked	0.14	0.22	0.97	2.56	1-2b
Tokke	Elvarheim	Peaked	0.07	0.08	2.06	3.18	1
Fortun	Fortun	Peaked	0.17	0.19	1.50	2.45	1-2b
Bardu	Fosshaug	Peaked	0.23	0.27	1.19	2.94	1-2b
Stjordalselva	Hegra bru	Peaked	0.34	0.80	0.98	2.40	1-2b
Otra	Heisel	Peaked	0.11	0.13	1.21	1.71	2b
Kafjord (Gáivuoneatnu)	Holm bru	Peaked	0.19	0.23	1.34	2.25	1-3
Mandal	Kjølemo	Peaked	0.26	0.37	1.31	2.02	2b
Nidelva	Rathe	Peaked	0.10	0.34	0.69	1.85	2b-3
Sokna	Sokna power plant	Peaked	0.15	0.17	1.25	2.07	1-3
Laerdalselvi	Stuvane	Peaked	0.15	0.34	0.75	1.75	2b
Laerdalselvi	Stuvane power plant	Peaked	0.06	0.26	0.27	0.76	2b
Storana	Ardalsvatn	Unpeaked	0.10	0.14	0.38	0.56	1
Austbygdai	Austbygdai	Unpeaked	0.16	0.25	0.12	0.33	1
Supphelleelvi	Boyumselv	Unpeaked	0.19	0.29	0.02	0.22	1
Flåmselva	Brekke	Unpeaked	0.17	0.20	0.22	0.48	1
Jolstra	Brulandsfoss	Unpeaked	0.09	0.11	0.31	0.50	1
Driva	Driva v/Risefoss	Unpeaked	0.14	0.19	0.10	0.26	1
Nidelva	Eggafoss	Unpeaked	0.17	0.20	0.13	0.28	1
Fusta	Fustvatn	Unpeaked	0.07	0.12	0.18	0.34	1
Storelva	Gloppenelv	Unpeaked	0.14	0.29	0.07	0.51	1
Helgaa	Grunnfoss	Unpeaked	0.19	0.21	0.32	0.58	1
Boelva	Hagadrag	Unpeaked	0.07	0.10	0.41	0.51	1
Forra	Høggås bru	Unpeaked	0.16	0.19	0.19	0.37	1
Nausta	Hovfoss	Unpeaked	0.19	0.33	0.13	0.88	1
Sokna	Hugdalen Bru	Unpeaked	0.23	0.28	0.21	0.43	1
Aardal	Kalltveit i Årdal	Unpeaked	0.23	0.28	0.09	0.14	1
Kileai	Kilen	Unpeaked	0.14	0.18	0.02	0.03	1
Nordelva	Krinsvatn	Unpeaked	0.13	0.20	0.04	0.12	1
Aurland	Lavisbrua	Unpeaked	0.08	0.14	0.07	0.14	1
Storana	Leirberget i Årdal	Unpeaked	0.11	0.18	0.09	0.29	1
Lilleelv	Lilleelv	Unpeaked	0.08	0.13	0.01	0.01	1
Manndalselva	Manndalen Bru	Unpeaked	0.13	0.18	0.04	0.09	1
Mevatnet	Mevatnet	Unpeaked	0.09	0.10	0.02	0.05	1
Oyensaa	Øyungen	Unpeaked	0.09	0.16	0.02	0.10	1
Guddalselva	Seimfoss	Unpeaked	0.10	0.16	0.03	0.08	1
Stryn	Strynsvatn	Unpeaked	0.05	0.07	0.11	0.20	1
Reisaelva	Svartfossberget	Unpeaked	0.07	0.10	0.12	0.27	1
Lygna	Tingvatn	Unpeaked	0.10	0.14	0.06	0.16	1

TABLE A.4: Norwegian gauged stations grouped by corresponding maximum and minimum value of hydropeaking indicators $HP1$ and $HP2$ and hydropeaking pressure class changes (calculated based on six year data record).

A.2.4 Statistical and sensitivity analysis

Preliminary χ^2 goodness-of-fit tests were run on each equivalent yearly data series (each gauged station for each year, for a total of 490 data series) to check for a possible normality of data; the tests were not significant for only 48 of 490 data series, thus allowing to reject the null hypothesis of normal distribution of discharge data and supports the choice of non-parametric estimators used in this analysis. The non-parametric thresholds defined by equations (A.6) and (A.7) can vary based on several factors, such as the climate of the investigated regions (i.e. southern or northern Alpine region or the Scandinavian Alps, in our case), the length of the considered $HP1_i^{unp}$ and $HP2_i^{unp}$ records (i.e single or multiple years), the breakdown time of the original dataset (data analysed at 15 or 60 minutes), and the number of stations used to compute them. If the hydropeaking thresholds change (eq. (A.6) and (A.7)), the same peaked gauged station may fall within different pressure classes, therefore we performed a set of analysis to assess the robustness of the method, and the sensitivity of the hydropeaking thresholds to the choice of reference unpeaked stream gauges. To achieve this goal thresholds calculation from the unpeaked group data was performed by building four different sub-datasets according to the following criteria, which correspond to the most relevant sources of variability in calculating the thresholds:

1. **Choice of country/geographical area:** thresholds were calculated by dividing the dataset in different countries (Italy, Switzerland and Norway). Multi-year datasets were available for every gauged station of Switzerland and Norway, and each year of record was considered as a different dataset;
2. **Choice of year:** thresholds were calculated for each year for all unpeaked stream gauges, when multiple years were available, for a total of 12 different threshold values for each indicator;
3. **Choice of number of stations required for the calculation:** thresholds calculation was repeated on an increasing number of stations extracted from the entire unpeaked dataset with a random sampling technique to avoid bias (random sampling without replacement). The random extraction was performed 1000 times from 2 to 275 stream gauges ($n-1$), thresholds were calculated for each extraction and a mean value of each threshold was eventually calculated over all the extracted thresholds;
4. **Choice of streamflow data time resolution:** thresholds were calculated from data with a resolution of 15 minutes and 60 minutes. Data acquired every 15 minutes were available only for the Italian and Swiss datasets. When data were collected at 15 minute intervals, we selected a subset of data corresponding to the hourly measurements (one out of four consecutive measurements).

The robustness of the method was assessed by applying a pairwise Mann-Whitney U, to test if each of the resulting sub-datasets was extracted by the same original population of data. If the test is not significant, each sub-dataset is extracted from the same population of unpeaked gauged stations. Mann-Whitney is the non-parametric ranking alternative of the Student t test. The following step consisted in calculating the thresholds using all the sub-datasets for each of the four criteria (i.e. 6 sub-datasets for the “Year” criterion), and applying the pairwise Mann-Whitney U test to assess whether the resulting thresholds correspond to the same class distribution for all dataset. Classes were iteratively calculated

using all possible combinations of hydropeaking thresholds for each sub-datasets (e.g Italian, or Swiss, or Norwegian unpeaked stations) and a Mann-Whitney test comparing each pair of classes within each subset was applied. For instance, six thresholds (three for each indicator) were calculated for different countries. Classes for each station were recalculated three times using the six different thresholds (three class values for each station). If the test is not significant, the classification of the stations does not significantly differ between each possible pair of thresholds within each sub-datasets.

A.2.5 Validation of the procedure

We have validated our method through the two following procedures. First we have randomly chosen an additional control dataset within a comprehensive list of Swiss hydrometric stations for which thirty year long streamflow data series at sub-daily time resolution is available. The random extraction selected six Swiss gauged stations with 30 year-long streamflow records for a total of 180 data series, which we did not label *a priori* as peaked or unpeaked. We then run the analysis using the thresholds calculated on the entire dataset to compute the classification. This “blind” classification exercise resulted in attributing to each of the 180 yearly datasets one of the four different classes of hydropeaking alteration. Only afterwards we have *a posteriori* verified whether each of the chosen six control stations are found downstream of intermittent hydropower releases from storage hydropower plants, labelling them as “peaked” or “unpeaked”. The final step of the validation has been to assess whether (i) yearly datasets, predicted by our method to have either moderate (classes 2a, 2b) or high hydropeaking pressure/alteration, belong to *a posteriori* identified “peaked” gauged stations; and whether (ii) yearly datasets belonging to *a posteriori* identified unpeaked stations group in class 1 (absent or low alteration). The outcome of such validation procedure for the proposed method has been considered satisfactory on the basis of the correspondence between the method predictions and the *a posteriori* assessment of the peaked and unpeaked stations.

The second procedure used to validate our method foresees to apply it to five peaked gauged stations located in Switzerland, for which an idealized natural flow regime reconstruction has been carried out by Jordan (2007), by means of an hydrological model that has been used to reconstruct the hourly streamflow time series corresponding to year 1993 in the absence of regulation provided by hydropower plants. These stations are: Rhone River at Branson, Saltina River at Brig, Rhone River at Sion and Port-du-Scèx and Vispa River at Visp.

A.3 Results

This analysis is conducted considering a total of 490 discharge equivalent yearly data series as defined at the end of Section A.2.1, corresponding to one year of data for each of the 105 examined gauging stations (see Table A.1) and for the entire length of the database (6 years or 1 year).

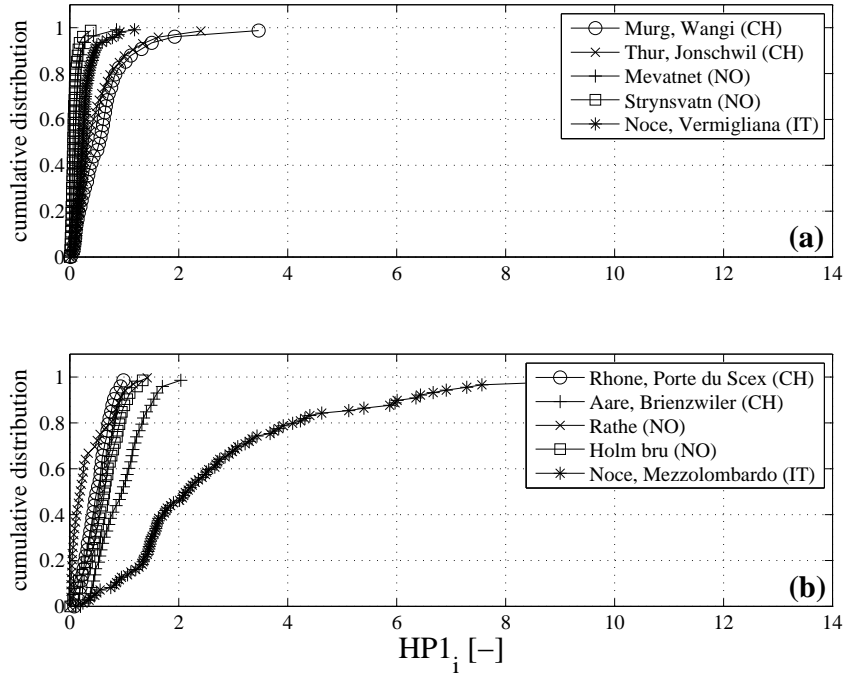


FIGURE A.2: Cumulative distribution of $HP1_i$ for some representative (a) unpeaked and (b) peaked gauged stations.

A.3.1 Peaked vs unpeaked stations: cumulative distributions of hydropeaking indicators

The cumulative distributions of the two indicators $HP1_i$ and $HP2_i$ are shown in Figures A.2 and A.3, respectively, for a selected subset of representative unpeaked and peaked stations: we selected the datasets with the highest and lowest median values of the two indicators, plus three datasets of random choice. The peaked stations show a higher degree of variability and larger median values and interquartile range for both indicators. The median value of $HP1$ for the entire dataset of unpeaked stations (282 data series) is 0.17 and the daily values $HP1_i$ are generally well-distributed around the median with interquartile distance equal to 0.26. Rare events (e.g. extreme summer storms, intense snow and ice-melting) are included in the higher 99th percentile (P_{99}) which equals to 2.33 with a maximum value of 15.00. The median value of $HP1_i$ for the peaked group is 0.46 and the interquartile distance 0.69, suggesting a greater inter- and intra- stations variability for this group. Extreme values for the peaked group are higher with a P_{99} of 3.52 and a maximum value of 24.

For the second indicator $HP2$ the differences between the two groups is more evident. In fact, the entire dataset of unpeaked stations has a median value of $0.17 \text{ m}^3\text{s}^{-1}\text{h}^{-1}$ and an interquartile range of $0.48 \text{ m}^3\text{s}^{-1}\text{h}^{-1}$ while the peaked group has a median value of $3.48 \text{ m}^3\text{s}^{-1}\text{h}^{-1}$ and an interquartile range of $9.74 \text{ m}^3\text{s}^{-1}\text{h}^{-1}$. Differences in extreme $HP2_i$ values between the two groups are qualitatively analogous to those detected in the case of $HP1_i$, with P_{99} of 8.69 and $39.53 \text{ m}^3\text{s}^{-1}\text{h}^{-1}$ and maximum values of $166 \text{ m}^3\text{s}^{-1}\text{h}^{-1}$ and $366 \text{ m}^3\text{s}^{-1}\text{h}^{-1}$ for the unpeaked and peaked group, respectively.

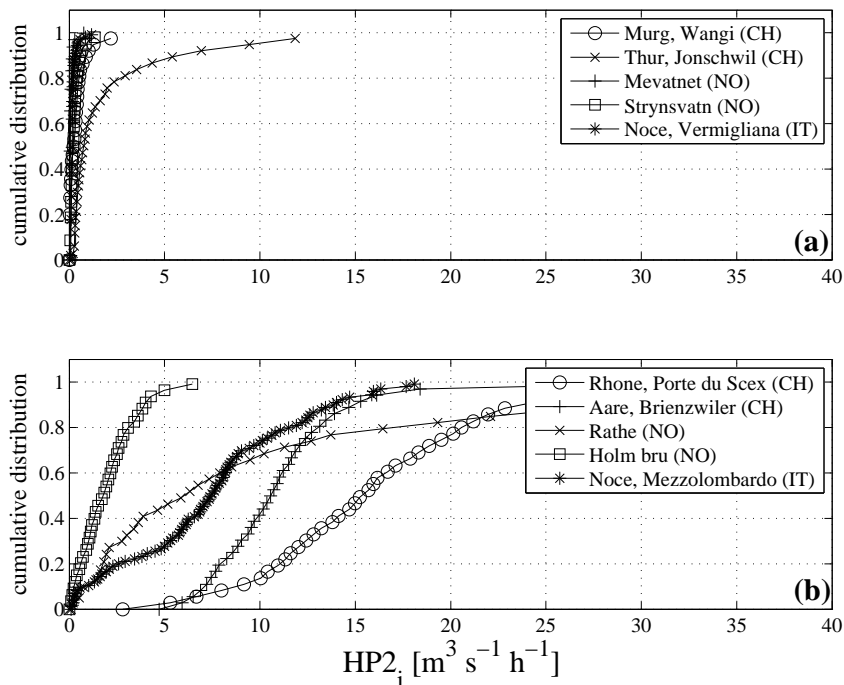


FIGURE A.3: Cumulative distribution of $HP2_i$ for some representative (a) unpeaked and (b) peaked gauged stations.

A.3.2 Class of hydropeaking alteration for the examined stations

Figure A.4 shows the distribution of the stations in the dataset in the $HP1$ and $HP2$ indicators space. Each panel refers to stations in a different country (a: Italy, b: Switzerland, c: Norway) and it is divided into four classes of hydropeaking alteration (or pressure, Section A.2.3) by the corresponding thresholds computed with reference to the unpeaked group of stations for that country. For each of the three different countries all the stations in the unpeaked group, except one, are below the hydropeaking thresholds TR_{HP1} and TR_{HP2} (class 1). Only one of the peaked stations falls in class 2a, i.e., river reaches characterized by high magnitude of hydropeaking (high $HP1$) and small values of the flow rate of change (small $HP2$) are very rare in the analysed dataset.

For the peaked group of the Italian dataset (Fig. A.4a and Table A.2), 43% of the gauged stations belong to class 3, 45% to class 2b, and 6.2% to class 1. Twenty-six percent of the Swiss peaked stations (Fig. A.4b and Table A.3) falls in the high pressure class (class 3) while 49% falls in the moderate pressure class 2b, and 25% in the low pressure class. Finally, the peaked Norwegian rivers (Fig. A.4c and Table A.4) are characterized by 11% of the dataset belonging to class 3, 69% to class 2b, and 20% to class 1.

The global distribution of the entire dataset is summarized in Figure A.5. Thresholds are calculated over the entire unpeaked dataset (282 data series). Ninety-eight percent of unpeaked stations belong to pressure class 1, 1% to class 2a and 1% to class 2b. Eighteen percent of peaked stations belong to class 1, 0.5% to class 2a, 56.5% to class 2b and 25% to class 3.

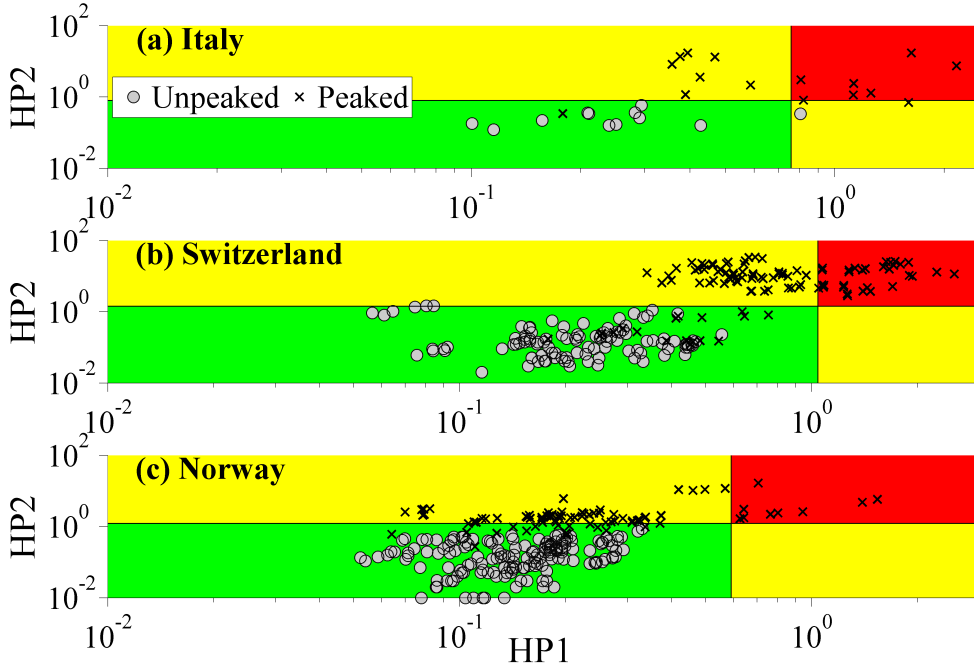


FIGURE A.4: Dataset distribution in classes of different pressures for Italian (panel a), Swiss (panel b) and Norwegian (panel c) data. Thresholds are calculated for each country. Different groups are denoted with cross (unpeaked) and circles (peaked). The space in the $HP1$ and $HP2$ plane is divided in 4 different regions identified by the two thresholds TR_{HP1} and TR_{HP2} which were computed for the three geographical regions considered. The four regions identify the three different classes of hydropeaking pressure: class 1 (absent or low pressure, green colour, left bottom); classes 2a and 2b (moderate pressure, yellow colour, right bottom and left top respectively) and class 3 (high pressure, red colour, right top).

A.3.3 Hydropeaking thresholds variability

We analysed how the hydropeaking thresholds TR_{HP1} and TR_{HP2} change depending on the sources of variability previously described in Section A.2.4. The results for the first three sources of variability (choice of country, year and number of reaches) are summarized in Table A.5. TR_{HP1} ranges between 0.96 and 1.14 and TR_{HP2} from 1.18 to 1.66 for the Swiss stations among all the years while TR_{HP1} ranges between 0.56 and 0.66 and TR_{HP2} from 1.10 to 1.59 for the Norwegian stations. Mann-Whitney tests pinpointed significant differences among the distributions of $HP1_i$ in the unpeaked group for the three countries ($p < 0.001$). In particular, the $HP1_i$ values for the Swiss stations were highly variable. The Mann-Whitney tests highlighted significant differences in $HP1_i$ and $HP2_i$ distributions ($p < 0.05$) between each pair of geographical areas.

The hydropeaking thresholds calculated using unpeaked flow data series belong to the same year were significantly different for each pairwise comparison (Mann-Whitney, $p < 0.001$), with the exception of pairwise comparison of indicators for years 2008 vs 2012 ($p = 0.40$ for $HP1$ and $p = 0.42$ for $HP2$). The assessment of the number of data series required to correctly define $HP1$ and $HP2$ thresholds showed that a minimum of 51 data series is required. In fact, using more than 50 unpeaked data series resulted in distributions of $HP1$ and $HP2$ not significantly different from the total distribution

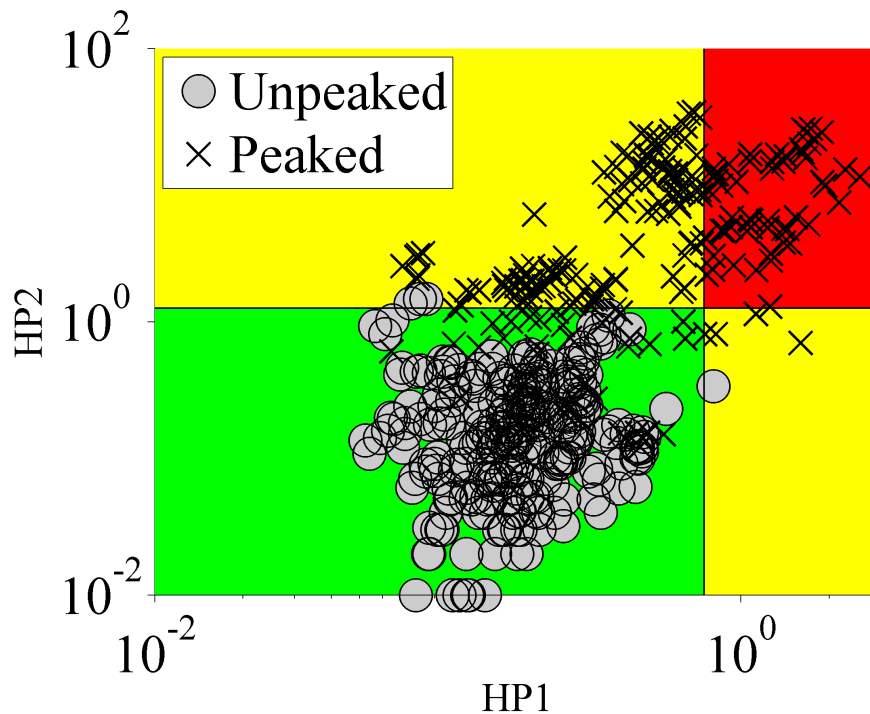


FIGURE A.5: Global distribution of all datasets in classes of different pressures. Thresholds calculated over the entire unpeaked dataset. Different groups are denoted with cross (unpeaked) and circles (peaked). The four regions identify the three different classes of hydropeaking pressure: class 1 (absent or low pressure, green colour, left bottom); classes 2a and 2b (moderate pressure, yellow colour, right bottom and left top respectively) and class 3 (high pressure, red colour, right top).

(Mann-Whitney tests, $p > 0.14$ for all pairwise comparisons), i.e., not further depending on the number of chosen yearly data series.

Finally we tested if the hydropeaking thresholds change for different distributions based on breakdown time, i.e. 15' vs 60'. The resulting distributions were highly different with $p < 0.001$ for both indicators. It is worth mentioning that the calculated confidence intervals were very narrow (0.7482 ± 0.001 for $HP1$ and $1.2315 \pm 0.002 \text{ m}^3\text{s}^{-1}\text{h}^{-1}$ for $HP2$, global thresholds), and therefore not included in the analysis of threshold variability.

A.3.4 Class changes of stations with thresholds variability

As the distributions used to calculate the thresholds significantly differed within each of the main criteria used to define the reference group of unpeaked stations (i.e. choice of country, year, number of stations and data resolution), we analysed if such thresholds variability would result in changes in the classification of hydropeaking alteration of the gauged stations, i.e. we investigated if a gauged station would change its hydropeaking pressure class due to thresholds changes. The class changes of the peaked group due to thresholds variations among the three countries were not significant ($p > 0.16$). For thresholds calculated referring to different years, changes were also not significant (lowest $p = 0.18$), although the comparisons were conducted between a one-year dataset of one station with thresholds calculated within the overall unpeaked data of that same year ($p < 0.001$). When the comparison of classes was performed with a progressively increasing

	Year	TR_{HP1}	TR_{HP2}
Italy	2012	0.76	0.79
	2007	1.10	1.61
Switzerland	2008	1.00	1.33
	2009	1.09	1.42
	2010	0.97	1.36
	2011	1.14	1.18
	2012	1.01	1.66
	Mean	1.04	1.43
Norway	2007	0.61	1.36
	2008	0.56	1.10
	2009	0.59	1.16
	2010	0.56	1.59
	2011	0.66	1.59
	2012	0.57	1.27
	Mean	0.59	1.21
	N° of data series		
	2	0.71	1.15
	5	0.73	1.17
	10	0.75	1.23
N° of data series	50	0.75	1.22
for the computation	100	0.75	1.23
	150	0.75	1.23
	200	0.75	1.23
Global thresholds	282	0.75	1.26

TABLE A.5: Hydropeaking threshold variability as function of: country, different years and number of gauged stations used for the computation.

number of stations, changes were significant only if thresholds were defined using less than 10 stream gauges ($p < 0.001$). Classes calculated using different data breakdown times were not significantly different with a minimum p value of 0.24. The classification of the unpeaked stations never changed significantly for any of the four criteria, with a lowest p value of 0.36.

Table A.6 summarizes the frequency of class changes associated with threshold variability due to different choice of country, years (Switzerland and Norway datasets), number of stations used for the calculation (from 2 stations up to 275) and breakdown time (15' vs 60', Switzerland and Italy datasets) to define the reference group of unpeaked stations. The frequency of class changes measures how many times a given data series of a station belongs to the same class. It is quantified through a value in the interval (0:1), with 0 meaning that no changes between classes occur, 1 meaning that changes in classes occur for each comparison within dataset. For instance, the frequency of 0.1 recorded in peaked Italian stations (first row and first column, table A.6) means that each stream gauge falls in the same class 90 % of the times, when classes were calculated using the three different country-specific thresholds values.

We verified which class changes occurred more frequently in the peaked stations (see Tables A.2, A.3, A.4, last column). The percentage of changes was always very low in

	Peaked			Unpeaked		
	IT	CH	NO	IT	CH	NO
Geographical areas	0.10 (0)	0.09 (0)	0.06 (0)	0.02	0.03	0
Years	-	0.09 (0)	0.15 (0.035)	-	0	0
Breakdown time	0 (0)	0.04 (0)	-	0	0.03	-
N° of data series	0.01 (0)	0 (0)	0 (0)	0	0.01	0

TABLE A.6: Frequency of class changes for different hydropeaking threshold, calculated for all the possible sub-datasets. In round brackets the frequency of changes between class 1 and class 3.

peaked stations and very often equal to zero in unpeaked stations. For all the possible sources of variability (Table A.6) the frequency of changes between class 1 and class 3, which is obviously the most critical for the robustness of the proposed methodology, was always zero except for one case (Norway, thresholds calculated referring to different years), still with a very low frequency (3.5%). Two Norwegian gauged stations were responsible for this change (see Table A.4): Sokna River station in Melhus at the Sokna power plant (once for the six year data record), and Holm Bru station (Kafjord River, twice). Considering the entire dataset, the most frequent changes occurred from class 2b to 3 (10.2 %) much less changes occurred between class 1 and 2b (4.2 %), while no changes were detected between 1 and 2a, 2a and 2b, and between 2a and 3.

A.3.5 Validation of the procedure

The random selection of the control dataset extracted station 2019, Aare-Brienzwiler; 2070, Emme-Emmenmatt; 2473, Rhein-Diepoldsau; 2152, Reuss-Luzern; 2372, Linth-Mollis and 2425, Kleine Emme-Littau. The control and the original dataset overlapped for eighteen yearly data series, i.e. six yearly data series for each of 2019, 2070 and 2473 stations. We computed the indicators ($HP1$, $HP2$) for the 180 yearly data series of the chosen six control stations and assigned classes of hydropeaking alteration using the global thresholds (see Table A.5, last row). Results are reported in Figure A.6. Three stations (2019, 2473, 2372) were predicted to lay always above at least one of the two thresholds for each of their thirty year long data series, therefore falling either in class 2b or in class 3 (Fig. A.6). The thirty yearly data series for each station always fell within the same class, except for station 2372 that shifted between classes 2b and 3 over time (after 1998), possibly due to changes in hydropower production patterns that altered both the rate and the magnitude of hydropeaking (denoted with a lozenge in Figure A.6). According to the procedure described in Section 2.5, were labelled as unpeaked. After the analysis, we have further verified whether or not the six control stations are actually found downstream of intermittent releases from storage hydropower plant: stations (2019, 2473, 2372) are actually located downstream storage hydropower plant releases, and have been therefore *a posteriori* labelled as peaked, while (2070, 2152, 2425) are not, and have been therefore *a posteriori* labelled as unpeaked. Finally, comparing the outcomes of the classification predicted by our method with the *a posteriori* labelling procedure has yielded a 100 % correspondence, namely: yearly datasets having either moderate (class 2b) or high (class 3) hydropeaking alteration, belong to *a posteriori* identified “peaked” gauged stations

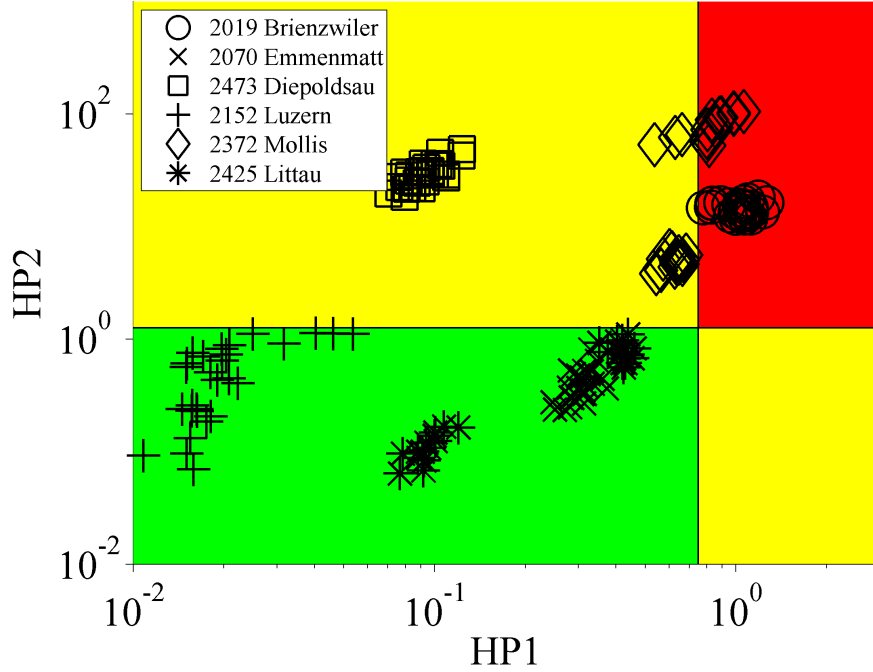


FIGURE A.6: Distribution of six stations used as control group. The displayed thresholds are the global thresholds. Different groups are denoted with cross (unpeaked) and circles (peaked). The four regions identify the three different classes of hydropeaking pressure: class 1 (absent or low pressure, green colour, left bottom); classes 2a and 2b (moderate pressure, yellow colour, right bottom and left top respectively) and class 3 (high pressure, red colour, right top).

(i.e. 2019, 2473, 2372); and yearly datasets belonging to *a posteriori* identified unpeaked stations (i.e. 2070, 2152, 2425) group in class 1 (absent or low hydropeaking alteration).

Results of the second validation procedure are given in Table A.7. For each station two hydropeaking classes have been computed. “Measured data” corresponds to the hydropeaking pressure class for that station obtained by computing the proposed indicators for the measured streamflow time series in 2007-2012 period. “Reconstructed data” refers to the hydropeaking class resulting after computing the indicators for the “natural” streamflow time series that has been reconstructed through an hydrological model by Jordan (2007) in the absence of hydropower plants. It clearly emerges how the proposed procedure is capable to discriminate peaked from unpeaked sub-daily streamflow series. In particular from the analysis of measured data it emerges that three stations fall into class 2b (Branson, Rhone; Porte du Scèx, Rhone; Sion, Rhone), one in class 3 (Visp, Vispa), and one in class 1 (Brig, Saltina) calculated using global thresholds. The analysis of the reconstructed data shows that all the five stations considered fall into class 1 even using the global thresholds. The station of Brig is in class 1 for both real and simulated data.

Watershed	Gauged station	Group	HP1	HP2	Class (simulated data)	Class (measured data)
Rhone	Porte du Scèx	Peaked	0.08	1.22	1	2b
Rhone	Branson	Peaked	0.07	1	1	2b
Rhone	Sion	Peaked	0.07	1.08	1	2b
Saltina	Brig	Peaked	0.06	0.28	1	1
Vispa	Visp	Peaked	0.09	0.18	1	3

TABLE A.7: Values of the two indicators calculated on the simulated data and comparison between classes of simulated data and measured data series.

A.4 Discussion

Several other studies have applied indicators in different countries to analyse and quantify sub-daily flow fluctuations in regulated rivers (Meile *et al.*, 2011; Zimmerman *et al.*, 2010; Sauterleute and Charmasson, 2014; Bevelhimer *et al.*, 2014). In our approach, the main hydrological differences between peaked and unpeaked rivers can be captured analysing the discharge signal focusing on two indicators: the magnitude of hydropeaking and the rate of change in discharge (*HP1* and *HP2*). The use of these two indicators allows classifying river stations based on their degree of alteration and assessing the sub-daily flow variations induced by water releases from storage hydropower plants.

The statistical analysis of class changes proposed by our method (see Table A.6) shows that classes remain the same even if the geographical location, year and temporal resolution of the discharge dataset used to calculate the thresholds changes. However, some stations moved between classes when different years were analysed. Two changes of class are particularly relevant: changes between medium and high hydropeaking pressure classes, and changes between low and any of the other hydropeaking pressure classes. Changes from medium to high pressure classes can be considered less relevant than changes between low pressure and any of the others for water managers, who should prioritize actions on heavily impacted river reaches. Only few stations (four in the Swiss dataset and one in the Norwegian dataset) slightly changed among peaked classes over time (from class 2b to 3 class). Some peaked stations were distributed near the thresholds and showed class changes between low and moderate pressure classes (1 to 2b). In this respect, the thresholds calculated on the entire dataset (Figs. A.5 and A.6) can be considered as *universal*, i.e. they clearly identify, for all the entire dataset, the stations with high hydropeaking pressure.

The robustness of the approach is confirmed by the example of the two Norway gauged stations (the Sokna power plant station on the Sokna River and the Holm bru station on the Kafjord River) which are the only gauged stations which showed extreme variability (e.g between low and high pressure classes) throughout the entire dataset. These stations were not regulated for part of the analysed period, which may explain the observed changes in class. The Sokna River station recorded periods of low peaking frequency, e.g. for a period in 2010 when the plant was shut down for maintenance, and in spring of 2012 when it ran continuously for weeks due to high inflow and large snowmelt. The Kafjord River experienced close-to-natural flood episodes especially in spring for the entire six year period, which may have been overimposed on the daily hydropeaking-induced flow regime alterations.

The thresholds derived by the application of our method are general and representative of a large set of unpeaked gauged stations. In fact, when validating the procedure, the unpeaked stations in the control dataset always grouped in class 1 of pressure classification (Fig. A.6 and Table A.7). Our analysis also showed that extreme class changes (from 1 to 3) are rare among peaked stations for different years, suggesting that the proposed methodology can characterize each station by using only one standard year. However, it is advisable to choose the longest available dataset in order to reduce the error rate; if a yearly dataset is chosen, it should be representative of the range of typical discharge variations, and it should be selected by technicians and practitioners with a good knowledge of the river systems.

A second outcome of our method regards the data breakdown interval at which the discharge data are measured. Previous research assessed the data breakdown time required to capture sub-daily flow variations (Zimmerman *et al.*, 2010; Bevelhimer *et al.*, 2014); these authors used both hourly and daily data and concluded that hourly data are necessary. Our results are in agreement with Bevelhimer *et al.* (2014) but as a further step we showed that a resolution lower than 60' is not necessary. In fact, the use of different breakdown time did not influence the indicators because class variations were not detected. Therefore, the classification is not statistically different using data at 15' or 60' breakdown time.

The methodology we proposed requires sub-daily data from unpeaked rivers to derive the thresholds to be used for the classification. From our analysis emerges that 10 data series of one year (e.g. 10 gauged stations for 1 year from unpeaked sites) are sufficient to produce robust thresholds. However, when 10 data series of one year are not available, the global thresholds (i.e. extracted from the entire dataset) defined in Table A.5 may be used for the classification. In fact, the exploration of all the possible sources of variability in the dataset (e.g. geographical areas, years, etc..) showed that unpeaked and peaked stations never significantly change classes when thresholds change (Table A.6). The caveat is to use data from similar climatic regions, in our case data from mountain streams and rivers.

Finally, our results show that the distributions from which the hydropeaking thresholds are computed differed significantly within each source of variability (country, years, etc.), and a minimum dataset size of 50 gauged stations is required to define the thresholds. In fact, this subset was statistically representative of the entire dataset of the unpeaked stations.

A.5 Conclusions

The method proposed here allows to classify river stations in four different classes of hydropeaking alteration defined on the basis of an unpeaked group of reference stations. Class changes among extreme classes are rare and can be explained by the different power plant management schemes for different years. Although the application of the proposed methodology is purely hydrological and has no direct significance for the assessment of the effects on the river ecology, the proposed methodology is nonetheless particularly interesting for management. In fact, because the stations with high pressure of hydropeaking never change class for different years, our method objectively identifies the stations where restoration projects should be implemented. Moreover, the robustness of this methodology, and the relative ease of application, can potentially lead to its use in regulatory and monitoring activities. For instance, the classification of the stream ecological state

as required by the EU Water Framework Directive (European Commission, 2000) introduces hydromorphology as one of the elements to be evaluated, together with water and biological quality, to obtain the evaluation and classification of the ecological status of a water body. The method proposed here could be integrated in a quantitative evaluation procedure to classify the stream hydrological quality.

The ease of use assures that the method could be used by competent authorities (i.e., public agencies, river basin managers); if calibrated according to the different climatic conditions of one country, it could cover the full range of physical conditions, morphological types, degree of artificial alterations existing there.